

University of Nottingham
UK | CHINA | MALAYSIA

The entrapment, manipulation, and transformations of inorganic materials at the nanoscale

Luke Thomas Norman, MSci.

Thesis submitted to the University of Nottingham

for the degree of doctor of Philosophy

July 2021

Abstract

The work presented in this thesis investigates demonstrates the unique ability of single-walled carbon nanotubes (SWNTs) to be able to use their interior channel as a nano test tube to study the structure and composition of inorganic materials at the nanoscale, as well as conduct chemical reactions within. Each system presented was strategically designed, and studied using a holistic analytical approach which combined a range of electron microscopy, and spectroscopic techniques and revealed nanomaterials with novel structures, compositions, and coordinations that are not possible to obtain using bulk synthetic techniques. The targeted synthesis of ultrathin rhenium disulfide nanoribbons was conducted within SWNTs using a stepwise methodology. Aberration-corrected high-resolution transmission electron microscopy (AC-HRTEM) was able to resolve the twisted structure of the synthesised nanoribbons, and the strong interactions between the host and guest resulting in an elliptical distortion of the SWNT. The differences of the two surface sites of SWNTs, the concave and convex, were examined by conducting a stepwise series of chemical reactions of osmium compounds on each site simultaneously. AC-HRTEM revealed that the concave surface produced size-templated sub-nm nanowires with reduced coordination and stabilised by the SWNT surface, whilst the convex surface produced larger nanoparticles with higher coordinations and novel shell structures stabilising the high number of dangling bonds. The insertion of thiomolybdate-based clusters into SWNTs was found to proceed by coulombic attraction initiated by electron donation from the nanotubes to the clusters, as demonstrated by Raman spectroscopy. Furthermore, their structure and orientations observed in AC-HRTEM were determined by correlation of projections with a rotation series of TEM simulations, and their fast translational motion was captured between sequential images. The reaction of the clusters with iodine resulted in molybdenum chalcogenide nanoribbons including Janus MoSSe; a species only synthesised as a monolayer

previously. *ChemTEM*, a process of the TEM electron beam simultaneously imaging a material whilst also providing energy to the system, was employed for studying the structures of synthesised tungsten disulfide nanoribbons within SWNTs and boron nitride nanotubes (BNNTs). Within SWNTs, the ejection of individual atoms and atomic chains were witnessed and promoted using the electron beam, resulting in the formation of a one atom thick nanowire which was characterised by contrast analysis. A BNNT containing amorphous material was imaged using AC-HRTEM; the electron beam was found to stimulate crystallisation and growth of tungsten disulfide quantum dots size-templated by the BNNT inner channel. Metal chalcogenide nanomaterials within SWNTs were tested as electrocatalysts towards the Hydrogen Evolution Reaction and found to perform well compared to larger nanostructures formed previously. This was a result of the SWNTs templating the formation of nanostructures with a high proportion of catalytically-active edge atoms, and being able to transport electrons to and from the guest species.

Acknowledgements

Firstly, I would like to thank my two supervisors Prof. Andrei Khlobystov and Prof. Peter Beton for all of their enthusiasm and guidance during the four years of my PhD. Their knowledge and expertise has helped the shape the project, and developed me into the scientist I am today.

Since my inception within the group in 2016 as an MSci student, there has always been one member of the group who has offered me unwavering support, mentorship, and friendship, and that is Dr. Craig Stoppiello. From our discussions of triangles in TEM images, to chats in the tea room about the brilliance of the film *Shrek*, he has been an excellent colleague and friend.

There also has to be a special mention for two members of the group, Dr. Max Astle and Dr. Jack Jordan who have assisted me scientifically with PXRD, TGA, and electrochemistry measurements, but also helped make these past four years incredibly enjoyable by being great friends.

This thesis would not be the thesis it is today without a group of collaborators who each assisted with electron microscopy, and spectroscopy techniques; *The Avengers* of materials characterisation.

The first is Dr. Graham Rance who has been very important to my thesis by performing Raman spectroscopy measurements of prepared materials, and taking time to discuss a lot of the underlying themes within this work. The second is the team at Ulm University consisting of Dr. Johannes Biskupek and Prof. Ute Kaiser who performed AC-HRTEM imaging of samples, and were excellent hosts during my trip to visit the outstanding SALVE centre. The third is Dr. Christopher Allen at the ePSIC facility at Diamond Light Source who performed

fast capture AC-HRTEM, which enabled the determination of novel structures and reveal new mechanisms.

A special thanks is also given to the team at the nmRC for training on equipment and to the Prof. Eugenio Coronado research group in Valencia, in particular to Dr. Antonio Alberola who supported me with work on thiomolybdate based clusters.

Not all those who wander are lost, especially those who are surrounded by a fellowship such as the Nottingham Nanocarbon Group. In particular, Steve, Rhys, Julie, Kayleigh, Will T, and Will C who have all made contributions to this thesis. I have also had the opportunity to help supervise three excellent MSci students; Ebuka Ezeugwa, Thomas Selby, and Tom Robinson; the latter of whom evaluated a range of materials towards electrocatalytic hydrogen production which became a chapter of this thesis.

I would like to thank my parents, Linda and Glenn, who have always provided love and support during my PhD. I would not be where I am now without them. The final thanks goes to my fiancée Bethan, she has been there for me since day one at the University of Nottingham, and her encouragement, motivation and support has meant the world to me every single day since.

Abbreviations and symbols

Abbreviation / symbol	Term
@	Encapsulated within
1D	One-dimensional
2D	Two-dimensional
AC-HRTEM	Aberration-corrected high-resolution transmission electron microscopy
BF	Bright field
BNNT	Boron nitride nanotube(s)
BWF	Breit-Wigner-Fano
CVD	Chemical vapour deposition
CNT	Carbon nanotube
DFT	Density functional theory
DSC	Differential scanning calorimetry
DWNTs	Double-walled carbon nanotubes
e-beam	Electron beam
EBIE	Electron beam induced ejection
EDX	Energy-dispersive X-ray analysis
EELS	Electron energy-loss spectroscopy
eV	Electron volts
FD-XAS	Fluorescence-detected X-ray absorption spectroscopy
FET	Field effect transistor
HAADF	High angle annular dark field

HER	Hydrogen evolution reaction
IR	Infrared spectroscopy
kV	kilovolts
LSV	Linear sweep voltammetry
MWNT	Multi-walled carbon nanotube
NR	Nanoribbon
NW	Nanowire
ORR	Oxygen reduction reaction
PCC	Perchlorocoronene
PL	Photoluminescence
POM	Polyoxometallate
PXRD	Powder X-ray diffraction
QD	Quantum dot
RBM	Radial breathing mode
RHE	Reversible hydrogen electrode
S-GNR	Sulfur-terminated graphene nanoribbons
STEM	Scanning transmission electron microscopy
SWNT	Single-walled carbon nanotube
TEM	Transmission electron microscopy
TGA	Thermogravimetric analysis
TMDC	Transition metal dichalcogenide
TTF	Tetrathiafulvalene
WDX	Wave-dispersive X-ray analysis
XPS	X-ray photoelectron spectroscopy

List of publications

[1] Morant-Giner M., Brotons-Alcázar I., Shmelev N. Y., Gushchin A. L., **Norman L. T.**, Khlobystov A. N., Alberola A., Tatay S., Canet-Ferrer J., Forment-Aliaga A., Coronado E., WS_2/MoS_2 Heterostructures through Thermal Treatment of MoS_2 Layers Electrostatically Functionalized with W_3S_4 Molecular Clusters, *Chem. Eur. J.* 2020, **26***,* 6670.

Part of a special issue of Chemistry: A European Journal entitled *Chemical Functionalization of 2D Materials*. The paper was later selected as a "Hot Paper" by the journal editors.

[2] **Norman L. T.,** Biskupek J., Rance G. A., Stoppiello C. T., Kaiser U., and Khlobystov A. N., Synthesis of ultrathin rhenium disulfide nanoribbons using nano test tubes, *Nano Res.*, 2022, **15**, 1282-1287.

[3] Astle M. A., Weilhard A., Rance G. A., Lemercier T., Stoppiello C. T., **Norman L. T.**, Alves Fernandes J., Khlobystov A. N., Guided etching of defects through the walls of carbon nanotubes: fabrication of porous carbon nanoreactors for catalysis, *ACS Nano.,* 2021 submitted.

[4] **Norman L. T.**, Stoppiello C. T., Allen C. S., Biskupek J., Rance G. A., Astle M. A., Lodge R. W., Kaiser U., Beton P. H., Khlobystov A. N., Exploiting both sides of nanotubes to support inorganic reactions: control of size, shape, and structure of osmium compounds by convex and concave surfaces at the nanoscale, 2021 (manuscript in prep.)

Table of contents

Abstract....1

Acknowledgements....3

Abbreviations and symbols....5

List of publications....7

Chapter 1: The entrapment, manipulation and transformations of materials at the nanoscale....12

1.1. The entrapment of materials at the nanoscale....12
1.1.1. Single-walled carbon nanotubes: structure and properties....13
1.1.2. The filling of materials into SWNTs....15

1.2. Techniques for characterising entrapped materials....25
1.2.1. TEM....25
1.2.1.1. Contrast formation and analysis....28
1.2.2. Spectroscopic methods....31
1.2.2.1. EDX....31
1.2.2.2. Raman....33
1.2.2.3. IR....37
1.2.2.4. XPS....39

1.3. Manipulation of entrapped materials....42

1.4. Inorganic transformations within carbon nanotubes....46
1.4.1. Thermal activations of guest species in nanotubes....46
1.4.2. Stepwise transformations of inorganic materials in nanotubes....48
1.4.2.1. Formation of transition metal dichalcogenides....51

1.5. Applications of filled carbon nanotubes....55

1.6. Aim and objectives....58

1.7. References....59

Chapter 2: Synthesis of ultrathin rhenium disulfide nanoribbons....69

2.1. Introduction....69

2.2. Results and Discussion....72
2.2.1. Synthetic route....72
2.2.2. Insertion of the carbonyl....73
2.2.3. Reaction to form the iodide....77
2.2.4. Reaction to form the sulfide....83

2.3. Conclusion 87

2.4. Experimental 88
2.4.1. Materials 88
2.4.2. Insertion of dirhenium decacarbonyl into SWNTs 88
2.4.3. Reaction of $Re_2(CO)_{10}$@SWNT with iodine 88
2.4.4. Reaction of n[$Re_6I_{14}^{2-}$]@SWNT^{2n+} with hydrogen sulfide 88
2.4.5. Electron microscopy and energy-dispersive X-ray analysis 89
2.4.6. Raman spectroscopy 89
2.4.7. X-ray photoelectron spectroscopy 89
2.4.8. TEM simulations 90

2.5. References 90

Chapter 3: Exploiting both sides of nanotubes to support inorganic reactions: control of size, shape, and structure of osmium compounds by convex and concave surfaces at the nanoscale 94

3.1. Introduction 94

3.2. Results and Discussion 96
3.2.1. Insertion of the carbonyl 98
3.2.2. Reaction to form the iodide 103
3.2.3. Reaction to form the sulfide species 112

3.3. Conclusions 120

3.4. Experimental 121
3.4.1. Materials 121
3.4.2. Encapsulation of $Os_3(CO)_{12}$ into single-walled carbon nanotubes 121
3.4.3. Preparation of osmium iodide 121
3.4.4. Preparation of osmium disulfide 122
3.4.5. Electron microscopy and energy-dispersive x-ray spectroscopy 122
3.4.6. TEM simulation 122
3.4.7. Raman spectroscopy 122
3.4.8. Infrared spectroscopy 123
3.4.9. X-ray photoelectron spectroscopy 123
3.4.10. Powder x-ray diffraction 124

3.5. References 124

Chapter 4: Triangular molybdenum chalcogen clusters: entrapment and transformations within nano test tubes 128

4.1. Introduction 128

4.2. Results and discussion 131
4.2.1. Tetrabutylammonium thiomolybdate hexabromide 131
4.2.1.1. Insertion of the cluster within SWNTs 132
4.2.1.2. Reaction with iodine 148
4.2.2. Tetrabutylammonium thio-selenomolybdate hexabromide 155

4.2.2.1. Insertion of the cluster within SWNTs 156
4.2.2.2. Reaction with iodine 164

4.3. Conclusions 175

4.4. Experimental 176
4.4.1. Materials 176
4.4.2. Insertion of $[Bu_4N]_2[Mo_3S_7Br_6]$ / $[Bu_4N]_2[Mo_3S_4Se_3Br_6]$ into SWNTs 177
4.4.3. Reaction to form MoS_2@SWNT / MoSSe@SWNT 177
4.4.4. Electron microscopy, energy-dispersive x-ray analysis, and wave-dispersive x-ray analysis 177
4.4.5. Raman spectroscopy 178
4.4.6. X-ray photoelectron spectroscopy 178
4.4.7. Structural modelling and TEM simulation 179

4.5. References 179

Chapter 5: Tungsten disulfide nanoribbons within carbon and boron nitride nanotubes: synthesis, structural and dynamic analysis by ChemTEM 183

5.1. Introduction 183

5.2. Results and Discussion 187
5.2.1. WS_2 within single-walled carbon nanotubes 187
5.2.1.1. Insertion of the $\{W_{12}\}$ POM into SWNTs 189
5.2.1.2. Reaction with H_2S to form WS_2 nanoribbons 193
5.2.2. WS_2 within boron nitride nanotubes 205
5.2.2.1. Insertion of the W_{12} POM into BNNTs 206
5.2.2.2. Reaction to form WS_2 in BNNTs 214

5.3. Conclusion 231

5.4. Experimental 232
5.4.1. Materials 232
5.4.2. Insertion of $\{W_{12}\}$ into SWNTs/BNNTs 233
5.4.3. Reaction to form WS_2@SWNT / WS_2@BNNTs 233
5.4.4. Electron microscopy, energy-dispersive x-ray analysis, and STEM-EDX mapping 233
5.4.5. Raman spectroscopy 234
5.4.6. X-ray photoelectron spectroscopy 234
5.4.7. Thermogravimetric analysis 235
5.4.8. Structural modelling and TEM simulations 235

5.5. References 235

Chapter 6: Measuring the hydrogen evolution ability of metal chalcogenide nanomaterials within carbon nanotubes 240

6.1. Introduction 240
6.1.1. Hydrogen Evolution Reaction (HER) 240

6.1.2. Platinum as an electrocatalyst 241
6.1.3. MoS_2 performance 242
6.1.4. Carbon nanotubes 243
6.1.5. Aim and objectives 244

6.2. Results and Discussion 245
6.2.1. Evaluation of the SWNT hosts 245
6.2.2. Comparison of 1D MoS_2 using different synthetic routes 248
6.2.2.1. *Synthesis of MoS_2@SWNT-A (via $Mo(CO)_6$)* 249
6.2.2.2. *Synthesis of MoS_2@SWNT-B (via $H_3PMo_{12}O_{40}$)* 253
6.2.2.3. *Synthesis of MoS_2@SWNT-C (via $[Mo_3S_7Br_6]^{2-}$)* 259
6.2.2.4. MoS_2@SWNT HER performance 264
6.2.3. Changing the metal 266
6.2.4. Comparison of the edge-site molecular mimic 269
6.2.5. Janus MoSSe and corresponding molecular mimic 272

6.3. Conclusion 275

6.4. Experimental 277
6.4.1. Materials 277
6.4.2. Formation of MoS_2@SWNT-A by using $Mo(CO)_6$ 278
6.4.3. Preparation of $H_3PMo_{12}O_{40}$ 278
6.4.4. Formation of MoS_2@SWNT-B by using $H_3PMo_{12}O_{40}$ 279
6.4.5. Formation of $n[Mo_3S_7Br_6]^{2-}$@$SWNT^{2n+}$ and MoS_2@SWNT-C 279
6.4.6. Formation of WS_2@SWNT by using $H_3PW_{12}O_{40}$ 280
6.4.7. Formation of $n[Mo_3S_4Se_3Br_6]^{2-}$@$SWNT^{2n+}$ and Janus MoSSe@SWNT 280
6.4.8. Electron microscopy and energy-dispersive x-ray analysis 280
6.4.9. Raman spectroscopy 280
6.4.10. Thermogravimetric analysis 281
6.4.11. Hydrogen Evolution Reaction Measurements 281

6.5. References 281

Chapter 7: Concluding Remarks 286

7.1. References 290

Chapter 1: The entrapment, manipulation and transformations of materials at the nanoscale

1.1. The entrapment of materials at the nanoscale

The nanoconfinement of materials can have extraordinary effects on their structure and properties and can occur within a wide range of host systems. For example, the encapsulation of gold nanoparticles within porous carbon microspheres derived from phoenix tree leaves has led to enhanced electrochemical performance demonstrated by excellent cycling stability for use as an electrode material in energy storage devices,[1] and metal organic frameworks filled with hydrophobic molecules have been found to improve energy transfer between the host and guest.[2] There are also examples of two-dimensional nanoconfinement, such as the entrapment of fullerenes between two layers of graphene allowing the analysis of the structure of the molecules and their dynamics at atomic resolution.[3] At the extreme end of the scale, zero-dimensional entrapment of individual metal atoms within fullerene molecular cages, denoted as endohedral metallofullerenes, have shown promise in applications as contrast agents for magnetic resonance imaging.[4] However, it is the quasi-one-dimensional host of single-walled carbon nanotubes (SWNTs) that have attracted extraordinary interest as containers for molecules and atoms since their discovery in 1993.[5, 6]

1.1.1. Single-walled carbon nanotubes: structure and properties

SWNTs are hollow cylindrical structures, that have diameters between 0.8 – 2.0 nm[7] and lengths up to the mm scale,[8] this high aspect ratio means that they bridge the gap between the macroscale and nanoscale. The one-dimensional structures boast an extraordinary range of physical properties such as; a tensile strength 50 times higher than steel,[9] thermal stability up to 2800 °C in vacuum, and a current carrying capacity 1000 times higher than copper.[10]

SWNTs can be hypothetically viewed as a sheet of graphene that is rolled up into a cylinder, with carbon atoms in sp^2 hybridisation. The roll up vector, which defines the circumference, is described by a relationship between the lattice vectors of graphene ($\boldsymbol{a_1}$ and $\boldsymbol{a_2}$), which define the unit cell of graphene and have a value of 2.46 Å, with parameters called chiral indices (*m* and *n*, Figure 1.1a), which stipulate the nanotube structure, as:

$$\boldsymbol{R} = m.\boldsymbol{a_1} + n.\boldsymbol{a_2}$$

Equation 1.1.

where $\boldsymbol{R}$ *– roll up vector, m and n – chiral indices of carbon nanotube, and* $\boldsymbol{a_1}$ *and* $\boldsymbol{a_2}$ *– lattice vectors of graphene.*[11]

These indices define the type of nanotube formed; zigzag (*n* = 0, Figure 1.1b), armchair (*n* = m, Figure 1.1c), or chiral ($n \neq m$, Figure 1.1d) and can also be used to determine the diameter of the SWNT using the following:

$$d_{SWNT} = \frac{a}{\pi}\sqrt{m^2 + n^2 + n.m}$$

Equation 1.2.

where *a* – length of the unit vector.

The structure of SWNTs also dictate their electronic properties as being either metallic or semiconducting in nature; metallic SWNTs must satisfy the conditions of $m - n = 3k$, whilst semiconducting SWNTs must satisfy $m - n \neq 3k$ – where k is an integer including zero.[12]

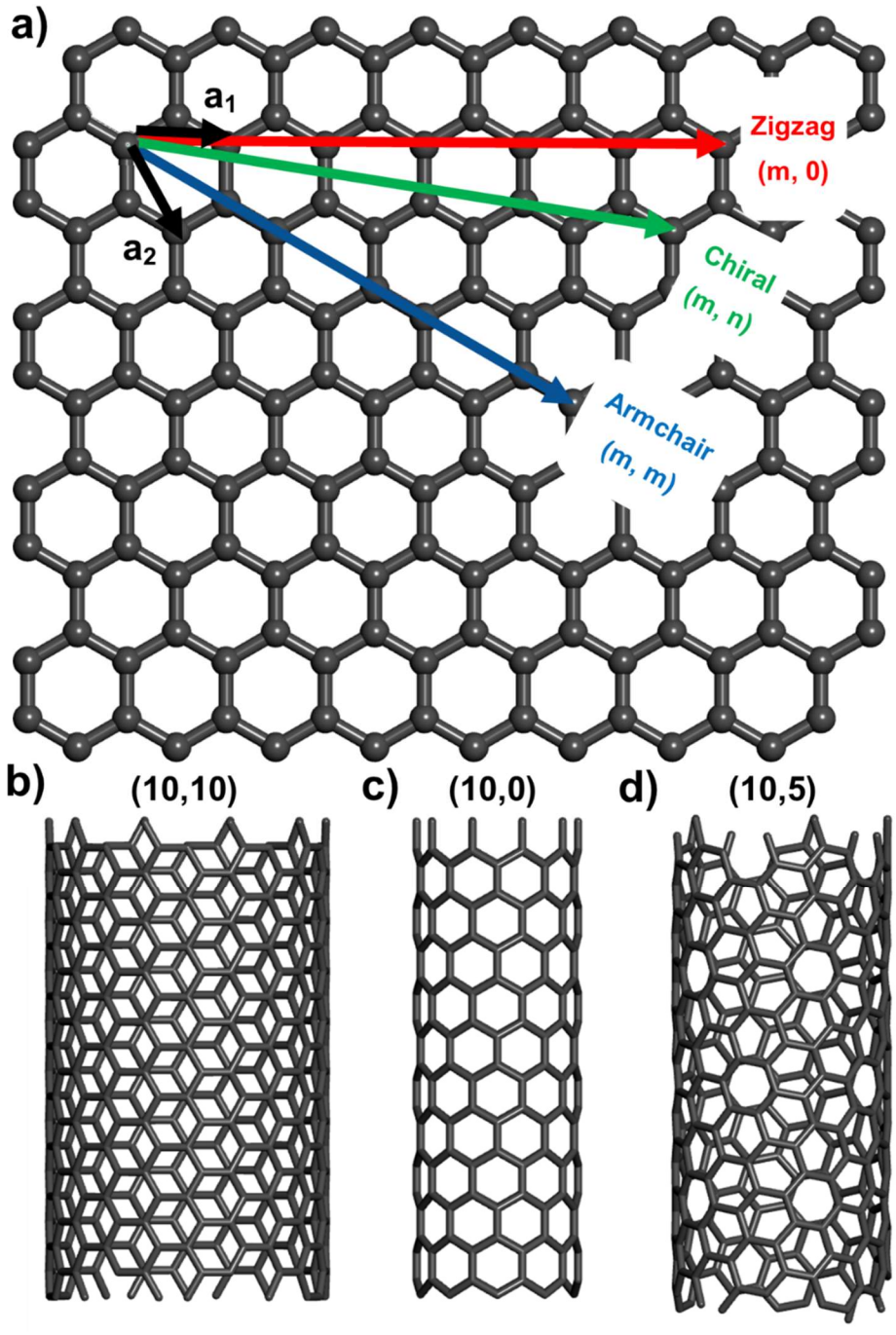


Figure 1.1. *(a) A sheet of graphene showing possible roll up vectors that lead to the formation of (b) armchair (n = m), (c) zigzag (n = 0), and (d) chiral (n ≠ m) SWNTs. Also shown are the lattice vectors of graphene labelled as* $\boldsymbol{a_1}$ *and* $\boldsymbol{a_2}$*.*

When SWNTs were first identified in 1993[5, 6], they were produced using carbon arc techniques which were only sufficient to produce enough material for small-scale investigations. However, in 1996, a laser vaporisation technique was developed in which laser pulses were fired at a carbon target modified with a nickel-cobalt alloy, at 1200 ^{o}C.[13] This was found to be a more efficient process, producing a SWNT yield of around 70% presented as bundles of between 100 to 500 SWNTs. A year later, an arc-discharge method was established which produced SWNTs on the gram scale using metal catalysts such as nickel, cobalt and iron, however, the method was shown to produce other carbon nanomaterials such as graphite and metal carbide nanoparticles, and thus the products do require purification.[14] More recently, it has been shown that the heterogeneous catalysis technique chemical vapour deposition (CVD) is also efficient for SWNT growth that requires lower temperatures than arc-discharge or laser vaporisation, making the procedure more favourable for industry use.[15] Nickel was found to be the optimum catalyst for low temperature growth using methane as a carbon feedstock and aluminium as the support layer.[16]

1.1.2. The filling of materials into SWNTs

The filling of SWNTs with guest species is strongly motivated by a number of factors; the first is the ability to image and study encapsulated species down to the atomistic level, using techniques such as transmission electron microscopy (TEM), with their mobility restricted along the nanotube axis.[17] A further motivation is the extreme confinement offered by SWNTs; this has the ability to template novel structures of existing materials, that are not exhibited in bulk.[18] The third is that SWNTs offer protection to guest species from the environment, such as oxidation by O_2 of air,[19] solvolysis during electrochemical measurements,[20] or hydrolysis in acidic or alkaline conditions.[21] Finally, the composite host-

guest material may be used towards a particular application; the electrically-conducting hosts can act as nano-electrodes ensuring electron transport to/from the guest,[22] moreover, the guest species will have a high proportion of surface atoms compared to core atoms which makes them more catalytically-active towards a range of processes such as the Hydrogen Evolution Reaction (HER).[23]

SWNTs can be filled either during their growth (in-situ) or post synthesis (ex-situ); the in-situ filling technique is a single-step process that can occur using either CVD or arc-discharge techniques, but examples in the literature are mostly limited to fillings within multi-walled carbon nanotubes (MWNTs) with catalytic metals, such as Fe or Ni, used in the synthesis.[24]

The number of in-situ fillings of SWNTs are scarce; an example was the encapsulation of bismuth nanoparticles after modifying an arc-discharge experimental procedure with bismuth as a cocatalyst.[25] Perhaps the most famous example was the accidental discovery of C_{60} fullerenes within the confines of single-walled carbon nanotubes (denoted as C_{60}@SWNT) that were a result of pulsed laser vaporisation of graphite by Smith, Monthioux, and Luzzi in 1998 (Figure 1.2).[26] The fullerenes were imaged by TEM and appeared as circular projections, 0.7 nm in diameter, that were separated by a regular distance between adjacent molecules, and the nanotube sidewalls, both by 0.3 nm corresponding to the graphitic Van der Waals gap; these structures were referred to as peapods. It was later determined that the encapsulation of C_{60} provides a 3 eV energy gain per molecule due to the van der Waals forces and geometric match of the concave surface with the fullerene shape, thus it is spontaneous and irreversible for the molecules to insert into SWNTs.[27]

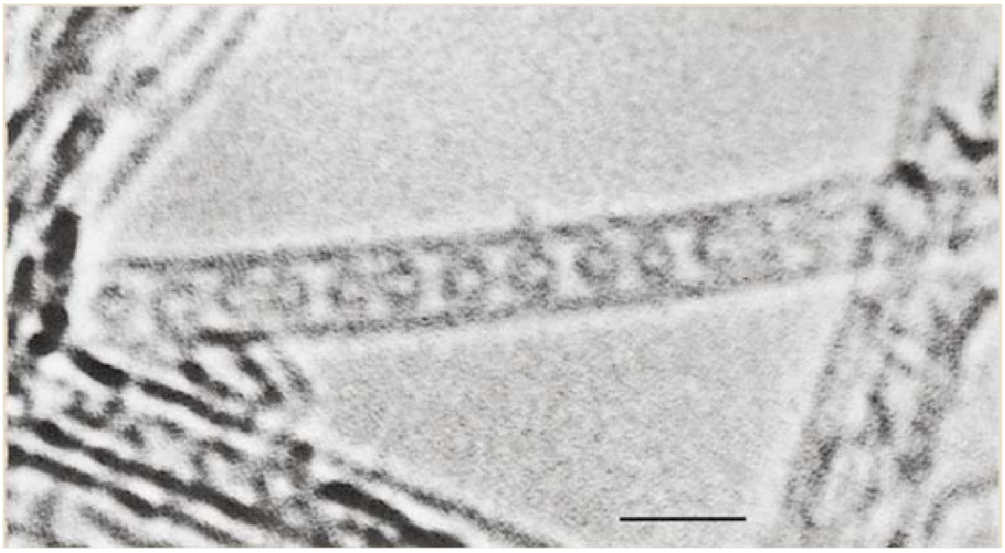


Figure 1.2. *100 kV HR-TEM image of C_{60} fullerenes within a 1.3 nm SWNT formed by pulsed laser vaporisation of graphite, resulting in a peapod structure.*[26]

Since the discovery of peapods, further investigations have filled SWNTs with fullerenes using ex-situ methods including by the vapour-phase,[28] molten-phase,[29] or solution-phase.[30] Ex-situ techniques first require the as-synthesised nanotubes to undergo either thermal[31] or acidic treatment[32] which removes the reactive end caps, for diffusion of materials into the inner channel.

Yudasaka *et al*. proposed two different methodologies towards solution-phase filling of fullerenes coined nano-extraction and nano-condensation which differ based on the relative affinities between the host, guest and solvent used. Nano-extraction relies on weak affinities between the solvent and both the host and guest, coupled with strong interactions between the host and guest. This leads to the C_{60} molecules being greatly attracted to the interior of the SWNTs and encapsulation occurring. Conversely, nano-condensation required strong affinities between the solvent, host and guest molecules; the mechanism of filling occurs by the guest solution depositing on the SWNT surfaces and the C_{60} molecules migrating and depositing within the SWNT interior. Both methodologies were shown to be successful for

the high filling of C_{60} into SWNTs and further develop the understanding of solution-phase encapsulation.

As well as TEM, spectroscopic techniques have also been used to study C_{60}@SWNT including Raman spectroscopy, which resolved the C_{60} active modes,[28] and UV-visible, which was used to quantify the level of filling.[33] These composite peapod materials have shown promise towards applications in solar cell production,[34] and have been predicted to be promising quantum information processing systems.[35]

The ex-situ filling offers better control towards the amount of material encapsulated, as well as opens up a wider range of materials that can be encapsulated, and thus the majority of the next section will focus on SWNTs that are filled with materials using ex-situ techniques.

Polyoxometalates (POMs) are molecular forms of metal oxides which are of interest due to their redox properties. Lindqvist tungsten POMs, $[W_6O_{19}]^{2-}$, were first studied within double-walled carbon nanotubes (DWNTs) to investigate their rotational and translational motion within the channel.[36, 37] It was found that rotational motion was restricted to one degree of freedom due to the steric shape of the anion, and that translational motion is controlled along the diameter of the DWNT. In a subsequent study, Keggin and Wells-Dawson tungsten POMs ($[PW_{12}O_{40}]^{3-}$ and $[P_2W_{18}O_{62}]^{6-}$) were encapsulated into SWNTs, and it was shown to occur via a coulombic attraction mechanism commencing by electron density donation from the host to the excess POMs in solution.[21] Moreover, the molecules were found to retain their redox properties whilst encapsulated, including in alkali conditions which POMs are not usually stable in.

As previously mentioned SWNTs offer protection to guest species from oxidation and this was a key driving force for the encapsulation of tetrahedral white phosphorus (P_4) molecules within SWNTs by Hart *et al*.[19] The material was encapsulated into SWNTs via the molten phase, under an inert atmosphere, and was initially shown using TEM to exist as strings of P_4

molecules; the structure and composition was further confirmed using a combination of structural modelling, TEM simulation, and X-ray photoelectron spectroscopy (XPS, Figure 1.3a - e). During imaging, continuous chains were produced with a zigzag structure; the formation of these new structures were attributed to the prolonged electron beam exposure. White phosphorus, in the bulk, undergoes spontaneous combustion upon exposure to oxygen releasing -2971 kJ mol^{-1} of energy; however, when encapsulated within SWNTs, this exothermic process was not exhibited which demonstrates the ability of the nanotube hosts to protect guest species from oxidation. It was shown via differential scanning calorimetry (DSC) and thermogravimetric analysis (TGA) that heating the material above 50 ^{o}C in air led to an exothermic combustion process by the P_4 molecules (Figure 1.3f), which provides a potential application as a controlled heat release material.

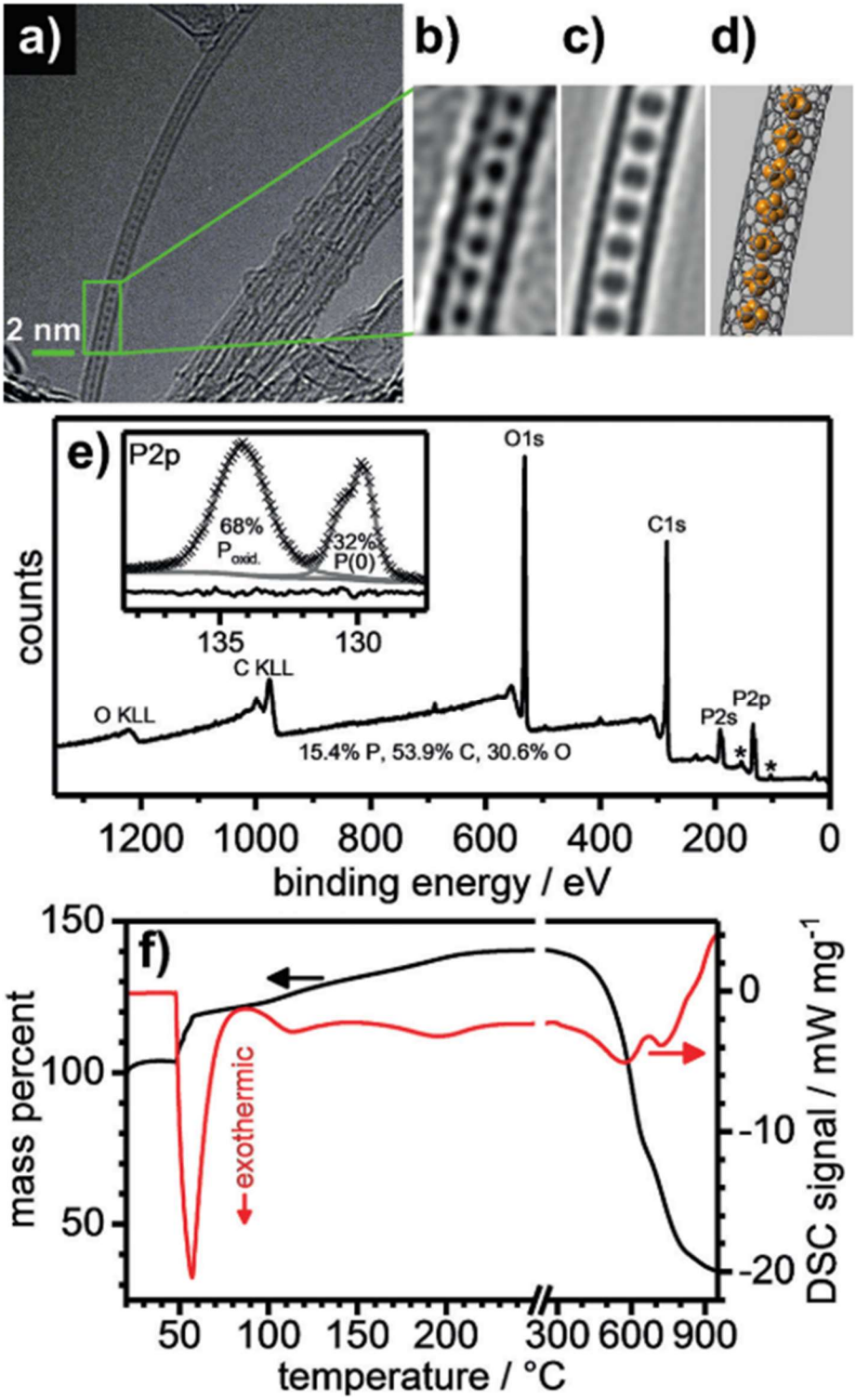


Figure 1.3. *(a) 80 kV TEM image of P_4@SWNT showing the strand of P_4 molecules within the interior channel; (b) noise-filtered TEM image of (a); (c) TEM simulation and the (d) corresponding structural model of P_4@SWNT; (e) XPS wide scan of P_4@SWNT (Inset is a high resolution spectrum of the P 2p region); (f) DSC/TGA analysis of P_4@SWNT.*[19]

As well as being a container for discrete molecules, continuous crystalline materials have also been studied within single-walled carbon nano test tubes to probe their structure, and composition of guest species. An early example of the encapsulation of a crystalline species within SWNTs was potassium iodide (KI), which exhibits a rock-salt structure in the bulk.[38] The quasi-1D structure was investigated by TEM and was found to also exhibit the same structural-type, however, the confinement of the SWNT enforced a two layer thick structure to form which was found to dramatically reduce the coordination of K:I from 6:6 to 4:4.

The phenomena of reduced atomic coordination under extreme confinement was also exhibited when the alkaline earth metal halide, barium iodide (BaI_2), was filled into SWNTs, using a molten-phase filling technique.[39] BaI_2 in the bulk exhibits Ba^{2+} in 9- coordination but when formed within a SWNT of 1.6 nm diameter, Ba^{2+} was found to be in 5- and 6-coordination. This was not explained simply by the known structure being restricted in dimensionality but by forming a new structure entirely which consisted of chains of edge-linked coordination polyhedral whilst still retaining the expected stoichiometry of elements (Figure 1.4a - j).

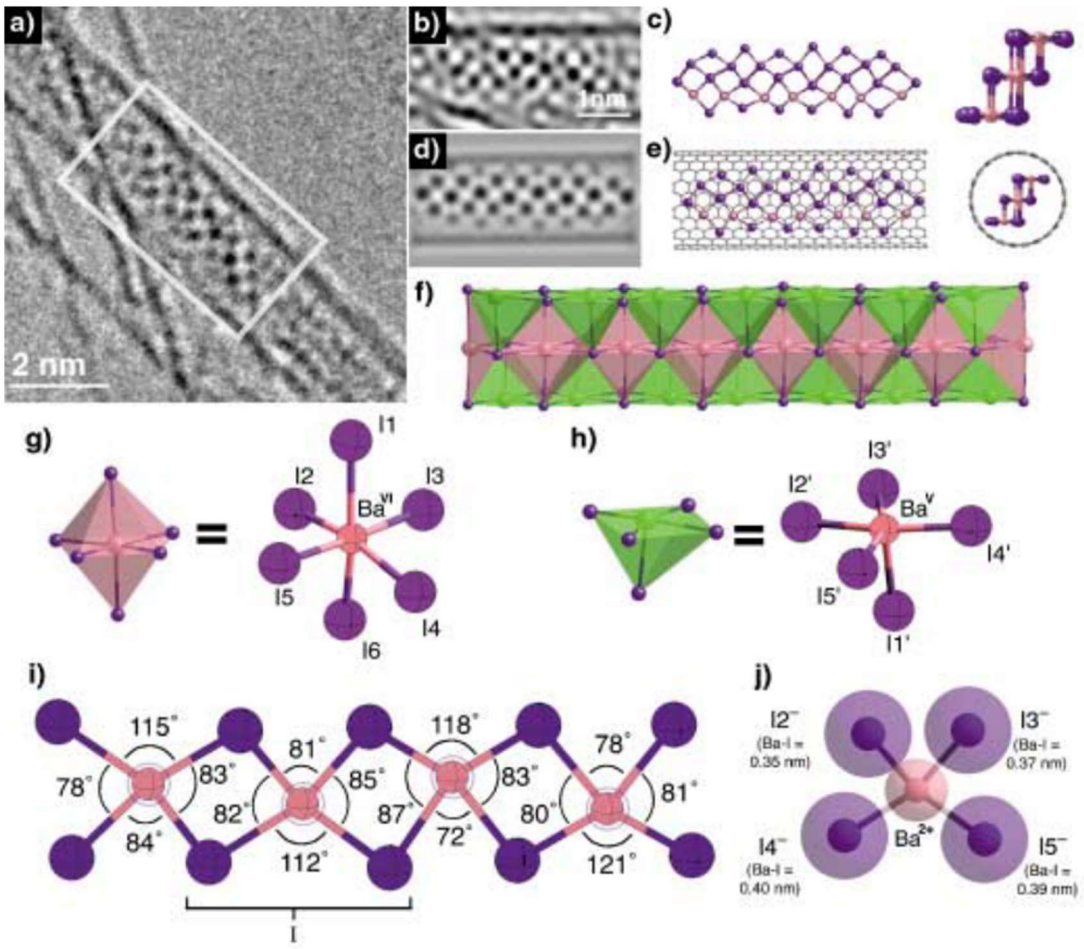


Figure 1.4. *(a) 300 kV TEM image of BaI_2@SWNT; (b) magnified TEM image of the area indicated in (a) by the white rectangle; (c) atomic structure plot based on 2D mapping analysis, and cross-sectional view (right); (d) simulated TEM image of BaI_2@SWNT; (e) structural model of BaI_2@SWNT, and cross-sectional view (right); (f) model demonstrating coordination structure; (g) 6-coordinate and (h) 5-coordinate ball and stick models of BaI_2 from (c); (i) and (j) structural models displaying the bond angles and distances for BaI_4 units of the BaI_2 quasi-1D chain.*[39]

A metal iodide that not only produced a different structure upon encapsulation but was also found to cause a dramatic effect on the structure of the host SWNT was cobalt iodide (CoI_2).[40] The material was encapsulated via a molten-phase filling technique and was shown to exist in a helically-twisted tetrahedral chain structure of Co_2I_4 units. Furthermore, the SWNT diameter projected on the plane of the TEM image was found to range from 1.1 to 1.3 nm in

accordance with the twisting of the helical nanostructure; this was a result of an elliptical distortion of the host SWNT in response to strong interactions with the cobalt iodide helical nanostructure.

In recent years, metal monochalcogenide materials have been extensively studied within the confinements of SWNTs because of their potential applications as thermoelectric[41], and optical properties.[42] The size templating ability of the SWNT inner channel has led to diameter-selective growth of nanowires (NW),[18, 43-45] and stoichiometric changes.[46]

Tin selenide[45] and telluride[18] were both encapsulated into SWNTs with a range of different diameters from 0.7 – 1.4 nm; this produced size templated novel structures. SnSe (Figure 1.5) formed a MoSe-type structure when encapsulated within 1.3 nm SWNTs, as demonstrated by aberration-corrected scanning transmission electron microscopy (AC-STEM) imaging. However, in the instance of being inserted in SWNTs of 0.7 nm diameter, a single atomic chain was formed; the most extreme nanowire that can be produced. Moreover, it was proposed that by tuning the diameter, and thus the structure produced, the thermoelectric properties of the NW could be significantly modified allowing design of a new range of functional materials.

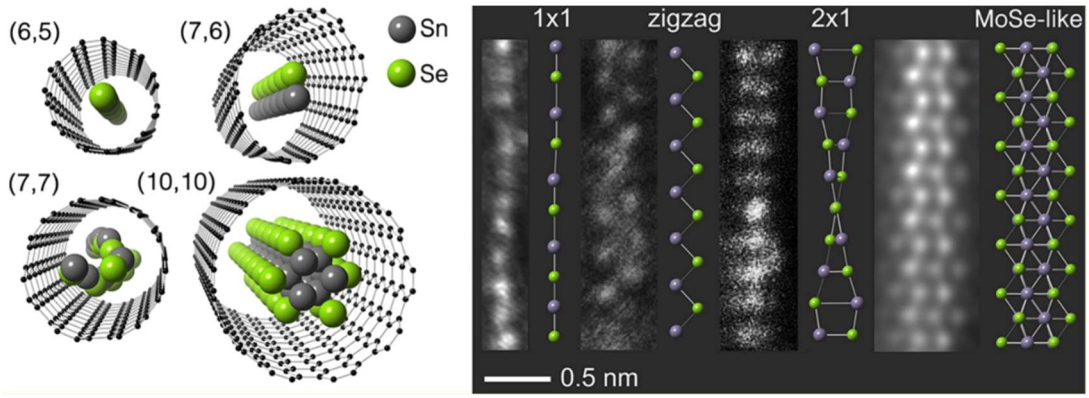


Figure 1.5. *80 kV AC-STEM images of SnSe within SWNTs of different diameters resulting in 1x1, zigzag, helical, and MoSe-like structures that are size-templated by the nanotube interior.*[18]

Germanium telluride is a phase change material that was predicted to only produce crystalline phases above 2 nm in size; however, when encapsulated within SWNTs of 1.3 nm diameter, a crystalline rock-salt structure was shown to have been formed using TEM.[47] Moreover, amorphous to crystalline phase transitions were observed within the SWNT channel triggered by electron beam irradiation. These two observations demonstrate the ability of SWNTs to stabilise thermodynamically unfavourable phases of the same material within the unique environment of the interior channel.

In addition to forming materials with new structures, their compositions can also be affected upon encapsulation. The insertion of molybdenum ditelluride, $MoTe_2$, into SWNTs by sublimation led to the formation of monochalcogenide nanowires, MoTeNW, confirmed by a combination of high-angle annular dark-field STEM (HAADF-STEM, Figure 1.6a), electron energy loss spectroscopy (EELS), and XPS. The MoTeNW only formed when the temperature of sublimation was above 1000 ^{o}C; this was explained by $MoTe_2$ becoming initially oxidised and then the sublimation step leading to the formation of gaseous MoO_x and Te which react within the SWNT channel to form MoTeNW (Figure 1.6b). Moreover, it was shown that the monochalcogenide nanowires were templated selectively by SWNTs with diameters of 1.3 ± 0.1 nm, and thus it was the van der Waals interactions between the host and guest that stabilised the structures.

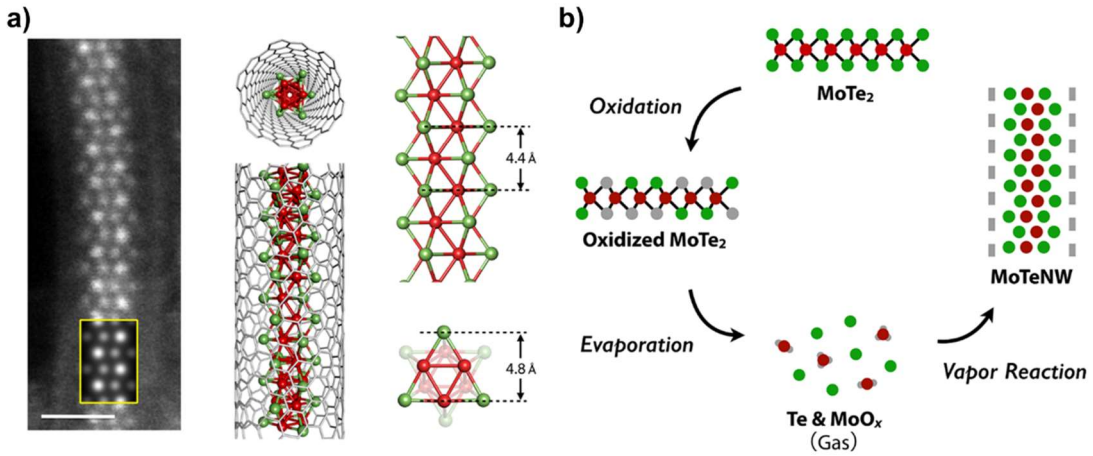


Figure 1.6. *MoTe nanowires (MoTeNW) formed within SWNTs of diameters 1.3 ± 0.1 nm upon sublimation of $MoTe_2$. (a) HAADF-STEM image of MoTeNW@SWNT (left), structural models of MoTeNW@SWNT showing the fit within the nanotube channel and the interatomic distances of the structure (right); (b) mechanism of formation of MoTeNW@SWNT from $MoTe_2$ via oxidation and evaporation processes. Figure adapted from Nagata et al.*[46]

1.2. Techniques for characterising entrapped materials

Once materials are encapsulated within SWNTs they require characterisation to determine their structure, composition, and electronic properties. This can be achieved by combining complementary electron microscopy and spectroscopy techniques such as TEM, energy-dispersive X-ray analysis (EDX), and Raman spectroscopy.

1.2.1. TEM

The ability to image individual atoms of a chemical species was referenced in a quote from Richard Feynman during a talk he presented on December 29th 1959 entitled *There's Plenty of Room at the Bottom* in which he said the following;[48]

"It would be very easy to make an analysis of any complicated chemical substance; all one would have to do would be to look at it and see where the atoms are".

The principle of producing an image of a material using TEM starts with the electron source which can be either a thermionic source (such as a W or LaB_6 filament) which produces electrons upon heating, or a field emission source (such as W) that produces electrons when an electric potential is applied between an anode and the source.[49] Most modern electron microscopes utilise field emission sources as they produce more monochromatic electrons; however, field emission sources require the surface must be free of contamination which can be achieved by two different methods. The first requires an ultra-high vacuum and the source to be used at ambient temperatures, coined as Schottky emitters, and the second can utilise poorer vacuum conditions by additionally heating the tip of the source, which are called "cold" emission sources. The field emission gun is then connected to two anodes which are positively charged and are responsible for drawing electrons from the tip via an extraction voltage, and the subsequent acceleration of electrons to the required voltage respectively (Figure 1.7). This then produces an electron beam (e-beam), of desired acceleration voltage, which is focussed onto the specimen using a series of electromagnetic lenses, which make up the condenser system, the electrons subsequently interact with the material and are either scattered or transmitted. Depending on the imaging mode, either the scattered or the transmitted electrons are selected by an aperture and an objective lens system then forms the image and is focussed and magnified onto a fluorescent screen by intermediate and projector systems.[50]

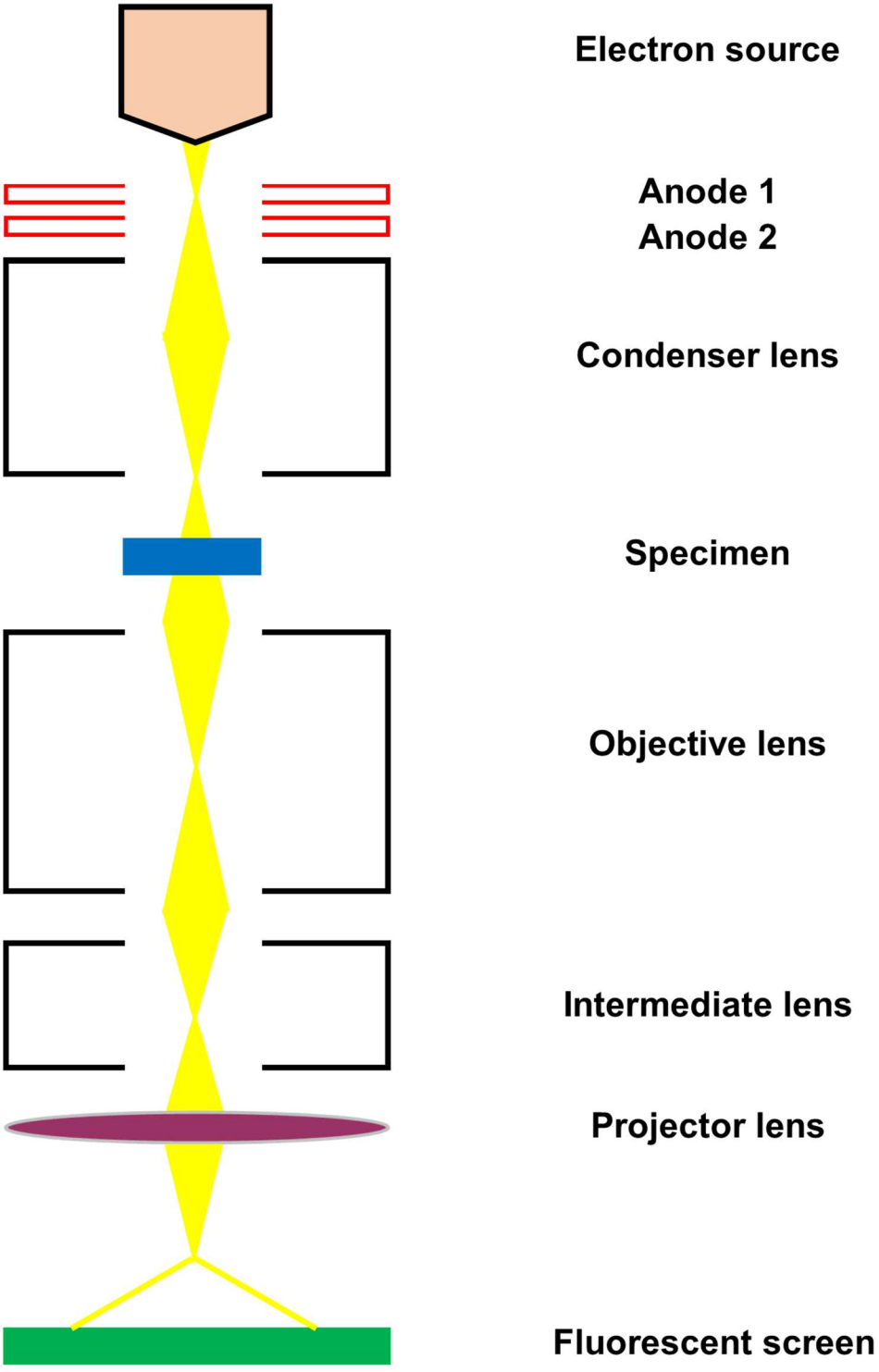


Figure 1.7. *Schematic representation of a transmission electron microscope showing e-beam path and the constituent sections comprised of; the electron source, the anode, the series of electromagnetic lens systems, the specimen holder, and the fluorescent screen.*

1.2.1.1. Contrast formation and analysis

The level of contrast in TEM is controlled by the level of elastic scattering of electrons by atoms in a material. In bright field (BF)-TEM, it is the scattered electrons that are excluded by the objective aperture, and therefore the resultant contrast is produced by transmitted (non-scattered) electrons. The scattering cross section is a function of both the atomic number of the element, as well as the thickness of the material (Figure 1.8).[49] This is such that the higher the Z number of an atom, and the thicker the specimen, the more the electrons will be scattered and thus fewer transmitted electrons will hit the phosphor screen and will produce a darker feature in the reconstructed image.

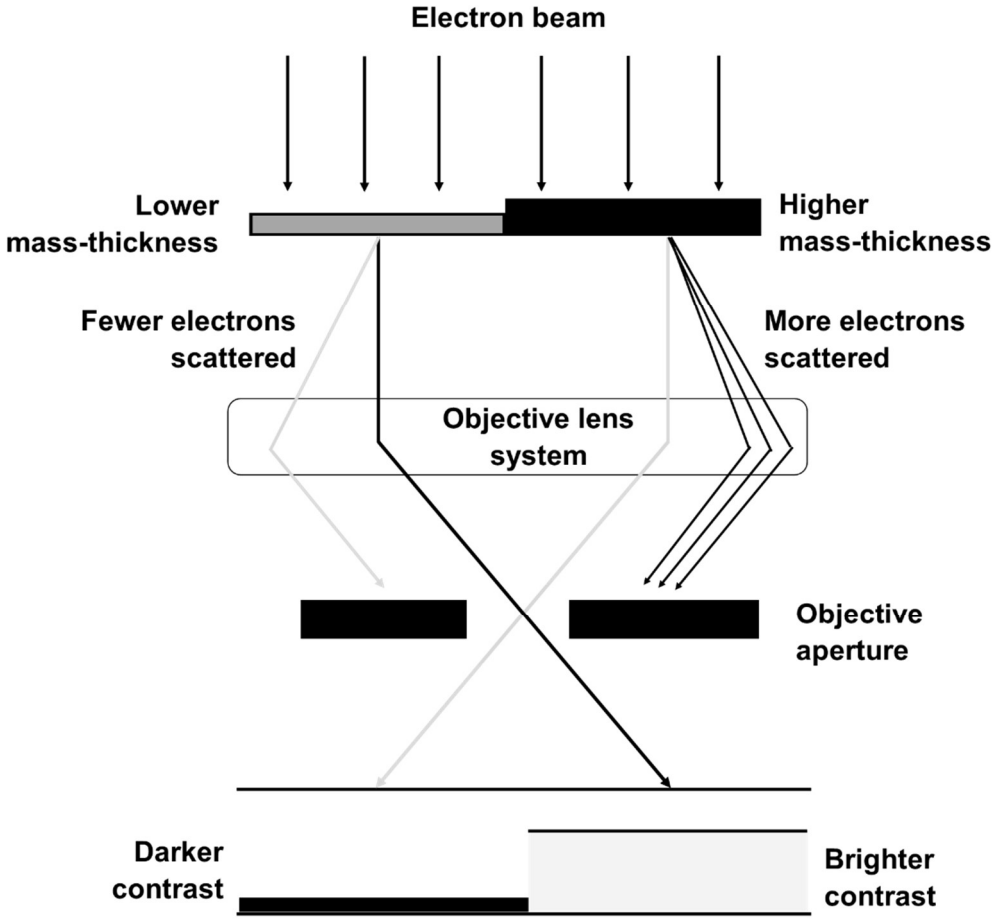


Figure 1.8. *Schematic diagram demonstrating the relationship between the mass-thickness of a specimen and the contrast produced in bright-field TEM.*

TEM contrast analysis is commonly used as a measuring tool and works by plotting the number of counts against distance measured displaying darker areas as troughs in the profile. Commonly, it is used to record nanotube diameters, or interatomic distances of guest species.[51] It has also been used to detect the presence of single atoms within C_{60} fullerenes encapsulated within SWNTs by measuring the contrast profile perpendicular to the SWNT axis across the centre of a fullerene.[52] The presence of the single F and O atoms occur by encapsulation of HF and H_2O into C_{60} followed by homolytic bond dissociation of X-H (where X is either F or O) by electron beam irradiation. Contrast profiles only detected the presence of the single atoms when the endofullerenes were in certain orientations that caused the overlap of two carbon atoms with either the F or O atom producing enhanced contrast originating from three atoms in projection.

The technique can also be used for TEM simulations of proposed structures to correlate against experimental profiles. This was the case for determining if a continuous siloxane-based guest species formed within a SWNT was a single-ladder or double-ladder structure.[53] The two profiles of TEM simulated images of the single and double ladder structures (Figure 1.9b and c) did both exhibit the same interatomic distances between silicon atoms, but it was shown that the single-ladder structure found the contrast of silicon to be lower than that of the nanotube sidewall. Conversely, the double-ladder structure measured silicon features to be higher in contrast than the sidewall, which was the observation of the experimental AC-HRTEM image (Figure 1.9a). This proved that the individual features observed in TEM were columns of two Si atoms in projection, characteristic of the double-ladder structure. The aberration-corrected HR-TEM image provided vital atomic resolution information which aided the deduction of the structure. Aberrations in TEM images arise from lens defects and comprise of two primary sources; spherical aberrations, and chromatic aberrations.[49] Spherical aberrations occur due to electrons intersecting the optical axis at a position shifted from the Gaussian image plane resulting in points appearing as disks; this

effect can be corrected using a system containing hexapole elements and lens doublets developed by Haider *et al.*[54] Chromatic aberrations refer to electrons being produced that are not monochromatic as intended which can be corrected by installing a monochromator in the system.[49]

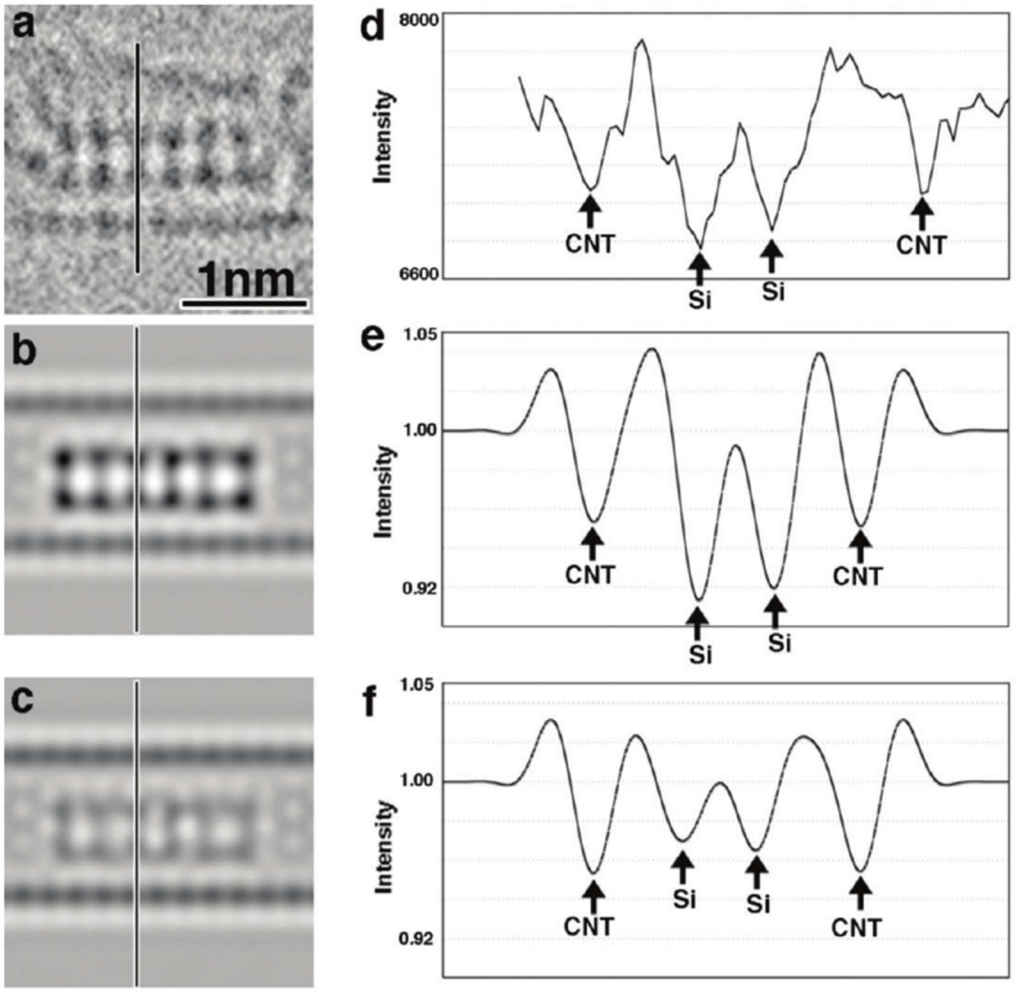


Figure 1.9. *(a) 120 kV AC-HRTEM image of $H_8Si_8O_{12}$@SWNT; (b) simulated TEM image of the double-ladder $H_8Si_{4n}O_{8n-4}$ structure within a (14,2) SWNT; (c) simulated TEM image of the single-ladder $H_8Si_{2n}O_{3n-2}$ structure within a (14,2) SWNT; (d – f) corresponding contrast analysis profiles of the areas indicated by black lines superimposed on experimental and simulated TEM images in (a –c). It is shown that the proportional contrast of Si features in the double-ladder structure with respect to that of the nanotube sidewall is closer to the experimental image than the single-ladder contrast proportions.*[53]

1.2.2. Spectroscopic methods

Electron microscopy is a powerful tool for the structure determination of guest species within SWNTs; however, in order to gain a holistic understanding of a host-guest system, it must be used in conjunction with other spectroscopic techniques to probe composition, and electronic communication between the host and guest.

1.2.2.1. EDX

EDX analysis is a spectroscopic technique which operates by the electron beam causing the ejection of an inner shell electron of an atom resulting in a hole.[55] An outer shell electron of higher energy then fills the hole and the energy difference between the inner and outer shell electrons is released in the form of an X-ray of which the energy is characteristic of the element / shell being studied. EDX is commonly used for determining the composition (both qualitatively and quantitatively) of guest species within SWNTs with examples including for; rhenium oxide clusters,[56] and antimony tellurides.[57]

The monitoring of the different stages of a cycloaddition reaction between an azide and an alkyne within SWNTs to form a triazole was conducted using EDX. The extreme spatial confinement of the SWNT appeared to increase the regioselectivity for the 1,4-triazole due to its linearity compared to the bent 1,5-triazole. EDX was first conducted on empty SWNTs as a reference which showed the presence of only carbon and oxygen from defects (Figure 1.10a), and then was recorded upon the formation of triazole@SWNT, which displayed a peak around 0.4 keV for nitrogen (a tracer element for the formation of the triazole, Figure 1.10b). An extraction step was performed to collect the product from the SWNT interior by sonication in an organic solvent and the total removal was confirmed by EDX by the loss of the nitrogen peak (Figure 1.10c). All spectra recorded were compared against spectra of the

same materials but recorded over the carbon film of the TEM grid to validate the results further.

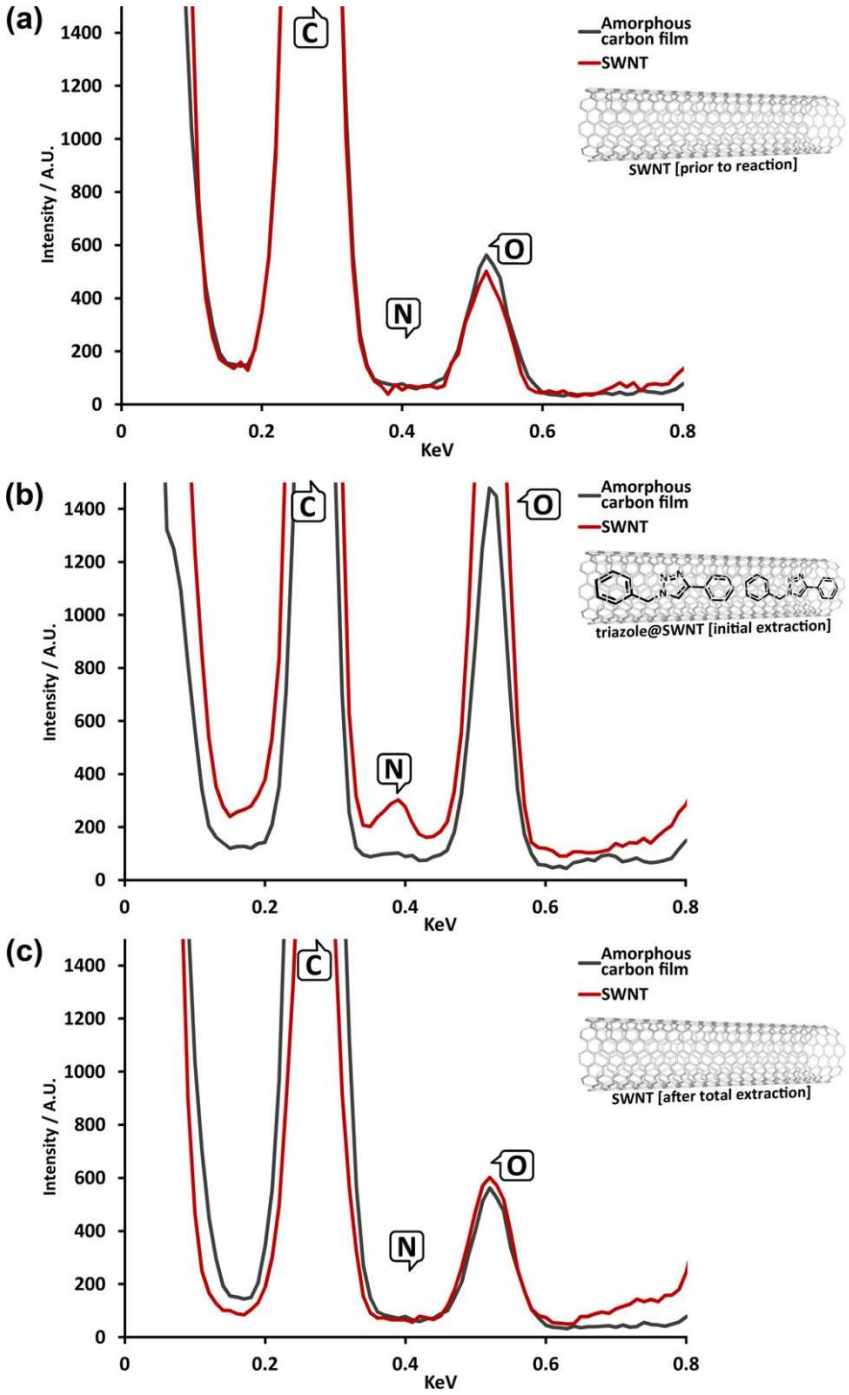


Figure 1.10. *EDX analysis at different stages of the formation of triazole@SWNT via the cycloaddition of an azide and an alkyne recorded (a) prior to the reaction commencing; (b) on formation of triazoles within the SWNT channel, and (c) after total extraction of the*

organic molecules from the SWNT channel. All spectra (red line) were compared against spectra recorded over amorphous carbon film from the TEM grid (black line).[58]

A primary limitation of EDX is the energy resolution (130 eV at Mn Kα) which results in the overlap of some elements such as Mo and S at approximately 2.2 – 2.6 keV.[59, 60] To overcome this challenge, wavelength-dispersive X-ray (WDX) analysis may be used which has an improved energy resolution (8 eV at Mn Kα) allowing the individual identifications of overlapped peaks.[61]

1.2.2.2. Raman

Raman spectroscopy of filled single-walled carbon nanotubes can produce a plethora of information about the composite system including direct evidence of encapsulation through observation of vibrational modes of the guest species,[62] as well as the effects of encapsulation on the structure and electronic properties of the host SWNT.[63] The Raman spectrum of SWNTs produces four prominent modes which are: the radial-breathing mode (RBM), defect (D)-band, graphitic (G)-band, and the D overtone (G' or 2D) band (Figure 1.11a).[64-66] The RBM provides information of the diameter of the SWNTs and are inversely proportionally related by:

$$\omega_{RBM} / \, cm^{-1} = \frac{248}{d_{NT}}$$

Equation 1.3.

where d_{NT} – diameter of the nanotube in nanometres.

The RBM can be affected by encapsulation of materials which may either cause an expansion or contraction of the nanotube diameter to accommodate the guest species.[63] The D-band

provides information on defects of the sp^2 carbon walls, and the G′ second harmonic of the D-band can detail about any strain or doping.[63]

The tangential G band (1550 – 1605 cm^{-1}) represents the in-plane stretching mode of C-C bonds and is most often used to distinguish between semiconducting and metallic SWNTs, as well as detect any electron transfer between the nanotube and guest species.[65] A blue shift of the G-band is representative of electron density transfer from the host SWNTs to a guest species whilst red shifting is indicative of SWNTs acting as electron acceptors.

It was determined in 1998 by Pimenta *et al.* that it was possible to resonantly enhance metallic SWNTs using laser excitation energies of between 1.7 and 2.2 eV producing tangential phonon modes of metallic SWNTs.[67] This produces a Breit-Wigner-Fano (BWF) profile of the G-band (Figure 1.11c) whilst resonant enhancement of semiconducting SWNTs produces a Lorentzian profile (Figure 1.11b).[68]

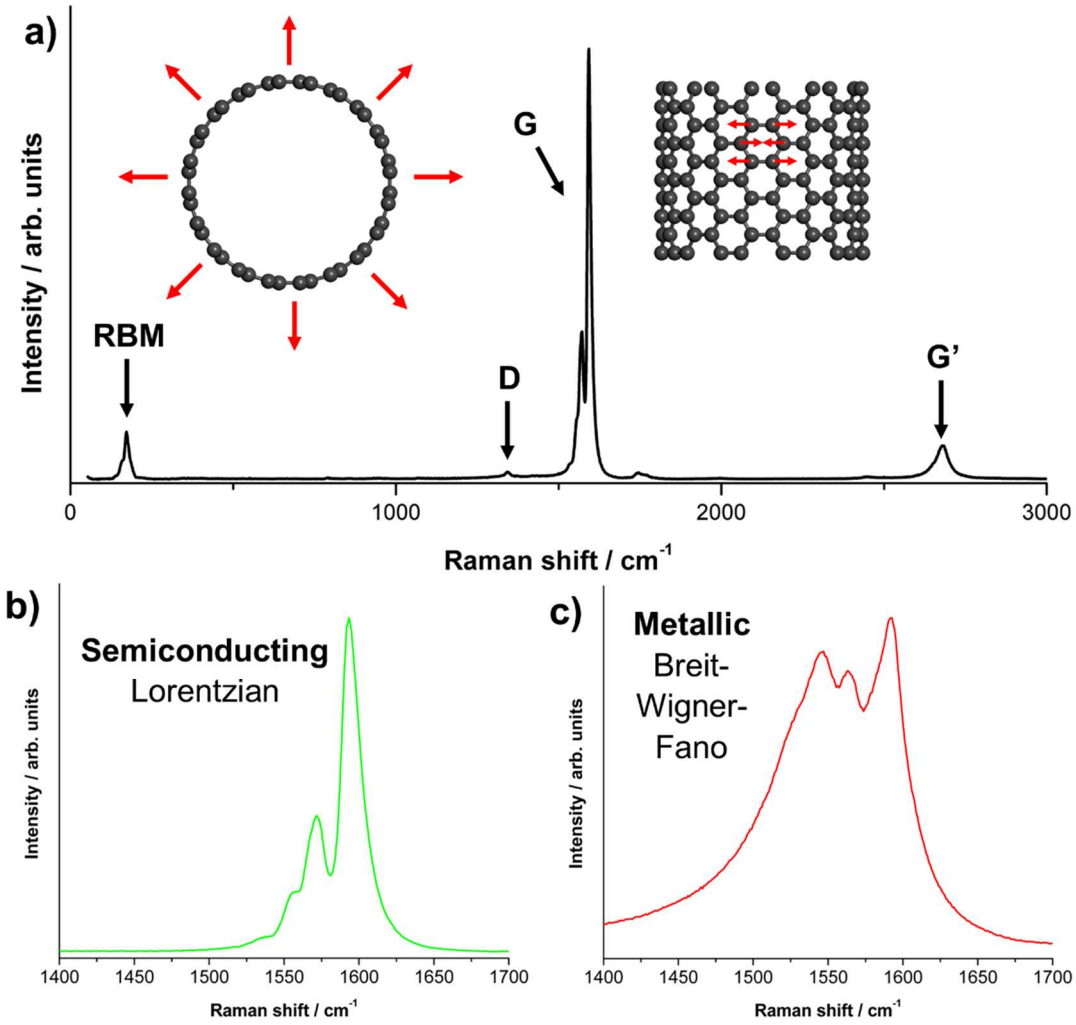


Figure 1.11. *(a) Raman spectrum of single-walled carbon nanotubes showing the four key modes observed; radial breathing mode (RBM), disorder-induced (D), graphitic (G), and second-order harmonic (G'). Superimposed are structural models depicting the RBM (left) and G (right) modes. Raman spectrum of SWNTs, (b) measured using a 532 nm laser in resonance with semiconducting SWNTs, showing the Lorentzian profile of the G-band and (c) measured using a 660 nm laser in resonance with metallic SWNTs, displaying the Breit-Wigner-Fano profile of the G-band.*

Transitions between the two types of SWNTs can be observed using resonant enhancement to excite a particular set and then observing a profile change upon filling with a material. Filling SWNTs with silver caused a -5 cm^{-1} red shift of the G-band, compared to empty SWNTs, when excited with a 514 nm laser in resonance with semiconducting SWNTs, which

demonstrated silver behaving as an electron donor towards the SWNTs.[69] This led to a profile change to resemble a more BWF-type G-band, correlating with a semiconducting to metallic transition. The opposite effect was observed for metallic SWNTs which were filled with manganese halogenides; a semiconducting to metallic transition was observed, accompanied by a blue-shift of the G-band.[70] Metal halides have been extensively studied and shown to have profound effects on the doping of SWNTs upon encapsulation, mostly acting as electron acceptors (Table 1.1).

Table 1.1. *Summary of the Raman shifts of the G-band of SWNTs filled with metal halides and any electron transfer between SWNT hosts and metal halide guests.*

Material	Excitation energy / nm	Raman shift vs empty SWNTs / cm^{-1}	Direction of electron transfer	Reference
AgCl	633	+13	SWNT ➔ Ag^{+}	[71]
$CdCl_2$	633	+6	SWNT ➔ Cd^{2+}	[72]
$CdBr_2$		+9		
CdI_2		+5		
$CoBr_2$	633	+13	SWNT ➔ Co^{2+}	[63]
CuCl	633	+14	SWNT ➔ Cu^{+}	[73]
CuBr		+16		

CuI		+11		
$[Mo_6I_{14}]^{2-}$	532	+15	SWNT ➔ Mo^{2+}	[62]
$NiBr_2$	633	+11	SWNT ➔ Ni^{2+}	[63]
$PbCl_2$	633	+10	SWNT ➔ Pb^{2+}	[74]
$PbBr_2$		+6		
PbI_2		+11		
PtI_2	532	0	No electron transfer observed	[75]
$TbCl_3$	633	+ 22	SWNT ➔ Tb^{3+}	[76]
$TbBr_3$		+ 19		
TbI_3		+16		
$[W_6I_{14}]^{2-}$	532	+15	SWNT ➔ W^{2+}	[62]
$ZnCl_2$	633	+9	SWNT ➔ Zn^{2+}	[77]

1.2.2.3. IR

The study of the infrared (IR)-active vibrational modes of encapsulated species within SWNTs is complicated by the poor transmittance of light by SWNTs.[78] Moreover, they lack a static dipole moment and thus only dynamic charges contribute to infrared active modes; these consist of two main groups of modes at around 1598 and 874 cm^{-1}.[79, 80] There is also a 10-

fold reduction of IR active mode cross sections of guest species within the interior channel compared to those adsorbed on the SWNT exterior surface;[81] a result of the polarisable π-electron system of SWNTs cloaking the guest species within their interior channel.[82] Despite these limitations, the technique can be valuable towards understanding the properties of guest species within SWNTs. Ferrocene was encapsulated within SWNTs by Guan *et al*. using a vapour diffusion method and IR spectroscopy was used to investigate the host-guest system.[83] The individual IR spectra of the host SWNT and the free ferrocene molecules were compared to ferrocene@SWNT which was found to be an approximate superposition of the constituent parts with some observable frequency shifting of some modes. The C-H stretch of ferrocene was found to be downshifted from 3100 to 2900 cm^{-1} and the C-C stretch of SWNTs was upshifted from 1566 to 1576 cm^{-1}; these were both attributed to the strong interactions between the π-electrons of the nanotubes and the encapsulated ferrocene molecules. The study of encapsulated octasilasesquioxanes, $H_8Si_8O_{12}$, within SWNTs and multi-walled carbon nanotubes (MWNT) of varying diameters also proved to be an excellent system to study using IR.[84] Insertion of the molecules into nanotubes with diameters slightly above the size of the molecule caused a large (15 – 19 cm^{-1}) red shift of the Si-H vibration (Figure 1.12a and b), compared to a solution of $H_8Si_8O_{12}$ in CCl_4 (Figure 1.12d). This was a result of dispersion forces between the host and guest causing an elongation of the Si-H bond. Meanwhile, nanotubes with diameters similar to that of the guest species were found to exert pressure on the $H_8Si_8O_{12}$ molecules, resulting in a lessening of the red shift (Figure 1.12c). Finally, when the nanotube diameter was considerably larger than the size of the molecule, a loss of the Si-H vibration was observed in the IR spectrum as a result of weak host-guest interactions causing loss of the molecules after a washing step by a solvent.

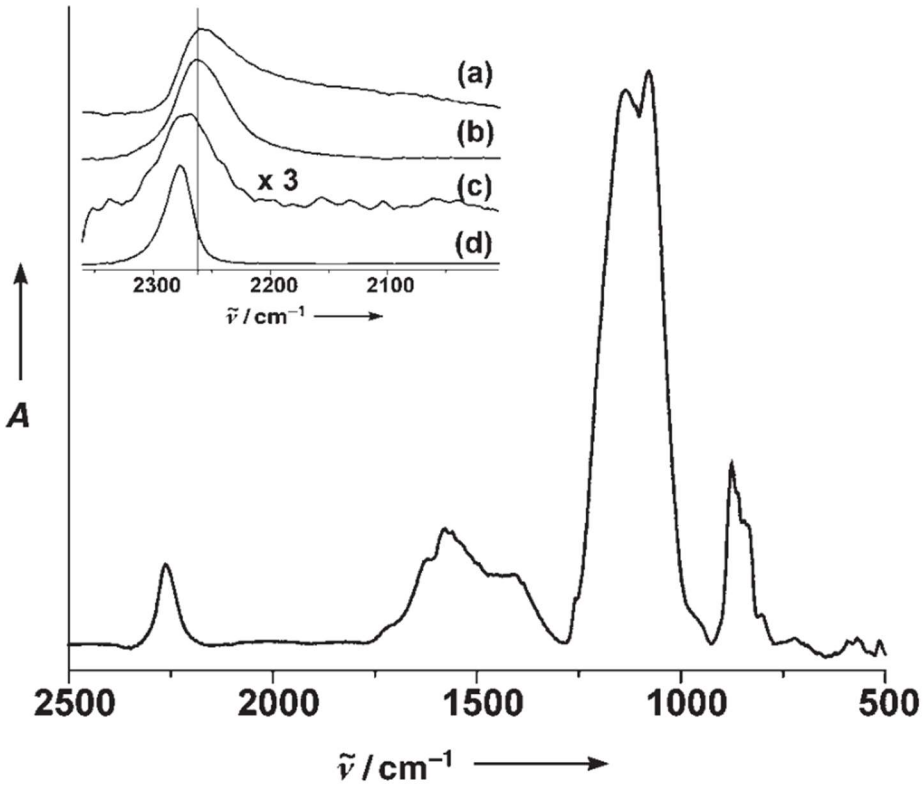


Figure 1.12. *An infrared spectrum of octasilasesquioxane within carbon nanotubes. Inset is a series of stacked IR spectra, focussed on the Si-H vibration frequency region, for $H_8Si_8O_{12}$ within (a) multi-walled and (b) single-walled carbon nanotubes of diameters slightly above the size of the molecules; (c) $H_8Si_8O_{12}$ within SWNT with diameters of a similar size to the molecules; (d) free $H_8Si_8O_{12}$ dissolved in CCl_4.*

1.2.2.4. XPS

XPS has been shown to be important for understanding any changes in the composition, or redox properties of guest species within SWNTs. A simple use of the technique is to confirm the guest species has not been altered upon insertion; this was the case for $H_3PW_{18}O_{62}$ polyoxometalates within SWNTs, as shown by the absence of an observable shift of the W 4f spin-orbit binding energies compared to the parent compound.[21] Iodine molecules were observed to undergo reduction when inserted into SWNTs which was proven by the binding

energy peak positions of the I 3d components being located at the position reported previously for polyiodides.[85] Measurements of entrapped cobaltocene molecules, $CoCp_2$@SWNT, displayed peaks in the expected positions for Co^{3+}; this was a result of electron transfer from the host SWNTs to the guest molecules forming $[CoCp_2]^+$@$SWNT^-$.[86]

The technique was also used to characterise the phenomena of mercury dichloride ($HgCl_2$) transforming into a new species when encapsulated within SWNTs.[87] Initial TEM imaging of the structure showed structures that appeared to be the (100) and (110) projections of Hg_2Cl_2, mercury (I) chloride. However, complementary EDX analysis was unable to precisely detect the Hg: Cl atomic ratio due to a low signal-to-noise ratio; therefore, XPS was conducted on the sample to examine the binding energy peak positions of the components of the Hg 4f and Cl 2p regions. The Cl 2p region produced a doublet of which the 3/2 component was measured to have a peak position closer to that expected for Hg_2Cl_2 than $HgCl_2$ (Figure 1.13a). Moreover, the Hg 4f region was also fitted to a doublet of which the 7/2 component was found at an energy characteristic also of the reduced species (Figure 1.13b). XPS also assisted with the understanding of the mechanism of reduction by observing a small shift of the C 1s peak which is indicative of electron density donation from the SWNTs to the guest species causing a lowering of the Fermi level (Figure 1.13c). The electron transfer induced reduction of $HgCl_2$ to Hg_2Cl_2 was further confirmed using Raman spectroscopy, which recorded a significant blue shift of the G band of the SWNT hosts.

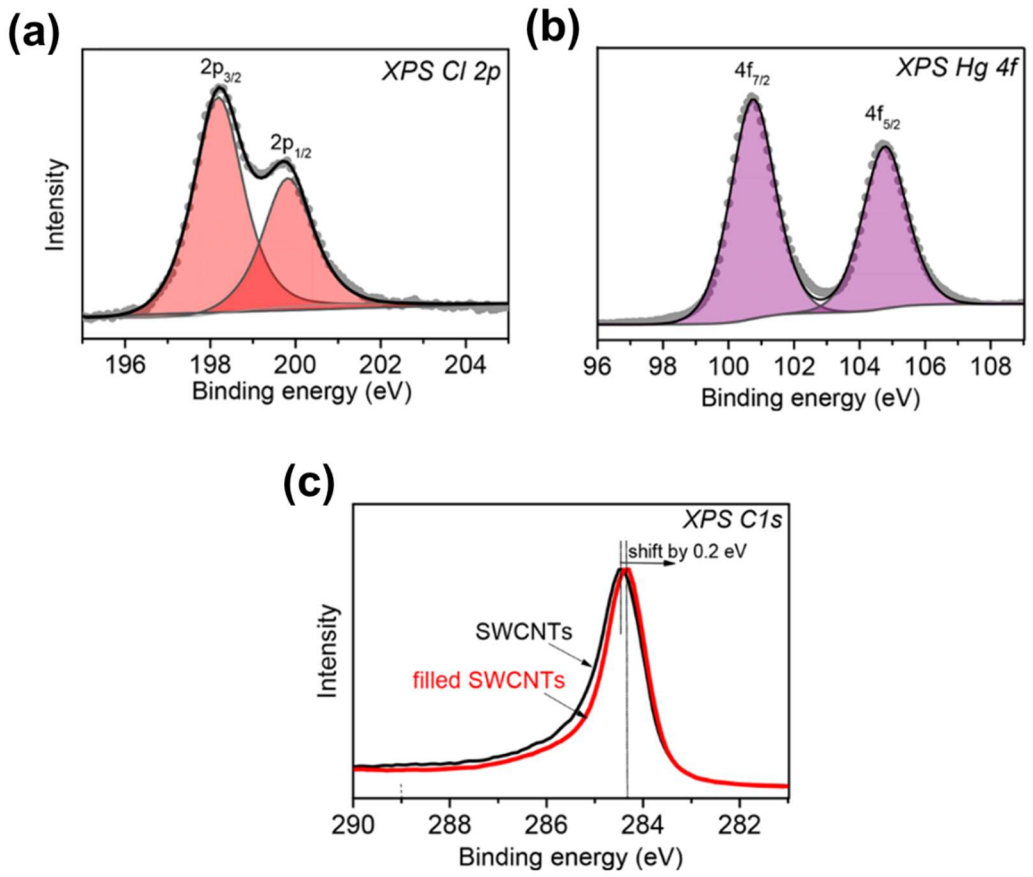


Figure 1.13. *XPS high resolution scans of Hg_2Cl_2@SWNT focussed on the (a) Cl 2p, (b) Hg 4f, and (c) C 1s regions. The binding energies of the Hg 4f and Cl 2p components were found to be closer in energy to Hg_2Cl_2 than $HgCl_2$, and the C 1s was found to be downshifted by 0.2 eV. Adapted from Fedoseeva et al.*[87]

Temperature dependence studies have also been performed on nickelocene molecules within SWNTs in which the position of the Ni 2p peaks were successively down shifted correlating to the production of nickel carbon alloys, and metallic nickel, followed by loss of the peaks indicating loss of nickel atoms from the host nanotube at temperatures above 800 ^{o}C.[88]

1.3. Manipulation of entrapped materials

As well as being a powerful tool for imaging the structure of nanomaterials, the electron beam in TEM can also act as a tunable source of energy, triggering reactions of entrapped molecules whilst simultaneously imaging the reactions in real time, and allowing novel products and intermediates to be identified (*ChemTEM* approach).[89] The maximum amount of an energy that a stationary atom receives upon a collision with an electron from the electron beam at a given energy is inversely proportional to the atomic weight of the element expressed as:

$$T_{max} = \frac{2ME(E + 2m_e c^2)}{(M + m_e)^2 c^2 + 2ME}$$

Equation 1.4.

where M - atomic weight of the element, E - energy of the incident electrons, m_e - electron mass, and c -speed of light.

Therefore, heavier elements receive less energy than lighter elements using the same e-beam energy. The rate of a chemical transformation is controlled by the electron dose rate which is the number of electrons per square nanometre and thus the rate of reaction can be changed by simply increasing or decreasing the electron dose rate during imaging demonstrated by:

$$k = j.n.\sigma_d$$

Equation 1.5.

where k – rate of a chemical reaction under the electron beam, j - electron dose rate, n - number of bonds in the molecule, and σ_d – collision cross section function.[90]

An example of the electron beam directly triggering chemical reactions within SWNTs was during the imaging of encapsulated C_{60} fullerenes that were found to undergo coalescence when subjected to the electron beam at 97 kV.[91] The energy of the beam was strong enough to cause displacement of carbon atoms of fullerenes leading to the formation of vacancies and dangling bonds which underwent reconstruction and bonding with adjacent molecules to produce peanut-shaped dimers and further extended structures resembling the structure of carbon nanotubes.

A more complex investigation was the imaging of perchlorocoronene (PCC) molecules within a SWNT using an 80 kV electron beam during aberration-corrected high-resolution TEM (AC-HRTEM).[89] Exposure to the e-beam triggered bond dissociation of C-Cl by momentum transfer from the e-beam to carbon atoms leading to the formation of angular adduct intermediates via Diels-Alder cycloaddition, which further rearranged into perchlorinated zigzag graphene nanoribbons (Figure 1.14a and e). The encapsulation of PCC molecules initially produced stacked arrangements which were a result of π- π interactions, and were found to be stable until disrupted by a high enough electron dose of the 80 kV e-beam. It was calculated that aryne formation would require 9.1 eV and rearrangement of the angular adduct would require 10.9 eV which were satisfied by the 10.9 eV maximum energy transferred to carbon atoms by the e-beam. However, the latter energy requirement was still quite high that not all electronic collisions were successful and thus allowed the angular adduct intermediate to be relatively stable within the SWNT channel for imaging (Figure 1.14b – d).

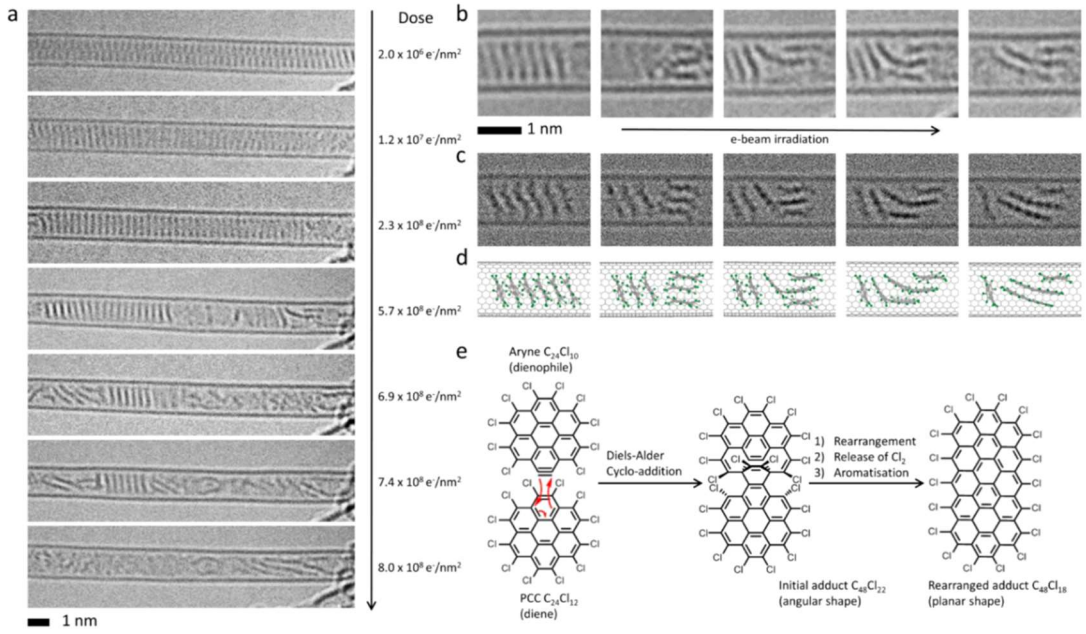


Figure 1.14. *(a) 80 kV AC-HRTEM time-series of perchlorocoronene molecules within a SWNT that shows the stepwise formation of angular adduct intermediates followed by rearrangement to form the planar chlorine-terminated structure; (b - d) comparison of AC-HRTEM image frames with TEM simulations of structural models of the reaction steps; (e) The intermolecular cycloaddition reaction mechanism showing the structure of the angular adduct, and subsequent rearrangement to form the planar shape.*[89]

The use of the electron beam to both image and provide a source of energy has also been extensively studied for metallic species encapsulated within SWNTs leading to some significant fundamental discoveries. It was demonstrated that Re nanoparticles are able to catalyse the formation of new carbon nanotube structures by irreversible displacement of carbon atoms from the host SWNT triggered by the e-beam, which are then adsorbed and transformed on the metal nanoparticle surface.[92] Another key fundamental process that was both promoted and imaged by the e-beam was the permeation of individual Pd atoms through defects in the SWNT structure (Figure 1.15). It was found that the process occurs by amorphization of crystalline Pd nanoparticles followed by individual Pd atoms being activated and bonding to the concave SWNT vacancy defect whilst the e-beam triggered the

breaking of metallic bonds. The individual atom then permeates through the vacancy and bonds with the convex surface where it can be sputtered by the e-beam into the vacuum.[93]

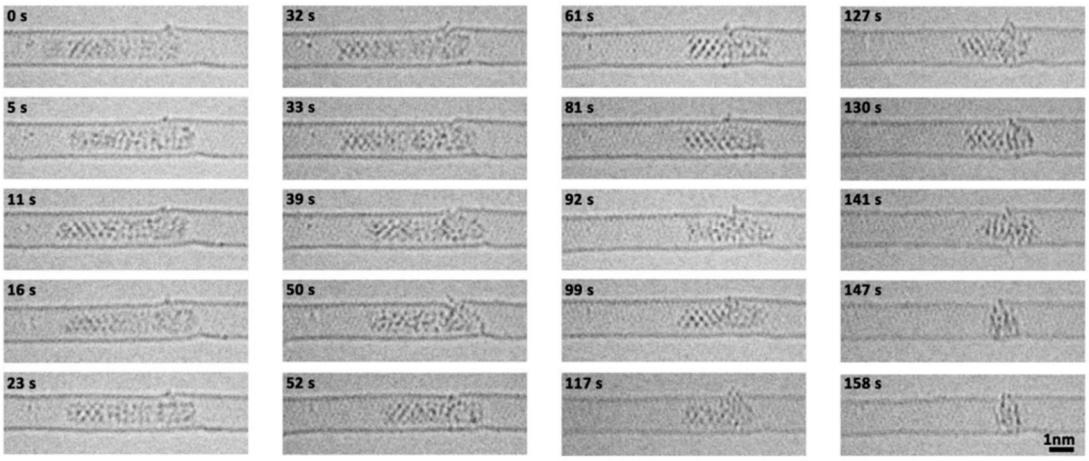


Figure 1.15. *80 kV AC-HRTEM time-series of Pd@SWNT showing the process of permeation of Pd atoms through a sub-nanometre vacancy defect in the SWNT lattice.*[93]

Another key chemical process which was captured using AC-HRTEM was the crystallisation of sodium chloride, NaCl, within modified SWNTs with conical ends by Nakamuro *et al*.[94] NaCl was inserted via the aqueous phase and initially during imaging, using an 80 kV electron beam, NaCl units displayed translational motion within the nanotube internal channel. Upon subsequent imaging, the units formed semi-ordered clusters which was a result of the nucleation process; these clusters continued to grow within the restrictions of the concave resulting in the production of a (4, 6) crystalline species containing 96 atoms (Figure 1.16a). The full process of nucleation, growth, and crystallisation was captured at the atomistic level allowing each process to be studied in full detail (Figure 1.16b). A nucleation process driven by the electron beam was also reported for transition metals (Fe, Au, and Re) within SWNTs using a similar *ChemTEM* methodology.[95]

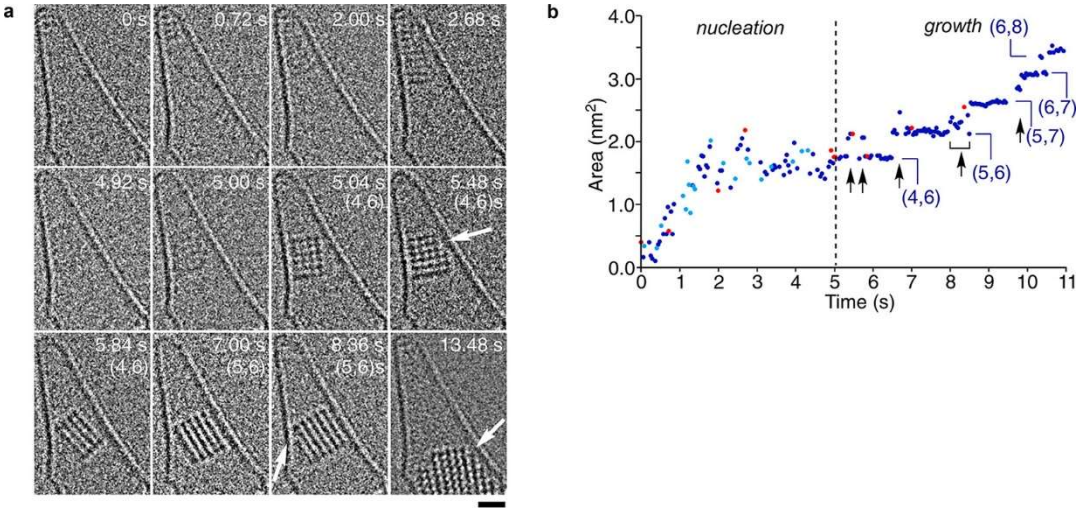


***Figure 1.16**. (a) 80 kV AC-HRTEM time-series showing the nucleation and growth events of a NaCl crystal within a conical SWNT; (b) Time evolution of 2D area of AC-HRTEM images during the nucleation and growth processes. The plot is labelled with the increasing crystal sizes, which is given as number of atoms.*[94]

1.4. Inorganic transformations within carbon nanotubes

Inorganic transformations within SWNTs can be triggered when the encapsulated species is subjected to a source of energy; this can be either in the form of heat, or electronic collisions by the e-beam during TEM imaging (see section 1.3). However, an early example of a transformation within a SWNT conducted a traditional metathesis reaction by simply reacting encapsulated silver nitrate with hydrochloric acid, which was shown to result in the formation of silver chloride nanowires.[96]

1.4.1. Thermal activations of guest species in nanotubes

One of the simplest forms of transformation that can take place occurs when a guest species is thermally-activated to produce a new material. Early cases of this were for the formation of metals within the nanotube interior channel from metal salts. The first example of this

was the preparation of ruthenium metal nanorods within single-walled carbon nanotubes by reduction of $RuCl_3$ in a stream of H_2 at 45 °C; the resultant nanorods were characterised by a combination of TEM and EDX.[32] Moreover, this has been extended to cover other d- and f-block metals including Au, Pt, and Pd which were produced via H_2 reduction of $HAuCl_4 \cdot XH_2O$, $H_2PtCl_6 \cdot 6H_2O$, and $PdCl_2$ respectively[97], as well as Ho (Figure 1.17), Fe, Gd, and Co all via their respective chloride salts.[98] The production of these metal nanowires within nanotubes can only occur via the metal salts as the melting points of the metals are too high to be encapsulated directly without destruction of the nanotube structure, e.g. the melting point of platinum is 1768 °C.

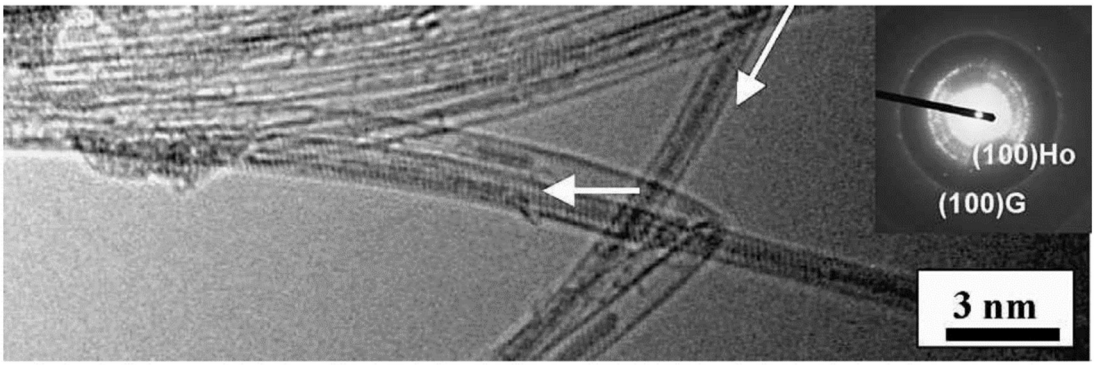


Figure 1.17. *100 kV TEM image of Ho nanowires within SWNTs synthesised via reduction of $HoCl_3$@SWNT using hydrogen. Inset is a selected area diffractogram pattern showing the (100) reflection of hexagonal close packed holmium metal, and the (100)G reflection of graphene.*[98]

Metal carbonyls have also been shown to be excellent precursors for the formation of metal nanoparticles (NP) when encapsulated within SWNTs and thermally-treated, releasing CO ligands.[99] This was first developed for W, Re, and Os, but was later extended to the remaining middle and late d-block elements.[100]

Sulfur-terminated graphene nanoribbons (S-GNR) were formed upon thermal treatment (or electron beam irradiation) of tetrathiafulvalene (TTF) molecules encapsulated within

SWNTs.[101] The resultant structures appeared as light contrast structures in TEM, with only the edge S atoms being clearly visible whilst still allowing features such as the helical twists be observed. As well as characterising the structures formed, it was also found that the TTF molecules, encapsulated using a molten-phase filling method, would only transform into S-GNR when the host SWNT was between 1 and 2 nm in diameter, due to smaller or larger diameter SWNTs possessing a lack of space or lack of confinement for quasi-1D growth.

1.4.2. Stepwise transformations of inorganic materials in nanotubes

The formation of cadmium sulfide, CdS, was the first stepwise chemical exchange reaction to take place within SWNTs, from two reactants, and proceeded by the insertion of cadmium iodide, CdI_2, and subsequently sulfur at elevated temperatures.[102] Upon encapsulation of CdI_2 into the SWNTs, there was a blue shift of the G band indicating electron transfer from the host to the CdI_2. The reaction with sulfur resulted in the production of CdS nanowires within the SWNT interior with widths of approximately 0.44 nm, and EDX found an excess of sulfur in the system resulting from the reaction of sulfur with the nanotube sidewalls (Figure 1.18); a blue shift of the G band, compared to empty SWNTs, was again witnessed but to a lesser extent compared to CdI_2@SWNT. The stepwise synthesis was then proven to be successful to form other metal monochalcogenide species, MX (M = Cd, Zn, Pb; X = S, Se, Te).

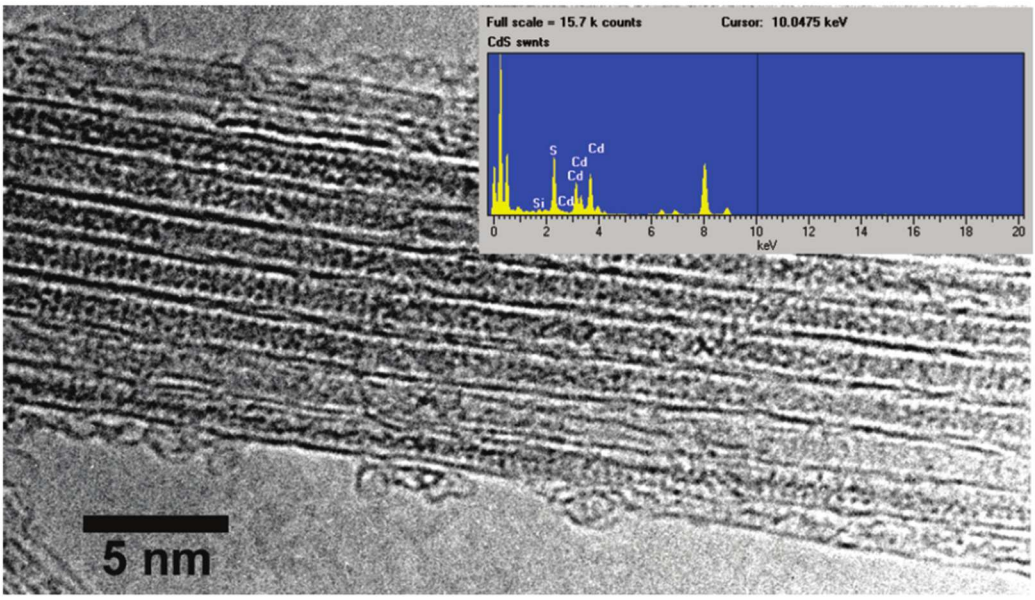


Figure 1.18. *TEM image of CdS@SWNT produced via the reaction of cadmium iodide with sulfur within the SWNT interior channel. Inset is an EDX spectrum confirming the presence of Cd and S in a 1: 1.5 atomic ratio.*[102]

A methodology was developed by Cui *et al*. which aimed to produce metal, metal oxide, and metal carbide NPs exclusively within the interior of SWNTs using a series of stepwise transformations (Figure 1.19).[103] The first step commenced with the sublimation of cycloalkene metal carbonyl complexes into SWNTs followed by the oxidation of the composite material in air resulting in the formation of metal oxide NPs. Importantly, the samples required an acid washing step in order to ensure there was no exterior material remaining. The synthetic route can then take two different pathways; hydrogen reduction, or carburization under an inert atmosphere, resulting in the formation in either metal or metal carbide nanoparticles respectively. The route was found to be successful for a range of 3d, 4d and 5d metals including; V, Mn, Fe, Co, Mo, and W. Products formed during each step were characterised using TEM and a series of complementary spectroscopic techniques.

The NPs displayed relatively narrow size distributions for each metal, demonstrating the lack of larger exterior physisorbed materials.

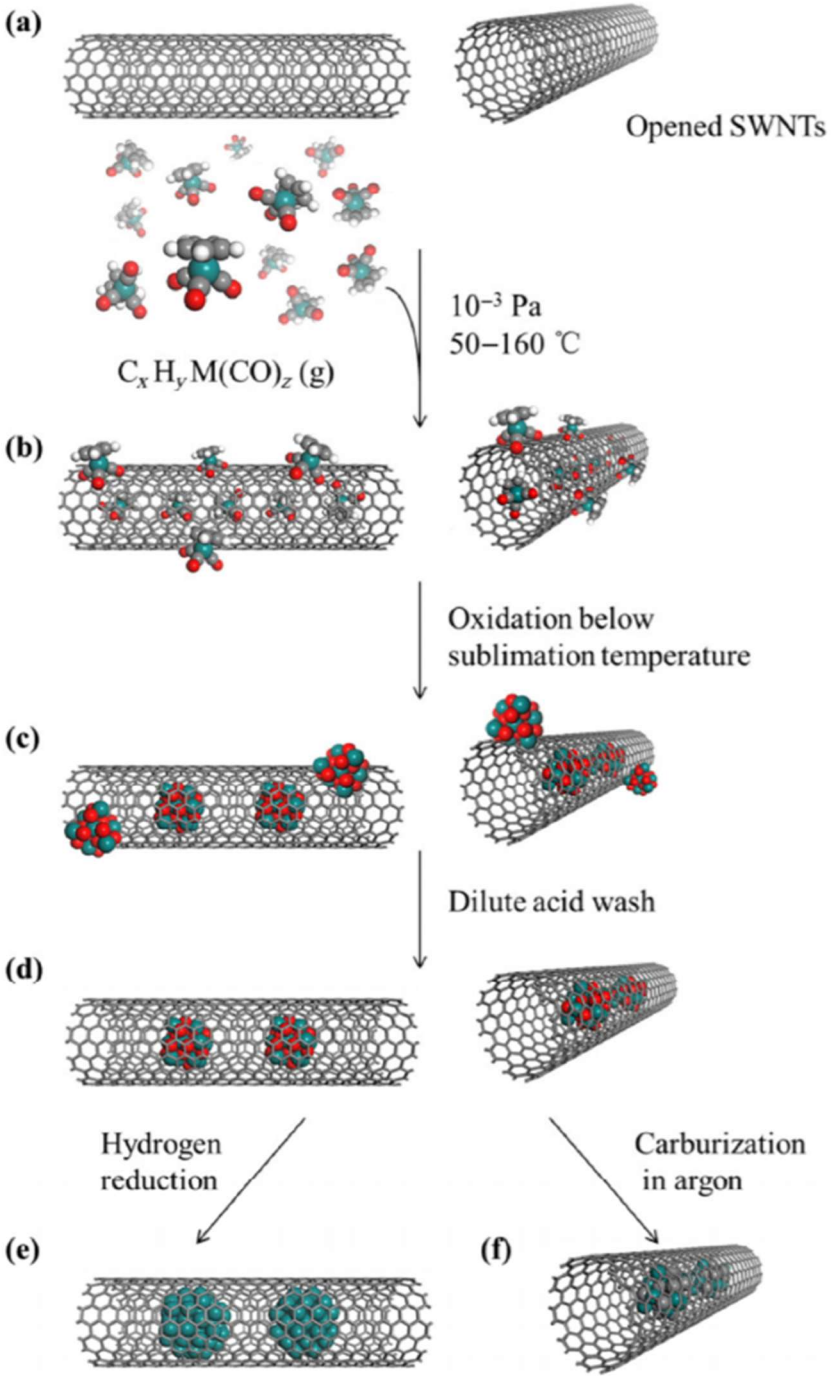


Figure 1.19. *A versatile stepwise methodology of forming 3d, 4d, and 5d metal, metal oxide, and metal carbide nanoparticles (NP). (a) The first step encapsulates cycloalkene metal carbonyl molecules into SWNTs via sublimation followed by (b) oxidation in air to produce*

metal oxide NPs. (c) An acid wash step is then performed to remove exterior material. The MO_x NPs can then either undergo (e) hydrogen reduction or (f) carburization in argon to form M or MC_x NPs respectively.[103]

1.4.2.1. Formation of transition metal dichalcogenides

Transition metal dichalcogenides (TMDCs) of the general formula MX_2 (X = S, Se or Te) are of particular interest due to their encouraging electronic and optical properties, which can be tuned at the nanoscale.[104, 105] They can form either hexagonal layered cadmium iodide-type or cubic pyrite-type structures depending on the ability of the metal to be stable in either a higher (+4) or lower (+2) oxidation state. These materials cannot be directly encapsulated within SWNTs as they have high melting points (1185 ^{o}C for MoS_2) which would decompose the SWNTs during an attempted molten-phase filling technique. To date, only nanoribbons of layered CdI_2-type M(IV) disulfides (M = Mo, W, and Pt) have been synthesised within the constraints of SWNTs.

Molybdenum and tungsten disulfide nanoribbons have both been prepared using two different stepwise methods. The first encapsulated Keggin POM of the general formula $H_3PM_{12}O_{40}$ (M = Mo and W) using an aqueous reflux technique and subsequently reacted them with a mixture of H_2/H_2S to produce MX_2 nanoribbons.[106, 107] Despite the in-depth characterisation of the disulfide nanoribbons using a combination of TEM, EDX, EELS, and Raman spectroscopy in the low-frequency region, there was an absence of investigation into the structure and composition of the encapsulated POMs as well as any electronic communication between the host and guests.

This phenomena of electronic communication between host and guest during the stepwise synthesis of TDMCs within SWNTs was the subject of a study by Botos *et al*. in 2016.[62] The multistep synthesis aimed to again produce MoS_2 and WS_2 nanoribbons but by using metal

carbonyls as the initial source of metal and proceeding via metal iodides as the intermediates (Figure 1.20). The initial encapsulation of both the metal carbonyl and iodine led to a strong blue shift of the G-band which was accompanied by production of polyiodide bands in the low frequency region of the Raman spectrum, as a result of electron transfer from the SWNTs to iodine. Thermal activation of the encapsulated reactants produced octahedral $[M_6I_{14}]^{2-}$ clusters which were also shown to be negatively charged by a blue shift of the G-band, compared to empty SWNTs. The final step was the reaction of the metal iodide species with H_2S to produce disulfide nanoribbons; MoS_2 nanoribbons were found to return the G-band to its original position for empty SWNTs resulting in a charge neutral species, conversely, WS_2 were found to be electron donating towards the SWNT from an apparent G-band red shift compared to empty SWNTs. The ability of SWNTs to act as a reservoir of electrons, denoted as redox active nanoreactors, makes them essential for enabling redox reactions of inorganic guest species, and the stabilisation of the reaction intermediates and products formed.

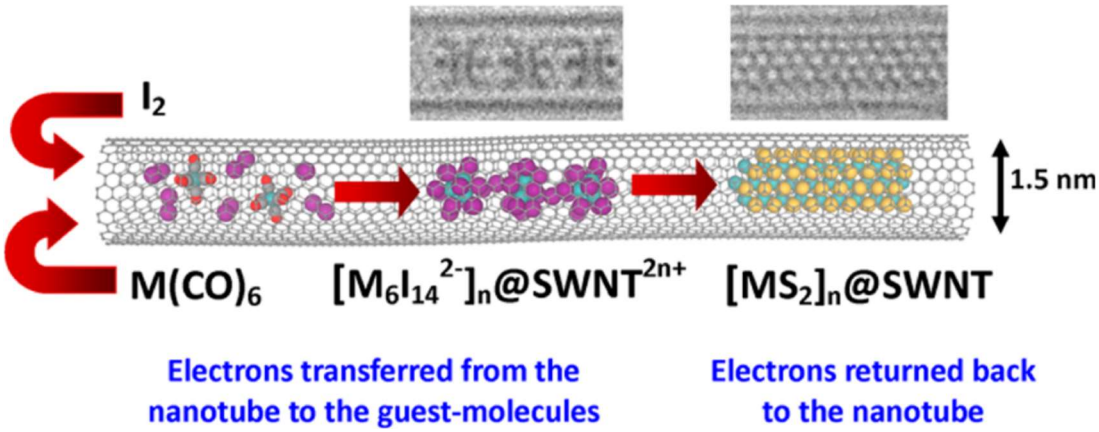


Figure 1.20. *Schematic diagram showing the stepwise production of MS_2 nanoribbons (M = Mo or W), with TEM images superimposed, using metal carbonyls as the source of metal. The metal carbonyl and iodine are simultaneously inserted within the SWNTs and then thermally-activated to produce octahedral $[M_6I_{14}]^{2-}$ clusters. The final step reacts the metal iodide clusters with H_2S to produce the MS_2 nanoribbons.*[62]

More recently, it was shown by Stoppiello *et al*. that quasi-1D platinum disulfide, PtS_2, could be synthesised within SWNTs using either a stepwise synthetic route using platinum acetylacetonate as the source of metal and dihydrogen sulfide as the source of sulfur, or by a one-pot one-reactant synthesis utilising $Pt(acac)_2(SCN)_2$ as the source of both platinum and sulfur.[75] The stepwise route proceeded via formation of PtI_2@SWNT by thermal activation of encapsulated $Pt(acac)_2$ and I_2, followed by ligand exchange using H_2S as the source of sulfur. Alternatively, the one-pot one-reactant synthesis simply thermally decomposed $Pt(acac)_2(SCN)_2$@SWNT under an inert atmosphere to produce the disulfide species. The structure of each PtS_2@SWNT was characterised by a combination of electron microscopy (Figure 1.21) and EDX and it was found that the stepwise route caused residual iodine to be entrapped within the SWNT after the reaction with H_2S, whilst this was not found to be an issue for the one-pot method. The two routes were examined at each stage using a combination of fluorescence-detected X-ray absorption spectroscopy (FD-XAS) and Raman spectroscopy to investigate any electronic communication between the SWNT host and Pt compound guests and the effect on the oxidation state of the metal against the free states. It was found from FD-XAS that encapsulation of $Pt(acac)_2$ and I_2 led to a -1.5 eV shift of the Pt L_{III} edge energy (compared to the free state) accompanied by a + 6 cm^{-1} blue shift of the SWNT G-band from Raman spectroscopy which strongly suggests electron transfer from the SWNT to Pt. Conversely, the encapsulation of $Pt(acac)_2(SCN)_2$ led to a -5 cm^{-1} G-band shift, compared to empty SWNTs, which is indicative of electron donor behaviour of the guest towards the host. Both PtI_2@SWNT and PtS_2@SWNT did not cause any shifts for each spectroscopic technique and thus were charge neutral within the host SWNTs and exhibiting oxidation states as expected for each material.

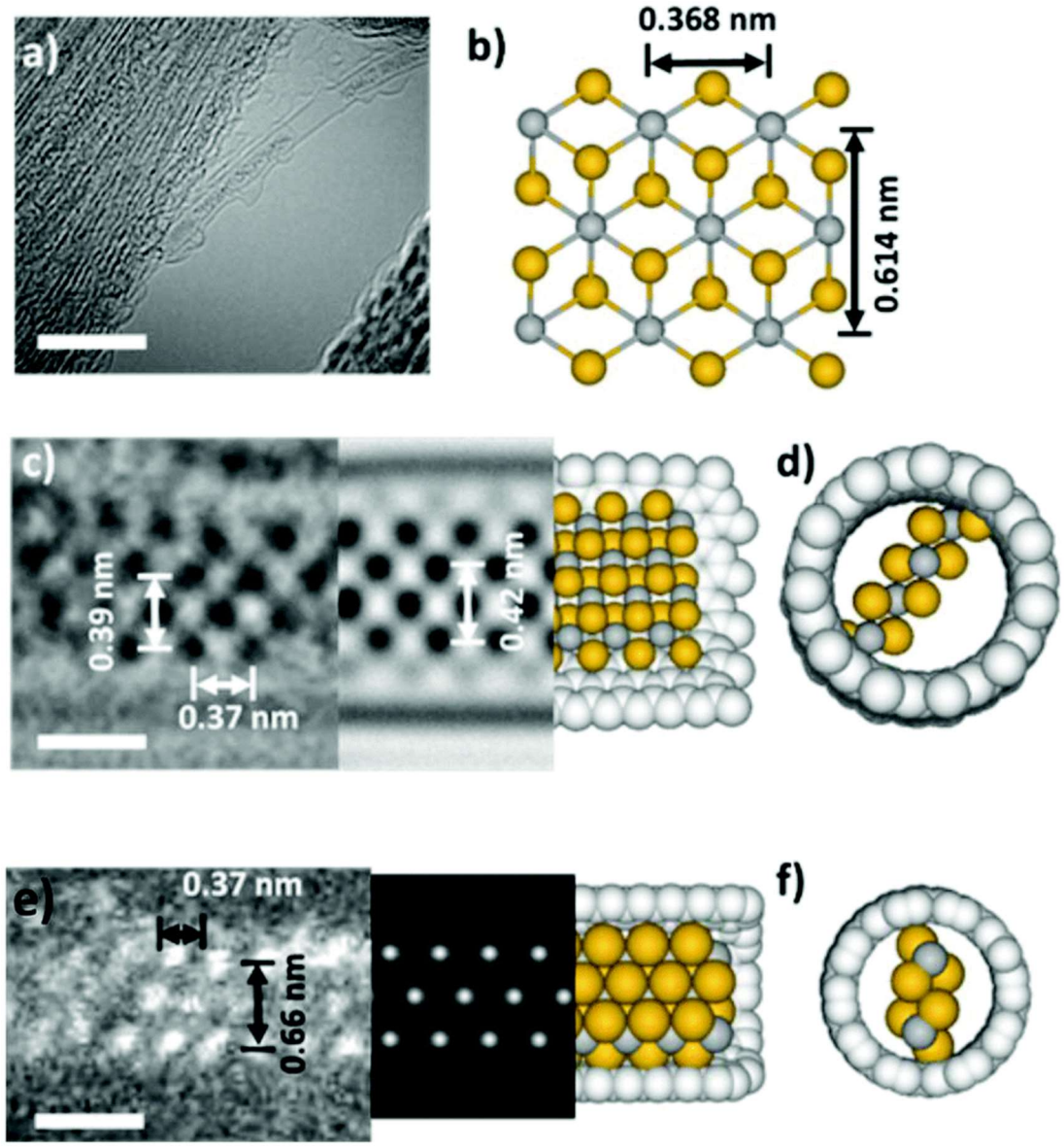


Figure 1.21. *The structure of PtS_2 nanoribbons formed within SWNT hosts by a stepwise synthetic route using $Pt(acac)_2$ as the source of platinum. (a) AC-HRTEM image of PtS_2@SWNT; (b) structural model of a portion of PtS_2 with characteristic interatomic distances superimposed; (c) AC-HRTEM image of a SWNT filled with PtS_2 (left), TEM simulation demonstrating the fit of the structure within a SWNT (middle), structural model of PtS_2@SWNT used to perform the TEM simulation (right); (d) cross-sectional view of PtS_2@SWNT showing the fit of the nanoribbon within the SWNT host; (e) HAADF-AC-STEM image of a PtS_2 nanoribbon within a (11,11) SWNT (left), STEM simulation of PtS_2@SWNT in a projection corresponding to the experimental image (middle), structural model used to*

perform the STEM simulation (right); (f) optimised cross-sectional projection of PtS_2@SWNT.[75]

1.5. Applications of filled carbon nanotubes

As stated in section 1.1.2, SWNTs offer three main advantages for encapsulated guest species which are; being electrically-conducting, possessing an interior channel which templates the formation of quasi-1D species with a high proportion of surface atoms, and protection from the environment, such as oxidation. These benefits provide many application routes for filled SWNTs, a couple of examples are described below.

One promising application for filled SWNTs are as electrocatalysts towards the Hydrogen Evolution Reaction, as SWNTs can act as electron transport vessels towards the guest species. It was shown by Cui *et al*. that molybdenum carbide formed within SWNTs performed better as an electrocatalyst than when it was formed on the exterior of SWNTs (Figure 1.21).[22] TEM and X-ray diffraction analysis proved that alpha-phase MoC_x nanoparticles of 2.9 nm average diameter were formed within the interior, whilst beta-phase Mo_2C nanoparticles of 6.5 nm average diameter were formed on the exterior. Brunauer–Emmett–Teller analysis showed that the surface area was greater for the encapsulated species, and XPS analysis highlighted a lower amount of oxidised material. Of the four main phases of molybdenum carbide, it was shown that the beta phase was the best performing material (exhibited by a lower overpotential at certain current densities), and the alpha phase was the worst performing.[108] Thus, the enhanced performance of the encapsulated species was attributed to the higher surface area and therefore a higher number of accessible active sites, as well as a lower amount of oxidised material which is inactive towards the HER.

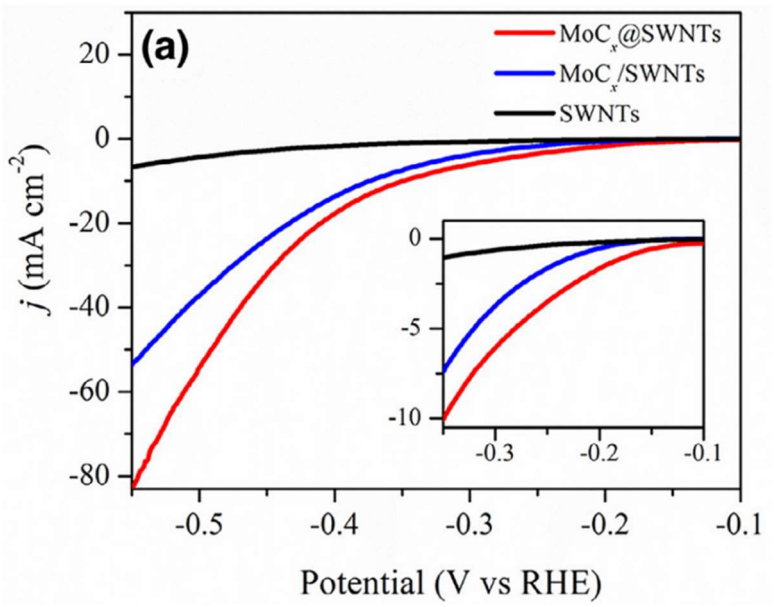


Figure 1.22. *Polarisation curves showing the electrocatalytic ability of molybdenum carbide nanoparticles on the exterior (blue), and interior (red) surfaces of SWNTs. Non-modified SWNTs (black) are also included as a reference.*[22]

The sidewalls of SWNTs are typically inert towards the oxygen reduction reaction (ORR); however, the encapsulation of phosphorus within the interior channel led to enhanced electrocatalytic activity.[109] The insertion of phosphorus (P_4) was found to cause an 11 cm^{-1} blue shift of the G-band of SWNTs, from Raman spectroscopy, which was the result of electron transfer from metallic SWNTs to the lowest unoccupied orbital of phosphorus. The modified positively-charged SWNTs resulted in improved ORR performance.

The use of a SWNT as a template for the formation of a quasi-1D species was exemplified by Clément *et al*. who produced metal nanowires of <1nm in diameter for use in electronic devices.[110] The SWNTs were filled with $M(acac)_2$ (where M = Cu or Pt) precursors, and then were subsequently deposited between electrode pairs. Annealing of the filled SWNTs at 200°C produced quasi-1D metallic nanowires with widths controlled by the diameter of the SWNT interior channel. Following this, the M@SWNT composites were exposed to an oxygen plasma treatment which removed the SWNT host whilst retaining the metal nanowires

between the electrode pairs (Figure 1.23a - b). Cu, Pt, and Cu-Pt alloy nanowires were synthesised and field effect transistor (FET) measurements conducted found to result in no gate dependence observed (Figure 1.23c). The use of SWNTs as templates for the formation of metallic nanowires to act as electrical conductors leads to promising applications in nanoscale FET device manufacturing.

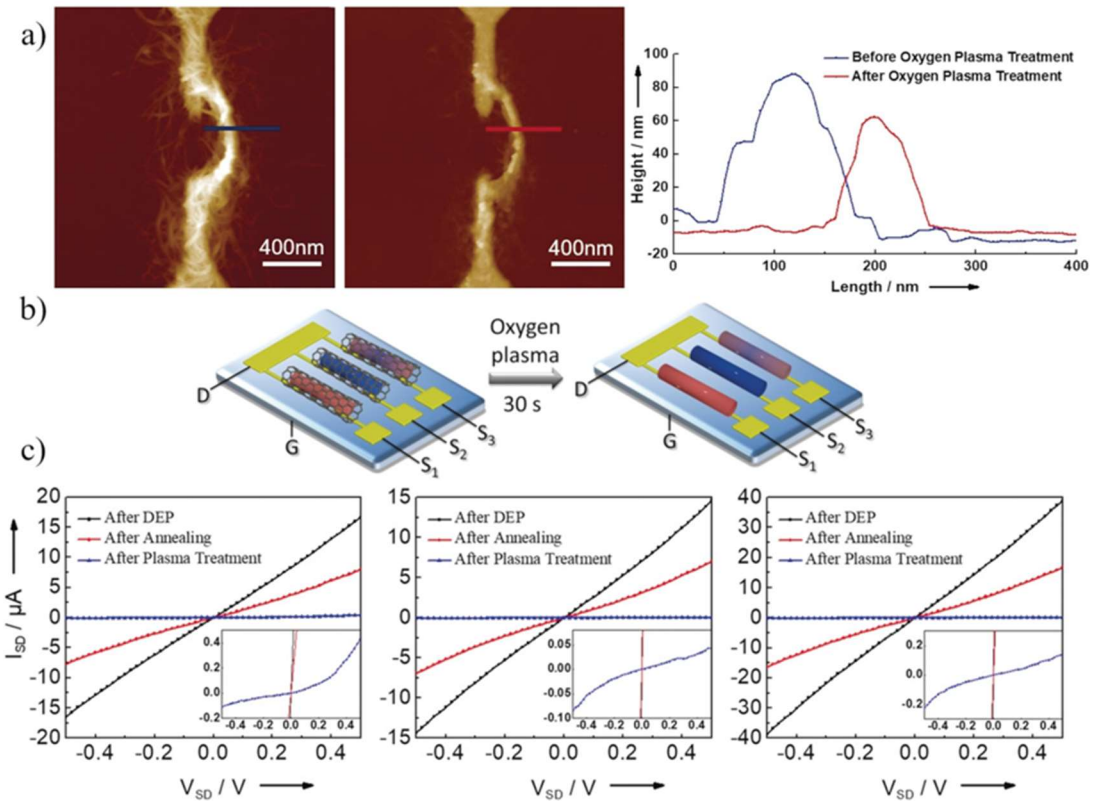


***Figure 1.23**. (a) AFM images and height profiles of Cu@SWNT before (left) and after (right) exposure to oxygen plasma for 30 seconds; (b) schematic diagram demonstrating the removal of the SWNT hosts from the as-produced metallic nanowires after oxygen plasma treatment; (c) I_{SD}-V_{SD} characterisation of $Cu(acac)_2$@SWNT (left), $Pt(acac)_2$@SWNT (middle), and $[Pt(acac)_2 + Cu(acac)_2]$@SWNT (right) after deposition onto the electrode pairs (black), annealing at 200°C (red), and oxygen plasma treatment (blue).*[110]

1.6. Aim and objectives

The encapsulation and subsequent transformations of low-dimensional species within the confinements of SWNTs has led to the formation of novel materials that are not possible to synthesise in the bulk. The aim of this thesis is to further develop the knowledge of the formation of low-dimensional materials using SWNTs as the nano test tube. Particular emphasis will be placed on the group VI to VIII transition metal dichalcogenides due to their tunable properties at the nanoscale. Moreover, to date only MoS_2, WS_2, and PtS_2 have been synthesised within a SWNT; thus this provides scope to investigate the synthesis of other types of metal dichalcogenide materials, such as ReS_2 and OsS_2 under extreme confinement.

Each chapter of this thesis will focus on the investigation of a particular transition metal (Mo, W, Re, Os) that will undergo stepwise reactions within SWNTs to produce novel structures, which may be in the form of discrete molecules or continuous nanoribbons. Each stepwise synthesis will be monitored using a holistic analytical approach that will combine electron microscopy, and spectroscopy techniques to determine structure and composition of each material, as well as any electronic communication between the host and guest.

The systems that will be studied are:

- The synthesis of rhenium disulfide (ReS_2) nanoribbons via the formation of rhenium iodide. ReS_2 is known to have electronic properties that are layer independent and thus there is a need to produce and characterise ultrathin structures for use in molecular scale electronic devices.
- The comparison of the two distinct surfaces of SWNTs; the concave and convex, towards the formation of low-dimensional structures of osmium. This work will conduct a stepwise synthesis of osmium compounds of which material on both surfaces will be subjected to the exact same reaction conditions.

- The entrapment and transformations of triangular molybdenum chalcogen clusters, which are molecular mimics of the edge sites of molybdenum dichalcogenide monolayers. Their molecular dynamics will be studied within the one-dimensional channel of SWNTs using state of the art aberration-corrected TEM.
- Dynamic analysis of tungsten disulfide nanoribbons within SWNTs and boron nitride nanotubes, using a *ChemTEM* approach. The structure and transformation of WS_2 nanoribbons under electron beam irradiation will be studied at the atomistic level.

Finally, a selection of materials synthesised within this thesis will be evaluated towards applications as electrocatalysts for the Hydrogen Evolution Reaction. This process will utilise and combine the electrical-conducting properties of SWNTs to act as nano-electrodes, as well as the high surface area of the catalytically active guest species.

1.7. References

1. H. Ma, Z. Chen, X. Gao, W. Liu and H. Zhu, *Sci Rep-Uk*, 2019, **9**, 17065.
2. Z. Xu, J. Zhang, T. Pan, H. Li, F. Huo, B. Zheng and W. Zhang, *Chem. Mater.*, 2020, **32**, 3553-3560.
3. R. Mirzayev, K. Mustonen, M. R. A. Monazam, A. Mittelberger, T. J. Pennycook, C. Mangler, T. Susi, J. Kotakoski and J. C. Meyer, *Sci. Adv.*, 2017, **3**, e1700176.
4. E.-Y. Zhang, C.-Y. Shu, L. Feng and C.-R. Wang, *J. Phys. Chem. B*, 2007, **111**, 14223-14226.
5. D. S. Bethune, C. H. Kiang, M. S. de Vries, G. Gorman, R. Savoy, J. Vazquez and R. Beyers, *Nature*, 1993, **363**, 605-607.
6. S. Iijima and T. Ichihashi, *Nature*, 1993, **363**, 603-605.
7. J. Wang, J. Yang, D. Zhang and Y. Li, *J. Phys. Chem. C*, 2012, **116**, 23826-23832.

8. S. Huang, X. Cai and J. Liu, *J. Am. Chem. Soc.*, 2003, **125**, 5636-5637.

9. S. Ziaei-Rad and N. Nouri, *Scientia Iranica*, 2010, **17**, -.

10. P. G. Collins and P. Avouris, *Sci. Am.*, 2000, **283**, 62-69.

11. M. S. Dresselhaus, G. Dresselhaus and R. Saito, *Carbon*, 1995, **33**, 883-891.

12. E. Joselevich, *ChemPhysChem*, 2004, **5**, 619-624.

13. A. Thess, R. Lee, P. Nikolaev, H. Dai, P. Petit, J. Robert, C. Xu, Y. H. Lee, S. G. Kim, A. G. Rinzler, D. T. Colbert, G. E. Scuseria, D. Tománek, J. E. Fischer and R. E. Smalley, *Science*, 1996, **273**, 483-487.

14. C. Journet, W. K. Maser, P. Bernier, A. Loiseau, M. L. de la Chapelle, S. Lefrant, P. Deniard, R. Lee and J. E. Fischer, *Nature*, 1997, **388**, 756-758.

15. Q. Fu and J. Liu, in *Carbon Nanotechnology*, ed. L. Dai, Elsevier, Amsterdam, 2006, pp. 81-107.

16. R. Seidel, G. S. Duesberg, E. Unger, A. P. Graham, M. Liebau and F. Kreupl, *J. Phys. Chem. B*, 2004, **108**, 1888-1893.

17. A. Chuvilin, A. N. Khlobystov, D. Obergfell, M. Haluska, S. H. Yang, S. Roth and U. Kaiser, *Angew. Chem. Int. Ed.*, 2010, **49**, 193-196.

18. C. A. Slade, A. M. Sanchez and J. Sloan, *Nano Lett.*, 2019, **19**, 2979-2984.

19. M. Hart, E. R. White, J. Chen, C. M. McGilvery, C. J. Pickard, A. Michaelides, A. Sella, M. S. P. Shaffer and C. G. Salzmann, *Angew. Chem. Int. Ed.*, 2017, **56**, 8144-8148.

20. R. L. McSweeney, T. W. Chamberlain, E. S. Davies and A. N. Khlobystov, *Chem. Commun.*, 2014, **50**, 14338-14340.

21. J. W. Jordan, G. A. Lowe, R. L. McSweeney, C. T. Stoppiello, R. W. Lodge, S. T. Skowron, J. Biskupek, G. A. Rance, U. Kaiser, D. A. Walsh, G. N. Newton and A. N. Khlobystov, *Adv. Mater.*, 2019, **31**, 1904182.

22. T. Cui, J. Dong, X. Pan, T. Yu, Q. Fu and X. Bao, *J. Energy Chem.*, 2019, **28**, 123-127.

23. S. A. Miners, G. A. Rance and A. N. Khlobystov, *Chem. Soc. Rev.*, 2016, **45**, 4727-4746.

24. A. Jedrzejewska, S. Costa, K. Cendrowski, R. Kalenczuk and E. Mijowska, *Mater. Sci-Poland*, 2012, **29**.

25. C.-H. Kiang, J.-S. Choi, T. T. Tran and A. D. Bacher, *J. Phys. Chem. B*, 1999, **103**, 7449-7451.

26. B. W. Smith, M. Monthioux and D. E. Luzzi, *Nature*, 1998, **396**, 323-324.

27. H. Ulbricht, G. Moos and T. Hertel, *Phys. Rev. Lett.*, 2003, **90**, 095501.

28. H. Kataura, Y. Maniwa, T. Kodama, K. Kikuchi, K. Hirahara, K. Suenaga, S. Iijima, S. Suzuki, Y. Achiba and W. Krätschmer, *Synth. Met.*, 2001, **121**, 1195-1196.

29. C. Xu, J. Sloan, G. Brown, S. Bailey, V. C. Williams, S. Friedrichs, K. S. Coleman, E. Flahaut, J. L. Hutchison, R. E. Dunin-Borkowski and M. L. H. Green, *Chem. Commun.*, 2000, 2427-2428.

30. M. Yudasaka, K. Ajima, K. Suenaga, T. Ichihashi, A. Hashimoto and S. Iijima, *Chem. Phys. Lett.*, 2003, **380**, 42-46.

31. P. M. Ajayan, T. W. Ebbesen, T. Ichihashi, S. Iijima, K. Tanigaki and H. Hiura, *Nature*, 1993, **362**, 522-525.

32. J. Sloan, J. Hammer, M. Zwiefka-Sibley and M. L. H. Green, *Chem. Commun.*, 1998, 347-348.

33. B. Burteaux, A. Claye, B. W. Smith, M. Monthioux, D. E. Luzzi and J. E. Fischer, *Chem. Phys. Lett.*, 1999, **310**, 21-24.

34. R. Hatakeyama, Y. Li, T. Kato and T. Kaneko, *Appl. Phys. Lett.*, 2010, **97**, 013104-013104.

35. S. C. Benjamin, A. Ardavan, G. A. D. Briggs, D. A. Britz, D. Gunlycke, J. Jefferson, M. A. G. Jones, D. F. Leigh, B. W. Lovett, A. N. Khlobystov, S. A. Lyon, J. J. L. Morton, K. Porfyrakis, M. R. Sambrook and A. M. Tyryshkin, *J Phys-Condens Mat*, 2006, **18**, S867-S883.

36. E. Bichoutskaia, Z. Liu, N. Kuganathan, E. Faulques, K. Suenaga, I. J. Shannon and J. Sloan, *Nanoscale*, 2012, **4**, 1190-1199.

37. J. Sloan, G. Matthewman, C. Dyer-Smith, A. Y. Sung, Z. Liu, K. Suenaga, A. I. Kirkland and E. Flahaut, *ACS Nano*, 2008, **2**, 966-976.

38. J. Sloan, M. C. Novotny, S. R. Bailey, G. Brown, C. Xu, V. C. Williams, S. Friedrichs, E. Flahaut, R. L. Callender, A. P. E. York, K. S. Coleman, M. L. H. Green, R. E. Dunin-Borkowski and J. L. Hutchison, *Chem. Phys. Lett.*, 2000, **329**, 61-65.

39. J. Sloan, S. J. Grosvenor, S. Friedrichs, A. I. Kirkland, J. L. Hutchison and M. L. H. Green, *Angew. Chem. Int. Edit.*, 2002, **41**, 1156-1159.

40. E. Philp, J. Sloan, A. I. Kirkland, R. R. Meyer, S. Friedrichs, J. L. Hutchison and M. L. H. Green, *Nat. Mater.*, 2003, **2**, 788-791.

41. K. Tyagi, B. Gahtori, S. Bathula, N. K. Singh, S. Bishnoi, S. Auluck, A. K. Srivastava and A. Dhar, *RSC. Adv.*, 2016, **6**, 11562-11569.

42. N. C. Fernelius, *Prog. Cryst. Growth Charact. Mater.*, 1994, **28**, 275-353.

43. A. A. Eliseev, N. S. Falaleev, N. I. Verbitskiy, A. A. Volykhov, L. V. Yashina, A. S. Kumskov, V. G. Zhigalina, A. L. Vasiliev, A. V. Lukashin, J. Sloan and N. A. Kiselev, *Nano Lett.*, 2017, **17**, 805-810.

44. P. V. C. Medeiros, S. Marks, J. M. Wynn, A. Vasylenko, Q. M. Ramasse, D. Quigley, J. Sloan and A. J. Morris, *ACS Nano*, 2017, **11**, 6178-6185.

45. A. Vasylenko, S. Marks, J. M. Wynn, P. V. C. Medeiros, Q. M. Ramasse, A. J. Morris, J. Sloan and D. Quigley, *ACS Nano*, 2018, **12**, 6023-6031.

46. M. Nagata, S. Shukla, Y. Nakanishi, Z. Liu, Y.-C. Lin, T. Shiga, Y. Nakamura, T. Koyama, H. Kishida, T. Inoue, N. Kanda, S. Ohno, Y. Sakagawa, K. Suenaga and H. Shinohara, *Nano Lett.*, 2019, **19**, 4845-4851.

47. C. E. Giusca, V. Stolojan, J. Sloan, F. Borrnert, H. Shiozawa, K. Sader, M. H. Rummeli, B. Buchner and S. R. P. Silva, *Nano Lett.*, 2013, **13**, 4020-4027.

48. R. P. Feynman, presented in part at the American Physical Society meeting, Pasadena, California, December 1959, December 1959.

49. D. B. Williams and C. B. Carter, *Transmission Electron Microscopy*, Springer, US, 2nd edn., 2009.

50. E. Britannica, transmission electron microscope, https://www.britannica.com/technology/transmission-electron-microscope#/media/1/602949/110686, (accessed 15th June, 2021).

51. S. Friedrichs, R. R. Meyer, J. Sloan, A. I. Kirkland, J. L. Hutchison and M. L. H. Green, *Chem. Commun.*, 2001, 929-930.

52. J. Biskupek, S. T. Skowron, C. T. Stoppiello, G. A. Rance, S. Alom, K. L. Y. Fung, R. J. Whitby, M. H. Levitt, Q. M. Ramasse, U. Kaiser, E. Besley and A. N. Khlobystov, *ACS Nano*, 2020, **14**, 11178-11189.

53. Z. Liu, S.-K. Joung, T. Okazaki, K. Suenaga, Y. Hagiwara, T. Ohsuna, K. Kuroda and S. Iijima, *ACS Nano*, 2009, **3**, 1160-1166.

54. M. Haider, H. Rose, S. Uhlemann, E. Schwan, B. Kabius and K. Urban, *Ultramicroscopy*, 1998, **75**, 53-60.

55. D. Shindo and T. Oikawa, in *Analytical Electron Microscopy for Materials Science*, eds. D. Shindo and T. Oikawa, Springer, Tokyo, Tokyo, 2002, pp. 81 - 102.

56. P. M. F. J. Costa, J. Sloan, T. Rutherford and M. L. H. Green, *Chem. Mater.*, 2005, **17**, 6579-6582.

57. S. R. Marks, K. Morawiec, P. Dluzewski, S. Kret and J. Sloan, *Acta Phys. Pol., A*, 2017, **131**, 1324-1327.

58. S. A. Miners, M. W. Fay, M. Baldoni, E. Besley, A. N. Khlobystov and G. A. Rance, *J. Phys. Chem. C*, 2019, **123**, 6294-6302.

59. P. J. Statham, *J. Res. Natl. Inst. Stand. Technol.*, 2002, **107**, 531-546.

60. J. Goldstein, D. E. Newbury, D. C. Joy, C. E. Lyman, P. Echlin, E. Lifshin, L. Sawyer and J. R. Michael, *Scanning Electron Microscopy and X-Ray Microanalysis*, Springer US, New York, US, 3rd edn., 2003.

61. S. J. B. Reed, in *X-Ray Spectrometry in Electron Beam Instruments*, eds. D. B. Williams, J. I. Goldstein and D. E. Newbury, Springer US, Boston, MA, 1995, pp. 221-238.

62. A. Botos, J. Biskupek, T. W. Chamberlain, G. A. Rance, C. T. Stoppiello, J. Sloan, Z. Liu, K. Suenaga, U. Kaiser and A. N. Khlobystov, *J. Am. Chem. Soc.*, 2016, **138**, 8175-8183.

63. M. V. Kharlamova, *J Spectrosc*, 2015, **2015**.

64. M. S. Dresselhaus, G. Dresselhaus, A. Jorio, A. G. Souza and R. Saito, *Carbon*, 2002, **40**, 2043-2061.

65. M. S. Dresselhaus, G. Dresselhaus, R. Saito and A. Jorio, *Phys. Rep*, 2005, **409**, 47-99.

66. Y. Park, K. P. S. S. Hembram, R. Yoo, B. Jang, W. Lee, S.-G. Lee, J.-G. Kim, Y.-I. Kim, D. J. Moon, J.-K. Lee and J.-K. Lee, *J. Phys. Chem. C*, 2019, **123**, 14003-14009.

67. M. A. Pimenta, A. Marucci, S. A. Empedocles, M. G. Bawendi, E. B. Hanlon, A. M. Rao, P. C. Eklund, R. E. Smalley, G. Dresselhaus and M. S. Dresselhaus, *Phys. Rev. B*, 1998, **58**, R16016-R16019.

68. M. S. Dresselhaus, A. Jorio and M. A. Pimenta, *An. Acad. Bras. Cienc.*, 2006, **78**, 423-439.

69. M. V. Kharlamova and J. J. Niu, *J. Exp. Theor. Phys.*, 2012, **115**, 485-491.

70. M. V. Kharlamova, *Appl. Phys. A*, 2016, **122**, 791.

71. M. V. Kharlamova, C. Kramberger, O. Domanov, A. Mittelberger, T. Saito, K. Yanagi, T. Pichler and D. Eder, *Phys. Status Solidi B*, 2018, **255**.

72. M. V. Kharlamova, L. V. Yashina and A. V. Lukashin, *J Mater Sci*, 2013, **48**, 8412-8419.

73. A. A. Eliseev, L. V. Yashina, N. I. Verbitskiy, M. M. Brzhezinskaya, M. V. Kharlamova, M. V. Chernysheva, A. V. Lukashin, N. A. Kiselev, A. S. Kumskov, B. Freitag, A. V.

Generalov, A. S. Vinogradov, Y. V. Zubavichus, E. Kleimenov and M. Nachtegaal, *Carbon*, 2012, **50**, 4021-4039.

74. M. V. Kharlamova, C. Kramberger, P. Rudatis, T. Pichler and D. Eder, *Appl Phys a-Mater*, 2019, **125**.

75. C. T. Stoppiello, J. Biskupek, Z. Y. Li, G. A. Rance, A. Botos, R. M. Fogarty, R. A. Bourne, J. Yuan, K. R. J. Lovelock, P. Thompson, M. W. Fay, U. Kaiser, T. W. Chamberlain and A. N. Khlobystov, *Nanoscale*, 2017, **9**, 14385-14394.

76. M. V. Kharlamova, C. Kramberger and A. Mittelberger, *Appl Phys a-Mater*, 2017, **123**.

77. M. V. Kharlamova, *Appl Phys a-Mater*, 2013, **111**, 725-731.

78. C. Branca, F. Frusteri, V. Magazù and A. Mangione, *J. Phys. Chem. B*, 2004, **108**, 3469-3473.

79. U. Kuhlmann, H. Jantoljak, N. Pfänder, P. Bernier, C. Journet and C. Thomsen, *Chem. Phys. Lett.*, 1998, **294**, 237-240.

80. K. Sbai, A. Rahmani, H. Chadli, J. L. Bantignies, P. Hermet and J. L. Sauvajol, *J. Phys. Chem. B*, 2006, **110**, 12388-12393.

81. D. V. Kazachkin, Y. Nishimura, H. A. Witek, S. Irle and E. Borguet, *J. Am. Chem. Soc.*, 2011, **133**, 8191-8198.

82. Á. Pekker, G. Németh, Á. Botos, H. M. Tóháti, F. Borondics, Z. Osváth, L. P. Biró, K. Walker, A. N. Khlobystov and K. Kamarás, *Phys. Status Solidi B*, 2016, **253**, 2457-2460.

83. L. Guan, Z. Shi, M. Li and Z. Gu, *Carbon*, 2005, **43**, 2780-2785.

84. J. Wang, M. K. Kuimova, M. Poliakoff, G. A. D. Briggs and A. N. Khlobystov, *Angew. Chem. Int. Ed.*, 2006, **45**, 5188-5191.

85. L. Grigorian, K. A. Williams, S. Fang, G. U. Sumanasekera, A. L. Loper, E. C. Dickey, S. J. Pennycook and P. C. Eklund, *Phys. Rev. Lett.*, 1998, **80**, 5560-5563.

86. T. Fukumaru, T. Fujigaya and N. Nakashima, *Sci Rep-Uk*, 2015, **5**, 7951.

87. Y. V. Fedoseeva, A. S. Orekhov, G. N. Chekhova, V. O. Koroteev, M. A. Kanygin, B. V. Senkovskiy, A. Chuvilin, D. Pontiroli, M. Riccò, L. G. Bulusheva and A. V. Okotrub, *ACS Nano*, 2017, **11**, 8643-8649.

88. M. V. Kharlamova, M. Sauer, T. Saito, Y. Sato, K. Suenaga, T. Pichler and H. Shiozawa, *Nanoscale*, 2015, **7**, 1383-1391.

89. T. W. Chamberlain, J. Biskupek, S. T. Skowron, A. V. Markevich, S. Kurasch, O. Reimer, K. E. Walker, G. A. Rance, X. Feng, K. Müllen, A. Turchanin, M. A. Lebedeva, A. G. Majouga, V. G. Nenajdenko, U. Kaiser, E. Besley and A. N. Khlobystov, *ACS Nano*, 2017, **11**, 2509-2520.

90. S. T. Skowron, I. V. Lebedeva, A. M. Popov and E. Bichoutskaia, *Nanoscale*, 2013, **5**, 6677-6692.

91. E. Hernández, V. Meunier, B. W. Smith, R. Rurali, H. Terrones, M. Buongiorno Nardelli, M. Terrones, D. E. Luzzi and J. C. Charlier, *Nano Lett.*, 2003, **3**, 1037-1042.

92. K. C. Cao, T. W. Chamberlain, J. Biskupek, T. Zoberbier, U. Kaiser and A. N. Khlobystov, *Nano Lett.*, 2018, **18**, 6334-6339.

93. K. C. Cao, S. T. Skowron, C. T. Stoppiello, J. Biskupek, A. N. Khlobystov and U. Kaiser, *Angew. Chem. Int. Ed.*, 2020.

94. T. Nakamuro, M. Sakakibara, H. Nada, K. Harano and E. Nakamura, *J. Am. Chem. Soc.*, 2021, **143**, 1763-1767.

95. K. Cao, J. Biskupek, C. T. Stoppiello, R. L. McSweeney, T. W. Chamberlain, Z. Liu, K. Suenaga, S. T. Skowron, E. Besley, A. N. Khlobystov and U. Kaiser, *Nat. Chem.*, 2020, 921-928.

96. E. Borowiak-Palen, *Phys. Status Solidi B*, 2007, **244**, 4311-4314.

97. A. Govindaraj, B. C. Satishkumar, M. Nath and C. N. R. Rao, *Chem. Mater.*, 2000, **12**, 202-205.

98. B. C. Satishkumar, A. Taubert and D. E. Luzzi, *J. Nanosci. Nanotechnol.*, 2003, **3**, 159-163.

99. T. W. Chamberlain, T. Zoberbier, J. Biskupek, A. Botos, U. Kaiser and A. N. Khlobystov, *Chem. Sci.*, 2012, **3**, 1919-1924.

100. K. Cao, T. Zoberbier, J. Biskupek, A. Botos, R. L. McSweeney, A. Kurtoglu, C. T. Stoppiello, A. V. Markevich, E. Besley, T. W. Chamberlain, U. Kaiser and A. N. Khlobystov, *Nat. Commun.*, 2018, **9**, 3382.

101. T. W. Chamberlain, J. Biskupek, G. A. Rance, A. Chuvilin, T. J. Alexander, E. Bichoutskaia, U. Kaiser and A. N. Khlobystov, *ACS Nano*, 2012, **6**, 3943-3953.

102. A. A. Eliseev, M. V. Chernysheva, N. I. Verbitskii, E. A. Kiseleva, A. V. Lukashin, Y. D. Tretyakov, N. A. Kiselev, O. M. Zhigalina, R. M. Zakalyukin, A. L. Vasiliev, A. V. Krestinin, J. L. Hutchison and B. Freitag, *Chem. Mater.*, 2009, **21**, 5001-5003.

103. T. Cui, X. Pan, J. Dong, S. Miao, D. Miao and X. Bao, *Nano Res*, 2018, **11**, 3132-3144.

104. Q. H. Wang, K. Kalantar-Zadeh, A. Kis, J. N. Coleman and M. S. Strano, *Nat. Nanotechnol.*, 2012, **7**, 699-712.

105. S. Manzeli, D. Ovchinnikov, D. Pasquier, O. V. Yazyev and A. Kis, *Nat. Rev. Mater.*, 2017, **2**, 17033.

106. Z. Wang, H. Li, Z. Liu, Z. Shi, J. Lu, K. Suenaga, S.-K. Joung, T. Okazaki, Z. Gu, J. Zhou, Z. Gao, G. Li, S. Sanvito, E. Wang and S. Iijima, *J. Am. Chem. Soc.*, 2010, **132**, 13840-13847.

107. Z. Wang, K. Zhao, H. Li, Z. Liu, Z. Shi, J. Lu, K. Suenaga, S.-K. Joung, T. Okazaki, Z. Jin, Z. Gu, Z. Gao and S. Iijima, *J. Mater. Chem.*, 2011, **21**, 171-180.

108. C. Wan, Y. N. Regmi and B. M. Leonard, *Angew. Chem. Int. Ed.*, 2014, **53**, 6407-6410.

109. J. Xu and L. Guan, *RSC. Adv.*, 2013, **3**, 5577-5582.

110. P. Clément, X. Xu, C. T. Stoppiello, G. A. Rance, A. Attanzio, J. N. O'Shea, R. H. Temperton, A. N. Khlobystov, K. R. J. Lovelock, J. M. Seymour, R. M. Fogarty, A. Baker,

R. A. Bourne, B. Hall, T. W. Chamberlain and M. Palma, *Angew. Chem. Int. Ed.*, 2019, **58**, 9928-9932.

Chapter 2: Synthesis of ultrathin rhenium disulfide nanoribbons

2.1. Introduction

Rhenium(IV) disulfide (ReS_2) has gained a lot of recent attention following the discovery that it, uniquely amongst the transition metal dichalcogenides (TMDCs), possesses layer-independent optical, electrical, and vibrational properties, as well as exhibiting in-plane anisotropicity.[1-3] The layered material has a distorted octahedral 1T structure comprised of covalent bonds between Re and S atoms and weak van der Waals' forces between the layers that form the bulk material (Figures 2.1a and b).[4] It is derived from the hexagonal lattices of MoS_2 and WS_2[5-7] but differs by having one extra valence electron causing it to form Re-Re bonds to produce Re_4 units;[8] this causes the in-plane anisotropicity of the layers, as demonstrated by Raman spectroscopy.[9] When exfoliated to a monolayer it retains its electronic properties as a direct bandgap semiconductor; however, the bandgap does slightly increase from 1.5 eV for the bulk material to 1.6 eV for the monolayer.[10] This is in stark contrast to most other TMDCs whose physical properties are layer-dependent and, when exfoliated to a monolayer, undergo an indirect to direct bandgap transition resulting in photoluminescence.[11, 12]

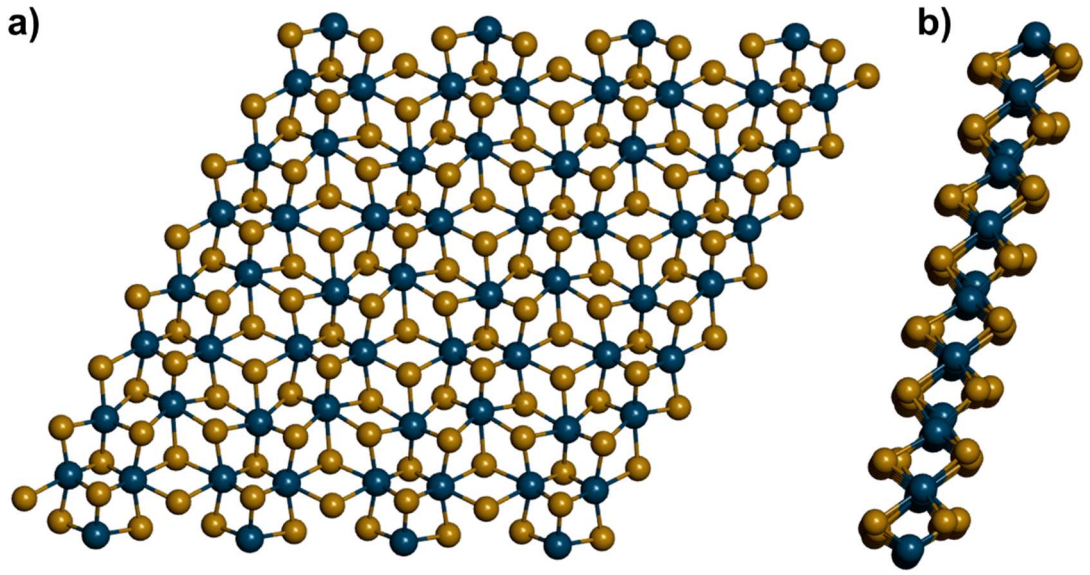


Figure 2.1. *The structure of rhenium(IV) disulfide shown in (a) face-on, and (b) edge-on projections.*

ReS_2-based nanomaterials, such as nanotubes, have been synthesised previously; these were formed upon reaction of a Re-containing solution with H_2S at the surface of multi-walled carbon nanotubes, which act as a template.[13] Colloidal nanoparticles with an average diameter of 5.5 nm have also been formed which were shown to be suitable for applications in therapy of tumour diseases.[14] Nanowires that were 180 nm in diameter were synthesised by An *et al*. using a chemical vapour deposition (CVD) technique.[15] ReS_2 nanoribbons were synthesised by He *et al.* also by a CVD process; the widths of the nanoribbons were approximately 50 nm and the lengths ranged from 10 – 30 μm.[16] These two CVD processes still produce ReS_2 nanomaterials that are contain a large proportion of core atoms, thus reducing use in catalytic applications, and thus new techniques require developing that can produce closer to one-dimensional materials such as nanoribbons. However, the structure and composition of ultrathin ReS_2 nanoribbons (1.3 – 3.8 nm) have only been studied computationally, where they were found to have a direct bandgap which is only weakly dependent on the nanoribbon width.[17]

Single-walled carbon nanotubes (SWNTs) can act as templates for the formation of quasi-1D nanomaterials and have been used to synthesise a range of species including; sulfur graphitised nanoribbons[18], MoS_2[19], WS_2[20], and PtS_2.[21] The stepwise method utilised by Botos *et al.* for the formation of group VI sulfides used metal carbonyls as the starting material to be encapsulated and was shown to be highly effective.[22] The paper provides a general strategy for encapsulating unique materials in nanotubes, which can be applied to any other metal precursors that can sublime to form new metal sulphides with novel structures. The anisotropic material was previously grown as nanosheets on the exterior of carbon nanotubes and has been tested as an anode material for Li-ion batteries and shown high capacitance and capacity retention after 100 cycles.[23] However, formation of the material within the concave of SWNTs will aid with the stability of ultrathin materials, and protect them from oxidation.

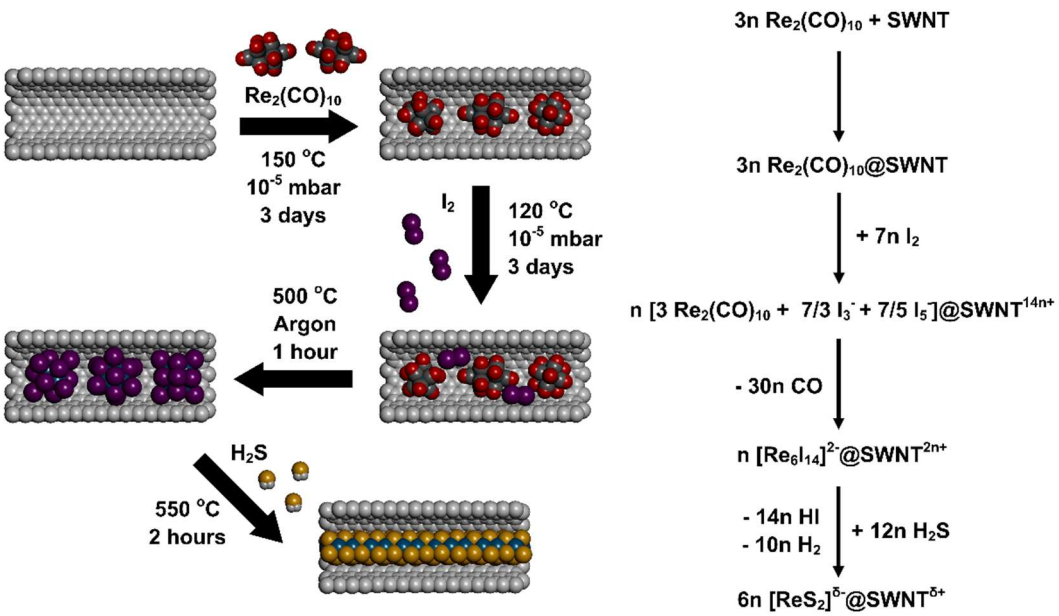
In this work, the synthesis of ultrathin single-layer ReS_2 nanoribbons with diameters in the range of 1 - 2 nm will be attempted, which have only been previously studied theoretically. The synthetic route will use dirhenium decacarbonyl as the source of rhenium, with rhenium iodide the intermediate in the final formation of ReS_2. This will not only provide bond directionality for the sulfide to form, but also allow the opportunity to study a one-dimensional rhenium iodide species inside a nano test tube. A holistic analytical approach will be utilised to probe the structure and composition of the materials at each stage of the stepwise synthesis. The resulting ReS_2 nanoribbons are predicted to retain their bulk electronic properties as direct bandgap semiconductors and being encapsulated with electronically conducting allows them to act as nano-electrodes. Whilst these materials may have applications in the fabrication of molecular scale electronic devices, the ability to

understand and control the fundamental inorganic transformations that lead to the functional materials is essential for the realisation of these potential applications.

2.2. Results and Discussion

2.2.1. Synthetic route

To prepare ultrathin rhenium iodide and sulfide materials a stepwise synthesis was utilised (Scheme 2.1). Dirhenium decacarbonyl, $Re_2(CO)_{10}$, was selected as the precursor due to its low sublimation temperature of 150 °C, and labile carbonyl ligands which are easily substitutable; and has shown success when preparing Re nanoparticles inside SWNTs by Cao *et al*.[24] The gas-phase encapsulation technique is also hugely beneficial as it allows restriction free access for the rhenium source to enter the nanotube internal channel. The SWNTs used have an internal diameter range between 0.8 – 2.0 nm and underwent two treatment steps; the first was a two hour reflux in 3M nitric acid followed by heating to 600 °C in air to remove the end caps and any amorphous carbon present. The reaction of the rhenium precursor with elemental iodine in a sealed environment at elevated temperatures allows loss of the ligands and the iodide to be formed, resulting in oxidation of the rhenium metal centres. Furthermore, a washing step is included to remove any exterior rhenium carbonyl from the SWNT exterior. An iodide is used as the intermediate as it offers the opportunity to examine entrapped forms of rhenium iodide which have not been previously studied. The final step of the synthesis involves the reaction of the iodide species with hydrogen sulfide to form the ReS_2 nanoribbons.



Scheme 2.1. *The synthesis of ReS_2@SWNT formed by the encapsulation and reaction of dirhenium decacarbonyl. The molecules are first reacted to form rhenium iodide clusters using iodine resulting in oxidation of the metal centre. This is followed by a subsequent inorganic transformation via ligand exchange that takes place to form rhenium disulfide nanoribbons using a suitable reactant (left). A balanced chemical reaction demonstrating the charge transfer between nanotube and guest-molecules is also shown (right).*

2.2.2. Insertion of the carbonyl

The insertion of the rhenium carbonyl in nanotubes was confirmed by 200 kV transmission electron microscopy (TEM) imaging, which displayed clusters with an average diameter of 0.6 nm (Figure 2.2a), separated by distances above 3 nm. A small number of the clusters grew during imaging to over 1 nm in size within the nanotube and thus are larger than expected due to electron beam-induced ejection of carbonyl ligands, resulting in Re_2 units that bond together forming rhenium nanoclusters.[24] Energy-dispersive X-ray (EDX) analysis of a bundle of cluster-filled nanotubes shows the presence of Re, C and O corresponding to the elements

in the carbonyl (Figure 2.2b). Quantitative EDX analysis using a focused e-beam positioned over a bundle of 6-7 filled nanotubes suspended over a hole shows the presence of rhenium, carbon, and oxygen from the guest species, and the host for carbon, and gives a Re: C atomic ratio of 1: 85 which will compared to ReS_2@SWNT to provide an indication of yield of the reaction.

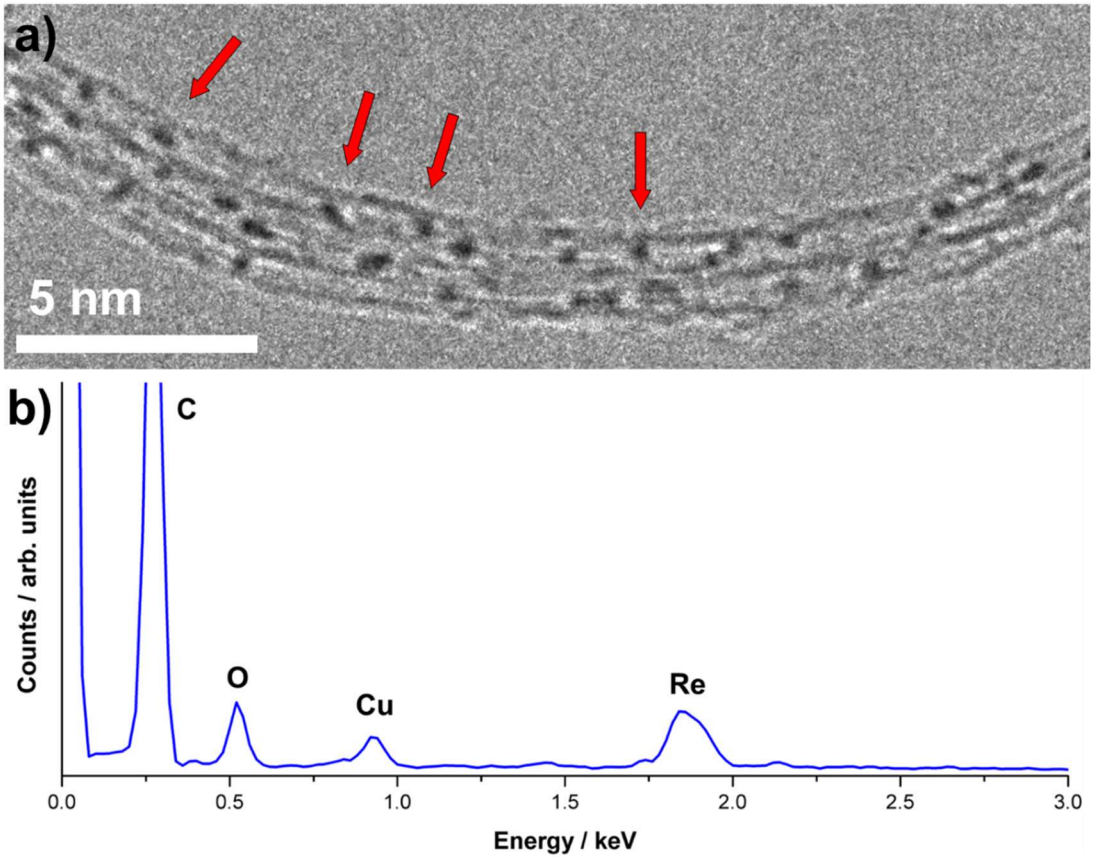


Figure 2.2. *(a) 200 kV TEM image of clusters formed from dirhenium decacarbonyl in a bundle of three SWNTs with an average internal diameter of 1.3 nm. A selection of the encapsulated clusters are indicated by red arrows superimposed on the image; (b) EDX spectrum identifying the presence of Re, C and O. The presence of copper peaks is due to the TEM grid support.*

X-ray photoelectron spectroscopy (XPS) was used to determine the binding state of the rhenium species in each step of the synthesis. The peaks for rhenium at 42.1 and 44.5 eV were assigned to Re 4f 7/2 and 5/2 respectively (Figure 2.3a). The peak energies are higher than rhenium metal, which is explained by the presence of five π-acceptor carbonyl ligands

per metal centre in $Re_2(CO)_{10}$ which increases the binding energy.[25] The C 1s peak at 284.5 eV (Figure 2.3b) is mostly contributed from the SWNT hosts and not the guest carbonyls and the O 1s peaks around 532 eV consists of multiple components arising from the various C-O bonds on the exterior of the SWNTs (Figure 2.3c).

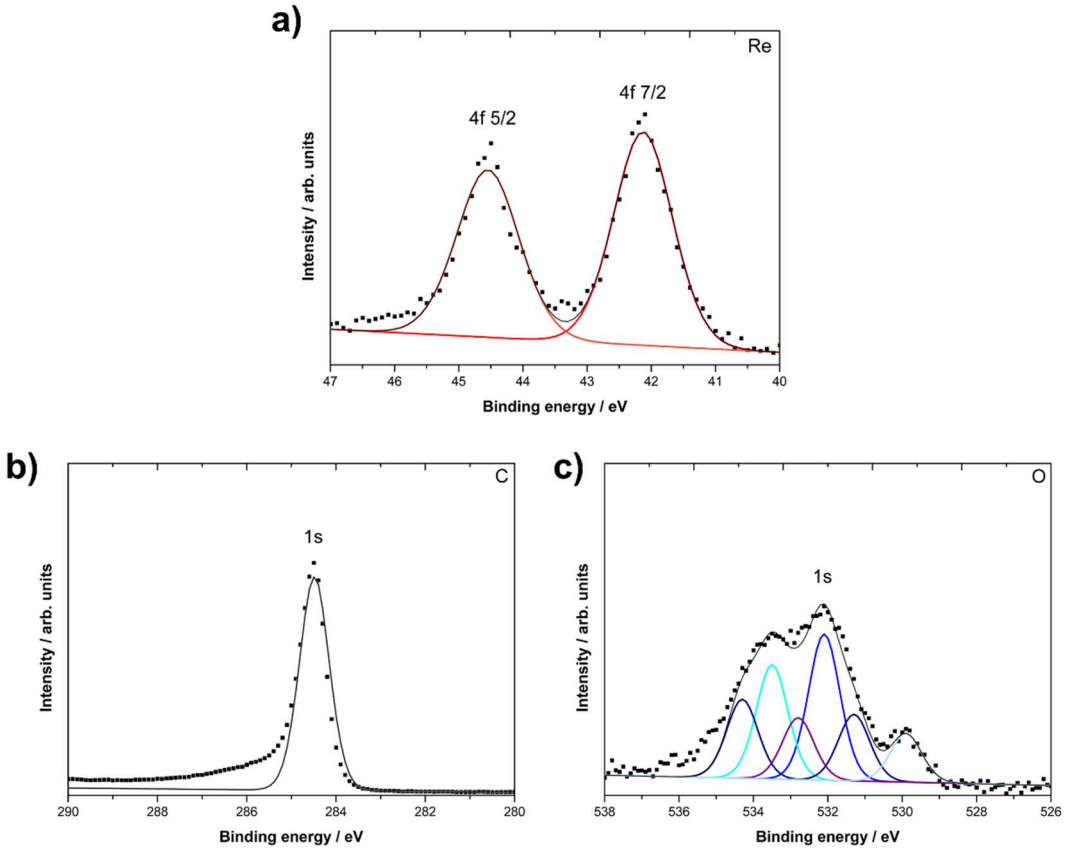


Figure 2.3. *XPS high resolution scans of the (a) Re 4f, (b) C 1s, and (c) O 1s regions.*

Van der Waals interactions are shown to be the main driving force for insertion of the carbonyl clusters into SWNTs as demonstrated by Raman spectroscopy (Figure 2.4 and Table 2.1). The G-band did not shift position for $Re_2(CO)_{10}$@SWNT compared to empty SWNTs in the 660 nm Raman spectrum, in resonance with metallic SWNTs, and thus there was no electronic communication observed between the host and guest upon insertion.

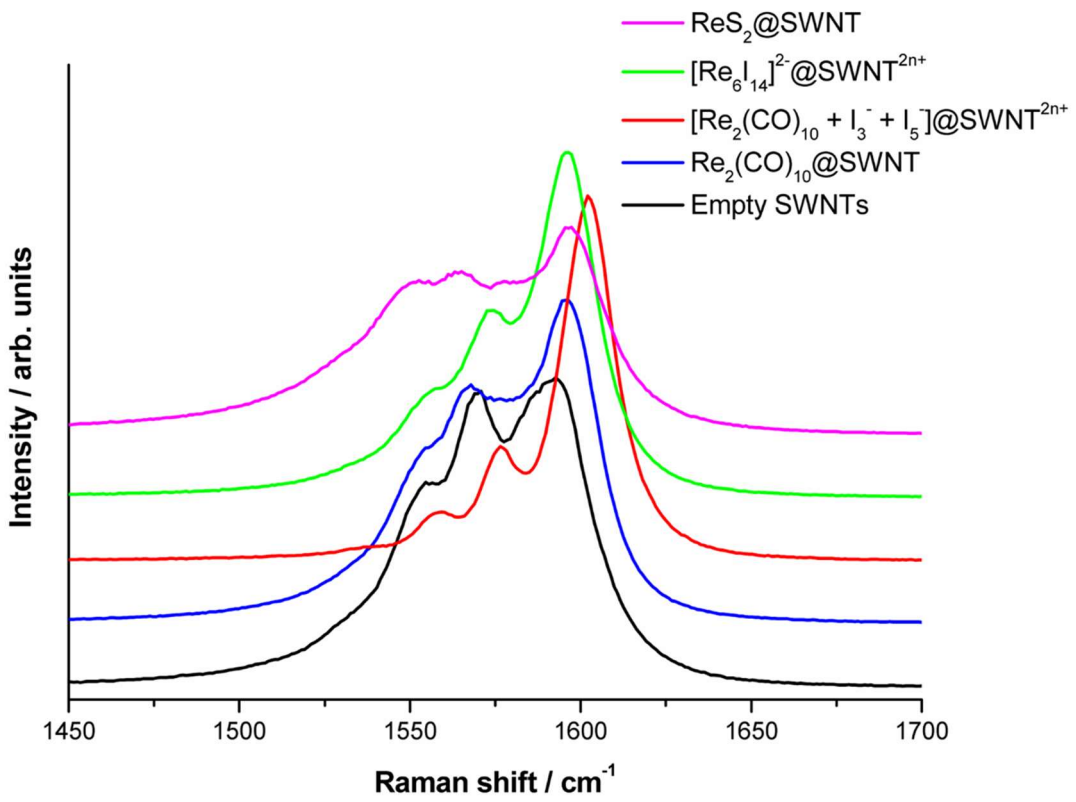


Figure 2.4. *Raman spectra overlay focused on the G-band region, for each material of the stepwise synthesis, using a 660 nm laser source in resonance with metallic SWNTs. No measurable shift of the G-band was observed for $Re_2(CO)_{10}$@SWNT (blue) compared to empty SWNTs (black) which therefore shows a lack of electronic interactions between host and guest. Upon encapsulation of iodine, a large blue shift of the G-band occurred in relation to electron density donation from the host SWNTs to iodine producing n[$Re_2(CO)_{10}$ + I_3^- + I_5^-]@$SWNT^{2n+}$ (red). The G-band of n[Re_6I_{14}]$^{2-}$@$SWNT^{2n+}$ (green) was blue shifted to a lesser extent, whilst ReS_2@SWNT (pink) underwent a small further blue shift compared to the iodide.*

Table 2.1. *G-band positions and shifts of each material in the stepwise synthesis using a 660 nm laser excitation.*

Material	G-band position / cm^{-1}	Shift w.r.t. empty SWNTs / cm^{-1}	Electron transfer direction
Empty SWNTs	1591.5	-	-
$Re_2(CO)_{10}$@SWNT	1591.2	-0.3	No electron transfer
$n[Re_2(CO)_{10} + I_3^- + I_5^-]$@$SWNT^{2n+}$	1602.1	+10.6	SWNT ➔ I_2
$n[Re_6I_{14}]^{2-}$ @$SWNT^{2n+}$	1596.4	+4.9	-ve charged species within SWNTs
ReS_2@SWNT	1597.4	+5.9	$ReS_2^{\delta-}$@$SWNT^{\delta+}$

2.2.3. Reaction to form the iodide

Iodine was then inserted into the SWNTs under vacuum from the gas phase at 120 °C to provide a source of iodine in order to synthesise the iodide species. The G-band in the 660 nm Raman spectra, in resonance with metallic SWNTs, was blue shifted to a larger extent (+10.6 cm^{-1}, Figure 2.4 and Table 2.1) and a change in the peak shape was recorded indicating a metallic to semiconducting transition due to Fermi level shift and band gap opening in the metallic SWNTs upon charge transfer.[26] This is further evidenced by the presence of low-

frequency bands at 106 and 175 cm^{-1} in a Raman spectrum recorded using 532 nm laser excitation; these have been shown previously to be the result of polyiodide formation and are attributed to I_3^- and I_5^- respectively (Figure 2.5). However, it should be noted that there is strong overlap of the I_5^- band with the radial breathing mode (RBM) of the SWNTs.[27]

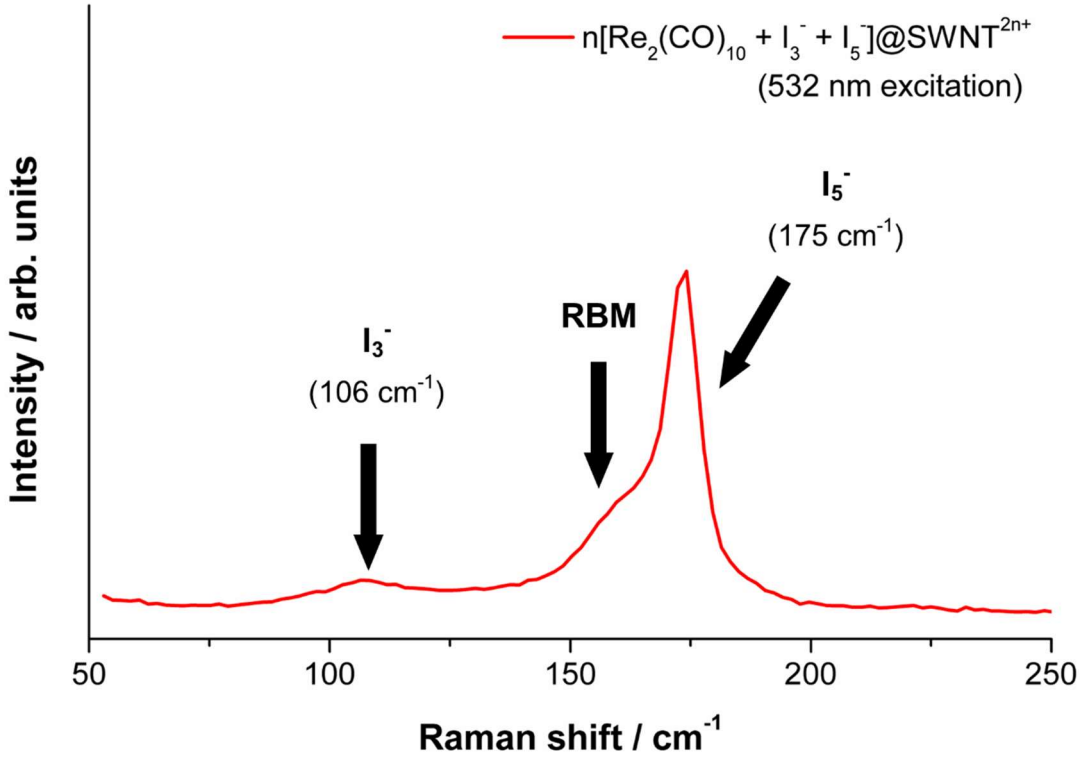


Figure 2.5. *Raman spectrum of $n[Re_2(CO)_{10} + I_3^- + I_5^-]@SWNT^{2n+}$ measured using a 532 nm excitation source. The spectrum is focussed on the low-frequency region and highlights the presence of two peaks at 106 and 175 cm^{-1} which are attributed to I_3^- and I_5^- respectively. The I_5^- band is shown to have strong overlap with the RBM of the SWNTs.*

The $n[Re_2(CO)_{10} + I_3^- + I_5^-]@SWNT^{2n+}$ system was subsequently heated to 500 °C, under inert atmosphere, to react together the encapsulants. Upon formation of the rhenium iodide species, the G-band of metallic SWNTs was found to red shift compared to the position of $n[Re_2(CO)_{10} + I_3^- + I_5^-]@SWNT^{2n+}$. However, it is still blue shifted compared to empty SWNTs, suggesting a positive charge on the nanotubes, and negatively-charged species are present within the SWNTs (Figure 2.4).

Aberration-corrected high-resolution TEM (AC-HRTEM) imaging at 60 kV after the thermally-activated reaction shows the presence of discrete tightly packed clusters of $[Re_6I_{14}]^{2-}$ 0.7 nm in diameter within the SWNT channel, only allowing minimal translation motion (Figures 2.6a - c). However, the clusters appear to rotate freely allowing various projections to be observed which could be investigated using modelling and simulations (Figures 2.6b - e).

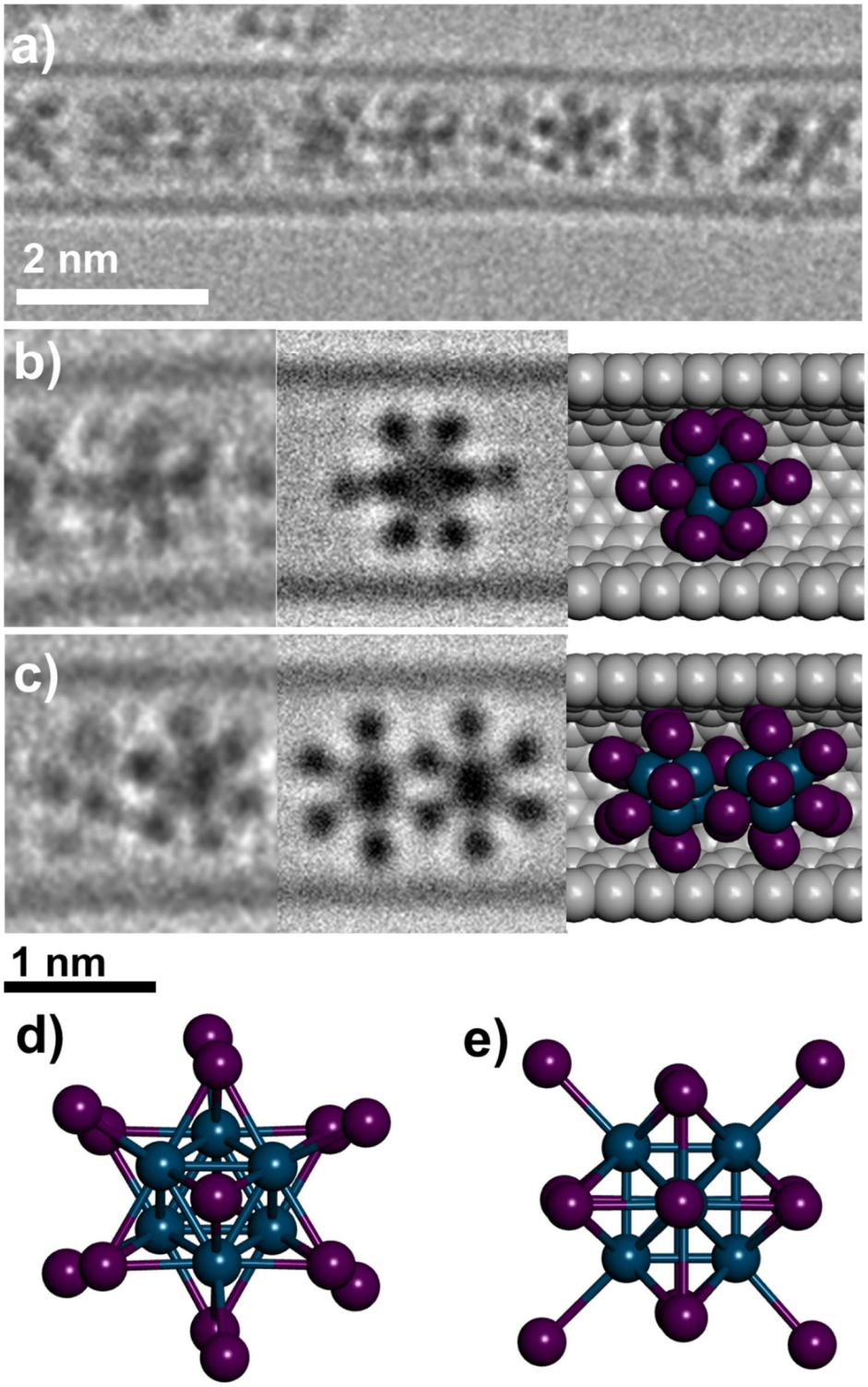


Figure 2.6. *(a) 60 kV AC-HRTEM image of $[Re_6I_{14}^{2-}]$@$SWNT^{2+}$; (b) and (c), experimental AC-HRTEM images, TEM image simulations and structural models of $n[Re_6I_{14}^{2-}]$@$SWNT^{2n+}$ and $[Re_6I_{12}]_2$@SWNT respectively; (d) and (e) structural diagrams of $[Re_6I_{14}]^{2-}$ cluster viewed along the C_3 and C_4 rotational axis of the molecule, respectively.*

The rhenium 4f 7/2 and 5/2 peaks, observed in the XPS high resolution scan, are shifted to higher binding energies compared to the carbonyl, at 42.7 and 45.0 eV, respectively (Figures 2.7a and b). The iodine 3d peaks were located at 619.6 and 631.1 eV for the 5/2 and 3/2 components, which are expected for such species.

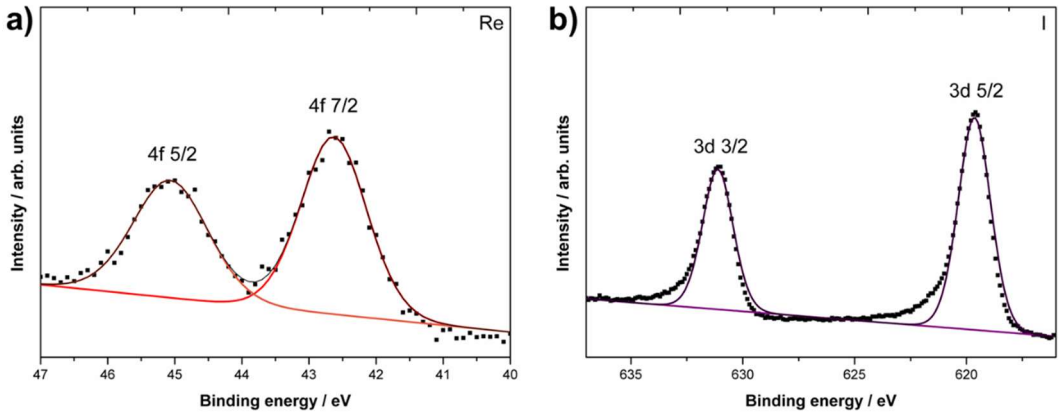


Figure 2.7. *XPS high resolution scans of the (a) Re 4f, and (b) I 3d regions.*

EDX analysis identified the presence of both rhenium and iodine in an atomic ratio of approx. 6: 14 (Figure 2.8). The stoichiometry observed combined with the geometries observed in the AC-TEM images identify the material as $[Re_6I_{14}]^{2-}$ clusters which are structurally analogous to those previously discovered for Mo and W.[22] The structure of $[Re_6I_{14}]^{2-}$ can therefore be concluded as an octahedron of rhenium atoms, with capping iodide ligands on each face, and terminal iodides at each vertex (Figures 2.6d and e).

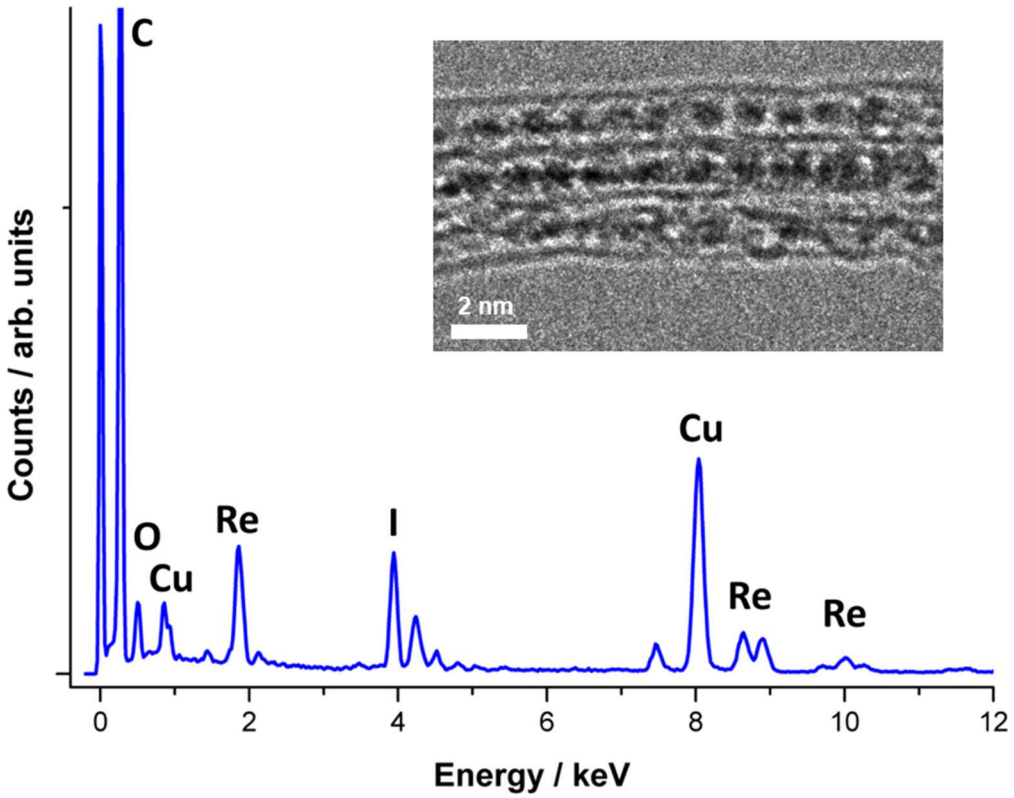


Figure 2.8. *EDX spectrum, recorded over a bundle of filled SWNTs (Inset TEM image) which shows the presence of Re and I in an atomic ratio of 6: 14.*

Structural models of the clusters were constructed and TEM simulations were conducted, the resultant images matched the observed projections (Figures 2.6b and c) such as a cluster having a projected octahedral geometry. Upon prolonged imaging of the clusters, the 60 kV electron beam causes dimerisation and chain formation (Figure 2.6c). This is due to the electron beam rupturing a terminal Re-I bond, forming an unsaturated Re cation which must bond with a μ_3-I from an adjacent cluster, resulting in the formation of polymeric iodide with a repeat unit of $[Re_6I_{12}]_n$. This is in contrast to $[W_6I_{14}]^{2-}$ that was reported to remain stable under the 80 kV e-beam irradiation[22], which considering that constituent atoms in $[Re_6I_{14}]^{2-}$ and $[W_6I_{14}]^{2-}$ molecules receive less energy from the e-beam, indicating the Re-I bond to be weaker than W-I, which may give access to new unique materials compared to tungsten.

2.2.4. Reaction to form the sulfide

The ligand exchange reaction of the $[Re_6I_{14}]^{2-}$ clusters with hydrogen sulfide gas produced nanoribbons of rhenium(IV) sulfide, ReS_2@SWNT, with lengths above 30 nm and width of approximately 1.3 nm. AC-HRTEM confirmed a crystalline atomic structure and a twisting shape to the nanoribbon whilst EDX analysis confirmed the presence of rhenium and sulfur in a 1: 3 ratio (atomic % of 0.64 and 2.10 respectively, Figures 2.9a and b). The higher than expected amount of sulfur is most likely due to residual sulfur deposited in the nanotubes during the reaction, also there was only a trace amount of iodine remaining in the system (equating to an atomic % of 0.08), most likely in the form of polyiodides, which signified the near completion of the reaction.

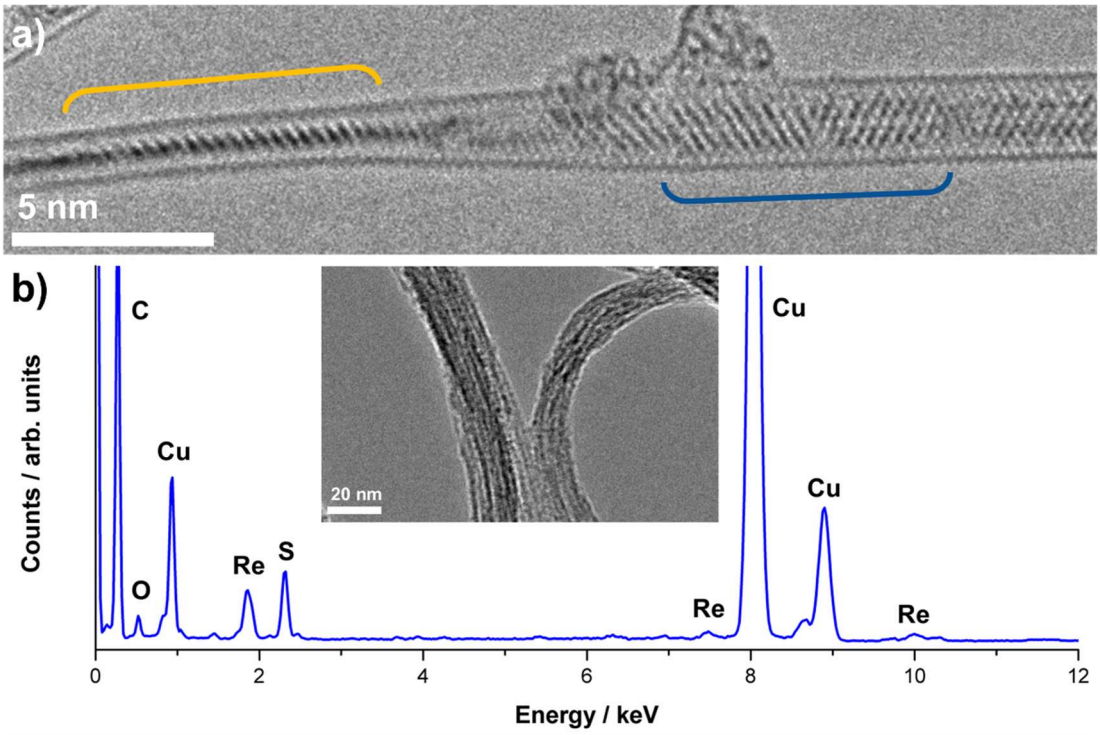


Figure 2.9. *(a) 60 kV AC-HRTEM image of a rhenium disulfide nanoribbon within a SWNT, ReS_2@SWNT; (b) EDX spectrum, measured over a bundle of filled SWNTs (Inset TEM image) which identifies Re and S in a 1: 3 stoichiometry.*

XPS analysis measures the binding energy of the Re 4f 5/2 and 7/2 peaks to be at 44.3 and 41.9 eV respectively (Figure 2.10a). The 4f 7/2 value is slightly shifted compared to a previous study (41.5 eV).[28] The slight electron deficient nature of the host SWNT causes the shift in XPS binding energy, and the confinement enforced on the material pushes this even further as it exaggerates this effect. The sulfur 2p 3/2 and 1/2 peaks were located at 164.3 and 165.5 eV respectively (Figure 2.10b). Raman spectroscopy analysis shows a small blue shift of the G-band compared to empty SWNTs suggesting the ReS_2 nanoribbon is a weak electron acceptor from the nanotubes (Figure 2.4 and Table 2.1).

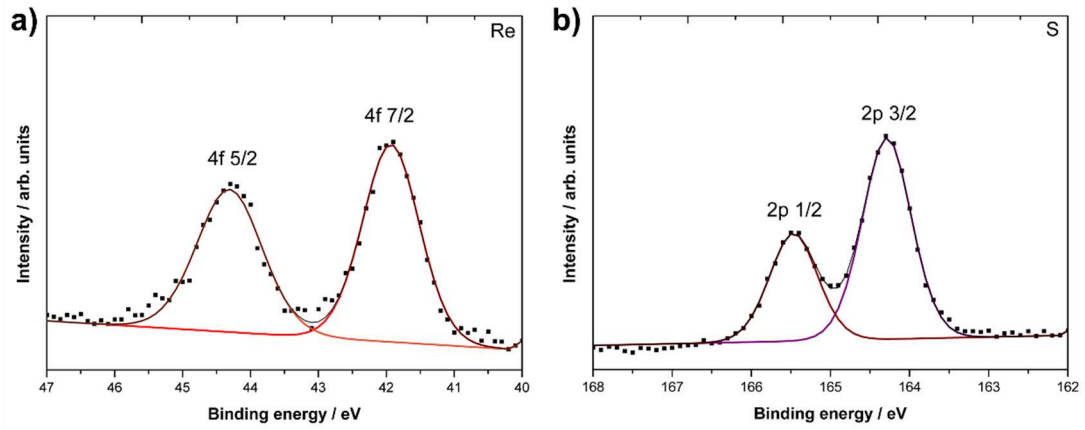


Figure 2.10. *XPS high resolution scans focussed on the (a) Re 4f, and (b) S 2p regions.*

Due to the large difference between the atomic numbers of rhenium (Z = 75) and sulfur (Z = 16), only rhenium atoms are observed in the bright-field AC-HRTEM image as the observed contrast is proportional to the square root of the atomic number of an element. On the left-hand side of the AC-HRTEM image the nanoribbon is in an edge-on orientation (yellow area, Figure 2.9a) in which the contrast is controlled by the thickness of the nanoribbon and the atoms overlapping in projection (Figure 2.11a). The atoms in the edge-on projection are separated by a distance of 0.29 nm. On the right-hand side the image displays clearly the face-on projection (blue area, Figure 2.9a), which consists of each Re atom forming three distinct Re…Re distances resulting in the establishment of Re_4 parallelograms; a distinct

feature of the distorted 1T structure (Figure 2.11b). The nanoribbon is four rhenium atoms in width which equates to two rows of parallelograms. Each Re is bonded to six sulfur atoms in octahedral geometry and the sulfur edges are in contact with the nanotube sidewall. The Re_4 parallelograms have a measured distance of 0.26 nm between adjacent rhenium atoms, whilst the two rows of parallelograms are separated by a distance of 0.40 nm. These values are in good agreement with those from a structural model, and subsequent TEM simulation, which was formed by extending the ReS_2 unit cell along the nanotube growth axis (Figures 2.11a and b).

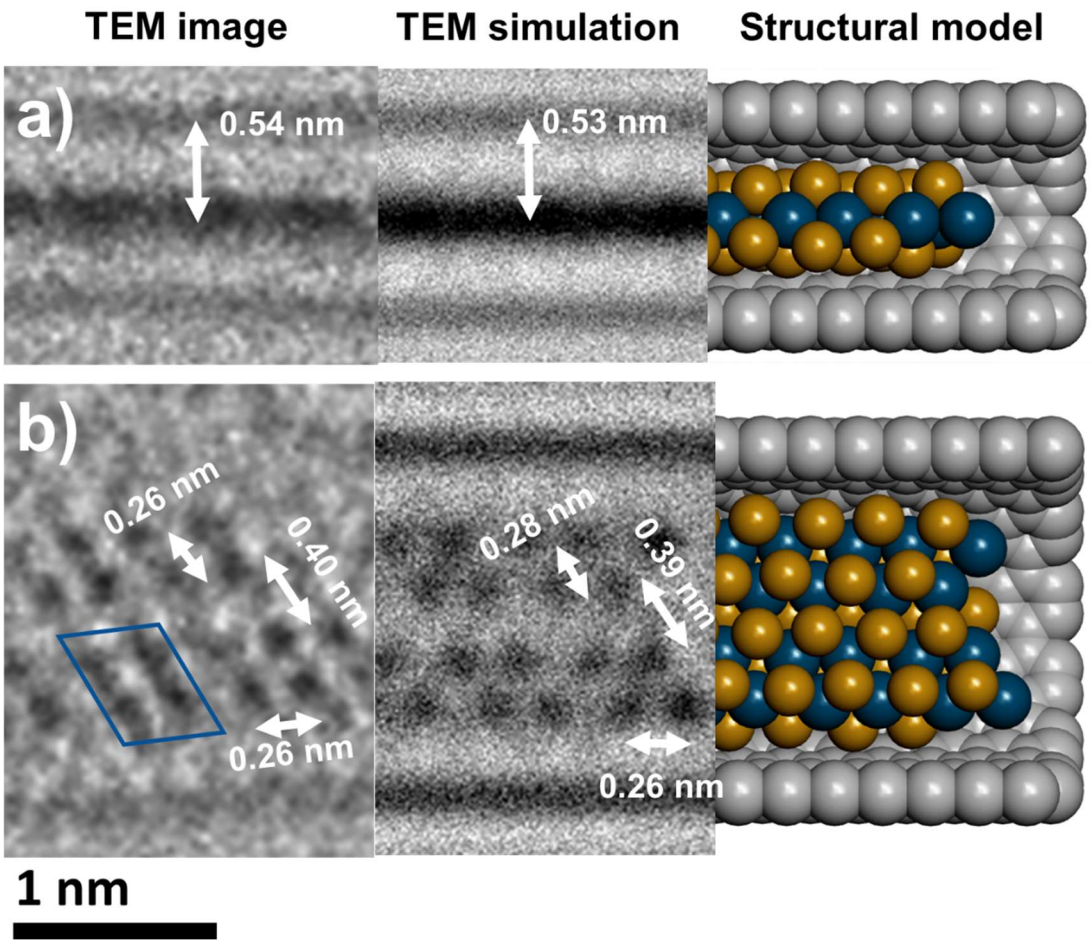


Figure 2.11. *(a) 60 kV AC-TEM image annotated with the Re…C interatomic distance; a TEM image simulation of an optimised structural model, showing the ReS_2 in an edge-on orientation; (b) 60 kV AC-TEM annotated with Re…Re interatomic distances and a*

parallelogram to illustrate the Re_4 structural units; a TEM image simulation of an optimised structural model, showing the ReS_2 nanoribbon in a face-on orientation.

AC-HRTEM identified not only the structure of the nanoribbon but also the striking radial deformation of the SWNT host (Figure 2.9a). The 660 nm Raman spectra, resonantly enhancing metallic SWNTs, showed a 2-3 cm^{-1} red shift in the position of the radial breathing mode (RBM, Figure 2.12a); however, this is not enough to explain the observed level of deformation, suggesting those nanotubes are out of resonance. The cross-section of the SWNT was measured to be a 1.1 x 1.8 nm ellipse, and the change in projected nanotube cross-section is perfectly matched with the twisting of the ReS_2 nanoribbon (Figure 2.12b). This demonstrates the strong interactions present between the nanoribbon and the nanotube and has been previously observed for MoS_2 filled SWNTs, as well as helical CoI_2 chains.[19, 29]

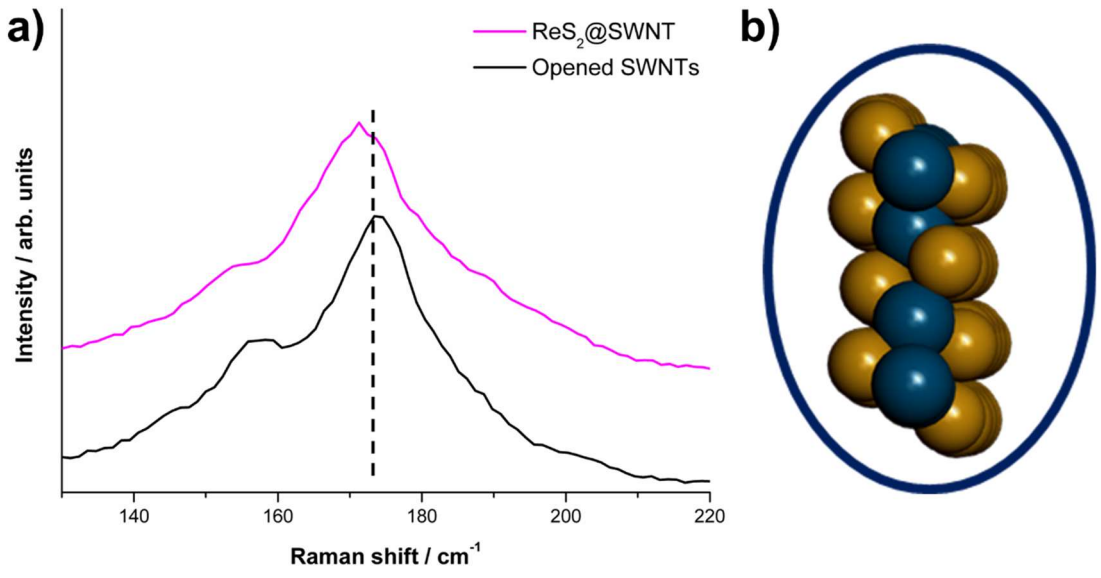


Figure 2.12. *(a) Raman spectrum, in resonance with metallic SWNTs, focussed on the low-frequency region showing the radial breathing modes of empty SWNTs (black), and ReS_2@SWNT (pink); (b) end-on structural model view depicting the radial deformation of the SWNT upon ReS_2 nanoribbon formation.*

2.3. Conclusion

Rhenium (IV) disulfide is an extraordinary transition metal dichalcogenide that retains its bulk electronic properties when exfoliated to a monolayer. Moreover, previous computational studies have shown that ultrathin nanoribbons also retain these properties and could therefore lead to being used in nanoscale electronic devices.

In this study, ultrathin ReS_2 nanoribbons were synthesised using the extreme confinement of SWNTs as nano test tubes. The insertion of the initial source of rhenium, dirhenium decacarbonyl, was shown to be aided by Van der Waals interactions indicated by the G-band not shifting position in the corresponding Raman spectra. The second step involved the inorganic transformation of dirhenium decacarbonyl into rhenium iodide clusters, $n[Re_6I_{14}^{2-}]@SWNT^{2n+}$. A combination of aberration-corrected TEM and EDX found these clusters were isostructural with Mo and W analogues formed inside SWNTs previously; however, the Re-I bond was found to be far more active than the W-I under the electron beam which resulted in the partial oligomerisation of rhenium iodide clusters to $[Re_6I_{12}]_n$.

The reaction of the rhenium iodide clusters with hydrogen sulfide resulted in the formation of ReS_2 nanoribbons of 1.3 nm in diameter. A radial deformation of the SWNTs occurred during the synthesis of the twisted ReS_2 nanoribbons in order to maximise the interactions of the surface of the nanoribbons with the interior concave of the nanotubes. The nanoribbons were found to have the same distorted 1T structure as per the bulk structure, shown by the presence of Re_4 parallelograms. The multistep synthesis within SWNTs was shown to be successful for the construction of ultrathin ReS_2 nanoribbons owing to the control of the dimensionality and composition that reactions within SWNTs allow.

2.4. Experimental

2.4.1. Materials

SWNTs (P2-SWNTs, arc discharge, Carbon Solutions, USA) were refluxed in nitric acid (50 ml, 3M) for 2 hours and then annealed at 600 °C for 17 min to remove their end caps and any amorphous carbon present, resulting in a 50% weight loss observed. Dirhenium decacarbonyl ($Re_2(CO)_{10}$, Sigma Aldrich), iodine (Sigma Aldrich), and hydrogen sulfide (Fisher Scientific) were used as supplied.

2.4.2. Insertion of dirhenium decacarbonyl into SWNTs

Freshly-opened SWNTs (10 mg) and dirhenium decacarbonyl (20 mg, 0.031 mmol) were sealed in a Pyrex ampoule under vacuum (10^{-5} mbar) and heated to 150 °C for 3 days. The ampoule was then placed in an ice bath to cease the sublimation process and then washed with tetrahydrofuran to remove any excess material from the exterior of the SWNTs.

2.4.3. Reaction of $Re_2(CO)_{10}$@SWNT with iodine

$Re_2(CO)_{10}$@SWNT (10 mg, 0.016 mmol) and a large excess of iodine (40 mg, 0.743 mmol) were sealed in a Pyrex ampoule under vacuum (10^{-5} mbar) and heated to 120 °C for 3 days. The ampoule was then placed in an ice bath to cease the sublimation process. The resultant material was then placed in a Pyrex ampoule and sealed under an inert argon atmosphere (0.7 bar) and heated to 500 °C for 1 hour to form n $[Re_6I_{14}^{2-}]$@$SWNT^{2n+}$.

2.4.4. Reaction of n$[Re_6I_{14}^{2-}]$@$SWNT^{2n+}$ with hydrogen sulfide

n$[Re_6I_{14}^{2-}]$@$SWNT^{2n+}$ was loaded onto a quartz boat and placed in the centre of a tube furnace and exposed to a flow of argon gas for one hour (15 mL/min), followed by a flow of dihydrogen sulfide (15 mL/min). The furnace was then heated to 550 °C for 2 hours under the flow of dihydrogen sulfide (15 mL/min) and then left to cool to room temperature under

a flow of argon (15 mL/min). Exhaust gas was flowed through the fumehood via a bleach bath (200 mL) to neutralise any excess H_2S.

2.4.5. Electron microscopy and energy-dispersive X-ray analysis

The samples were dispersed in isopropyl alcohol using an ultrasonic bath and drop cast onto lacey carbon copper TEM grids (Agar Scientific). HR-TEM imaging was performed on a JEOL 2100F FEG-TEM microscope operated at 200 kV. AC-HRTEM was performed at the University of Ulm using the dedicated CC/CS corrected SALVE (sub-Ångström low voltage electron microscope) TEM operating a 60 kV.[30] EDX spectra were acquired using an Oxford Instruments INCA X-ray microanalysis system.

2.4.6. Raman spectroscopy

Micro Raman spectroscopy was performed using a Horiba Jobin Yvon LabRAM HR Raman microscope. Spectra were acquired using either a 532 or 660 nm laser (at ~0.2 mW power), a 100x objective and a 200 µm confocal pinhole. To simultaneously scan a range of Raman shifts, a 600 lines mm^{-1} rotatable diffraction grating along a path length of 800 mm was employed, conferring a spectral resolution better than 1.9 and 1.2 cm^{-1} for the 532 and 660 nm lasers, respectively. Spectra were detected using a Synapse CCD detector (1024 pixels) thermoelectrically cooled to −60 °C. Before spectra collection, the instrument was calibrated using the zero-order line and a standard Si (100) reference band at 520.7 cm^{-1}. For single point measurements, spectra were acquired over a minimum range 125-3400 cm^{-1} with an acquisition time of 15-120 seconds and 2 accumulations to automatically remove the spikes due to cosmic rays and improve the signal to noise ratio. Spectra were collected from at least three random locations and averaged to give a mean spectrum.

2.4.7. X-ray photoelectron spectroscopy

Samples were analysed using the Kratos AXIS ULTRA with a mono-chromated Al kα X-ray source (1486.6eV) operated at 10 mA emission current and 12 kV anode potential (120 W.)

Spectra were acquired with the Kratos VISION II software. A charge neutralizer filament was used to prevent surface charging. Hybrid –slot mode was used measuring a sample area of approximately 300 x 700 µm. The analysis chamber pressure was better than 5 x 10-9 mbar. Three areas per sample were analysed. A wide scan was performed at low resolution (Binding energy range 1400 eV to -5 eV, with pass energy 80 eV, step 0.5 eV, sweep time 20 minutes). High resolution spectra at pass energy 20 eV, step of 0.1 eV, and sweep times of 10 minutes each were also acquired for photoelectron peaks from the detected elements and these were used to model the chemical composition. The spectra were charge corrected to the C 1s peak set to 284.5 eV.

2.4.8. TEM simulations

TEM image simulation was carried out using the multislice program QSTEM which uses the Dirac–Fock scattering potential of Rez et al.[31] A fixed number of 20 slices per nanotube were chosen and images were calculated with a sampling of 0.125 Å per pixel. The aberration coefficients and defocus parameters d_f, C_S, A_1, and B_2 were matched to the imaging conditions in the specific experiment and the convergence angle was fixed at 0.5 mrad. The effect of limited electron dose was emulated by applying noise to the calculated images using a custom-made Monte-Carlo program exploiting the Poisson statistics of electrons. Structural models of SWNTs were built using a custom-made program taking into account different nanotube chiralities, to be matched closely with experimental images. The structural models of the inorganic nanomaterials are based on scaled bulk structures.

2.5. References

1. M. Rahman, K. Davey and S.-Z. Qiao, *Adv. Funct. Mater.*, 2017, **27**, 1606129.

2. E. Liu, Y. Fu, Y. Wang, Y. Feng, H. Liu, X. Wan, W. Zhou, B. Wang, L. Shao, C.-H. Ho, Y.-S. Huang, Z. Cao, L. Wang, A. Li, J. Zeng, F. Song, X. Wang, Y. Shi, H. Yuan, H. Y. Hwang, Y. Cui, F. Miao and D. Xing, *Nat. Commun.*, 2015, **6**, 6991.

3. Y. Feng, W. Zhou, Y. Wang, J. Zhou, E. Liu, Y. Fu, Z. Ni, X. Wu, H. Yuan, F. Miao, B. Wang, X. Wan and D. Xing, *Phys. Rev. B*, 2015, **92**, 054110.

4. H. H. Murray, S. P. Kelty, R. R. Chianelli and C. S. Day, *Inorg. Chem.*, 1994, **33**, 4418-4420.

5. H. S. S. Ramakrishna Matte, A. Gomathi, A. K. Manna, D. J. Late, R. Datta, S. K. Pati and C. N. R. Rao, *Angew. Chem. Int. Ed.*, 2010, **49**, 4059-4062.

6. E. S. Kadantsev and P. Hawrylak, *Solid State Commun.*, 2012, **152**, 909-913.

7. A. Klein, S. Tiefenbacher, V. Eyert, C. Pettenkofer and W. Jaegermann, *Phys. Rev. B*, 2001, **64**, 205416.

8. R. He, J.-A. Yan, Z. Yin, Z. Ye, G. Ye, J. Cheng, J. Li and C. H. Lui, *Nano Lett.*, 2016, **16**, 1404-1409.

9. D. A. Chenet, O. B. Aslan, P. Y. Huang, C. Fan, A. M. van der Zande, T. F. Heinz and J. C. Hone, *Nano Lett.*, 2015, **15**, 5667-5672.

10. S. Tongay, H. Sahin, C. Ko, A. Luce, W. Fan, K. Liu, J. Zhou, Y.-S. Huang, C.-H. Ho, J. Yan, D. F. Ogletree, S. Aloni, J. Ji, S. Li, J. Li, F. M. Peeters and J. Wu, *Nat. Commun.*, 2014, **5**, 3252.

11. A. Splendiani, L. Sun, Y. Zhang, T. Li, J. Kim, C.-Y. Chim, G. Galli and F. Wang, *Nano Lett.*, 2010, **10**, 1271-1275.

12. W. Zhao, Z. Ghorannevis, L. Chu, M. Toh, C. Kloc, P.-H. Tan and G. Eda, *ACS Nano*, 2013, **7**, 791-797.

13. M. Brorson, T. W. Hansen and C. J. H. Jacobsen, *J. Am. Chem. Soc.*, 2002, **124**, 11582-11583.

14. W. Tu and B. Denizot, *J. Colloid Interface Sci.*, 2007, **310**, 167-170.

15. Q. An, Y. Liu, R. Jiang and X. Meng, *Nanoscale*, 2018, **10**, 14976-14983.

16. X. He, F. Liu, P. Hu, W. Fu, X. Wang, Q. Zeng, W. Zhao and Z. Liu, *Small*, 2015, **11**, 5423-5429.

17. Z. G. Yu, Y. Cai and Y.-W. Zhang, *Sci Rep-Uk*, 2015, **5**, 13783.

18. A. Chuvilin, E. Bichoutskaia, M. C. Gimenez-Lopez, T. W. Chamberlain, G. A. Rance, N. Kuganathan, J. Biskupek, U. Kaiser and A. N. Khlobystov, *Nat. Mater.*, 2011, **10**, 687-692.

19. Z. Wang, H. Li, Z. Liu, Z. Shi, J. Lu, K. Suenaga, S.-K. Joung, T. Okazaki, Z. Gu, J. Zhou, Z. Gao, G. Li, S. Sanvito, E. Wang and S. Iijima, *J. Am. Chem. Soc.*, 2010, **132**, 13840-13847.

20. Z. Wang, K. Zhao, H. Li, Z. Liu, Z. Shi, J. Lu, K. Suenaga, S.-K. Joung, T. Okazaki, Z. Jin, Z. Gu, Z. Gao and S. Iijima, *J. Mater. Chem.*, 2011, **21**, 171-180.

21. C. T. Stoppiello, J. Biskupek, Z. Y. Li, G. A. Rance, A. Botos, R. M. Fogarty, R. A. Bourne, J. Yuan, K. R. J. Lovelock, P. Thompson, M. W. Fay, U. Kaiser, T. W. Chamberlain and A. N. Khlobystov, *Nanoscale*, 2017, **9**, 14385-14394.

22. A. Botos, J. Biskupek, T. W. Chamberlain, G. A. Rance, C. T. Stoppiello, J. Sloan, Z. Liu, K. Suenaga, U. Kaiser and A. N. Khlobystov, *J. Am. Chem. Soc.*, 2016, **138**, 8175-8183.

23. F. Qi, J. He, Y. Chen, B. Zheng, Q. Li, X. Wang, B. Yu, J. Lin, J. Zhou, P. Li, W. Zhang and Y. Li, *Chem. Eng. J.*, 2017, **315**, 10-17.

24. K. C. Cao, T. W. Chamberlain, J. Biskupek, T. Zoberbier, U. Kaiser and A. N. Khlobystov, *Nano Lett.*, 2018, **18**, 6334-6339.

25. R. D. Feltham and P. Brant, *J. Am. Chem. Soc.*, 1982, **104**, 641-645.

26. M. V. Kharlamova, *Appl. Phys. A*, 2016, **122**, 791.

27. L. Grigorian, K. A. Williams, S. Fang, G. U. Sumanasekera, A. L. Loper, E. C. Dickey, S. J. Pennycook and P. C. Eklund, *Phys. Rev. Lett.*, 1998, **80**, 5560-5563.

28. S. M. Davis, *Catal. Lett.*, 1989, **2**, 1-7.

29. E. Philp, J. Sloan, A. I. Kirkland, R. R. Meyer, S. Friedrichs, J. L. Hutchison and M. L. H. Green, *Nat. Mater.*, 2003, **2**, 788-791.

30. M. Linck, P. Hartel, S. Uhlemann, F. Kahl, H. Müller, J. Zach, M. Haider, M. Niestadt, M. Bischoff, J. Biskupek, Z. Lee, T. Lehnert, F. Börrnert, H. Rose and U. Kaiser, *Phys. Rev. Lett.*, 2016, **117**, 076101.

31. D. Rez, P. Rez and I. Grant, *Acta Crystallogr. A*, 1994, **50**, 481-497.

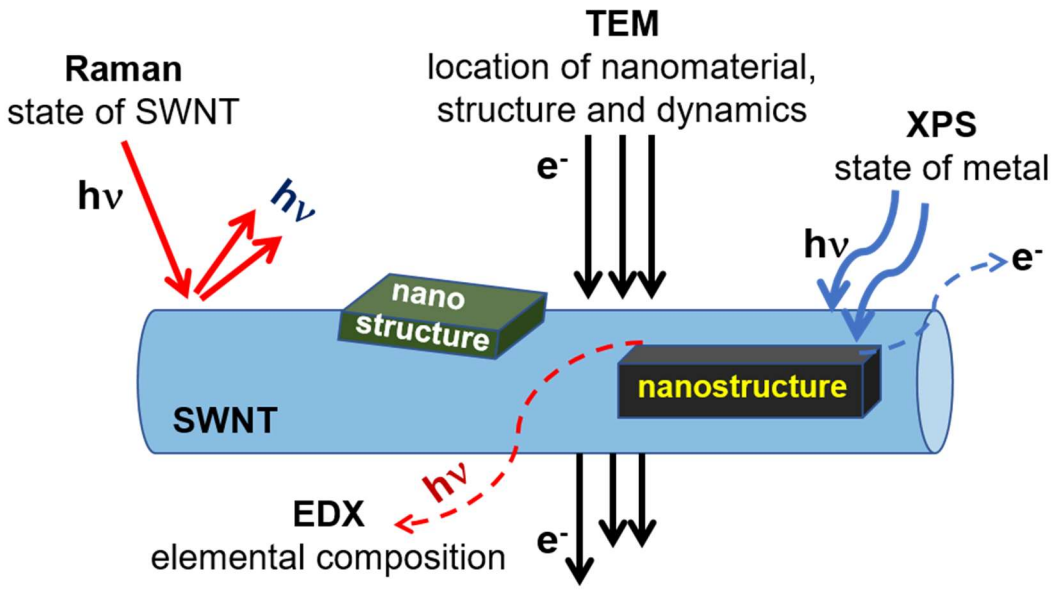
Chapter 3: Exploiting both sides of nanotubes to support inorganic reactions: control of size, shape, and structure of osmium compounds by convex and concave surfaces at the nanoscale

3.1. Introduction

Control of the dimensions of an inorganic material has been shown to highly improve its physical and chemical properties such as the critical temperature for superconductivity, electron mobility in transistor materials, and catalytic activity in processes such as the hydrogen evolution reaction.[1-3] Single-walled carbon nanotubes (SWNTs), cylinders of graphitic carbon with diameters at the nanoscale and nearly macroscopic length scales, offer a particularly powerful template for the controlled growth of nanomaterials, due to two different surfaces - the exterior convex surface and the interior concave.[4] The convex surface aids the formation of nanomaterials with high, easily accessible surface areas suitable for catalytic and sensor uses,[5] whilst the concave surface forms the interior channel of between 0.7 – 2.0 nm[6, 7] and can act as a template for the formation of quasi-1D materials[8-11] or as a vessel for a variety of suitably-sized molecules such as C_{60} fullerenes.[12-14] As detailed in section 1.4, stepwise reactions can also take place within the concave of SWNTs triggered by stimuli such as heat[15, 16] or the electron beam[17], leading to products with reduced dimensionality.[11, 18] In the literature, there have been many examples of these taking place to form metal iodide and sulfide nanowires such as MoS_2[16, 19], WS_2[20], and PtS_2[21]. However, these were found to only exhibit small deviations from the bulk geometries, and were

studied exclusively under extreme confinement. In order to exploit the full power of nanoscale confinement it is necessary to demonstrate control of the atomic structure of the material as well as dimensionality, which could be achieved using structurally flexible guest-species that can exist in more than one crystal phase with distinct lattice symmetries. Among transition metal sulfides, OsS_2 is good candidate for this purpose as it is known to form a cubic pyrite-type lattice.[22, 23] Moreover, the iodides of osmium, in particular the monoiodide, are considered to be amorphous in bulk[24] thus offering an opportunity to demonstrate SWNT nanocontainers for the creation of previously unknown forms of low-dimensional materials.

In this chapter, the synthesis and nanoscale control of osmium materials utilising the interior and exterior of SWNTs is demonstrated. The synthetic route will utilise triosmium dodecacarbonyl as the initial source of osmium which will be independently studied and then subsequently reacted stepwise to produce novel osmium iodide and sulfide nanostructures. In order to ensure that both the concave and convex surfaces of the SWNTs are subjected to the same experimental conditions during each reaction, the system will not be washed after the initial encapsulation of $Os_3(CO)_{12}$ which will lead to both the encapsulation of the species within the concave as well as physisorption onto the convex. A combination of complementary imaging and analysis techniques including aberration-corrected high-resolution transmission electron microscopy (AC-HRTEM), energy-dispersive X-ray analysis (EDX), X-ray photoelectron spectroscopy (XPS) and Raman spectroscopy (Scheme 3.1) will allow a comprehensive characterisation of new nanomaterials and reveal mechanisms controlling the structure and properties of osmium compounds at nanoscale. Moreover, details of the structure, composition, and coordination of each material will also be determined using the combination of techniques.

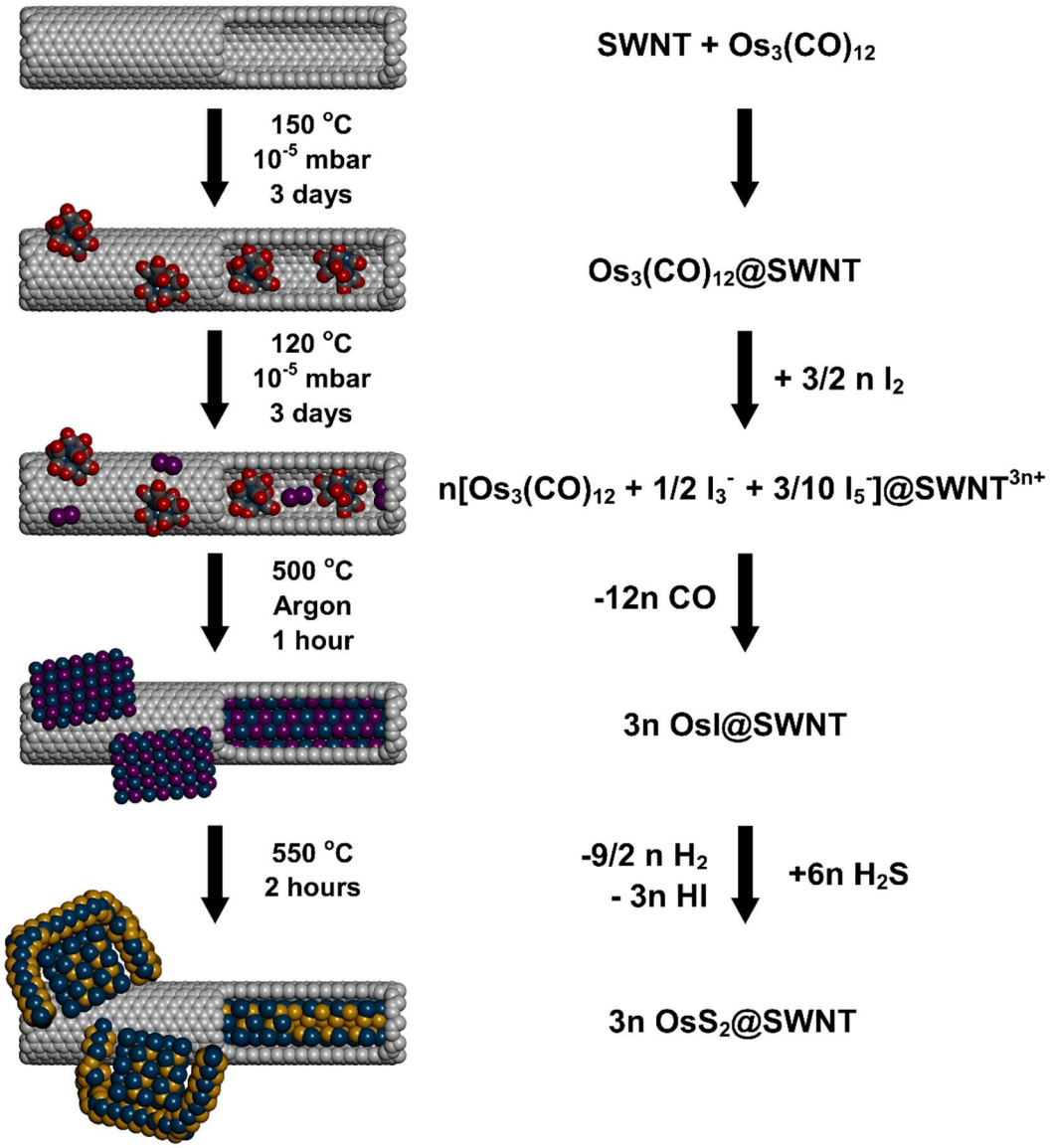


Scheme 3.1. *A combination of complementary methods of imaging and analysis provides a holistic analytical methodology for a complete characterisation of nanotube composites with inorganic nanomaterials.*

3.2. Results and Discussion

Organometallic complexes of osmium, such triosmium dodecacarbonyl, $Os_3(CO)_{12}$, and triosmium decacarbonyl-bis-acetonitrile, $[Os_3(CO)_{10}(NCMe)_2]$, have been demonstrated previously as effective precursors for Os metal clusters generated in nanotubes[25] and on a turbostratic graphitic surface[26] or multi-walled carbon nanotubes[27] respectively. An exohedral fullerene, $[Os_3(CO)_{11}(\eta^2\text{-}C_{60})]$, has also been encapsulated in SWNTs resulting in strong van der Waals interactions between the fullerene-based ligand and concave surface of nanotube.[28, 29] Osmium complexes have also been used to functionalise the SWNT sidewall by cycloaddition of osmium tetroxide, OsO_4, under photoirradiaiton, which was found to tune the electronic properties of the SWNTs by increasing their resistance.[30] In this study $Os_3(CO)_{12}$ was selected as a starting point for chemical transformations because it can be readily converted to other forms of osmium without generating any impurities, e.g. residual

ligands (Scheme 3.2).[29] To subsequently form the iodide species, a two-step procedure was employed in which iodine was initially sublimed into the SWNTs followed by thermal activation of the system to react the components together. Finally, the sulfide nanostructures were produced upon reaction of osmium iodide with hydrogen sulfide gas, H_2S, at an elevated temperature in the presence of an inert atmosphere.



Scheme 3.2. *Stepwise synthetic route showing the reactions and transformations that take place simultaneously on the concave and convex surfaces. The first step introduces $Os_3(CO)_{12}$ into the system via sublimation which is then subsequently reacted with iodine to produce*

osmium iodide. The final step transforms the iodide species into osmium disulfide using dihydrogen sulfide as the source of sulfur.

3.2.1. Insertion of the carbonyl

In the first step $Os_3(CO)_{12}$ was encapsulated in pre-opened SWNTs by sublimation *in vacuo*. TEM imaging using the 100 kV e-beam and low-dose conditions provided the ideal conditions for studying $Os_3(CO)_{12}$ in SWNTs, with individual molecules appearing as high-contrast elliptical features (Figure 3.1a). Previous attempts of imaging delicate organometallic metal carbonyl complexes have been unsuccessful as the impact of the e-beam in TEM is known to break meta-ligand bonds rapidly leading to the formation of metal clusters.[25] However, under these less harsh imaging conditions discrete molecular species, approximately 0.65 nm in diameter, were observed to be translating and rotating within the confinements of the SWNTs. Image analysis demonstrates a complimentary fit of $Os_3(CO)_{12}$ within the concave surface of the 1.2 nm SWNT; the guest-molecules are large enough to form close van der Waals' interactions with the host-nanotube, but have enough space to rotate freely within the hollow nanotube interior. Multiple projections of the molecules were observed including face-on and edge-on with respect to the electron beam, as well as some which were intermediates; these were demonstrated using a structural model of $Os_3(CO)_{12}$@SWNT (Figure 3.1b). Complementary EDX analysis, recorded over a bundle of filled SWNTs, confirms that the features observed contain only carbon, oxygen and osmium (Figure 3.1c). The presence of carbonyl ligands within nanotubes was also confirmed by infrared spectroscopy (IR, Figure 1d). All vibrational bands in the carbonyl region of the parent molecule, $Os_3(CO)_{12}$, (1985, 1995, 2016, 2028, 2042 and 2068 cm^{-1}) were also observed for $Os_3(CO)_{12}$@SWNT.

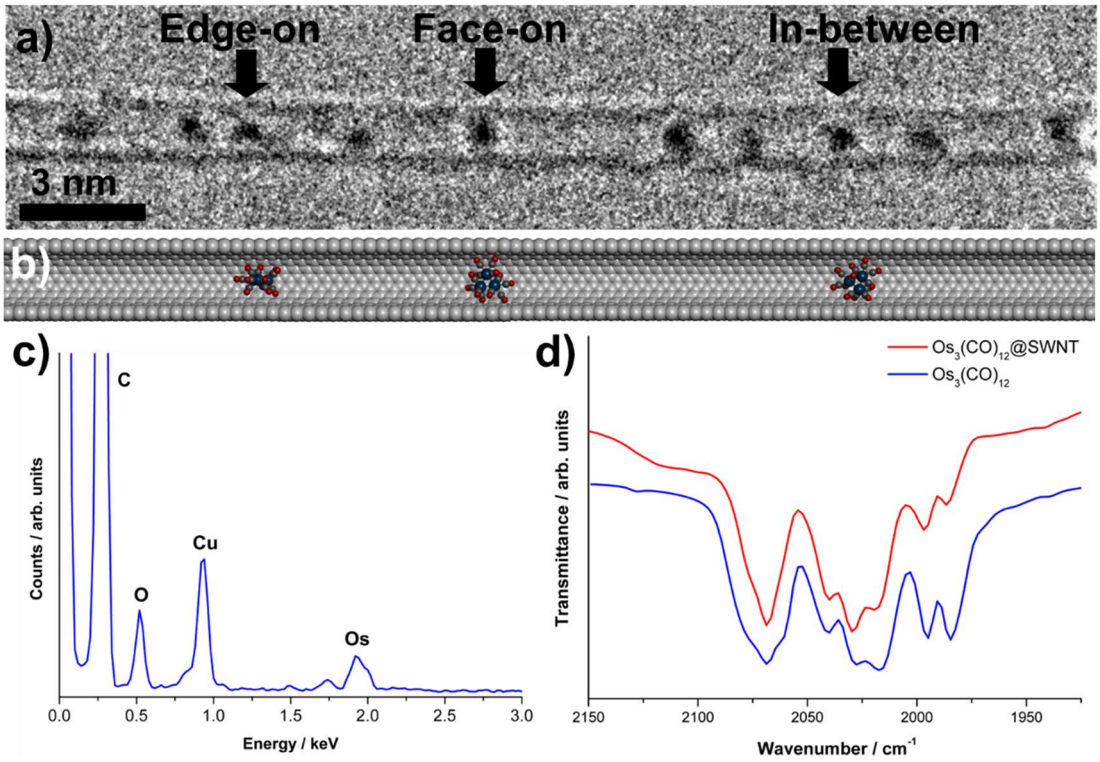


Figure 3.1. *(a) 100 kV TEM image of $Os_3(CO)_{12}$@SWNT showing the presence of discrete molecules of triosmium dodecacarbonyl within the confinements of a SWNT; (b) structural model showing three orientations of $Os_3(CO)_{12}$ within a (10, 10) SWNT; (c) EDX, recorded over a bundle of filled SWNTs, which identify the constituent elements of the carbonyl and host nanotubes. The presence of copper originates from the TEM grid used; (d) infrared spectra overlay focussed on the carbonyl region of free $Os_3(CO)_{12}$ molecules (blue), and $Os_3(CO)_{12}$ (red).*

After prolonged exposure to the electron beam the carbonyl ligands were ejected and the molecules transformed into metallic osmium clusters which were identified by larger diameters caused by coalescence leading to a lower number of overall nanoparticles. These Os NPs then proceeded to promote etching of the nanotube sidewall in an electron beam induced ejection (EBIE) process (Figure 3.2).[31]

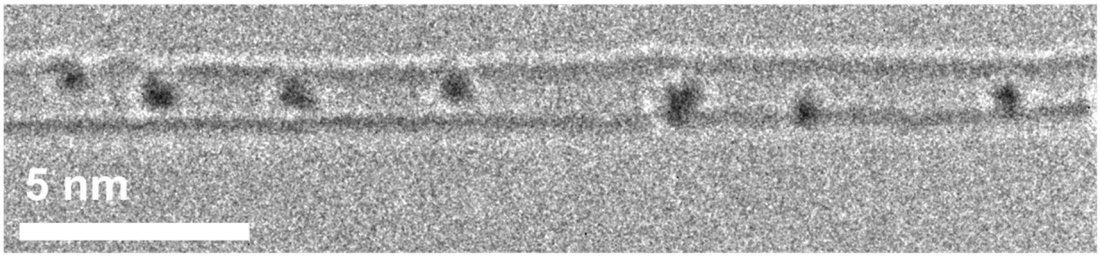


Figure 3.2. *100 kV TEM image of $Os_3(CO)_{12}$@SWNT after a few seconds of exposure to the electron beam which causes the molecules to combine and release CO ligands to produce metallic osmium nanoparticles that promote etching of the nanotube sidewall.*

XPS measurements determined the state of osmium in $Os_3(CO)_{12}$@SWNT (Figure 3.3a) from the binding energy peak position of Os 4f 7/2 at 52.4 eV which is higher than observed for free carbonyl molecules previously (51.6 eV)[32] indicating a slightly electron deficient environment of the concave surface of the SWNTs with respect to the guest-molecules. The C 1s high resolution scan showed a low intensity peak at 288.2 eV which is indicative of the carbonyl species (Figure 3.3b).[32] Also observed in the C 1s region were two peaks at 284.5 eV and 285.1 eV which are representative of the SWNT hosts and amorphous carbon from the adhesive used to secure the sample during measurements respectively. The O 1s region was fitted to a range of components that correspond to the different defect environments of the SWNT around 532 eV as well as the oxygen present in the carbonyl at approximately 534 eV (Figure 3.3c).

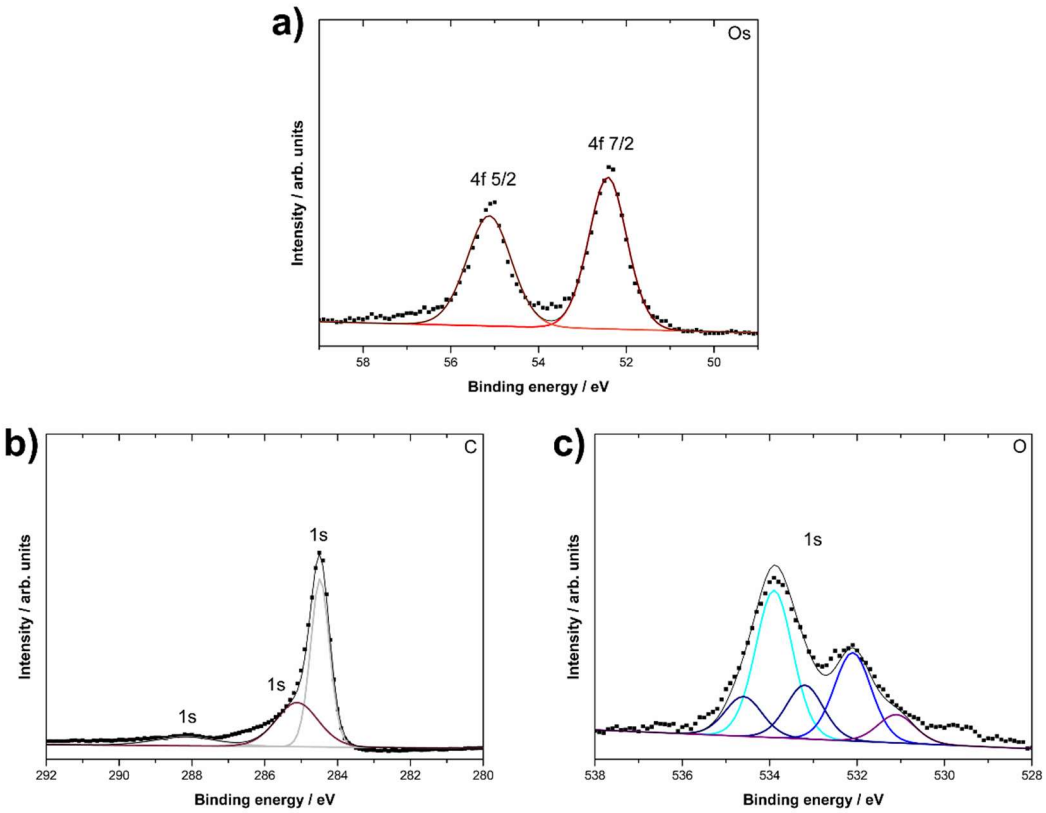


Figure 3.3. *XPS high resolution scans of $Os_3(CO)_{12}$@SWNT focussed on the (a) Os 4f, (b) C 1s, and (c) O 1s regions.*

The host-guest interactions were then studied using Raman spectroscopy with an excitation wavelength of 660 nm, in resonance with metallic SWNTs. The insertion of $Os_3(CO)_{12}$ into the SWNTs appeared to be primarily driven by van der Waals' forces as evidenced by a negligible red shift compared to empty SWNTs (-1.3 cm^{-1}) below the spectral resolution of the instrument of the G-band (Figure 3.4 and Table 3.1). This strongly suggests there was no electronic communication present between the host and guest. A small red shift of the radial breathing mode (RBM, -3.2 cm^{-1}), compared to empty SWNTs, was witnessed indicating an expansion of the SWNT diameter upon filling to accommodate the $Os_3(CO)_{12}$ molecules.

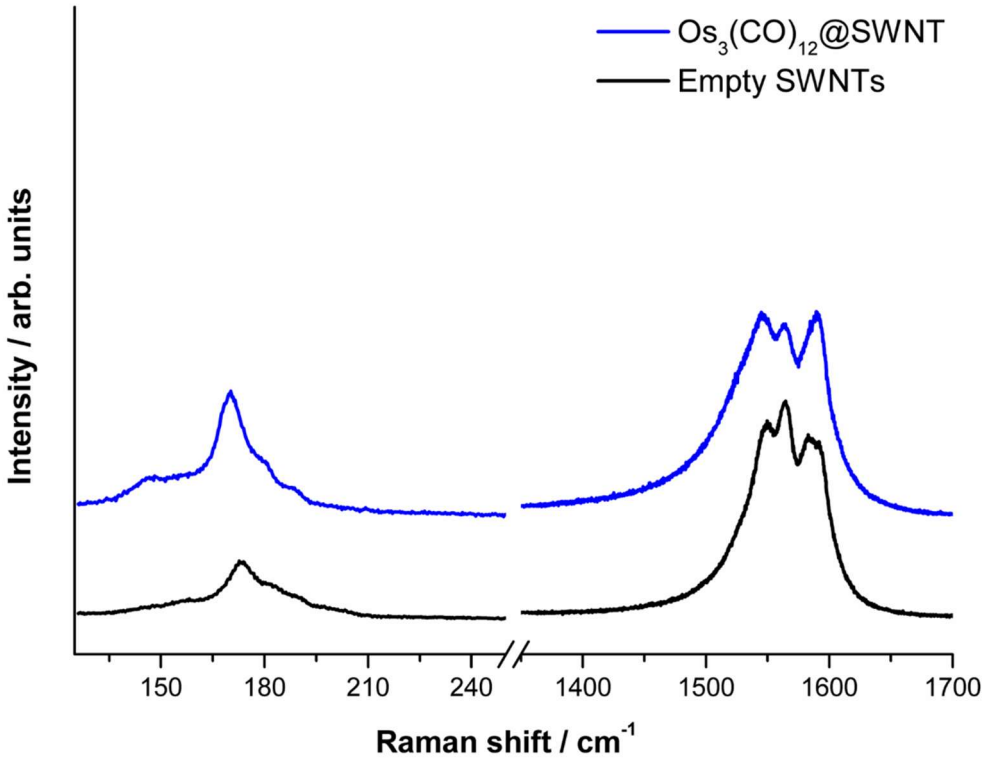


Figure 3.4. *Raman spectra overlay for $Os_3(CO)_{12}$@SWNT (blue), and empty SWNTs as reference (black), measured using a laser excitation (660 nm) in resonance with metallic SWNTs. The spectra are focussed on the low frequency region displaying the RBM of each material, as well as the G-band region.*

Table 3.1. *Raman band positions and shifts for empty SWNTs and $Os_3(CO)_{12}$@SWNT measured using a 660 nm laser excitation in resonance with metallic SWNTs.*

Material	RBM position / cm^{-1}	Shift w.r.t. empty SWNTs	G-band position / cm^{-1}	Shift w.r.t. empty SWNTs	Electron transfer
Empty SWNTs	173.2	-	1591.4	-	-

$Os_3(CO)_{12}$@SWNT	170.0	-3.2	1590.1	-1.3	Below spectral resolution

3.2.2. Reaction to form the iodide

The next steps were to introduce iodine into the nanotubes via sublimation and thermally activate the system to form an osmium iodide species (Scheme 3.2). On insertion of iodine, via sublimation, to $Os_3(CO)_{12}$@SWNT the Raman G-band, in resonance with metallic SWNTs, was blue shifted by +3.6 cm^{-1} compared to empty SWNTs (Figure 3.5, Table 3.2). Additionally, there was a change in the shape of the G-band to resemble a Lorentzian profile which is a result of a metallic to semiconducting transition.[33]

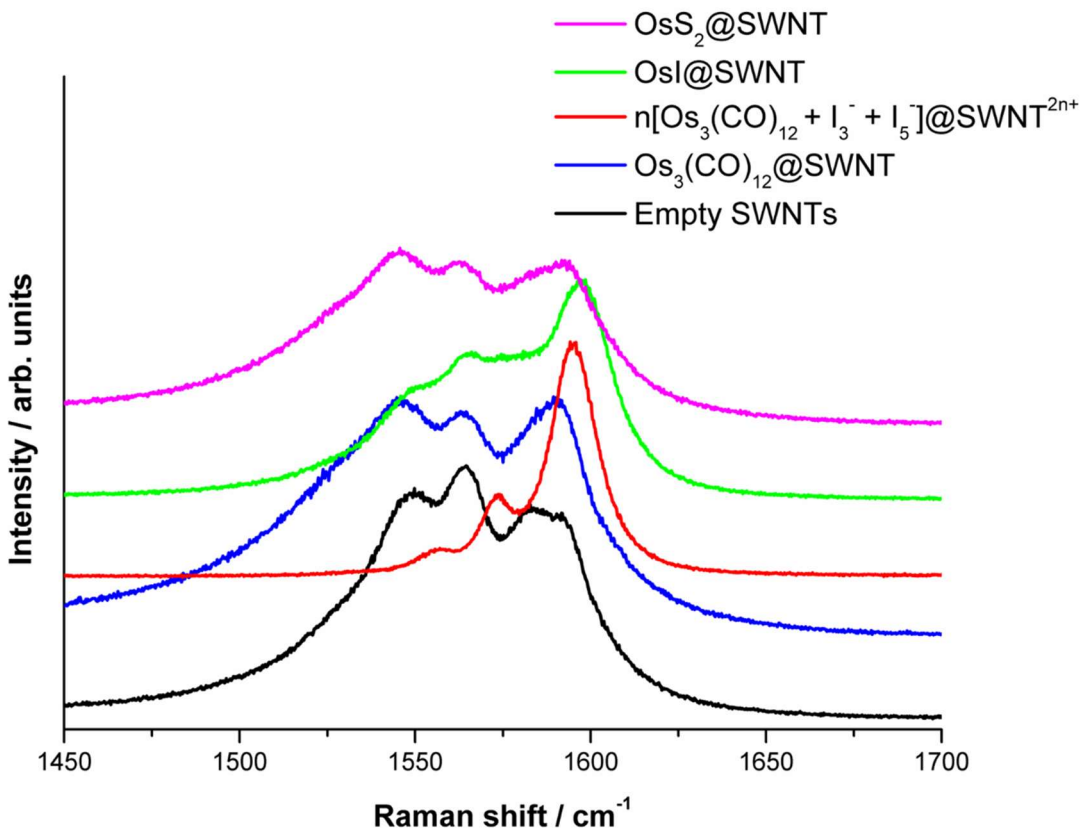


Figure 3.5. *Raman spectra overlay, measured using a 660 nm laser source in resonance with metallic SWNTs, focussed on the G-band region. The materials investigated were; empty*

SWNTs (black), $Os_3(CO)_{12}$@SWNT (blue), n[$Os_3(CO)_{12}$ + I_3^- + I_5^-]@$SWNT^{2n+}$ (red), OsI@SWNT (green), and OsS_2@SWNT (pink).

Table 3.2. *Raman spectroscopy G-band positions and shifts for* n[$Os_3(CO)_{12}$ + I_3^- + I_5^-]@$SWNT^{2n+}$, OsI@SWNT, and OsS_2@SWNT *recorded using a 660 nm laser excitation in resonance with metallic SWNTs.*

Material	G-band position / cm^{-1}	Shift w.r.t. empty SWNTs / cm^{-1}	Electron transfer direction
Empty SWNTs	1591.4	-	-
n[$Os_3(CO)_{12}$ + I_3^- + I_5^-]@$SWNT^{2n+}$	1595.0	+3.2	SWNT ➔ I_2
OsI@SWNT	1597.0	+5.2	$OsI^{\delta-}$@$SWNT^{\delta+}$ / SWNT ➔ residual I_2
OsS_2@SWNT	1592.6	+1.2	Below spectral resolution

The observation of the blue shift and profile change of the G-band are both indicative of electron donation from the SWNTs to iodine resulting in the formation of polyiodide ions, and is further evidenced by the presence of an I_3^- band at 109 cm^{-1}, and an I_5^- band at 175 cm^{-1} overlapping with the SWNT RBM, in the spectrum recorded using a 532 nm excitation (Figure 3.7).[34] The resultant material is thus characterised as n[$Os_3(CO)_{12}$ + I_3^- + I_5^-]@$SWNT^{2n+}$.

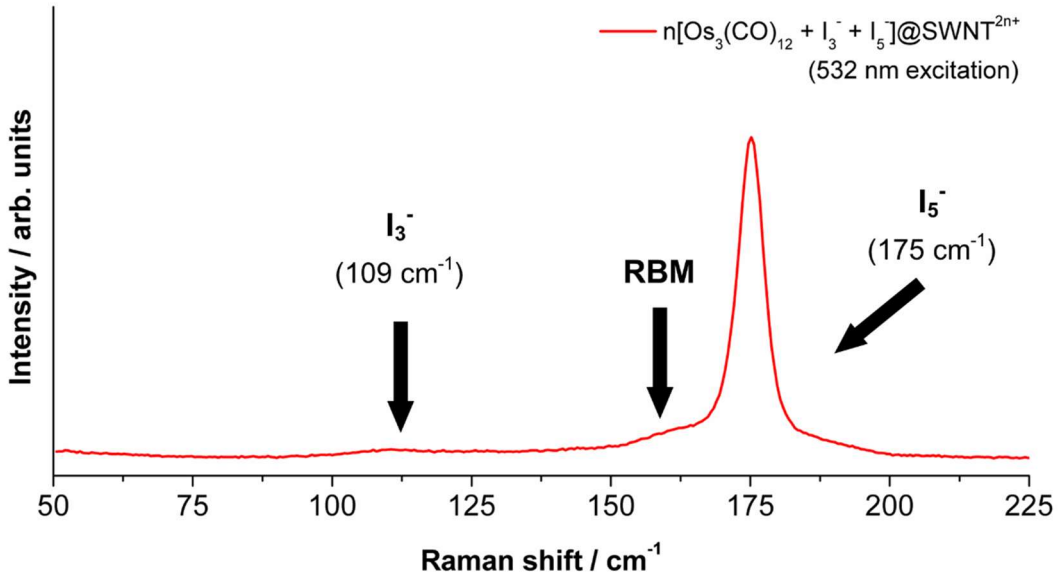


Figure 3.7. *Low-frequency region Raman spectrum of $n[Os_3(CO)_{12} + I_3^- + I_5^-]@SWNT^{2n+}$ recorded using a 532 nm excitation, displaying the peaks at 109 and 175 cm^{-1} corresponding to polyiodide ions of I_3^- and I_5^- respectively. The latter of which is found to be overlapping with the RBM of SWNTs.*

Heating $n[Os_3(CO)_{12} + I_3^- + I_5^-]@SWNT^{2n+}$ at 500 °C, under an inert atmosphere, triggered a chemical reaction between osmium and iodine, which resulted in a blue shift the G-band of metallic SWNTs by a further +2 cm^{-1} to 1597 cm^{-1}, compared to that of the previous material (Figure 3.5, Table 3.2) which suggests that either the formed material is a more effective electron acceptor than iodine or that further iodine has been converted to polyiodide, with the latter being more likely as the I_3^- band was found to increase in intensity. The binding energy peak positions of the osmium 4f 7/2 and 5/2 components in the thermally-activated system were found to be 51.0 and 53.7 eV, with partial overlap with a component of the iodine 4d doublet at 49.3 eV (Figure 3.7a). The binding energies of the iodine 3d doublet were 619.3 and 630.9 eV (5/2 and 3/2 respectively), which are in the typical range for metal iodides (Figure 3.7b).[35]

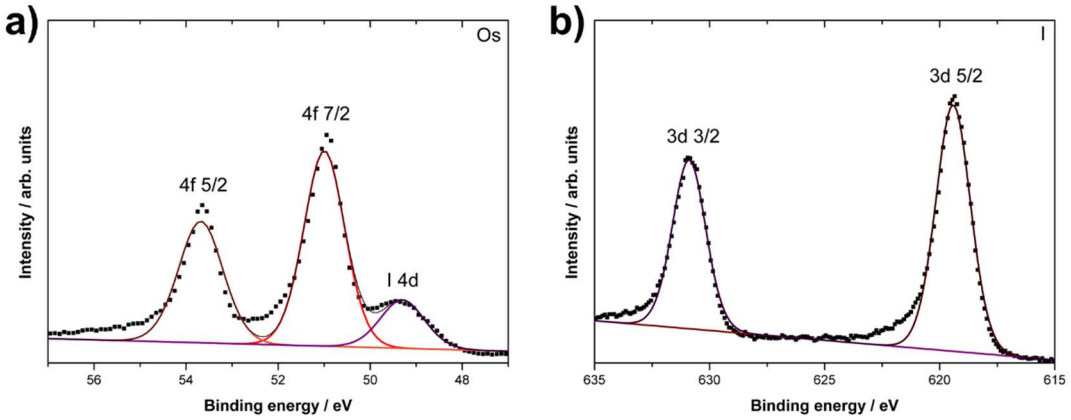


Figure 3.7. *XPS high resolution scans of OsI@SWNT focussed on the (a) Os 4f, and (b) I 3d regions.*

TEM imaging of the resulting material revealed the presence of nanoparticles on the exterior convex of the SWNT bundles which had grown during the thermal activation process (Figure 3.8a). Nanoparticle size analysis indicates a size range between 2 and 8 nm with a mean diameter of 5.1 ± 0.9 nm (Figure 3.8b). Local EDX analysis of a nanoparticle recorded the presence of osmium and iodine in a 1: 1.2 stoichiometry suggesting an osmium monoiodide species (Figure 3.8c).

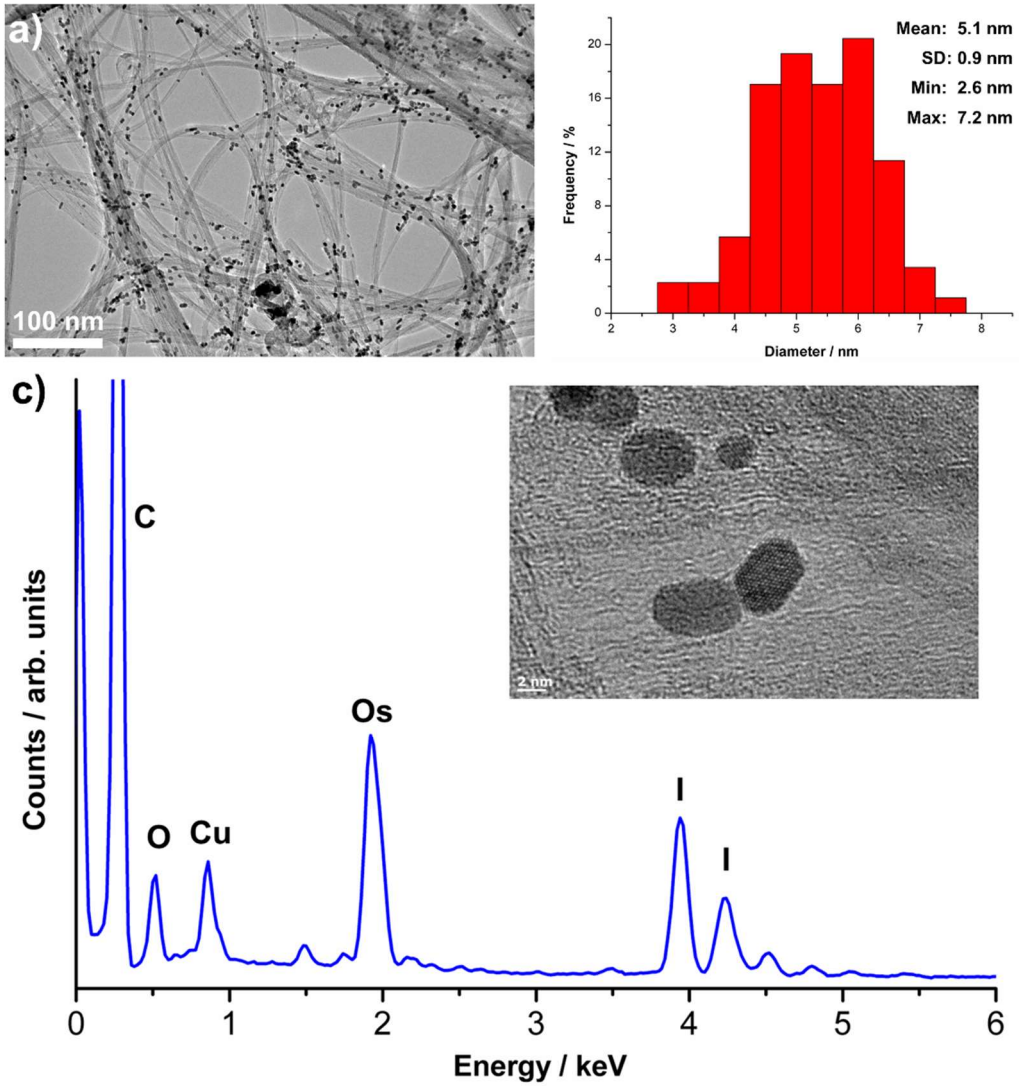


Figure 3.8. *(a) 200 kV HR-TEM large field of view image of OsI@SWNT showing nanoparticles on the exterior of the SWNTs; (b) size distribution histogram of osmium iodide nanoparticles highlighting a mean size of 5.1 ± 0.9 nm; (c) EDX spectrum of OsI nanoparticles suspended over the lacey carbon film of the TEM grid. The atomic ratio of Os: I was recorded to be 1: 1.2.*

AC-HRTEM imaging of a nanoparticle showed it was a crystalline species, appearing as rows of atoms, with a regular d-spacing of 0.26 nm (Figure 3.9a). This was further evidenced by a second set of two overlapping nanoparticles in the projection which exhibited the same spacings, as well as having a second area in which a hexagonal pattern was identified (Figure

3.9b). The two projections observed from AC-HRTEM correspond well to the face-on and diagonal projections of NaCl-type structures.[36] This couples well with the local EDX quantification and thus the structure is proposed as NaCl-type osmium monoiodide with both osmium and iodine in 6-coordinate configurations and local octahedral geometry (Figure 3.9c).

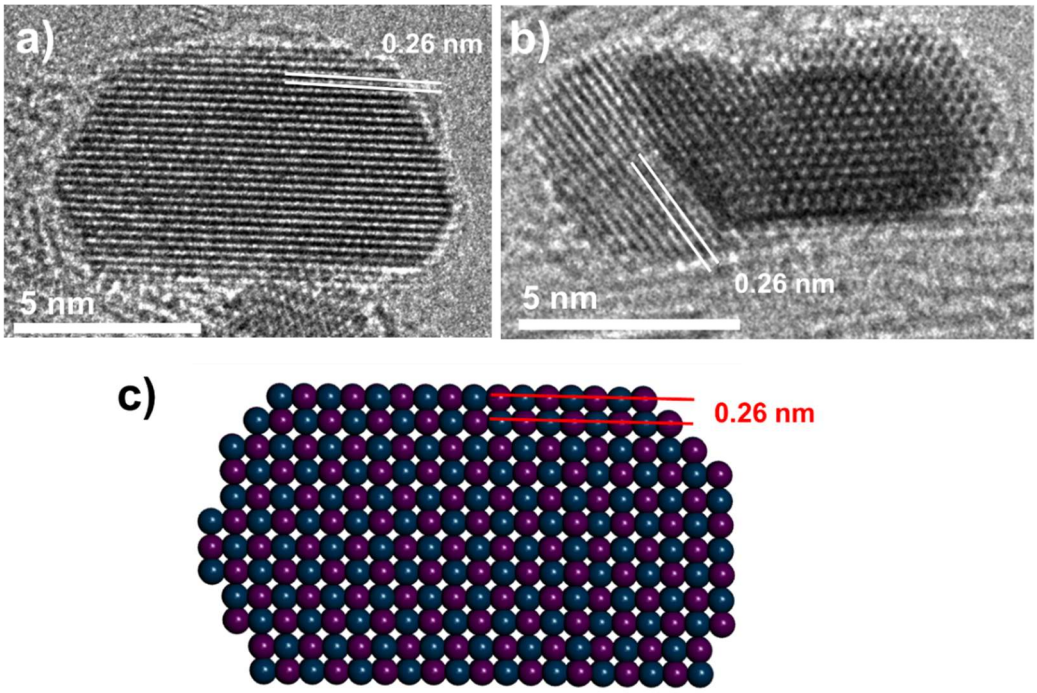


Figure 3.9. *(a) 80 kV AC-HRTEM image of an OsI nanoparticle showing 0.26 nm d-spacing; (b) 80 kV AC-HRTEM image showing two overlapping nanoparticles. The left side of the image shows the nanoparticle depicts the same d-spacing as in (a), the right side of the image shows a hexagonal projection; (c) Structural model showing the proposed structure and d-spacing.*

AC-HRTEM was then used to image the OsI nanostructures within the nanotubes, revealing two-atom thick nanowires within a 1.7 nm SWNT that extend along the full length of the SWNTs (Figures 3.10a - c). The two parallel nanowires are separated by a distance of 0.31 nm with their rotation and translation appearing to be independent of each other. EDX analysis of a bundle of SWNTs filled with nanowires (Figure 3.10f) confirms both iodine and osmium present in the sample with an atomic ratio of near 1:1 signifying preferential formation of

osmium monoiodide as observed for the exterior nanoparticles.[21] The distance between each OsI nanowire and the nanotube concave surface was measured as 0.31 nm, which corresponds to a typical van der Waals gap in graphitic materials.[14] The rotations, around the nanotube axis of the nanowires allow the detailed analysis of the structure across multiple projections. The contrast of the features along each row of atoms are consistently similar indicating that the contrast from each feature was caused by an osmium and an iodine atom which overlay in the projection of the image.[21] The third image of the time-series shows the two nanowires in different projections with the bottom nanowire appearing as two parallel lines; this is due to a tilt in the nanowire axis (Figure 3.10c). The distance between the two lines was found to be 0.28 nm, which is close to the d-spacing observed in the exterior nanoparticles formed on the convex outer surface of the SWNT (0.26 nm). The top nanowire in the third image has measured distances between nearest neighbours of 0.31 and 0.36 nm. A structural model and unit cell were proposed (Figures 3.10d and e), based on the interatomic distances and this corresponds to a distorted cubic NaCl-type phase with only osmium-iodine bonds present, with each iodine being bonded to 3 Os atoms. The generated AC-HRTEM simulations were in good agreement with the experimental images (Figures 3.10a - c).

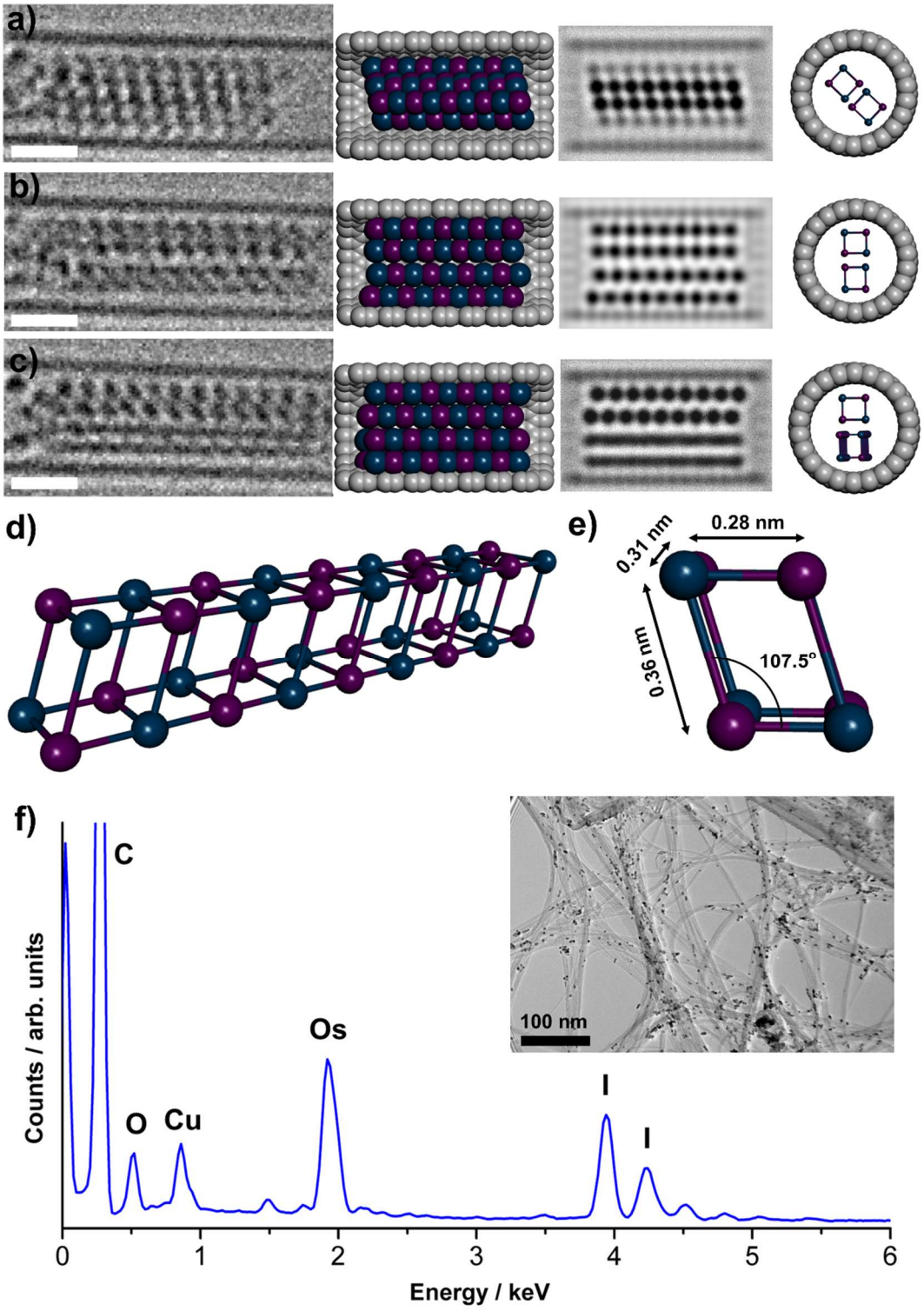


Figure 3.10. *(a) 60 kV AC-HRTEM image of OsI@SWNT showing two osmium iodide nanowires (a) overlapping in projection, (b) demonstrating the gap between the nanowires and (c) the bottom nanowire rotating perpendicular to the nanotube axis, the scale bar is 1 nm; structural models showing the proposed orientations of the nanowires inside the SWNT*

host (blue spheres represent osmium atoms and purple spheres represent iodine atoms), TEM simulations of the proposed models and cross-sectional views of the nanowires; (d) Structural model of the osmium iodide nanowire; (e) unit cell representation of the osmium iodide structure displaying key lattice parameters; (f) EDX spectrum of OsI@SWNT showing the presence of osmium and iodine in the sample conducted over an area containing both nanoparticles and nanowires of osmium iodide (inset, the copper peak is due to the TEM grid).

Whilst two of the AC-HRTEM images (Figures 3.10b and c) distinctly show the presence of two nanowires in different orientations upon rotations within the SWNT channel (Figures 3.11a and c); the first image (Figure 3.10a) shows four rows of atoms in close proximity. The rotations described are in reference against the unit cell projection in figure 3.10e. Additionally, the middle two rows of atoms are significantly darker in contrast than the top and bottom rows. These two phenomena arise from the nanowires being in 45^{o} rotations compared to the unit cell projection defined, and one of the nanowires rotating in the SWNT to be in front of the other, overlapping two rows of atoms causing higher contrast in TEM (Figure 3.11b).

Bulk osmium monoiodide was previously shown to be amorphous by Fergusson *et al*.[24] and thus this discovery highlights the importance of the role of SWNT concave in templating and stabilising low oxidation and low coordination compounds of osmium. It is interesting to note that the distorted cubic OsI formed inside nanotubes has the same structure as the OsI formed outside, both being NaCl-type structures. However, the Os in the nanoparticles is 6-coordinate and the Os in the nanowires is 3 coordinate which suggests that the concave of SWNT appears to be stabilising the large surface area and forced low coordination of distorted cubic OsI nanowires, as well as templating 1D growth, whereas OsI formed without confinement is stable in 6 coordination, with a smaller fraction of surface atoms and thus does not require stabilisation.

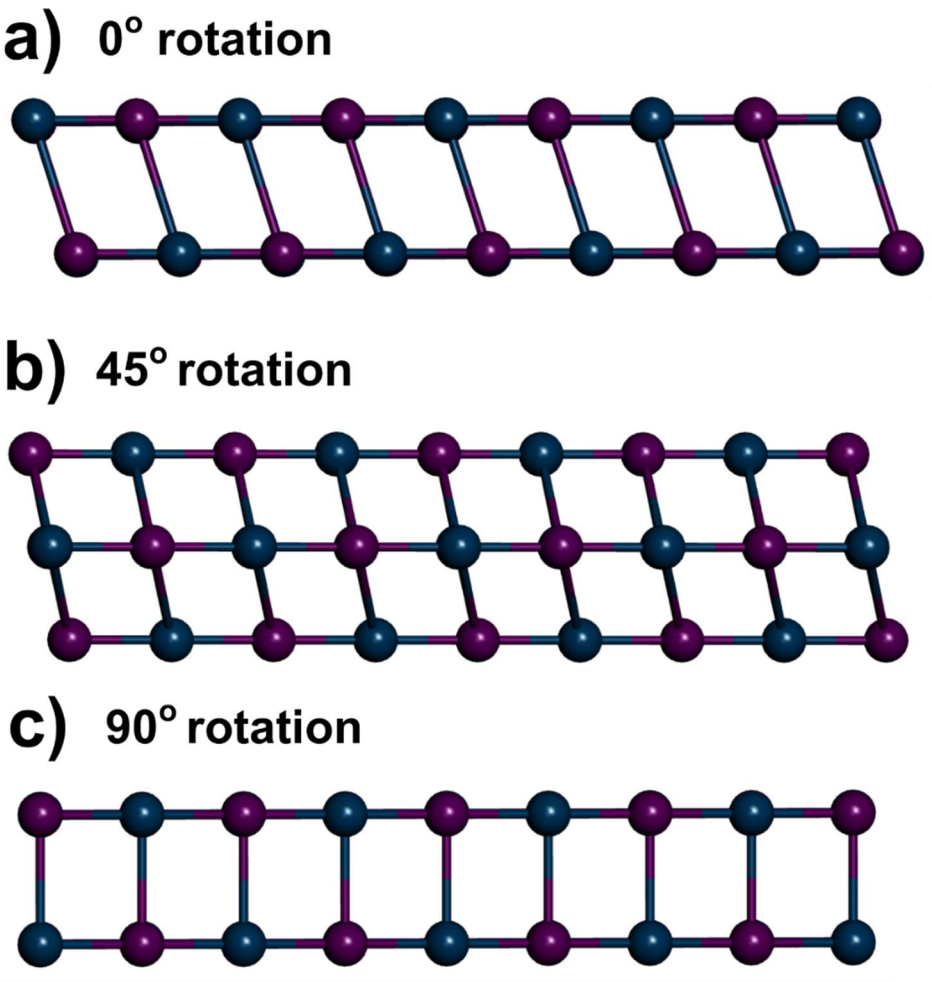


Figure 3.11. *Structural models of the OsI distorted Na-Cl type nanowires in various orientations; (a) 0º, (b) 45º, and (c) 90º rotations compared to the projection of the unit cell in figure 3.10e.*

3.2.3. Reaction to form the sulfide species

Hydrogen sulfide was introduced to OsI@SWNT at an elevated temperature to convert osmium monoiodide nanoparticles and nanowires to osmium disulfide. The position of the G-band of metallic SWNTs returned to the original position of empty SWNTs after this step which demonstrated the presence of a charge neutral product (Figure 3.5). The XPS peak position of osmium 4f 7/2 was found at 50.8 eV (Figure 3.12a) which is 0.5 eV higher than observed for bulk osmium disulfide (50.3 eV).[37] The S 2p region presented two sets of

doublets at 163.9 and 165.2 eV, and 168.5 and 169.6 eV which correspond to OsS_2 and SO_X species respectively (Figure 3.12b); the latter of which may be the result of functionalisation of the SWNT sidewall with excess H_2S.

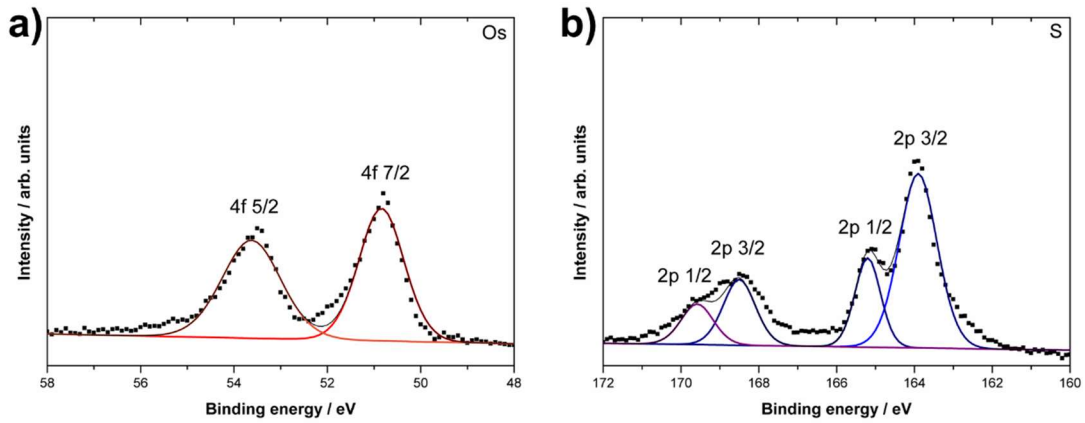


Figure 3.12. *XPS high resolution scans of OsS_2@SWNT focussed on the (a) Os 4f, and (b) S 2p regions.*

TEM imaging of osmium disulfide nanoparticles on the convex surfaces of the SWNT showed a mixture of regular nanocrystals and core-shell nanoparticles with a range of 1-3 shells observed (Figures 3.13a, c, and d inset). The mean diameter of the nanoparticles was calculated to be 2.6 nm ± 0.5 nm (Figure 3.13b). Local EDX analysis conducted on two core-shell nanoparticles identified both osmium and sulfur in a 1: 1.6 atomic ratio (Figure 3.13d). Powder x-ray diffraction (PXRD) conducted on the sample and compared against the known diffraction pattern of OsS_2[23] produced seven prominent peaks; three of which corresponded to the SWNT hosts (2θ = 25.9˚, 26.4˚ and 44.3˚) and the other four to cubic osmium disulfide (2θ = 27.1˚, 31.7˚, 45.4˚ and 53.8˚, Figure 3.13e).

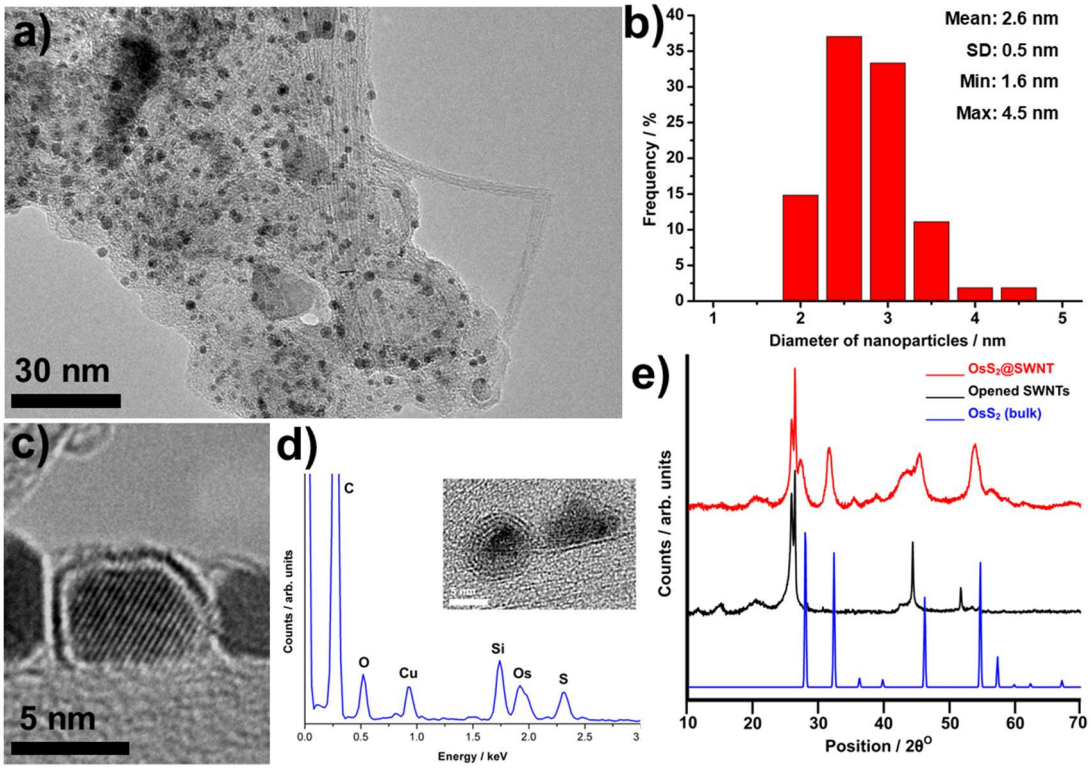


Figure 3.13. *(a) 200 kV HR-TEM image of OsS_2@SWNT highlighting the exterior nanoparticles; (b) size distribution histogram of osmium sulfide nanoparticles producing a mean size of 2.6 ± 0.5 nm; (c) 200 kV HR-TEM image of osmium sulfide nanoparticles that exhibit core-shell structures; (d) local EDX spectrum of two core-shell nanoparticles (inset) identifying osmium and sulfur in a 1: 1.6 stoichiometry (the copper peak is due to the TEM grid); (e) PXRD overlay showing the diffraction patterns for empty SWNTs (black), bulk osmium disulfide (blue) and OsS_2@SWNT (red).*

Aberration-corrected imaging of a core-shell nanoparticle identified the 0.23 nm d-spacing of the core which corresponds to the (211) plane of pyrite-type cubic OsS_2 (Figure 3.14a).[23] The structure of the shell was also revealed (Figure 3.14b) and resembles that of edge-on WS_2 nanoribbons[20] in which there is a series of dark contrast features surrounded each by two lighter contrast features on either side suggesting the presence of osmium and sulfur respectively. The interatomic distance within the central row of atomic columns was found

to be 0.27 nm, and a structural model was proposed to illustrate the projection (Figure 3.14c).

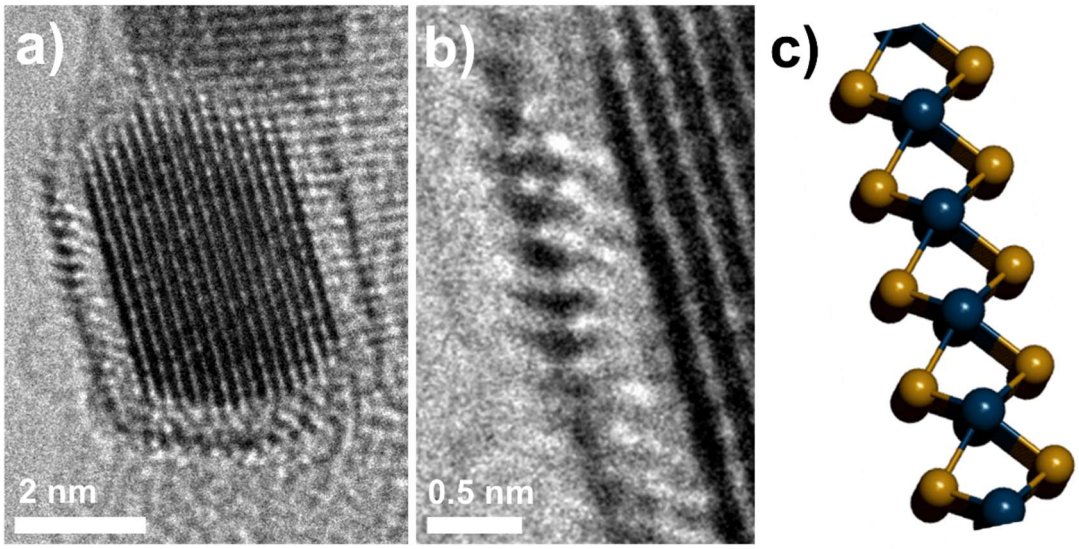


Figure 3.14. *(a) 80 kV AC-HRTEM image of a core-shell OsS_2 nanoparticle; (b) digitally-magnified image from (a) highlighting the atomic structure of the nanoparticle shell; (c) structural model of hexagonal OsS_2 in an edge-on view.*

A second nanoparticle was shown to be only partially covered by a shell over the cubic OsS_2 core and was in a projection which allowed the structure to be viewed (Figure 3.15a). At a higher magnification (Figure 3.15b) a hexagonal lattice shell structure was revealed of the shell material in which the vertices had alternate contrast intensities; the interatomic distance between adjacent dark features was 0.24 nm. A structural model of hexagonal OsS_2 was constructed (Figure 3.15c), based on the existing structure of WS_2, and a TEM simulation of the layer was performed revealing the same hexagonal structure and alternate contrast pattern (Figure 3.15d). The lighter features were proven to be the S_2 units in projection whilst the darker features were identified as osmium atoms.

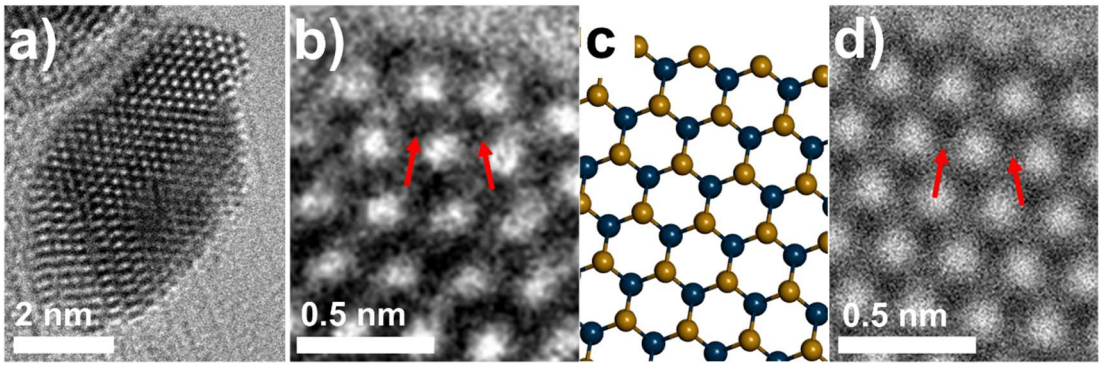


Figure 3.15. *(a) 80 kV AC-HRTEM image of a nanoparticle that is partially covered by a shell layer; (b) digitally-magnified image from (a) highlighting the hexagonal nature of a section of the shell placed over the vacuum. Red arrows are superimposed on the image to indicate the alternating contrast of the vertices; (c) structural model of hexagonal OsS_2 in a face-on view; (d) TEM simulation of the structural model in (c) which shows the hexagonal structure. Red arrows are superimposed on the image to indicate the alternating vertex contrast observed in the experimental image.*

AC-HRTEM and contrast analysis of both of these nanoparticles has provided strong evidence that the shell and core structures are structurally distinct from one another and consist of different phases of osmium disulfide (hexagonal WS_2-type and cubic pyrite-type respectively, Figures 3.16a and b).[38, 39] The hexagonal disulfide phase is most commonly observed for molybdenum and tungsten, but it has not been observed for osmium previously. The most likely explanation for the formation of new form of hexagonal OsS_2 is the need to stabilise the dangling bonds of few-nm sized particles of cubic OsS_2 which are not possible to stabilise by the convex surface of SWNT: while the nanotube surface curves away from nanoparticles, a hexagonal layer of OsS_2 envelopes cubic OsS_2 thus stabilising the surface, in a similar way as graphitic phase of carbon stabilised nanodiamonds.[38, 39]

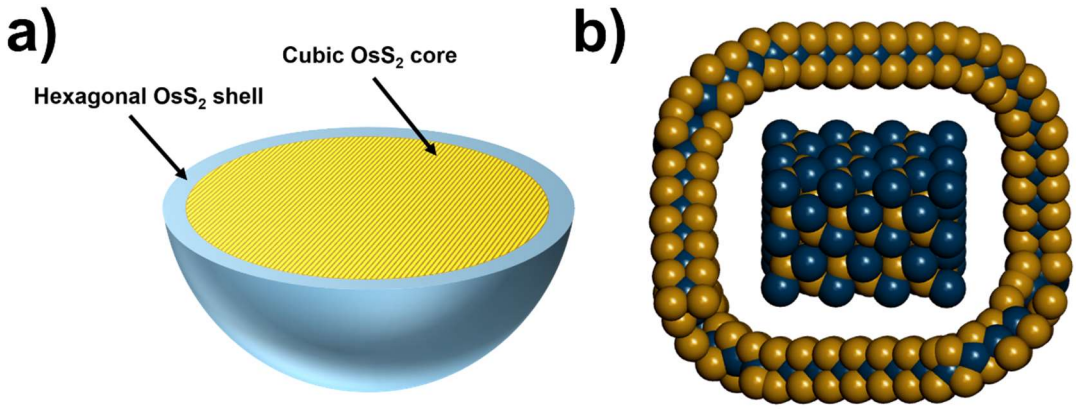


Figure 3.16. *(a) Schematic diagram of the core-shell nanoparticle (yellow - cubic OsS_2, and blue - hexagonal OsS_2); and (b) a corresponding structural model.*

The structure of OsS_2@SWNT, formed within the convex, was then probed by HR-TEM (Figure 3.17a) which revealed the formation of a three-atom thick nanowire measuring 0.6 nm in diameter, which is the approximate size of the unit cell of cubic OsS_2. The nanowire extends parallel to the nanotube axis across the entire length of the SWNT (approximately 40 nm) and is representative of all filled SWNTs. EDX of a bundle of filled SWNTs confirms the loss of iodine and the presence of osmium and sulfur in the nanotube in a 1:3 stoichiometry which demonstrates the transformation from osmium iodide to osmium sulfide has taken place (Figure 3.17h). The excess sulfur is most likely caused by reaction of H_2S with the SWNT sidewalls. Contrast analysis along the rows of atoms, parallel to the nanotube axis identifies alternating intensities suggesting that either the nanowire consists of alternate osmium and sulfur atoms, or that there is a difference in the number of atoms overlapping in projection (Figures 17e and f). Sulfur, in comparison to osmium has a lower atomic number and individual atoms would not be distinguishable in TEM images.[21] This means that the features observed must correspond to columns containing varying number of osmium atoms. A face-on projection of the osmium disulfide unit cell has two overlapping osmium atoms on each corner of the unit cell, one osmium atom in the middle of each edge and two overlapping osmium atoms in the centre of the square face (Figure 3.17g). A

structural model of the nanowire was built by extending the unit cell along only the nanotube axis. A TEM simulation of this model confirmed the alternating contrast pattern observed experimentally as well as the regular spacings observed between columns (0.31 nm, Figures 3.17b and c). This correlation of experimental and simulated analysis confirms the structure of the nanowire to be consistent with pyrite-type cubic osmium disulfide but restricted to grow in only one-dimension. A closer inspection of the nanowire reveals it to have helical twists, which may maximise the interactions with the nanotube walls, and relieve strain within the structure. Multiple projections of the nanowire are observed in the TEM image including face-on and diagonal, and simulations of a twist in the structure confirm the proposed structural model (Figures 3.17b and c). The cubic phase of OsS_2 extended into a single unit cell wide nanowire contains a very high proportion of dangling bonds; however, the material is stabilised by interactions with the SWNT concave surface which curves around the structure. This parallels the observations for the core-shell cubic-OsS_2@hexagonal-OsS_2 nanoparticles formed on the convex surface of SWNT where the hexagonal shell stabilises dangling bonds of the cubic core, where it is not possible for the convex of the SWNT to form a stabilising shell due to the surface curving away from the nanoparticles.

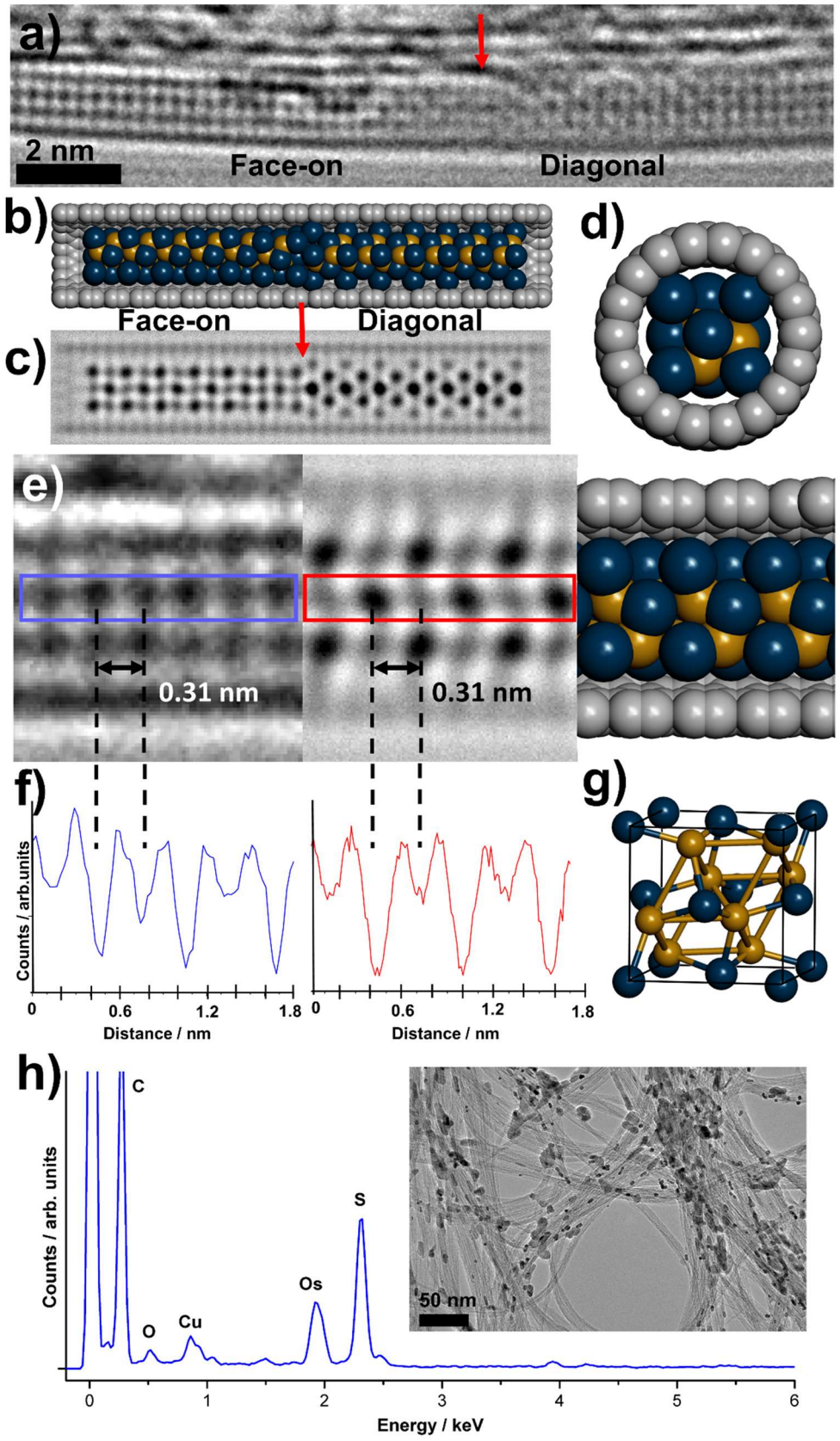


Figure 3.17. *(a) 100 kV HR-TEM image showing a OsS_2@SWNT containing a three-atom thick nanowire. A red arrow is superimposed to indicate the twist point of the nanowire; (b)*

structural model showing the 1D OsS_2 nanowire fit inside the SWNT (blue spheres represent osmium atoms and yellow spheres represent sulfur atoms); (c) TEM image simulation of the twisted OsS_2 nanowire model highlighting the projections observed in (a). A red arrow demonstrates the twist point of the nanowire; (d) structural model showing the cross-section of the host-guest system; (e) Magnified HR-TEM image in (a) showing the periodic distance (0.31 nm) between adjacent atoms (left), TEM image simulation demonstrating this periodic distance (middle), structural model proposed that the simulation was conducted on (right); (f) image contrast analysis of the areas shown in the HR-TEM image and simulation in (e) evidencing the alternate contrast pattern between adjacent atoms; (g) unit cell of cubic osmium disulfide; (h) EDX spectrum of an area containing both core-shell nanoparticles and twisted nanowires (inset) identifying both sulfur and osmium present.

3.3. Conclusions

Carbon nanotubes are known as excellent supports as well as nanocontainers for inorganic materials and are exploited in many applications. In this study, both the external (convex) and internal (concave) surfaces of SWNT are utilised, and demonstrate a profound impact of the type of the surface on the structure of inorganic nanomaterials, using transformations of osmium compounds as an example system. Confinement inside nanotubes serves a dual purpose – the nanotube cavity templates the growth of OsI and OsS_2 nanowires along one crystallographic direction, limiting two dimensions, and simultaneously the SWNT concave wraps around the nanowires of cubic/ distorted cubic phases of the osmium compounds thus stabilising highly unstable surfaces of nanowires with a large proportion of dangling bonds. When the synthesis of osmium compounds is conducted on the external convex of nanotube, the absence of spatial confinement allows growth in all three dimensions resulting in plate-like cubic and spheroidal core-shell nanoparticles of OsI and OsS_2 respectively. The

arrangement of atoms in the externally formed OsI is 6 coordinate which is drastically reduced to 3-coordinate for distorted cubic OsI inside nanotubes, whereas external OsS_2 has the same cubic structure as OsS_2 inside nanotubes, but in order stabilise its surface atoms, a new form of OsS_2 with a hexagonal lattice, isostructural with WS_2, wrapped around the nanoparticle, imitating the nanotube concave. The use of nanotubes as platforms for inorganic reactions in this study allows us to broaden the chemistry of osmium, with three previously unknown compounds discovered at nanoscale, and elucidate mechanisms of inorganic nanostructures formation and stabilisation using our holistic analytical approach.

3.4. Experimental

3.4.1. Materials

SWNTs (P2-SWNTs, arc-discharge, Carbon Solutions, USA) were annealed at 600 °C for 17 min to remove their end caps and any amorphous carbon from their internal cavities, resulting in a 50% mass loss. Triosmium dodecacarbonyl (Alfa Aesar), iodine (Fisher Scientific) and hydrogen sulfide (CK Special Gases) were all used as supplied.

3.4.2. Encapsulation of $Os_3(CO)_{12}$ into single-walled carbon nanotubes

Freshly opened SWNTs were added to a Pyrex ampoule (d = 10 mm, l = 15 cm) along with $Os_3(CO)_{12}$ (10 mg, 0.0055 mmol) and sealed under vacuum (10^{-4} mbar). The ampoule was heated to 130 °C for 3 days and then cooled in an ice-bath to cease the sublimation process.

3.4.3. Preparation of osmium iodide

Iodine (20 mg, 0.039 mmol) was added to a Pyrex ampoule containing $Os_3(CO)_{12}$@SWNT (5 mg) and sealed under vacuum (10^{-4} mbar). The ampoule was heated for 3 days at 120 °C and then cooled in an ice-bath. The resultant material was then heated to 500 °C for 1 hour under argon to produce OsI@SWNT.

3.4.4. Preparation of osmium disulfide

Argon was flowed over OsI@SWNT (5 mg) in a tube furnace for 1 hour at room temperature, followed by a flow of hydrogen disulfide at room temperature. The sample was then heated to 550 °C for 2 hours whilst being subjected to a flow of hydrogen disulfide (15 mL / min). The sample was then cooled under argon at a rate of 5 °C / min back to room temperature to produce OsS_2@SWNT.

3.4.5. Electron microscopy and energy-dispersive x-ray spectroscopy

Samples were suspended in propan-2-ol and dropcast onto lacey carbon copper TEM grids (Agar). HR-TEM was conducted using a JEOL 2100F FEG-TEM microscope operated at 100 and 200 kV. EDX analysis was performed using an Oxford Instruments INCA X-ray microanalysis system. AC-HRTEM of the osmium iodide nanowires was performed at Ulm University using a C_s corrected SALVE TEM microscope operated at 60 kV. AC-HRTEM of the osmium iodide and disulfide nanoparticles was performed at the Electron Physical Science Imaging Centre at Diamond Light Source on a JEM ARM300CF operated at 80 kV.

3.4.6. TEM simulation

TEM image simulations were carried out using QSTEM, a multislice program which uses the Dirac-Fock scattering potential of Rez *et al*.[40] A fixed number of 10 slices per nanotube were chosen and images were calculated with a sampling of 0.005 nm per pixel. The defocus and aberration parameters were set according to the values used in experimental imaging. The effect of limiting electron dose to the images was conducted using a custom made Monte-Carlo program that applies noise by utilising the Poisson statistics of electrons.

3.4.7. Raman spectroscopy

Samples were suspended in methanol and dropcast onto Si(100) wafers. Raman spectroscopy was performed on a Horiba Jobin Yvon LabRAM HR Raman microscope using a 660 nm laser excitation (at ~0.2 mW power), a 100x objective, and a 200 µm confocal

pinhole. The Raman shift was calibrated using the Rayleigh peak and the 520.7 cm^{-1} silicon line from a Si (100) reference sample. To simultaneously scan a range of Raman shifts, a 600 lines mm^{-1} rotatable diffraction grating along a path length of 800 mm was employed, conferring a spectral resolution better than 1.2 cm^{-1} for the 660 nm laser. Spectra were detected using a Synapse CCD detector (1024 pixels) thermoelectrically cooled to −60 °C. Before spectra collection, the instrument was calibrated using the zero-order line and a standard Si (100) reference band at 520.7 cm^{-1}. For single point measurements, spectra were acquired over a minimum range 125-3400 cm^{-1} with an acquisition time of 15-120 seconds and 2 accumulations to automatically remove the spikes due to cosmic rays and improve the signal to noise ratio. Spectra were collected from at least three random locations and averaged to give a mean spectrum.

3.4.8. Infrared spectroscopy

Thin film Infrared Spectroscopy was performed using a Bruker FT-IR spectrometer over the range of 600 – 4000 cm-1. The samples were prepared using KBr pellets.

3.4.9. X-ray photoelectron spectroscopy

X-ray photoelectron spectroscopy: Samples were analysed using the Kratos AXIS ULTRA with a mono-chromated Al kα X-ray source (1486.6eV) operated at 10 mA emission current and 12 kV anode potential (120 W.) Spectra were acquired with the Kratos VISION II software. A charge neutralizer filament was used to prevent surface charging. Hybrid –slot mode was used measuring a sample area of approximately 300 x 700 µm. The analysis chamber pressure was better than 5 x 10-9 mbar. Three areas per sample were analysed. A wide scan was performed at low resolution (Binding energy range 1400 eV to -5 eV, with pass energy 80 eV, step 0.5 eV, sweep time 20 minutes). High resolution spectra at pass energy 20 eV, step of 0.1 eV, and sweep times of 10 minutes each were also acquired for photoelectron

peaks from the detected elements and these were used to model the chemical composition. The spectra were charge corrected to the C 1s peak set to 284.5 eV.

3.4.10. Powder x-ray diffraction

Powder x-ray diffraction measurements were performed on a PANalytical X'pert Pro diffractometer operating with a Cu K(α) radiation source (λ = 1.5432 Å, 40 kV, 40 mA) in Bragg-Brentano geometry. Samples were mounted on Si zero-background holders using propan-2-ol to secure them. The parameters used were: 5˚ start angle, 70˚ stop angle, 0.0262˚ step size and 1996 s time per step and measurements were conducted at ambient temperature.

3.5. References

1. E. Navarro-Moratalla, J. O. Island, S. Manas-Valero, E. Pinilla-Cienfuegos, A. Castellanos-Gomez, J. Quereda, G. Rubio-Bollinger, L. Chirolli, J. A. Silva-Guillen, N. Agrait, G. A. Steele, F. Guinea, H. S. J. van der Zant and E. Coronado, *Nat. Commun.*, 2016, **7**, 1-7.
2. B. Radisavljevic, A. Radenovic, J. Brivio, V. Giacometti and A. Kis, *Nat. Nanotechnol.*, 2011, **6**, 147-150.
3. J. D. Benck, T. R. Hellstern, J. Kibsgaard, P. Chakthranont and T. F. Jaramillo, *ACS Catal.*, 2014, **4**, 3957-3971.
4. Z. Chen, W. Thiel and A. Hirsch, *ChemPhysChem*, 2003, **4**, 93-97.
5. S. Ju, J. M. Lee, Y. Jung, E. Lee, W. Lee and S.-J. Kim, *Sens. Actuators B Chem.*, 2010, **146**, 122-128.
6. S. Iijima and T. Ichihashi, *Nature*, 1993, **363**, 603-605.
7. D. S. Bethune, C. H. Kiang, M. S. de Vries, G. Gorman, R. Savoy, J. Vazquez and R. Beyers, *Nature*, 1993, **363**, 605-607.

8. A. A. Eliseev, M. V. Chernysheva, N. I. Verbitskii, E. A. Kiseleva, A. V. Lukashin, Y. D. Tretyakov, N. A. Kiselev, O. M. Zhigalina, R. M. Zakalyukin, A. L. Vasiliev, A. V. Krestinin, J. L. Hutchison and B. Freitag, *Chem. Mater.*, 2009, **21**, 5001-5003.

9. C. E. Giusca, V. Stolojan, J. Sloan, F. Borrnert, H. Shiozawa, K. Sader, M. H. Rummeli, B. Buchner and S. R. P. Silva, *Nano Lett.*, 2013, **13**, 4020-4027.

10. M. Nagata, S. Shukla, Y. Nakanishi, Z. Liu, Y.-C. Lin, T. Shiga, Y. Nakamura, T. Koyama, H. Kishida, T. Inoue, N. Kanda, S. Ohno, Y. Sakagawa, K. Suenaga and H. Shinohara, *Nano Lett.*, 2019, **19**, 4845-4851.

11. S. A. Miners, G. A. Rance and A. N. Khlobystov, *Chem. Soc. Rev.*, 2016, **45**, 4727-4746.

12. M. Yudasaka, K. Ajima, K. Suenaga, T. Ichihashi, A. Hashimoto and S. Iijima, *Chem. Phys. Lett.*, 2003, **380**, 42-46.

13. B. W. Smith, M. Monthioux and D. E. Luzzi, *Nature*, 1998, **396**, 323-324.

14. A. N. Khlobystov, D. A. Britz and G. A. D. Briggs, *Acc. Chem. Res.*, 2005, **38**, 901-909.

15. D. A. Britz, A. N. Khlobystov, K. Porfyrakis, A. Ardavan and G. A. D. Briggs, *Chem. Commun.*, 2005, 37-39.

16. Z. Wang, H. Li, Z. Liu, Z. Shi, J. Lu, K. Suenaga, S.-K. Joung, T. Okazaki, Z. Gu, J. Zhou, Z. Gao, G. Li, S. Sanvito, E. Wang and S. Iijima, *J. Am. Chem. Soc.*, 2010, **132**, 13840-13847.

17. T. W. Chamberlain, J. Biskupek, G. A. Rance, A. Chuvilin, T. J. Alexander, E. Bichoutskaia, U. Kaiser and A. N. Khlobystov, *ACS Nano*, 2012, **6**, 3943-3953.

18. S. A. Miners, G. A. Rance and A. N. Khlobystov, *Chem. Commun.*, 2013, **49**, 5586-5588.

19. A. Botos, J. Biskupek, T. W. Chamberlain, G. A. Rance, C. T. Stoppiello, J. Sloan, Z. Liu, K. Suenaga, U. Kaiser and A. N. Khlobystov, *J. Am. Chem. Soc.*, 2016, **138**, 8175-8183.

20. Z. Wang, K. Zhao, H. Li, Z. Liu, Z. Shi, J. Lu, K. Suenaga, S.-K. Joung, T. Okazaki, Z. Jin, Z. Gu, Z. Gao and S. Iijima, *J. Mater. Chem.*, 2011, **21**, 171-180.

21. C. T. Stoppiello, J. Biskupek, Z. Y. Li, G. A. Rance, A. Botos, R. M. Fogarty, R. A. Bourne, J. Yuan, K. R. J. Lovelock, P. Thompson, M. W. Fay, U. Kaiser, T. W. Chamberlain and A. N. Khlobystov, *Nanoscale*, 2017, **9**, 14385-14394.

22. K. G. Snetsinger, *Am. Mineral.*, 1971, **56**, 1501-1506.

23. T. Stingl, B. Muller and H. D. Lutz, *Z. Kristallogr. Cryst. Mater*, 1992, **202**, 161.

24. J. E. Fergusson, B. H. Robinson and W. R. Roper, *J. Chem. Soc.*, 1962, 2113-2115.

25. K. Cao, T. Zoberbier, J. Biskupek, A. Botos, R. L. McSweeney, A. Kurtoglu, C. T. Stoppiello, A. V. Markevich, E. Besley, T. W. Chamberlain, U. Kaiser and A. N. Khlobystov, *Nat. Commun.*, 2018, **9**, 3382.

26. A. Pitto-Barry, L. M. A. Perdigao, M. Walker, J. Lawrence, G. Costantini, P. J. Sadler and N. P. E. Barry, *Dalton Trans.*, 2015, **44**, 20308-20311.

27. K.-F. Yung and W.-T. Wong, *J. Cluster Sci.*, 2007, **18**, 51-65.

28. T. W. Chamberlain, N. R. Champness, M. Schroder and A. N. Khlobystov, *Chem-Eur J*, 2011, **17**, 668-674.

29. T. Zoberbier, T. W. Chamberlain, J. Biskupek, N. Kuganathan, S. Eyhusen, E. Bichoutskaia, U. Kaiser and A. N. Khlobystov, *J. Am. Chem. Soc.*, 2012, **134**, 3073-3079.

30. J. Cui, M. Burghard and K. Kern, *Nano Lett.*, 2003, **3**, 613-615.

31. T. Zoberbier, T. W. Chamberlain, J. Biskupek, M. Suyetin, A. G. Majouga, E. Besley, U. Kaiser and A. N. Khlobystov, *Small*, 2016, **12**, 1649-1657.

32. R. Zanoni, V. Carinci, R. H. Abu-Samn, R. Psaro and C. Dossi, *J. Mol. Struct.*, 1985, **131**, 363-369.

33. M. V. Kharlamova, *Appl. Phys. A*, 2016, **122**, 791.

34. L. Grigorian, K. A. Williams, S. Fang, G. U. Sumanasekera, A. L. Loper, E. C. Dickey, S. J. Pennycook and P. C. Eklund, *Phys. Rev. Lett.*, 1998, **80**, 5560-5563.

35. J. F. Moulder, W. F. Stickle, P. E. Sobol and K. D. Bomben, *Handbook of X-ray Photoelectron Spectroscopy: A Reference Book of Standard Spectra for Identification and Interpretation of XPS Data*, Physical Electronics Division, Perkin-Elmer Corporation, 1992.

36. T. Nakamuro, M. Sakakibara, H. Nada, K. Harano and E. Nakamura, *J. Am. Chem. Soc.*, 2021, **143**, 1763-1767.

37. T. Schwarzlose, S. Fiechter and W. Jaegermann, *Ber Bunsenges. Phys. Chem*, 1992, **96**, 887-893.

38. G. Lan, Y. Qiu, J. Fan, X. Wang, H. Tang, W. Han, H. Liu, H. Liu, S. Song and Y. Li, *Chem. Commun.*, 2019, **55**, 1430-1433.

39. B. Liang, L. Zhang, W. Wang, G. Xu, W. Zhang, Y. Zhang, R. Zhang, L. Yang and L. Zhang, *Mater. Res. Express*, 2019, **6**, 045609.

40. D. Rez, P. Rez and I. Grant, *Acta Crystallogr. A*, 1994, **50**, 481-497.

Chapter 4: Triangular molybdenum chalcogen clusters: entrapment and transformations within nano test tubes

4.1. Introduction

Metal chalcogen based clusters are species that contain 1 - 4 metal centres (usually Mo or W) attached to chalcogenide ligands (S or Se) that exist in different bonding environments; the d^n configuration of the metal dictates the shape of the overall cluster (n = 1 dumb-bell, n = 2 triangular, n = 3 tetrahedral, and n = 4 octahedral).[1] The most common clusters studied in literature are those consisting of a $[Mo_3S_7]^{4+}$ core, which can be tuned through modification of the ligands to produce species with more interesting optical and magnetic properties.[2-4]

Ammonium thiomolybdate, $[NH_4]_2[Mo_3S_{13}]\cdot 2H_2O$, was the first trinuclear group VI cluster to be formed where the metal was in d^2 configuration, resulting in the triangular structure.[1] The complex was formed on reaction of ammonium polysulfide with $[NH_4]_6Mo_7O_{24}\cdot 4H_2O$ and $NH_2OH\cdot HCl$, and the structure was resolved which resolved that sulfur was in three different bonding environments; terminal and μ_2-bridging disulfide ligands, and a μ_3-capping sulfur in the centre of the Mo_3 plane (Figure 4.1). Moreover, the donor atoms in the bridging μ_2-S_2 ligands were found to be coordinately non-equivalent, resulting in S atoms in and above the Mo_3 plane, which are termed as equatorial and axial respectively. The capping sulfur is found on the opposite side of the plane to the axial sulfur atoms.

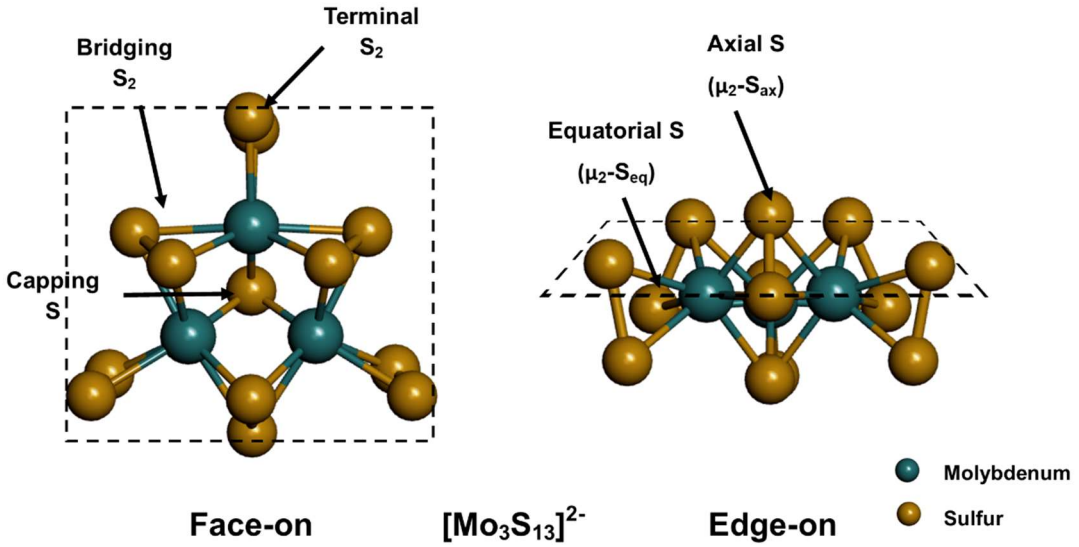


***Figure* 4.1.** *Face-on and edge-on views of the thiomolybdate cluster displaying the types of sulfur ligands present, as well as the asymmetrical coordination of bridging S_2 ligands. The blue and yellow spheres represent molybdenum and sulfur atoms respectively.*

Chemical reactions of the trinuclear cluster have afforded more details about the reactivity of each set of ligands, as well as produced a plethora of new compounds with modified properties. The reaction of $[NH_4]_2[Mo_3S_{13}]\cdot 2H_2O$ with bromine and tetraethyl ammonium bromide, by Fedin *et al.* resulted in the nucleophilic substitution of the terminal disulfide ligands to produce $[Et_4N]_2[Mo_3S_7Br_6]$ in which the $[Mo_3S_7]^{4+}$ core was preserved;[5] this compound was later determined to have an orthorhombic crystal structure.[6] The newly formed compound was discovered to have highly electrophilic axial sulfur atoms which allowed the cluster to behave as an electron acceptor towards the formation of charge transfer salts.[7, 8]

Conversely, the bridging disulfide ligands have also been modified upon reactions of triangular thiohalide clusters, $[Et_4N]_2[Mo_3S_7X_6]$ (X = Cl, Br or I), with reagents such as $SePPh_3$.[9] By following the reaction using isotope-labelled compounds it was established that it was the equatorial sulfur atoms that were substituted for selenium atoms resulting in the first compounds with S-Se ligands such as $[Et_4N]_2[Mo_3S_4Se_3Br_6]$. This is explained by the longer

the Mo-S_{eq} bond compared to Mo-S_{ax} (2.485 and 2.391 Å respectively).[2] Ligand exchange of thiomolybdate-based clusters has led to compounds being formed that have modified non-linear optical, and magnetic properties, using ligands such as; oxalate and 1,3-dithia-2-thione-4,5-dithiolate.[3, 4, 10]

More recently, these clusters, $[Mo_3S_{13}]^{2-}$ in particular, have been identified as molecular mimics of the edge sites of molybdenum disulfide (MoS_2).[11] This is significant as the edge sites have been found to be highly-active catalytic centres, compared to the basal plane of the 2D monolayer, towards processes such as the Hydrogen Evolution Reaction (HER).[12-14]

Their functional tunable properties and applications towards hydrogen production make these excellent candidate species to study when under extreme confinement. In this work, thiomolybdate-based clusters are inserted into electrically-conducting SWNTs with diameters of approximately 1 - 2 nm to investigate their structure, composition, and electronic communication between host and guest. In particular, thiomolybdate hexabromide and thio-selenomolybdate hexabromide ($[Bu_4N]_2[Mo_3S_7Br_6]$ and $[Bu_4N]_2[Mo_3S_4Se_3Br_6]$ respectively) are chosen as the presence of terminal bromide ligands will be easily visible and distinguishable during imaging and elemental analysis to examine if they are affected upon encapsulation. Moreover, the substitution of equatorial S atoms for Se atoms will allow the investigation of the different axial and equatorial environments of the bridging ligands. SWNTs are known as nanoreactors which can provide a reservoir of electrons to contribute towards the encapsulation mechanism, as well as the stabilisation of encapsulants and formed quasi-one-dimensional (1D) products.[15] This, coupled with the electron acceptor ability of the thiomolybdate clusters, may lead to interesting host-guest interactions which will be studied using Raman spectroscopy in resonance with different chiralities of SWNTs. Furthermore, inorganic reactions of the clusters with iodine will take

place to investigate if any ligand exchanges or transformations take place to produce new and exciting species caused by the templating effect of the ultrathin SWNT concave channel.

4.2. Results and discussion

4.2.1. Tetrabutylammonium thiomolybdate hexabromide

The first cluster to be investigated within the confinements of SWNTs was thiomolybdate hexabromide $[Mo_3S_7Br_6]^{2-}$. The structure consists of three Mo(IV) centres bonded together to form a Mo_3 triangular core; between each pair of metal centres is a bridging S_2 ligand in which the S atoms are either axial or equatorial to the Mo_3 plane, and each centre is also bonded to two terminal bromide ligands (Figure 4.2).[5, 6] A capping sulfur is bonded in the centre of the Mo_3 structure.

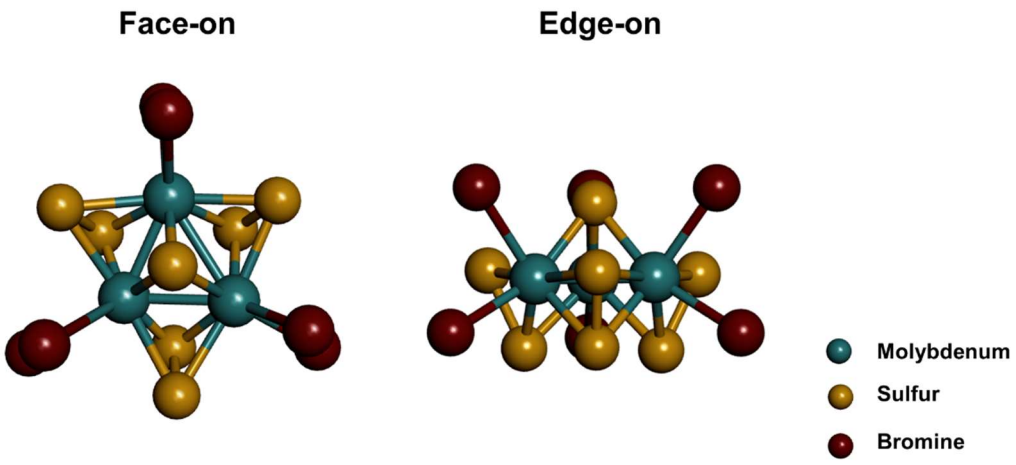


Figure 4.2. *Structural model depicting the $[Mo_3S_7Br_6]^{2-}$ cluster in both the face-on and edge-on projection. Each side of the Mo_3 triangle is bridged by a disulfide ligand and each vertex is bonded terminally to two bromide ligands. A capping sulfur ligand in bonded in the centre of the Mo_3 structure. The blue, yellow and red spheres correspond to molybdenum, sulfur, and bromine atoms respectively.*

4.2.1.1. Insertion of the cluster within SWNTs

$[Bu_4N]_2[Mo_3S_7Br_6]$ was inserted into SWNTs using a solution-phase filling method which required dissolving the compound (Figure 4.3a) in acetonitrile forming a yellow solution (Figure 4.3b); the opened SWNTs were then added to the solution which caused the solution to turn off-yellow/green in colour (Figure 4.3c). The reaction mixture was then filtered after three days to isolate the product.

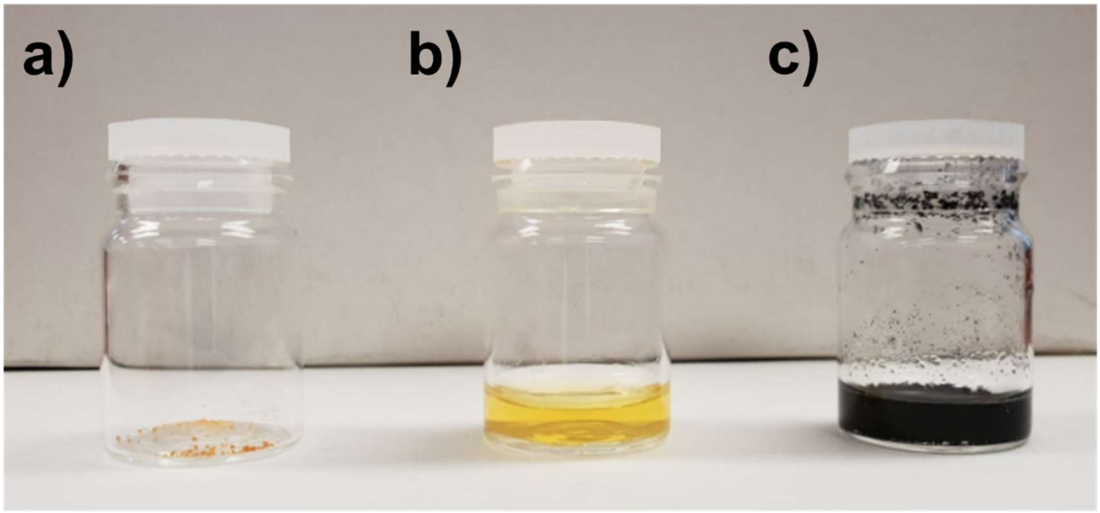


Figure 4.3. *Solution-phase filling method of tetrabutylammonium thiomolybdate hexabromide into SWNTs. (a) $[Bu_4N]_2[Mo_3S_7Br_6]$ presenting as an orange powder; (b) the compound was dissolved in acetonitrile to form a saturated solution that was yellow in colour; (c) opened SWNTs were added to the solution which caused it to turn yellow/green in colour.*

Initial TEM imaging showed that the SWNTs were filled but there was also a high presence of an exterior coating (Figures 4.4a and b). This material during imaging presented itself as a mixture of lower contrast chain-like features and higher contrast elliptical features, the latter of which measured approximately 0.58 x 0.40 nm by TEM image contrast analysis. These distances match with those measured of a structural model of thiomolybdate hexabromide in edge-on orientation with respect to the electron beam (Figure 4.4d), and the observed contrast is representative of the expected contrast of a species containing heavy elements

including molybdenum and bromine. Therefore, the evidence deduces the tetrabutylammonium cation as the source of the chain-like amorphous features as carbon has a lower atomic number than Mo, Br, and S and thus will appear lighter in contrast; moreover, it is comprised of flexible butyl chains which would explain the amorphous features observed in the TEM image (Figures 4.4b and c).

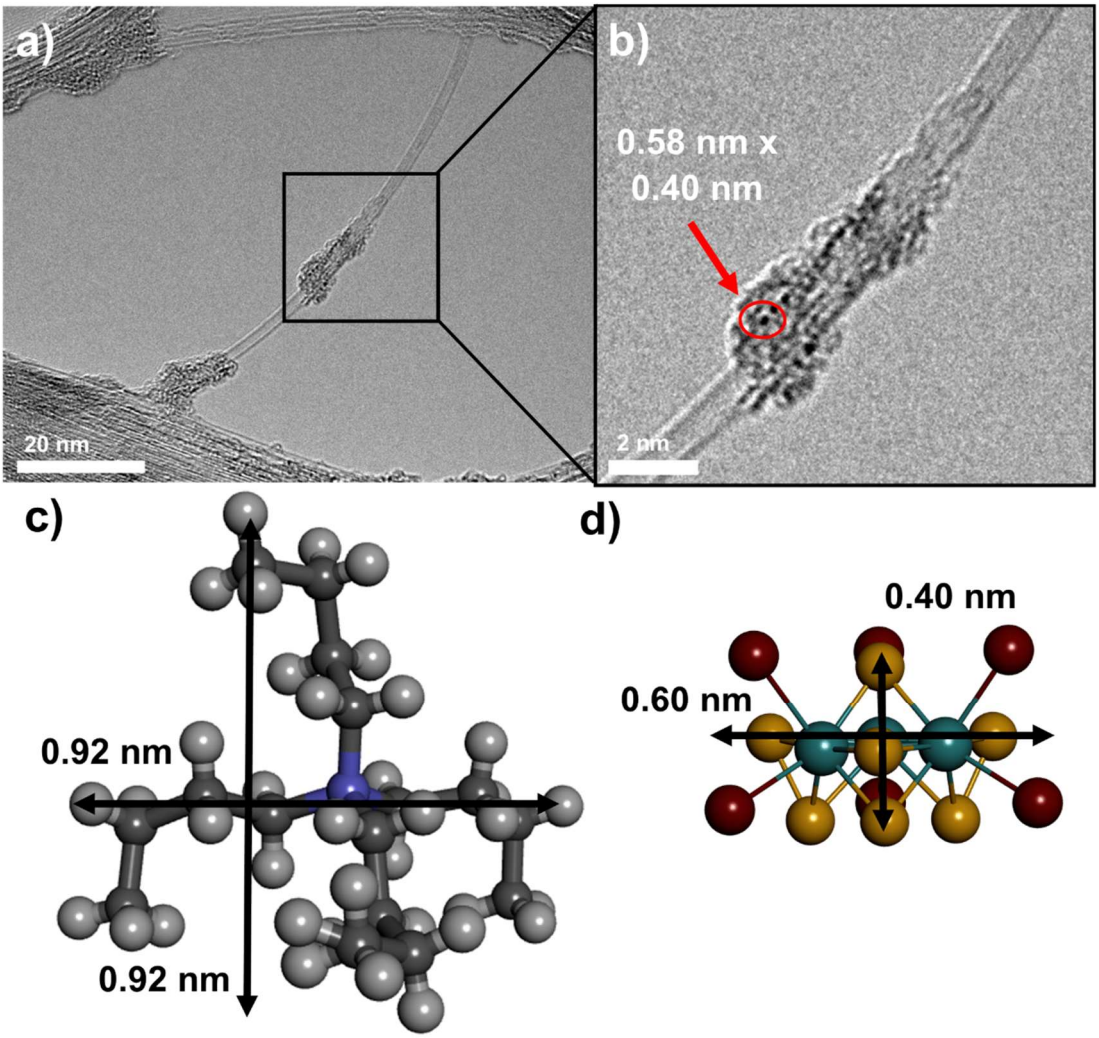


Figure 4.4. *(a) 100 kV TEM image of* $[Bu_4N]_2[Mo_3S_7Br_6]$*@SWNT showing a single nanotube partially-modified with an external coating; (b) digitally-magnified image of (a) which identified the coating as a combination of chain-like and elliptical features (red arrow); (c) structural model of the tetrabutylammonium cation, labelled with the dimensions; (d) structural model of the thiomolybdate hexabromide anion, in edge-on projection, also*

labelled with the dimensions which correlate well with the elliptical features observed in the TEM image.

The sample was cleaned by washing with acetonitrile during the filtration step until the filtered solution turned clear; TEM imaging confirmed the coating around the SWNT had been removed revealing the presence of distinct elliptical and triangular shapes within the SWNT confinements, denoted as $n[Mo_3S_7Br_6]^{2-}$@$SWNT^{2n+}$ (Figure 4.5a). The image displays most of the clusters in close packing confirmed by 2D contrast analysis, measured parallel along the nanotube axis, which recorded a periodic distance of 1.2 nm between the centres of each feature (Figures 4.5b and c). The sizes of each of the different features observed were also measured which were found to be 0.61 x 0.54 nm (elliptical, Figure 4.5d) and 0.61 x 0.63 nm (triangular, Figure 4.5e). Structural models were proposed for the features observed and TEM simulations were conducted on them to correlate against the experimental images. The elliptical feature was found to be the projection of the edge-on orientation of the molecule (Figure 4.5d) as observed previously on the exterior coating of the uncleaned material, whilst the triangular shape was the result of the face-on projection (Figure 4.5e) with the overlap of two bromide ligands producing the high contrast of each vertex of the triangle.

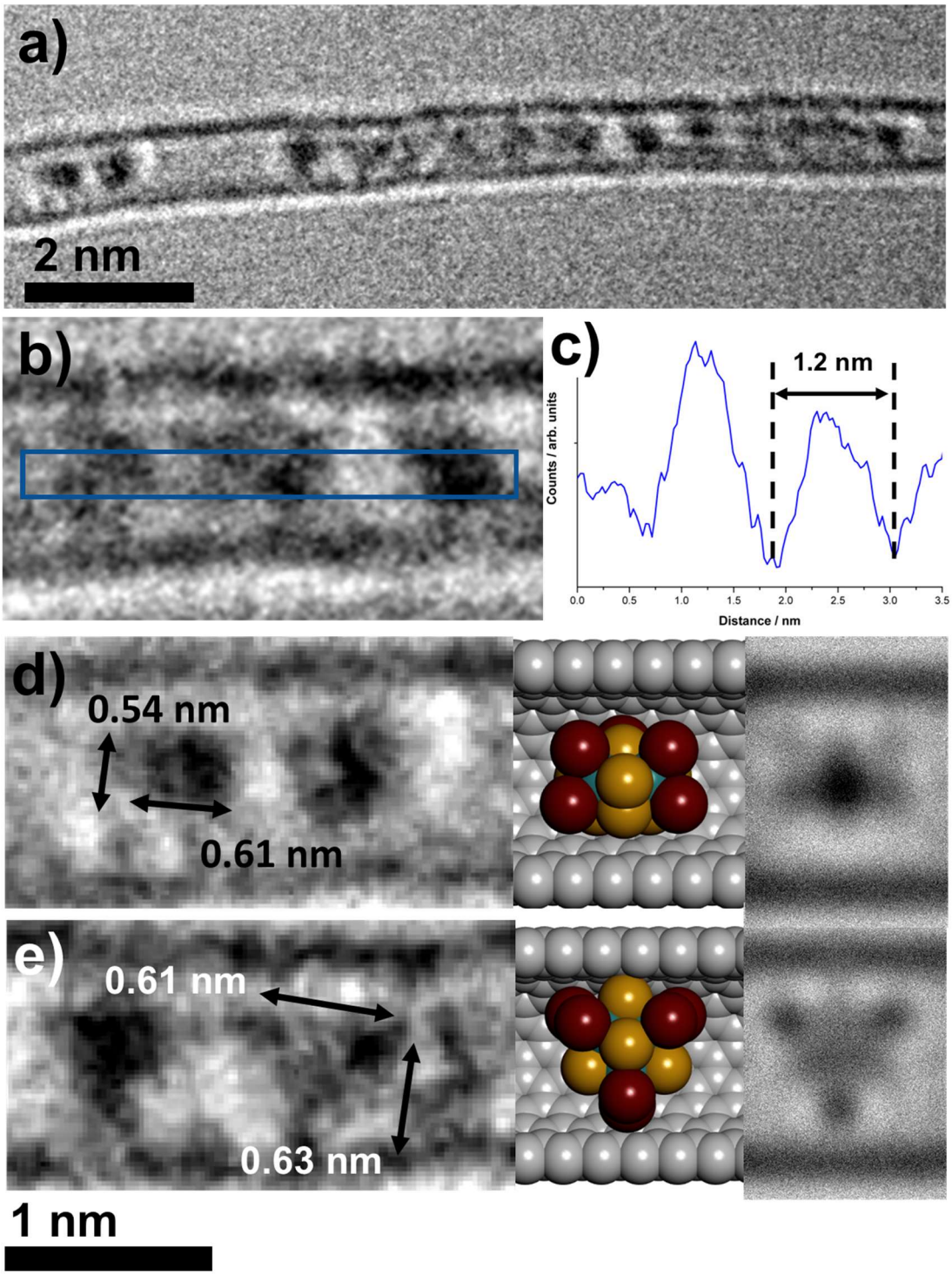


Figure 4.5. *(a) 100 kV TEM image of cleaned* $n[Mo_3S_7Br_6]^{2-}$*@SWNT*$^{2n+}$ *showing the presence of discrete features within a 1.4 nm SWNT; (b) digitally-magnified section of (a) showing the close contact of the clusters; (c) 2D contrast analysis parallel across the features along the nanotube axis in (b) which measures the equidistance clusters separated by 1.2 nm. 100 kV TEM image of two features observed in (d) elliptical projection and (e) triangular projection*

with height and width superimposed (left), structural model of the $[Mo_3S_7Br_6]^{2-}$ cluster in (d) edge-on and (e) face-on orientation with respect to the e-beam within a 1.4 nm SWNT (middle), TEM simulations of corresponding structural models (right).

EDX was conducted over a bundle of filled SWNTs to determine if the composition of the molecule had changed upon encapsulation (Figure 4.6). The spectrum identified the presence of carbon and oxygen from the SWNT hosts, copper from the TEM grid used, as well as Mo, S, and Br from the guest-molecules, and the loss of nitrogen which is indicative of the cation. Overlap of the Mo and S peaks was found resulting in a broad peak and a shoulder section at a slightly higher energy; the individual components were resolved using wave-dispersive x-ray (WDX, Figure 4.6 inset) analysis which revealed the broad overlap to be the result of the Mo Lα, and S Kα peaks at 2.29 and 2.31 keV respectively, and the Mo Lβ and S Kβ at 2.39 and 2.46 keV respectively forming the peak shoulder. The Mo: Br atomic ratio was found to be 1: 2 from EDX,[16] whilst the Mo: S atomic ratio was found to be 3: 7, from WDX, which overall confirms that the composition of the thiomolybdate hexabromide species was not affected upon encapsulation.

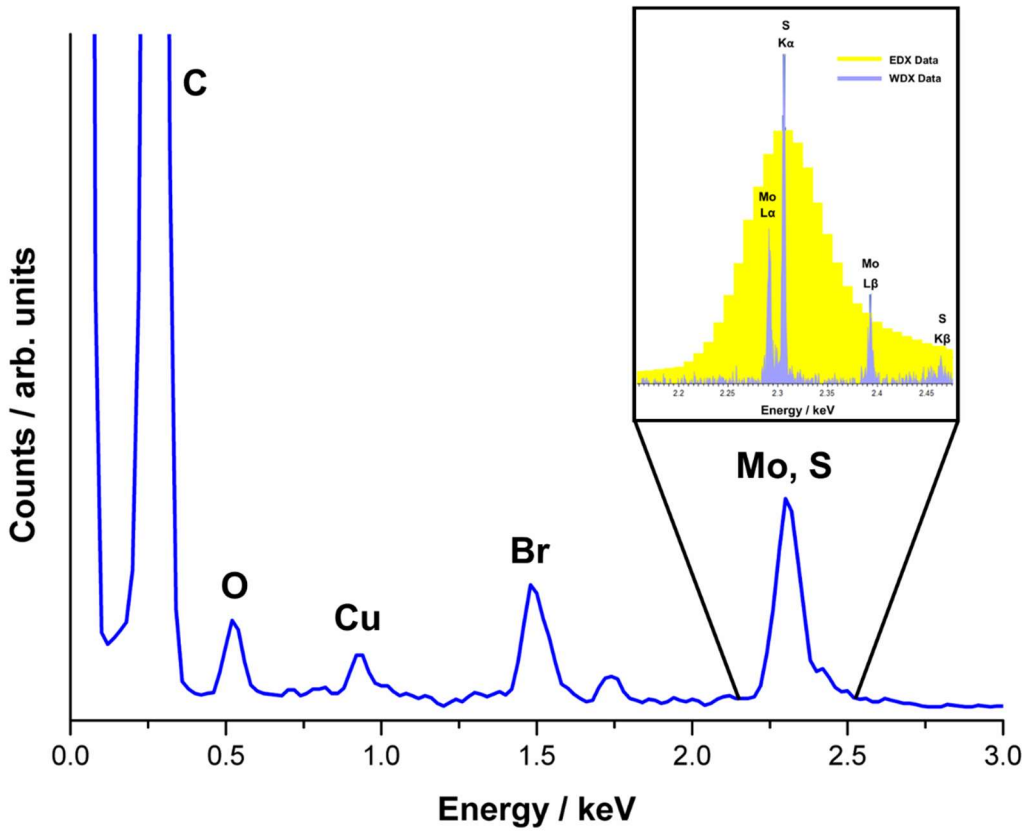


Figure 4.6. *EDX spectrum of cleaned n[$Mo_3S_7Br_6$]$^{2-}$@SWNT^{2n+} displaying the presence of Mo, S and Br from the cluster, as well as C and O from the host SWNTs. The Mo and S peaks are shown to be overlapping. Inset is a WDX spectrum recorded over the Mo and S region which resolved the individual components responsible for the overlap.*

As further evidence, X-ray photoelectron spectroscopy (XPS) measurements were conducted on the composite host-guest material to examine if the chemical state of the component elements of the guest had been affected, by comparing to measurements performed on the parent compound. A high-resolution spectrum, focussed on the Mo 3d region of the compound, showed the presence of three peaks at 232.6, 229.5, and 227.6 eV which were assigned as the doublet of the Mo 3d 5/2 and 3d 7/2, and the overlap with the S 2s peak respectively (Figure 4.7a). These three peaks were all retained in the host-guest system with each of the Mo 3d components being down-shifted by 0.5 eV and the S 2s upshifted by only 0.2 eV (233.1, 230.0, and 227.8 eV for the Mo 3d 5/2, 7/2, and S 2s respectively, Figure 4.7d). The S 2p region of the compound was fitted to four components of two doublets (Figure

4.7b); this is explained by the two different sulfur environments in the anion which are the capping sulfur and the bridging S_2 ligands. The lower intensity, lower energy doublet at 162.9 and 162.0 eV was assigned to the μ_3-capping sulfur whilst the second higher intensity and energy doublet at 164.7 and 163.4 eV was assigned to the μ_2-bridging S_2 ligands. The two sets of doublets were again retained in the spectrum of the host-guest system but were all upshifted by 0.3 - 0.4 eV to 163.2 and 162.4 eV for the μ_3-S, and 165.1 and 163.8 eV for the μ_2-S_2 ligands (Figure 4.7e). Finally, the Br 3d region of the free compound was fitted to a doublet of 3d 5/2 and 3/2 components at 69.0 and 67.9 eV respectively (Figure 4.7c). As with the S peaks, the Br components of the host-guest material had upshifted by 0.3 – 0.4 eV to 69.3 and 68.3 eV (Figure 4.7f). The shifts are not significant enough to suggest that the oxidation state of the elements have changed but are more of a reflection on the environment of the SWNT host, suggesting that it is slightly electron deficient with respect to the guest-molecules.

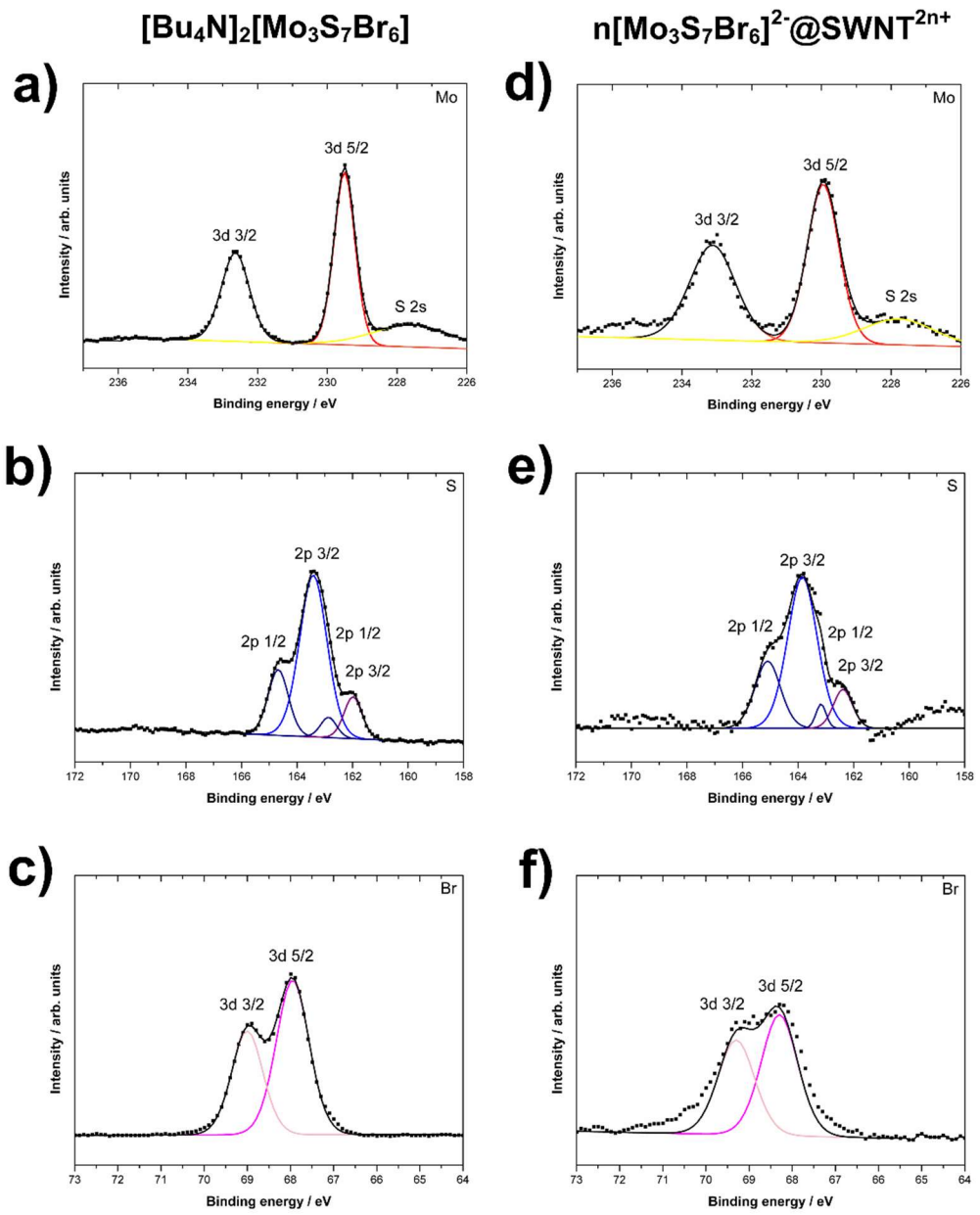


Figure 4.7. *XPS high resolution scans of free $[Bu_4N]_2[Mo_3S_7Br_6]$ focussed on the (a) Mo 3d, (b) S 2p, and (c) Br 3d regions, and $n[Mo_3S_7Br_6]^{2-}@SWNT^{2n+}$ focussed on the (d) Mo 3d, (e) S 2p, and (f) Br 3d regions.*

The sample was then imaged by aberration-corrected high-resolution transmission electron microscopy (AC-HRTEM) which can achieve atomic resolution imaging (Figures 4.8a - f). A time-series over approximately 8 seconds was recorded which displayed four clusters, within a SWNT of 1.3 nm internal diameter, that were found to translate and rotate within the confines of the SWNT. The orientations of the individual clusters in each frame were

determined by comparing to a simulation table that was designed to run TEM simulations of $[Mo_3S_7Br_6]^{2-}$ after sequential rotations in the x and then y directions (Figure 4.9). This library of simulated images could be then directly compared to the projections observed in the experimental AC-HRTEM image. For example, the first frame (Figure 4.8a) shows the four clusters in their initial projections and their assigned orientations (left to right) are given in the general format of (X, Y, Z clockwise rotation) as; (45°, 60°, 60°), (90°, 0°, 180), (0°, 30°, 180°), and (75°, 45°, 0°). As well as rotational motion, the clusters are also shown to translate along the nanotube axis; between sequential images the distance travelled by the clusters was measured and thus the speed could be calculated. For example, between the final two frames, the cluster on the right hand side of the image travelled 5.88 nm in 1.28 seconds achieving a speed of approximately 16,500 nanometres per hour (Figures 4.8e and f).

As an addition to the motions of the clusters, they also experienced reactivity that was triggered by the electron beam resulting in the oligomerisation of two adjacent clusters to form a dimer. This process of the electron beam both activating and capturing a chemical reaction was coined as *ChemTEM* by Chamberlain *et al.* who first used it to study the polycondensation of perchlorocoronene.[17] This technique not only allows control of the amount of energy being provided to the system being studied through control of the electron beam voltage and dose rate, but can also directly image the structures of intermediates formed during the reaction pathway. In the first frame (Figure 4.8a), the clusters are shown as four discrete species, then during the time span of frames 8b and 8c the two clusters on the left hand side appear to be bonded together along the bottom row of atoms by a bridging Br ligand. The mechanism for this reaction is proposed to occur by the 80 kV electron beam transferring up to 1.97 eV to a molybdenum atom of the cluster (Figure 4.8g); this was calculated via the T_{max} equation (Equation 4.1) that determines the maximum amount of energy received by a stationary atom on collision with an electron, and is controlled by the e-beam energy.[17]

$$T_{max} = \frac{2ME(E + 2m_e c^2)}{(M + m_e)^2 c^2 + 2ME}$$

Equation 4.1.

where M – mass of atom, E – energy of the electron beam, m_e – mass of electron, and c – speed of light.

This is enough energy to rupture the Mo-Br bond which leaves the Mo cation coordinatively unsaturated; this causes the molecule to form a bridging bond with a Br ligand from the adjacent molecule recompleting the coordination of the Mo atom. This process occurs during the first three frames (Figures 4.8a – c) and thus it could be proposed that the second frame (Figure 4.8b) shows the unsaturated intermediate. Between the third and fourth frames (Figures 4.8c and d) of the time-series, the process occurs again as demonstrated by the presence of two sets of bridging Br ligands in the image forming a dimer species of $[Mo_3S_7Br_5]_2^{2-}$.

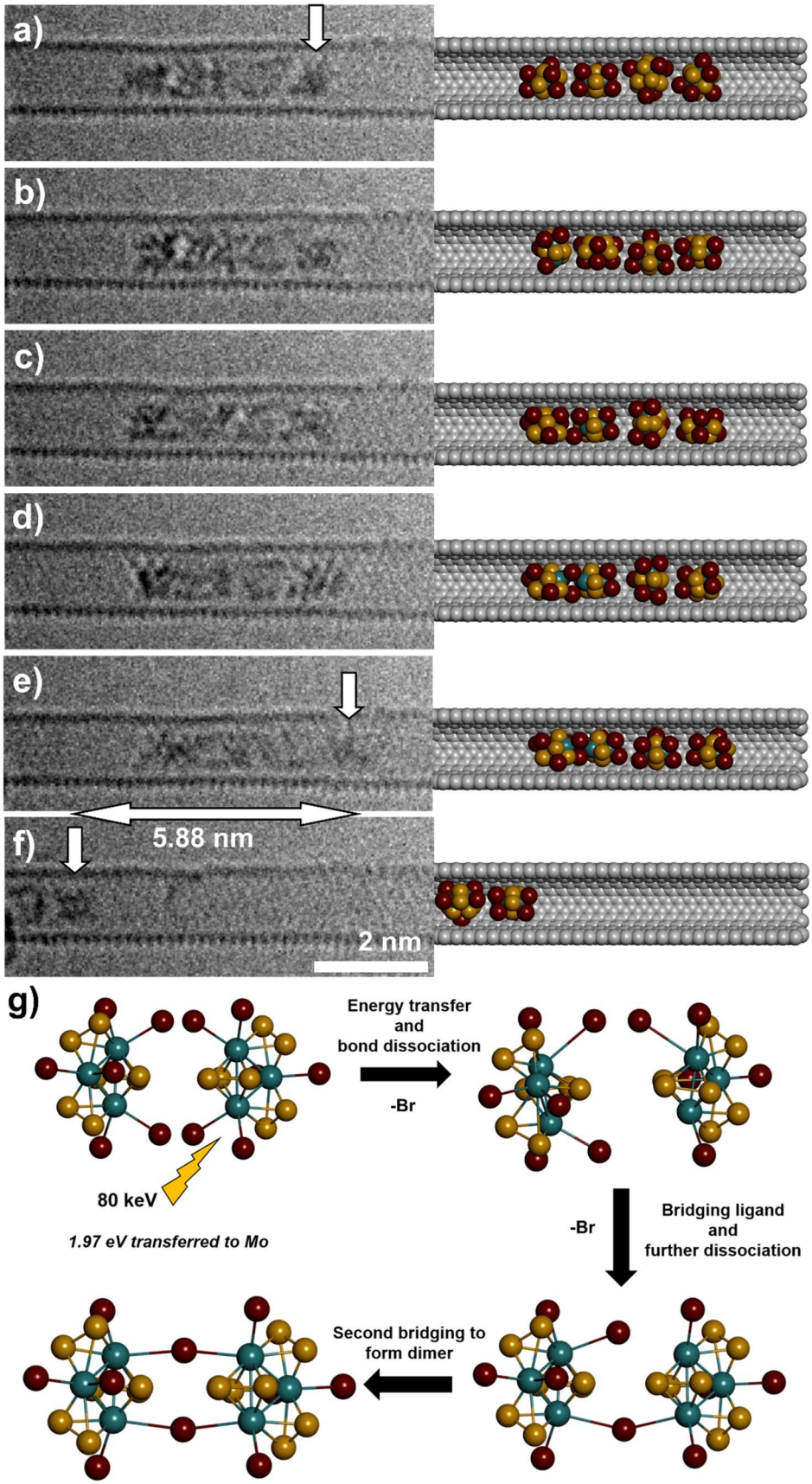


Figure 4.8. *(a - f) 80 kV AC-HRTEM analysis of* $n[Mo_3S_7Br_6]^{2-}$*@SWNT*$^{2+}$ *showing four clusters within the SWNT concave projected in different orientations demonstrated by structural*

models. The molecules are shown to translate along the nanotube axis, and the oligomerisation of adjacent molecules can also be observed; (g) schematic diagram showing the energy transfer from the electron beam causing Mo-Br bond dissociation resulting in the intermolecular bonding via bridging Br bonds.

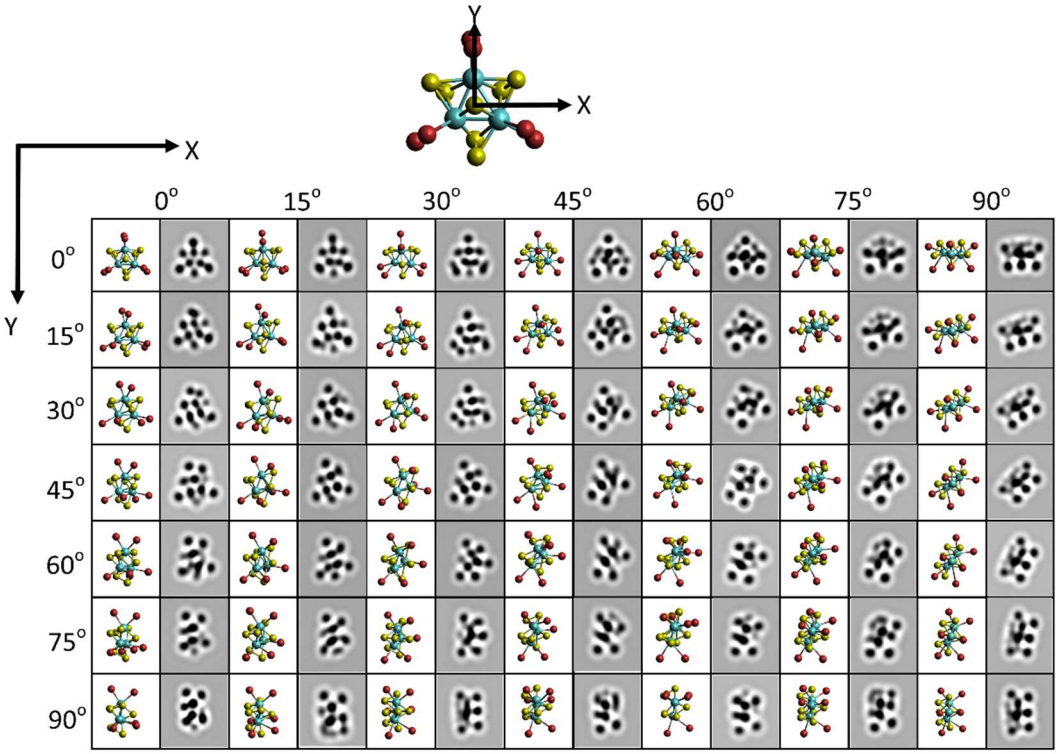


Figure 4.9. *Simulation table of $[Mo_3S_7Br_6]^{2-}$ using 15° rotation steps in the X and then Y direction sequentially.*[15]

Raman spectroscopy was conducted on the $[Mo_3S_7Br_6]^{2-}$ filled SWNT material using 532 and 660 nm excitation laser sources, which are in resonance with semiconducting and metallic SWNTs respectively, in order to investigate their electronic properties. Empty SWNTs were used as a reference to compare and investigate any charge transfer effects by examining any shifts in the graphitic G-band (Table 4.1). The spectrum in resonance with semiconducting SWNTs showed only a +1.1 cm^{-1} shift of the G-band compared to the empty SWNTs; this is below the spectral resolution and thus is not evidence of charge transfer (Figure 4.10a). However, the radial breathing mode (RBM) was blue shifted by +10.6 cm^{-1}, compared to

empty SWNTs, which was partial evidence of filling as the nanotube diameter has undergone a contraction to maximise the van der Waals contacts with the guest species. The spectrum, measured using an excitation in resonance with metallic SWNTs, shows a +3.3 cm^{-1} blue shift of the G-band which indicates electron donation from the SWNT to the $[Mo_3S_7Br_6]^{2-}$ cluster (Figure 4.10b). As further evidence, there was also a slight change in the profile of the G-band resembling a more Lorentzian-type band which suggests a metallic to semiconducting transition due to band gap opening.[18] Therefore this material will be referred to as $n[Mo_3S_7Br_6]^{2-}@SWNT^{2n+}$. The RBM, of metallic SWNTs (Figure 4.10b, Table 4.1), was blue-shifted to a lesser extent (+3.1 cm^{-1}) than for semiconducting SWNTs (Figure 4.10a, Table 4.1), which means that the metallic SWNTs contracted to a lesser degree, and thus are more greatly filled with the guest-species. This indicates that electron-transfer aided encapsulation is the potential pathway for the thiomolybdate hexabromide species and predominantly occurs within metallic SWNTs.

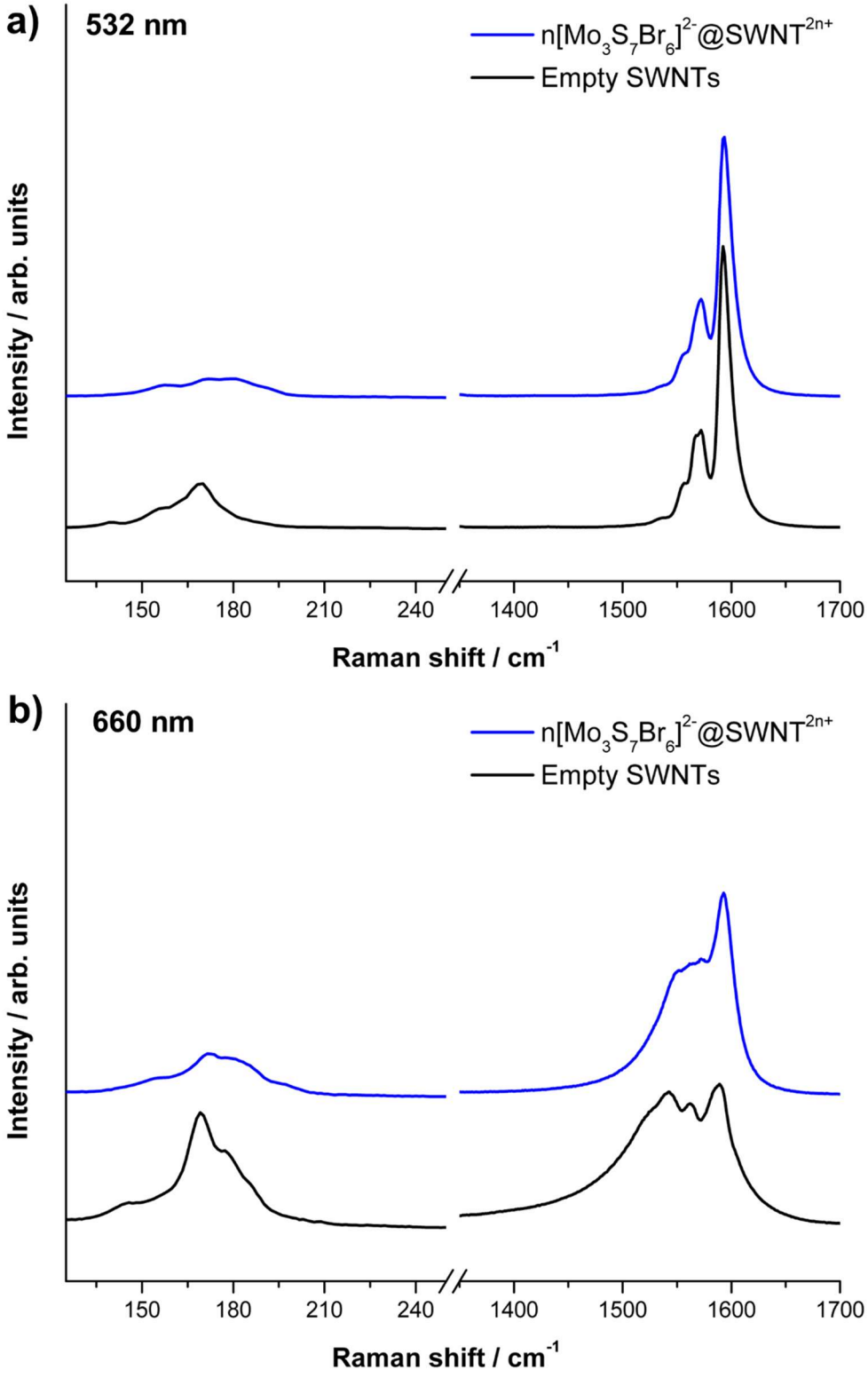


Figure 4.10. *Raman spectra overlay for $n[Mo_3S_7Br_6]^{2-}$@$SWNT^{2n-}$ (blue), and empty SWNTs as reference (black), measured using laser excitations in resonance with (a) semiconducting (532 nm) and (b) metallic (660 nm) SWNTs. The spectra are focussed on the low frequency region*

displaying the RBM of each material, as well as the G-band region. The spectrum in resonance with metallic SWNTs (b) shows a +3.3 cm^{-1} blue shift of the G-band as well as change in the profile of the band to resemble a Lorentzian shape.

Table 4.1. *Raman band positions and shifts for empty SWNTs and $n[Mo_3S_7Br_6]^{2-}@SWNT^{2n+}$ measured using 532 nm and 660 nm laser excitations in resonance with semiconducting and metallic SWNTs respectively.*

Excitation laser used / nm	Material	RBM position / cm^{-1}	Shift w.r.t. empty SWNTs	G-band position / cm^{-1}	Shift w.r.t. empty SWNTs	Electron transfer
532	Empty SWNTs	169.0	-	1592.6	-	-
	$n[Mo_3S_7Br_6]^{2-}@SWNT^{2n+}$	179.6	+10.6	1593.7	+1.1	Below spectral resolution
660	Empty SWNTs	169.0	-	1589.4	-	-
	$n[Mo_3S_7Br_6]^{2-}@SWNT^{2n+}$	172.1	+3.1	1592.7	+3.3	SWNT ➔ $[Mo_3S_7Br_6]^{2-}$

In terms of the full mechanism of encapsulation, it was shown from Raman spectroscopy that $[Mo_3S_7Br_6]^{2-}$ behaves as an electron acceptor. This behaviour has been observed before during the preparation of a range of charge-transfer salts using the bis(ethylenedithio)tetrathiafulvalene (ET) ligand, and was the result of the electrophillic nature of the axial sulfur atoms.[7] Polyoxometalates (POMs) have previously been shown to encapsulate into SWNTs via coulombic attraction caused by an initial electron transfer from host to guest.[19] Thiomolybdate-based compounds are related to POMs as both contain

polynuclear metal centres with chalcogen ligands that have an overall negative charge on the complex. Therefore, following the same mechanism, it is proposed that the metallic SWNTs donate electron density to $[Mo_3S_7Br_6]^{2-}$ resulting in them having a positive charge, $SWNT^{2n+}$, and formation of a reduced $[Mo_3S_7Br_6]^{4-}$ species (Figures 4.11a and b). Native $[Mo_3S_7Br_6]^{2-}$ anions, present in excess in the solution, are then coulombically-attracted to the positively-charged SWNTs and become encapsulated (Figure 4.11c); this results in the SWNTs being the charge balancing cationic species for the anionic guest and thus the reduced $[Mo_3S_7Br_6]^{4-}$ species and $[Bu_4N]^+$ cations are washed away from the SWNT surface during the cleaning step (Figure 4.11d).

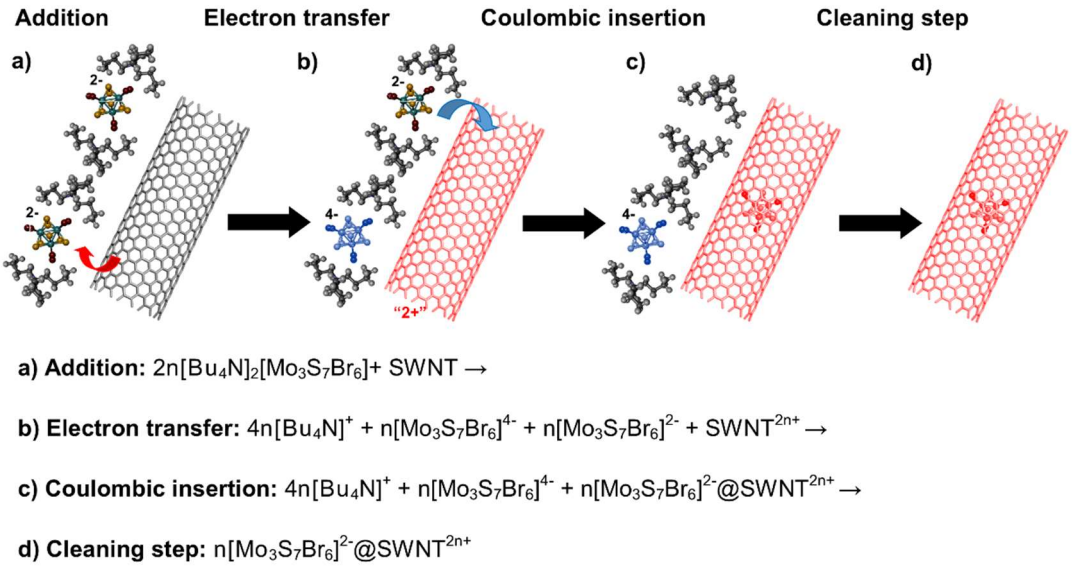


Figure 4.11. *Schematic diagram showing the coulombic force driven insertion mechanism of thiomolybdate clusters into SWNTs. The reaction proceeded by (a) addition of SWNTs to the compound in solution (b) electron transfer from the SWNT hosts to $[Mo_3S_7Br_6]^{2-}$ forming $[Mo_3S_7Br_6]^{4-}$ anions. (c) Native anions, $[Mo_3S_7Br_6]^{2-}$ (present in excess in solution) were then coulombically-attracted to the SWNTs and encapsulated within, leaving cations and reduced anions physisorbed on the exterior. (d) A cleaning step was then introduced to wash away the surface adsorbed species.*

This mechanism proposed not only fits the existing knowledge of thiomolybdate-based anions and related materials,[7, 19] but also correlates well with the analytical data recorded. This includes; Raman spectroscopy observations of charge transfer, EDX and XPS measurements which suggested the composition and oxidation state had not changed upon encapsualtion, and TEM which initially showed the presence of excess cation and anions on the exterior before the washing step was applied, and then only the anions within the SWNT channel after cleaning.

4.2.1.2. Reaction with iodine

After the filling of $[Mo_3S_7Br_6]^{2-}$ into SWNTs was proved to be successful, the next investigation was to encapsulate another species into the filled SWNTs and thermally-activate the system to allow them to undergo a chemical reaction. Iodine is a versatile reagent that can be used to substitute ligands as well as act as a transport agent during chemical vapour transport, in particular for the formation of molybdenum sulphide (MoS_2).[20, 21] This would then either produce an iodide-substituted species or potentially quasi-1D MoS_2 nanoribbons. The initial filling of iodine was achieved by sublimation at 120 ^oC; a temperature pre-determined to cause a solid to vapour transition at a required pressure (10^{-5} mbar).

Upon encapsulation of iodine, Raman spectroscopy, in resonance with semiconducting SWNTs, detected the presence of two new primary peaks at 110 and 175 cm^{-1} which correspond to I_3^- and I_5^- respectively;[22] the latter of which overlaps significantly with the radial breathing mode of SWNTs (Figure 4.12).

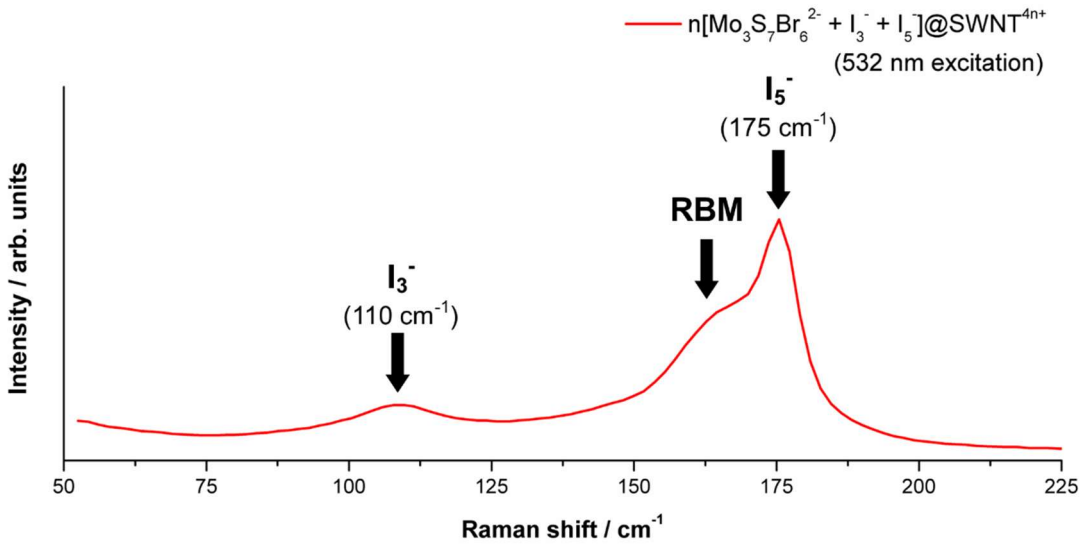


Figure 4.12. *Low-frequency region Raman spectrum of $n[Mo_3S_7Br_6^{2-} + I_3^- + I_5^-]@SWNT^{2n+}$, measured using a 532 nm excitation, highlighting the peaks at 110 and 175 cm^{-1} corresponding to polyiodide ions of I_3^- and I_5^- respectively.*

Moreover, the G-bands of semiconducting and metallic SWNTs were found to have blue shifted by 8.6 and 11.1 cm^{-1} respectively (Figures 4.13a and b, Table 4.2), thus confirming that after encapsulation of iodine, the SWNTs donated electron density to iodine forming polyiodide ions. The G-band of metallic SWNTs also changed profile to signify band gap opening upon charge transfer. This material will thus be referred to as *$n[Mo_3S_7Br_6^{2-} + I_3^- + I_5^-]@SWNT^{4n+}$*.

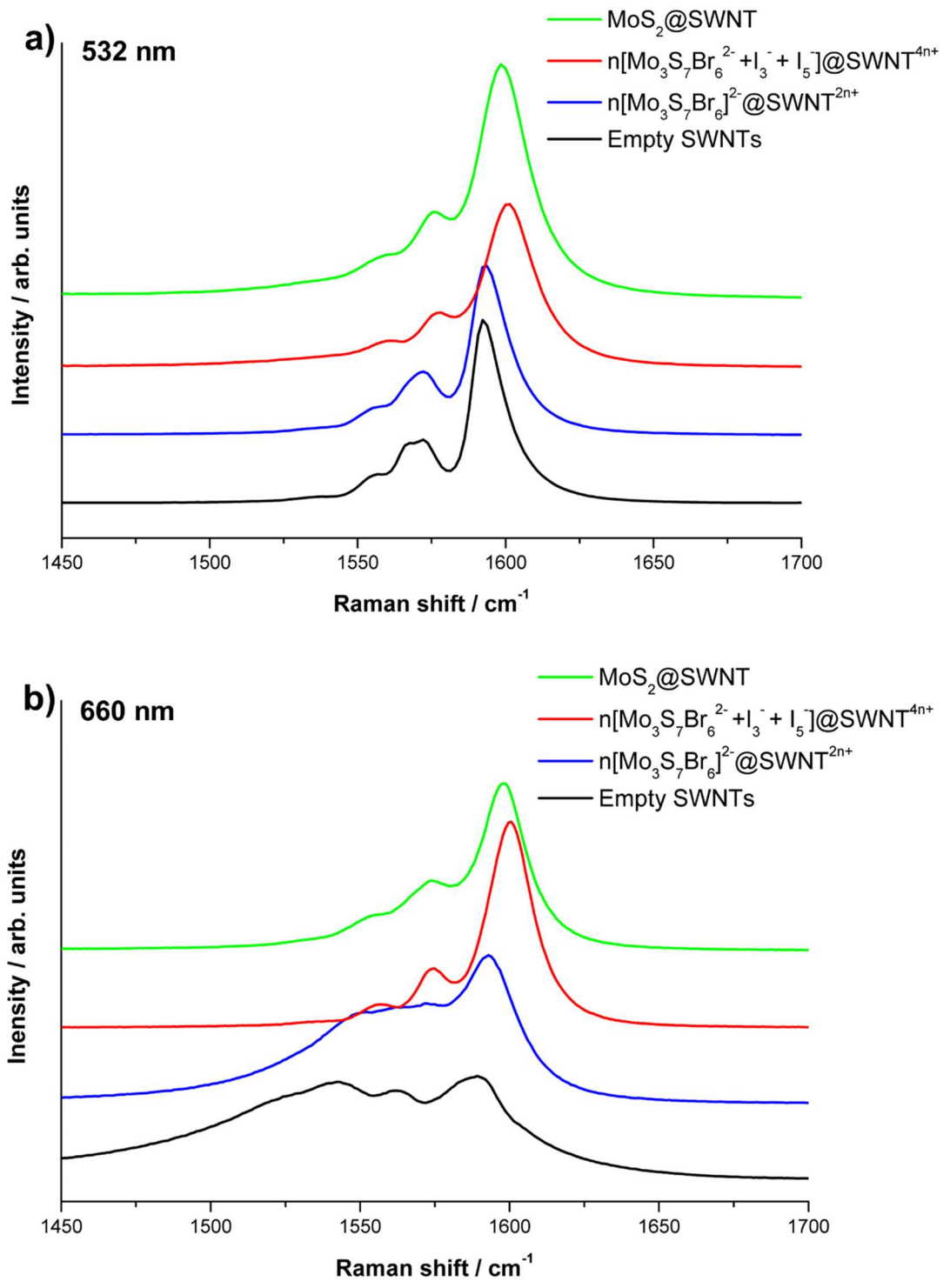


Figure 4.13. *Raman spectra overlay for the encapsulation of $n[Mo_3S_7Br_6]^{2-}$@$SWNT^{2n-}$ (blue), $n[Mo_3S_7Br_6^{2-} + I_3^- + I_5^-]$@$SWNT^{4n+}$(red), and MoS_2@SWNT (green), as well as empty SWNTs as reference (black), measured using laser excitations in resonance with (a) semiconducting (532 nm) and (b) metallic (660 nm) SWNTs.*

Table 4.2. *Raman spectroscopy G-band positions and shifts for empty SWNTs and* $n[Mo_3S_7Br_6^{2-} + I_3^- + I_5^-]@SWNT^{4n+}$*, and after thermal activation to form* MoS_2*@SWNT, measured using 532 nm and 660 nm laser excitations in resonance with semiconducting and metallic SWNTs respectively.*

Excitation laser used / nm	Material	G-band position / cm^{-1}	Shift w.r.t. empty SWNTs	Electron transfer
532	Empty SWNTs	1592.6	-	-
	$n[Mo_3S_7Br_6^{2-} + I_3^- + I_5^-]@SWNT^{4n+}$	1601.2	+8.6	SWNT ➔ I_2
	MoS_2@SWNT	1599.3	+6.7	SWNT ➔ MoS_2 / residual I_2
660	Empty SWNTs	1589.4	-	-
	$n[Mo_3S_7Br_6^{2-} + I_3^- + I_5^-]@SWNT^{4n+}$	1600.5	+11.1	SWNT ➔ I_2
	MoS_2@SWNT	1598.3	+8.9	SWNT ➔ MoS_2 / residual I_2

Upon thermal activation of the system, consisting of heating the material under an inert atmosphere, the G-band of the SWNT hosts red shifted compared to $n[Mo_3S_7Br_6^{2-} + I_3^- + I_5^-]@SWNT^{4n+}$, but was still significantly blue shifted with respect to the empty SWNTs (Figures 4.13a and b, and Table 4.2). The presence of the I_3^- mode was still detected in the spectrum recorded using a 532 nm laser excitation. However, in the spectrum measured using a laser excitation of 660 nm recorded the presence of two new bands in the low-frequency region

at 383 and 408 cm^{-1}, which are characteristic of the E_{2g} and A_{1g} modes of MoS_2 (Figure 4.14).[23, 24] These observations suggests that a transformation of the anionic clusters within the SWNT channel had occurred, after thermal activation, to produce MoS_2 nanostructures, but with additional intercalated iodine/polyiodide present within the SWNTs as well.

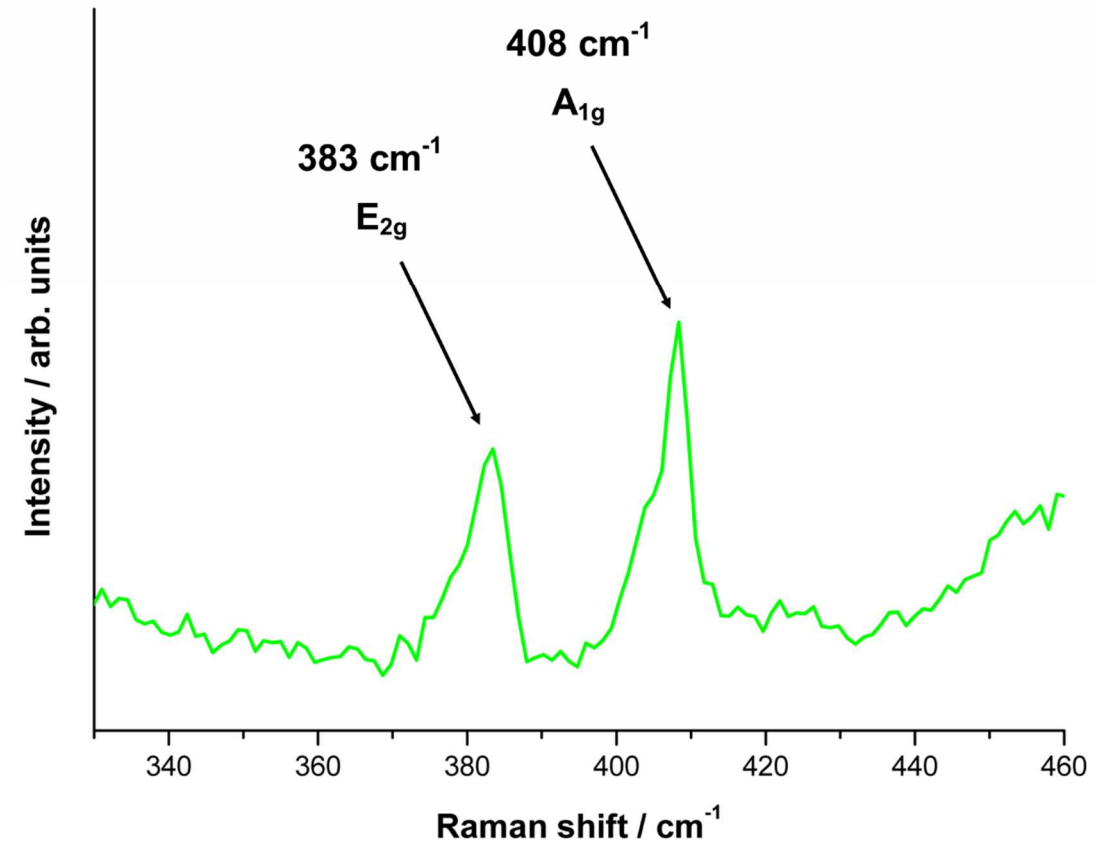


Figure 4.14. *Low frequency region of Raman spectrum of MoS_2@SWNT, recorded using a laser excitation of 660 nm. Bands at 383 and 408 cm^{-1} correspond to the E_{2g} and A_{1g} modes of MoS_2.*

TEM imaging of the MoS_2@SWNT showed bundles of SWNTs filled with high contrast extended nanostructures (Figure 4.15a). AC-HRTEM was able to identify the presence of a MoS_2 nanoribbon in face-on orientation with the characteristic Mo…Mo interatomic distance of 0.32 nm (Figure 4.15b). The image displays the hexagonal lattice of MoS_2 that is three molybdenum atoms in thickness and in a zigzag edge configuration and thus can be described as a 3ZMoS_2NR. The nodes of the hexagons in the structure were shown to display an

alternate contrast pattern which is expected for MoS_2 as two sulfur atoms in projection (Z = 2 x 16 = 32) produce lower contrast than one molybdenum atom (Z = 42). A structural model of a 3ZMoS_2NR within a (11,11) SWNT was constructed and a TEM simulation was performed in order to verify the identification of the nanostructure (Figure 4.15b). The TEM simulation confirmed the observed hexagonal lattice as well as the alternate contrast pattern. EDX analysis was conducted over a bundle of filled SWNTs (Figure 4.15c) and identified the presence of molybdenum and sulfur in a near 1:2 atomic ratio (0.28: 0.51 atomic %), which is lower than the 3:7 atomic ratio of $[Mo_3S_7Br_6]^{2-}$, along with the loss of bromine (0.03 atomic %) as a result of the transformation. This lower Mo: S stoichiometry strongly suggests that the capping sulfur is lost during the reaction, as well as the six bromide ligands which results in the correct stoichiometry to form MoS_2. However, a high amount of iodine (1.37 atomic %) was detected and strongly suggests that iodine as well acting as a vapour transport agent for the formation of MoS_2 has intercalated into any free space within the SWNT hosts in the form of polyiodide but was not witnessed during TEM imaging. Cleaning steps including sublimation and washing with chloroform were attempted but did not significantly lower the level of iodine in the system due to the strong coulombic attractions between the host and guest.

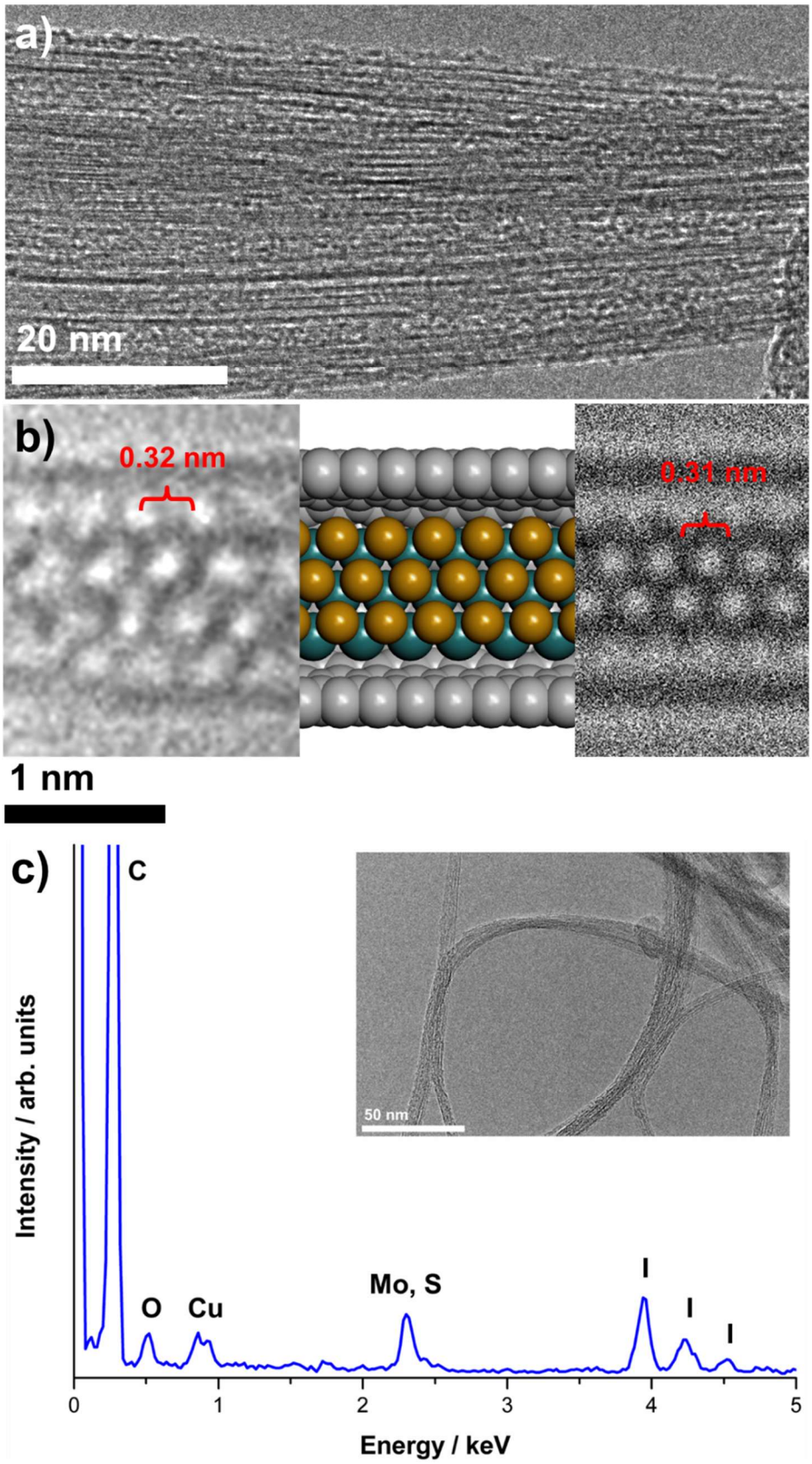


Figure 4.15. *(a) 200 kV TEM image of MoS_2@SWNT showing a large bundle of filled SWNTs; (b) 80 kV AC-HRTEM image of a section of a MoS_2 nanoribbon in face-on orientation within a*

SWNT clearly displaying the hexagonal lattice (left), structural model depicting a 3ZMoS_2NR within a (11,11) SWNT (middle), TEM simulation of the structural model displaying the same hexagonal lattice as in the experimental image (right); (c) EDX spectrum recorded over a bundle of filled SWNTs (inset TEM image) which shows the presence of Mo and S in a near 1:2 atomic ratio, as well as a high level of intercalated iodine.

4.2.2. Tetrabutylammonium thio-selenomolybdate hexabromide

The next thiomolybdate-based cluster to be investigated was thio-selenomolybdate hexabromide, $[Mo_3S_4Se_3Br_6]^{2-}$, which was formed upon reaction of $[Mo_3S_7Br_6]^{2-}$ with $SePPh_3$ to cause selective substitution of the equatorial bridging sulfur atoms.[9] The substitution of half of the sulfur atoms in the disulfide ligands for selenium atoms results in bridging S-Se ligands that should produce higher contrast in TEM and allow them to be easily distinguished (Figure 4.16). Moreover, the product of the reaction of the cluster with iodine has three possible pathways for formation of either MoS_2, $MoSe_2$, or the mixed chalcogenide MoSSe and these can be distinguished using a combination of TEM, EDX, and XPS.

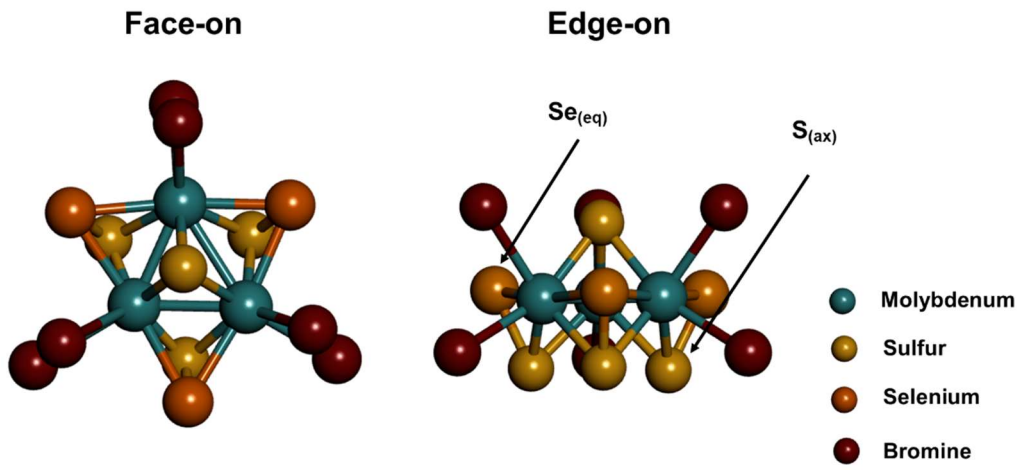


Figure 4.16. *Structural model of the $[Mo_3S_4Se_3Br_6]^{2-}$ cluster shown in face-on and edge-on projections. The equatorial sulfur atoms of $[Mo_3S_7Br_6]^{2-}$ are substituted for selenium atoms*

resulting in bridging S-Se ligands. The blue, yellow, orange, and red spheres correspond to molybdenum, sulfur, selenium, and bromine atoms respectively.

4.2.2.1. Insertion of the cluster within SWNTs

The insertion of $[Mo_3S_4Se_3Br_6]^{2-}$ into SWNTs was achieved using a solution-phase filling method which dissolved the compound in acetonitrile to produce a red/orange solution (Figure 4.17a). Upon addition of opened SWNTs, the solution turned to a yellow/green colour, which may be evidence of charge transfer between the host and guest species (Figure 4.17b). Following from previous analysis of $n[Mo_3S_7Br_6]^{2-}@SWNT^{2+}$ which showed that without cleaning, excess compound was physisorbed onto the surface of the SWNTs; this filling procedure was also followed by a cleaning step to remove excess material, the product was then isolated by filtration.

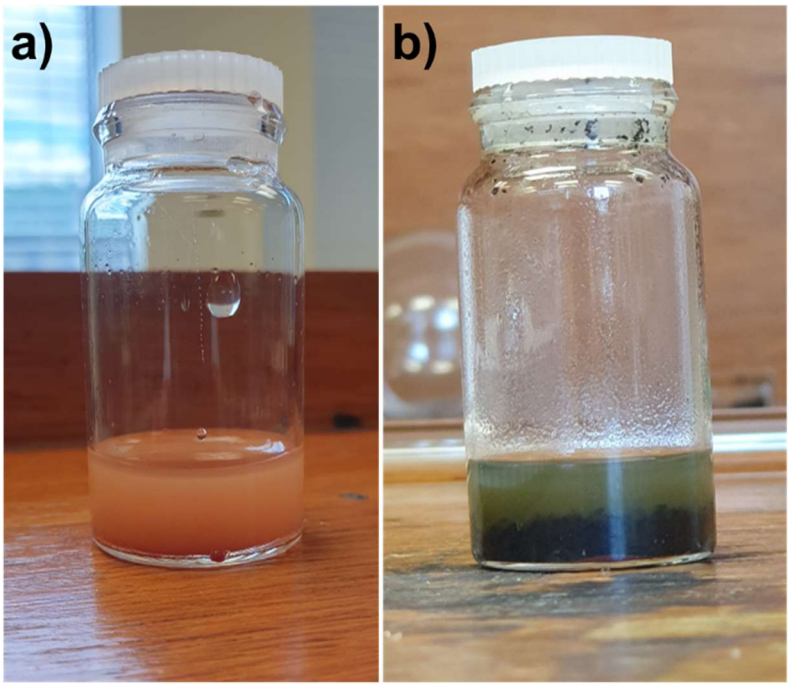


Figure 4.17. *The solution-phase filling of $[Mo_3S_4Se_3Br_6]^{2-}$ into SWNTs via (a) $[Bu_4N]_2[Mo_3S_4Se_3Br_6]$ dissolved in acetonitrile which produced a red/orange coloured solution; (b) addition of SWNTs to the solution which causes it to turn yellow/green in colour.*

TEM imaging showed high filling throughout the sample with the anions appearing as high contrast elliptical features; this was spotlighted using a bundle of filled SWNTs (Figure 4.18a). EDX was measured over the bundle and identified the presence of carbon (SWNTs), oxygen (TEM grid and SWNTs), copper (TEM grid), and molybdenum, sulfur, selenium, and bromine all from the guest species (Figure 4.18b). The peaks of molybdenum and sulfur were once again overlapped, as observed for $n[Mo_3S_7Br_6]^{2-}$@$SWNT^{2n+}$, also overlapped were selenium and bromine between 1.3 – 1.6 keV. Both sets of overlapped peaks were resolved using WDX which found the Se/Br peak to be comprised of components from; Se Lα and Lβ, as well as Br Lα and Lβ (Figure 4.18b inset). The atomic ratio of Mo: S: Se: Br, recorded using WDX, was found to be 3.0: 4.3: 2.4: 7.2 which is close to the expected ratio and suggests the cluster had retained its chemical composition.

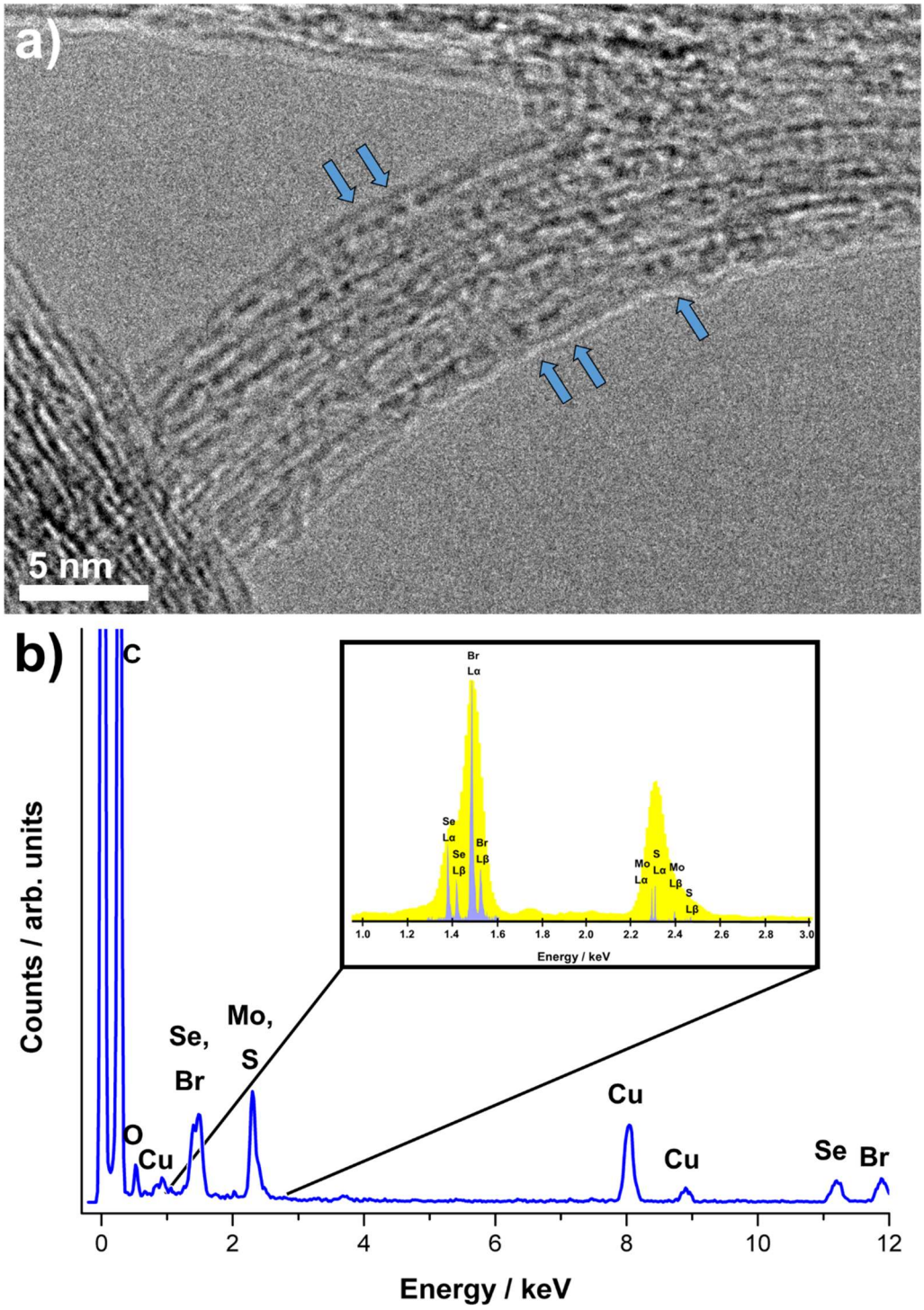


Figure 4.18. *(a) 100 kV TEM image showing a bundle of SWNTs filled with* $[Mo_3S_4Se_3Br_6]^{2-}$ *anions; superimposed on the image are blue arrows indicate examples of the guest-molecules); (b) EDX spectrum of the bundle of filled SWNTs identifying the presence of Mo, S, Se, and Br in the sample. Inset is a WDX spectrum focussed on the 1.0 – 3.0 keV region resolving the overlap of the Mo and S, and Se and Br overlapping component peaks.*

XPS was conducted on the filled SWNTs which was compared against the parent compound for reference and examine any encapsulation effects. The Mo 3d region of the free compound showed the presence of a doublet at 229.4 and 232.5 eV for the 3/2 and 5/2 components respectively; there was also an overlap with the S 2s peak at 226.7 eV (Figure 4.19a). The Mo 3/2 peak was found to be upshifted by 0.6 eV upon filling into SWNTs, and there was also the presence of a second lower intensity doublet at 231.3 and 235.9 eV which may be attributed to a small amount of material physisorbed onto the SWNT exterior surface (Figure 4.19e). The S 2p region of the parent compound was fitted to two sets of doublets (161.8, 162.8, and 163.4, 164.5 eV) as well as a doublet from the overlapping Se 3p (160.9, 167.3 eV, Figure 4.19b). The two separate components are the result of the capping sulfur and the sulfur of the thio-seleno bridging ligands; these were all retained but upshifted in the n$[Mo_3S_4Se_3Br_6]^{2-}$@$SWNT^{2n+}$ spectrum by between 0.6 – 1.0 eV (162.8, 163.4, and 164.0, 165.1 eV, Figure 4.19f). The Se 3d and Br 3d regions were each fitted to a doublet at 55.2 and 56.0 eV for Se (Figure 4.19c), and 67.9 and 68.9 eV for Br (Figure 4.19d). These were both upshifted by 0.9 – 1.0 eV to 56.1 and 57.0 eV for Se (Figure 4.19g), and 68.9 and 69.9 eV for Br (Figure 19h). This correlates well with the shifts observed for n$[Mo_3S_7Br_6]^{2-}$@$SWNT^{2n+}$.

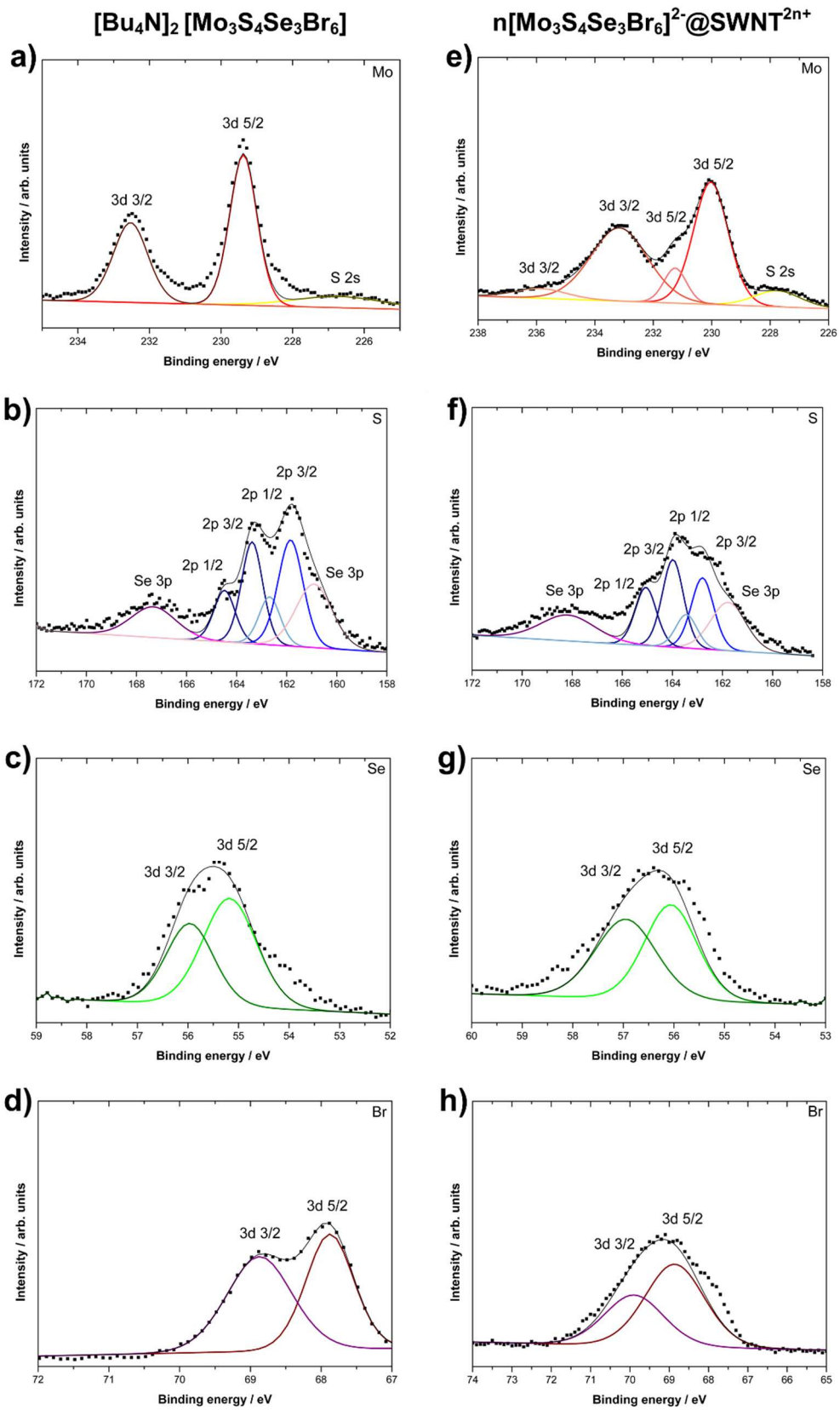


Figure 4.19. *XPS high resolution scans of $[Bu_4N]_2[Mo_3S_4Se_3Br_6]$ focussed on the (a) Mo 3d, (b) S 2p, (c) Se 3d, and (d) Br 3d regions. XPS high resolution scans of $n[Mo_3S_4Se_3Br_6]^{2-}@SWNT^{2n+}$ focussed on the (e) Mo 3d, (f) S 2p, (g) Se 3d, and (h) Br 3d regions.*

Aberration-corrected TEM was used to examine the orientations of the guest-molecules within the SWNT inner channel; however, a time series of images taken over 180 seconds shows them as blurry features which do not exhibit atomistic detail (Figures 4.20a - d). This indicates that the molecules are rotating rapidly within the 1.5 nm SWNT channel at a speed faster than the acquisition time (0.5 s) of the AC-HRTEM which was not observed for the $[Mo_3S_7Br_6]^{2-}$ anions. This may be rationalised by the main difference between the two species which is the substitution of the equatorial sulfur atoms for selenium. This asymmetry of chalcogenides in the S/Se ligands is proposed to lead to rotational motion on collision with electrons from the e-beam. The fast translational motion of the clusters which was observed for $n[Mo_3S_7Br_6]^{2-}@SWNT^{2n+}$ was also exhibited by $n[Mo_3S_4Se_3Br_6]^{2-}@SWNT^{2n+}$, as well as the formation of dimers and further polymeric structures (Figures 4.20c and d). The images show the structures in close contact bonded together by Br ligands witnessed along the bottom of each molecule. These oligomerisation processes are triggered by the electron beam causing the rupture of the Mo-Br bonds causing unsaturated Mo centres to bond with adjacent molecules via bridging bromide ligands.

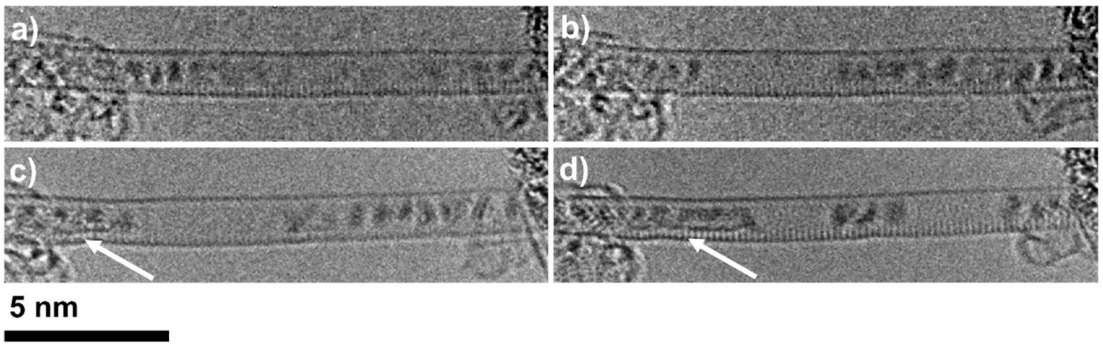


Figure 4.20. *60 kV AC-HRTEM image series of* $n[Mo_3S_4Se_3Br_6]^{2-}@SWNT^{2n+}$ *taken over approximately three minutes. The frames are recorded at (a) 0 s, (b) 13 s, (c) 137 s and (d) 179 seconds with an exposure time of 0.5 seconds. The images show the presence of discrete molecules within the SWNT interior channel but are not shown to be atomically-resolved due to fast rotational motion. Frames (c) and (d) show extended structures (indicated by the white arrows); this is the result of oligomerisation triggered by the electron beam.*

Upon insertion of the cluster into the SWNTs, the G-band, in resonance with semiconducting SWNTs, was found to only undergo a small blue shift (+0.7 cm^{-1}) which is below the spectral resolution (Figure 4.21a and Table 4.3). However, the spectrum in resonance with metallic SWNTs measured a +4.0 cm^{-1} blue shift indicating charge transfer from the SWNT host to the cluster guests (Figure 4.21b and Table 4.3). Also noted was a profile change of the band to resemble a semiconducting G-band profile which provides further evidence of the donor properties of the metallic SWNTs to cause band gap opening. These phenomena correlate well with observations recorded with the filling of $[Mo_3S_7Br_6]^{2-}$ into both types of SWNTs including the extent of G-band blue shift for metallic SWNTs, and thus that the filling of the thio-seleno variant occurs via the same coulombic attraction mechanism. The RBM positions of $n[Mo_3S_4Se_3Br_6]^{2-}$@$SWNT^{2n+}$, compared to empty SWNTs, were found to record relatively low shifts (-2.3 and +1.5 cm^{-1} for semiconducting and metallic SWNTs respectively), compared to empty SWNTs, and thus filling had minimal effect on the SWNT diameter upon filling (Figures 4.21a and b, Table 4.3).

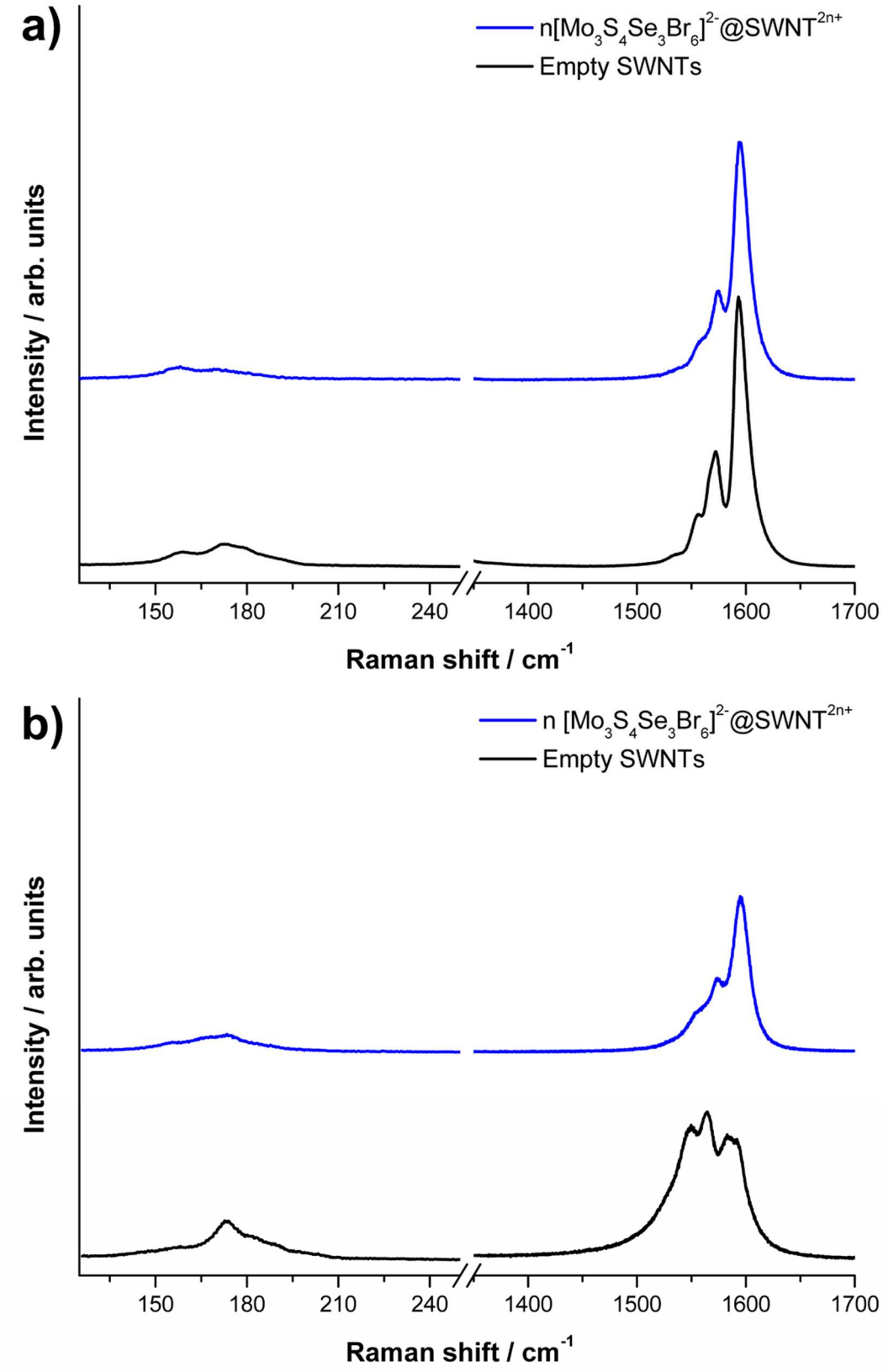


Figure 4.21. *Raman spectra of $n[Mo_3S_4Se_3Br_6]^{2-}@SWNT^{2n+}$ (blue) and empty SWNTs as reference (black) recorded using (a) 532 nm and (b) 660 nm laser excitations in resonance with semiconducting and metallic SWNTs respectively. The 660 nm spectrum exhibits a +4.0*

cm-1 blue shift of the G-band compared to empty SWNTs signifying charge transfer from the SWNT hosts to the $[Mo_3S_4Se_3Br_6]^{2-}$ clusters.

Table 4.3. *Raman band positions for empty SWNTs and $n[Mo_3S_4Se_3Br_6]^{2-}@SWNT^{2n+}$ measured using 532 nm and 660 nm laser excitations in resonance with semiconducting and metallic SWNTs respectively.*

Excitation laser used / nm	Material	RBM position / cm^{-1}	Shift w.r.t. empty SWNTs	G-band position / cm^{-1}	Shift w.r.t. opened SWNTs	Electron transfer
532	Empty SWNTs	172.8	-	1593.8	-	-
	$n[Mo_3S_4Se_3Br_6]^{2-}@SWNT^{2n+}$	170.5	-2.3	1594.5	+ 0.7	Below spectral resolution
660	Empty SWNTs	171.5	-	1591.6	-	-
	$n[Mo_3S_4Se_3Br_6]^{2-}@SWNT^{2n+}$	173.0	+1.5	1595.6	+4.0	SWNT ➔ $[Mo_3S_4Se_3Br_6]^{2-}$

4.2.2.2. Reaction with iodine

As observed for the $[Mo_3S_7Br_6]^{2-}$ cluster, insertion of iodine into the $n[Mo_3S_4Se_3Br_6]^{2-}@SWNT^{2n+}$ resulted in a blue-shift of the G-band of both semiconducting and metallic SWNTs by 4.3 and 7.7 cm^{-1} respectively (Figures 4.22a and b, Table 4.4). Also noted was the presence of polyiodide ion (I_3^- and I_5^-) bands at 109 and 175 cm^{-1}; this is all in good agreement with the SWNTs donating electrons to iodine forming polyiodide ions. Thermal activation of the system caused a red shift of the G-band of both types of SWNTs by 1.4 and 1.7 cm^{-1}

(semiconducting and metallic respectively), in comparison to the positions for n[$Mo_3S_4Se_3Br_6^{2-}$ + I_3^- + I_5^-]@$SWNT^{4n+}$ (Figures 4.22a and b, Table 4.4); also accompanied was the loss of the I_5^- band at 175 cm^{-1}. However, the G-band was still blue shifted compared to empty SWNTs thus showing the encapsulated nanostructures are accepting electron density from the SWNTs but to a lesser degree than observed for MoS_2@SWNT earlier. This may be a result of either; the produced structure behaving as a better electron acceptor, or a lower amount of residual iodide entrapped within the SWNTs. This will be later explored during EDX analysis.

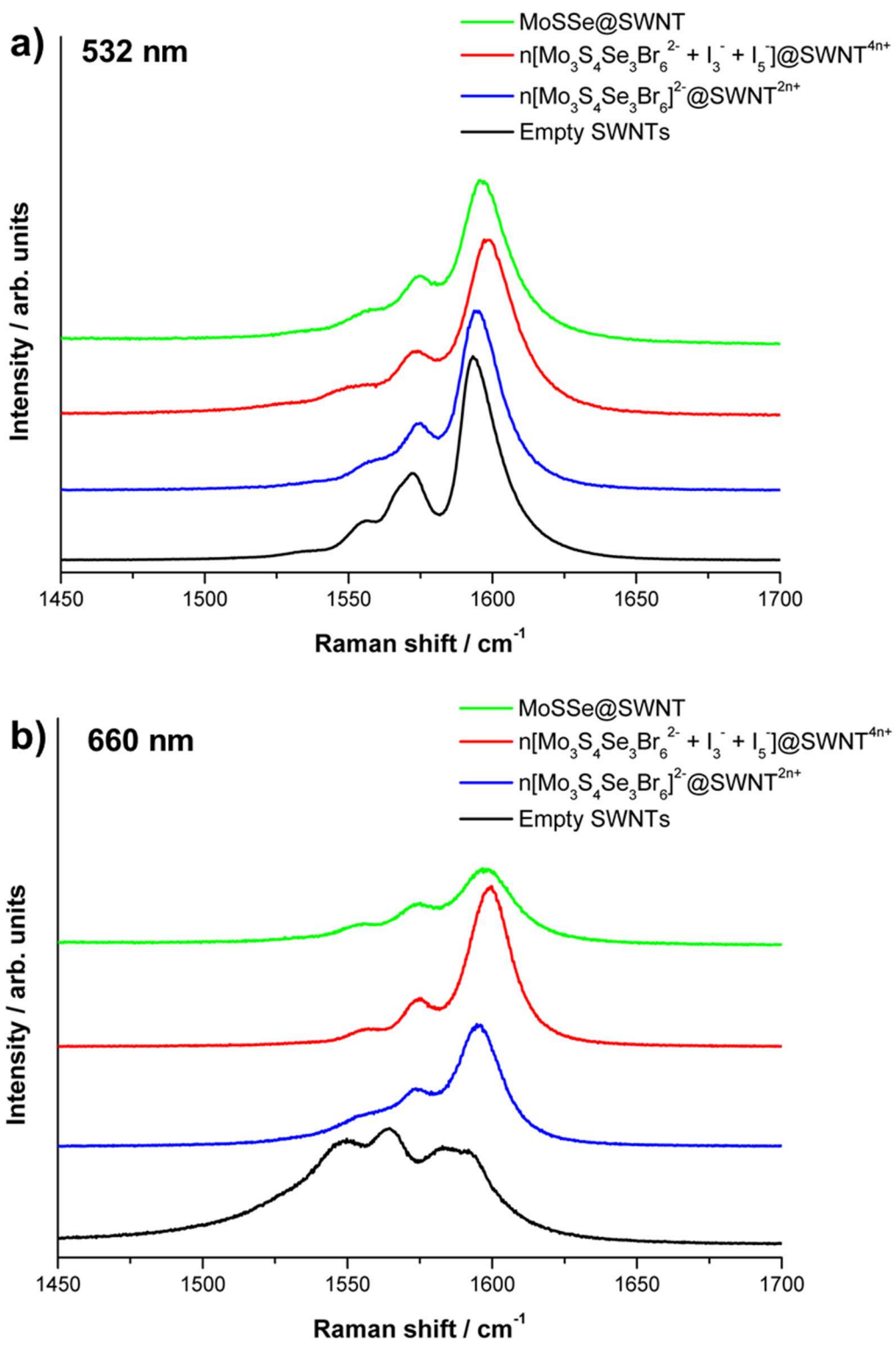


Figure 4.22. *Raman spectra of each step of the stepwise synthesis; $n[Mo_3S_4Se_3Br_6]^{2-}$ @$SWNT^{2n+}$ (blue), ; $n[Mo_3S_4Se_3Br_6^{2-} + I_3^- + I_5^-]$@$SWNT^{4n+}$ (red), MoSSe@SWNT (green), and opened SWNTs as reference (black) recorded using (a) 532 nm and (b) 660 nm laser excitations in resonance with semiconducting and metallic SWNTs respectively.*

Table 4.4. *Raman band positions for $n[Mo_3S_4Se_3Br_6^{2-} + I_3^- + I_5^-]@SWNT^{4n+}$, MoSSe@SWNT, and empty SWNTs, measured using 532 nm and 660 nm laser excitations in resonance with semiconducting and metallic SWNTs respectively.*

Excitation laser used / nm	Material	G-band position / cm^{-1}	Shift w.r.t. opened SWNTs	Electron transfer
532	Empty SWNTs	1593.8	-	-
	$n[Mo_3S_4Se_3Br_6^{2-} + I_3^- + I_5^-]@SWNT^{4n+}$	1598.1	+4.3	SWNT ➔ I_2
	MoSSe@SWNT	1596.7	+2.9	SWNT ➔ MoSSe / residual I_2
660	Empty SWNTs	1591.6	-	-
	$n[Mo_3S_4Se_3Br_6^{2-} + I_3^- + I_5^-]@SWNT^{4n+}$	1599.3	+7.7	SWNT ➔ I_2
	MoSSe@SWNT	1597.6	+6.0	SWNT ➔ MoSSe / residual I_2

TEM imaging showed a transformation of the encapsulated species from discrete trinuclear clusters to continuous nanoribbons (Figure 4.23a). The TEM image shows two nanoribbons in edge-on orientation within two adjacent SWNTs of between 1.0 and 1.1 nm internal diameters. An initial observation of the nanoribbons showed them to exhibit asymmetrical contrast perpendicular to the nanotube axis with the top of each nanoribbon appearing higher in contrast than the bottom; this was confirmed by 2D contrast analysis perpendicular across both filled SWNTs (Figure 4.23b). The contrast plot showed that the highest contrast

of each nanoribbon was not directly in the centre of each SWNT but instead closer to the top of the nanotube wall.

EDX analysis, recorded over a bundle of filled SWNTs, identified Mo, S and Se in a near 1:1:1 stoichiometry (Mo: S: Se in 0.98: 1.03: 1.04 atomic %), as well as the loss of bromine (0.09 atomic %) and a small amount of residual iodine (0.57 atomic %) from the thermal activation step (Figure 4.23c). The proportion of iodine remaining in the system compared to the constituent elements of the nanoribbon was far lower than observed for the thermal activation of $n[Mo_3S_7Br_6^{2-} + I_3^- + I_5^-]@SWNT^{4n+}$; this is thought to be caused by the slightly larger size of $[Mo_3S_4Se_3Br_6]^{2-}$ which restricts a higher amount of iodine entering the SWNTs. This stoichiometry indicates that the reaction has produced a MoSSe-type species which can be narrowed down to be either the MoSSe alloy (Figure 4.24a) or Janus MoSSe (Figure 4.24b).[25-27] The latter of the two options consists of a layer of molybdenum atoms surrounded above and below by a layer of sulfur and selenium atoms, and is thus isostructural to MoS_2 apart from the crucial aspect of the breaking of the mirror symmetry.[28]

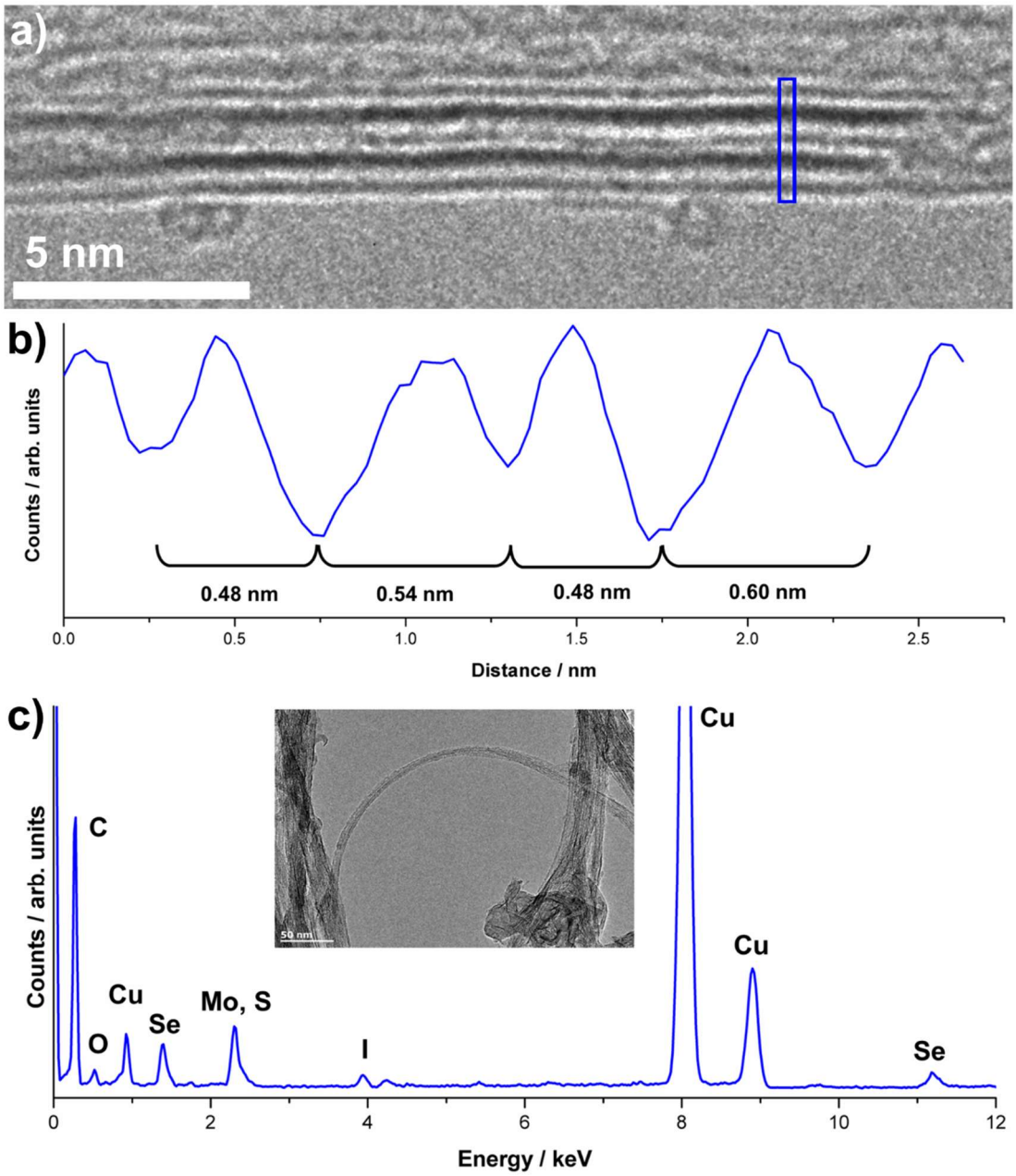


Figure 4.23. *(a) 200 kV TEM image of two adjacent SWNTs that are both filled with a nanoribbon in edge-on projection; (b) 2D contrast analysis of the area indicated by a blue rectangle in (a) which measures the distances between the SWNT outer walls and the centre of each nanoribbon; (c) EDX spectrum measured over a bundle of filled SWNTs (inset TEM image) and identifies Mo, S, and Se in a near 1: 1: 1 atomic ratio, as well as the presence of some residual iodine from the reaction.*

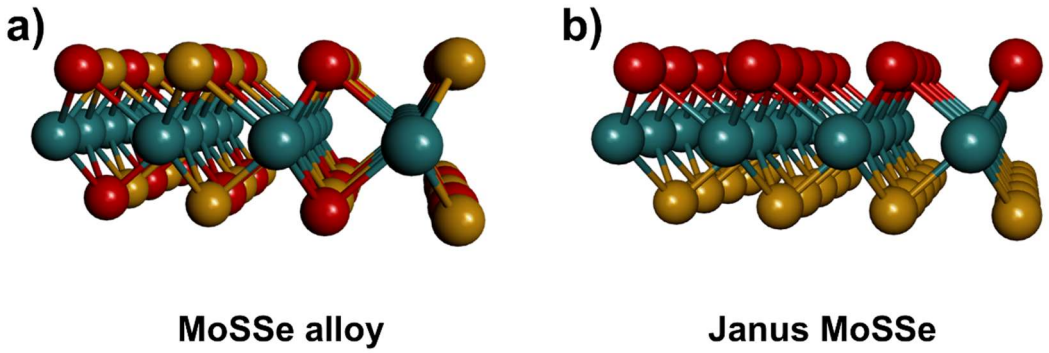


Figure 4.24. Structural models showing the structures of two possible identifications of the synthesised nanoribbons as (a) the MoSSe alloy, and (b) Janus MoSSe.

XPS analysis of MoSSe@SWNT showed more clearly defined peaks than observed for the $n[Mo_3S_4Se_3Br_6]^{2-}$@$SWNT^{2n+}$, and the survey scan recorded no peaks in the Br 3d region. The Mo 3d region was fitted to only a single doublet located at 229.4 and 232.5 eV for the 5/2 and 3/2 components, as well as a single S 2s peak at 226.8 eV (Figure 4.25a). The S 2p 3/2 and 1/2 components were located at 162.4 and 163.6 eV respectively, whilst the overlapping Se 3p peaks were located at 161.2 and 166.5 eV (Figure 4.25b). Finally, the Se 3d 5/2 and 3/2 components were at 54.8 and 55.6 eV respectively (Figure 4.25c). Compared to a previous study by Zhang *et al*. on Janus MoSSe 2D monolayers, the peak positions in MoSSe@SWNT were found to be consistently 1 eV higher in energy, and matched the number of peaks observed, as well as the peak profiles in Janus MoSSe 2D monolayers, thus confirming the species to be Janus MoSSe.[25] This shift in energy was also witnessed for $n[Mo_3S_4Se_3Br_6]^{2-}$@$SWNT^{2n+}$ and thus provides further evidence for the carbon nanoreactor host affecting the peak positions of the encapsulant through confinement effects, and electronic communications between host and guest. This a result of the partial positive charge on the SWNTs (according to Raman spectroscopy) which shifts the XPS peak positions to higher binding energies.

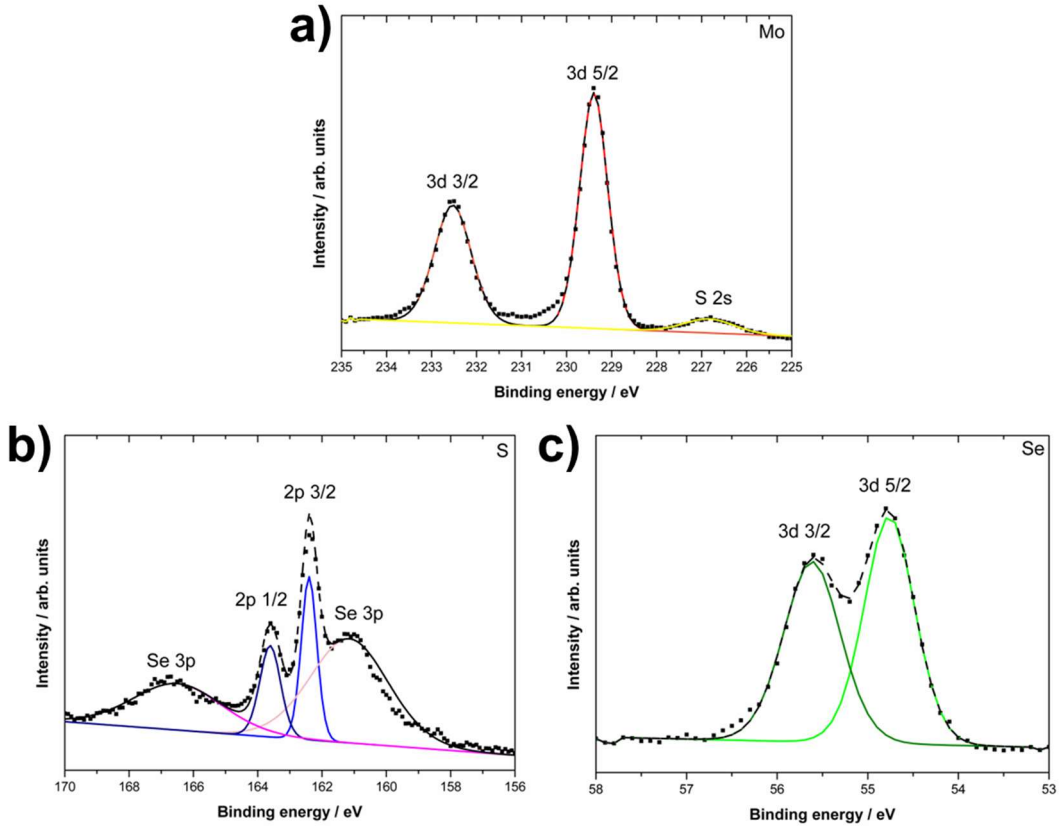


Figure 4.25. *XPS high resolution scans of Janus MoSSe@SWNT focussed on the (a) Mo 3d, (b) S 2p, and (c) Se 3d regions.*

AC-HRTEM was then used to probe the structure of the nanoribbons; the material was found to rotate around the nanotube axis allowing multiple projections to be observed (Figures 4.26a and d). The first image analysed depicted the nanoribbon in a near edge-on projection with respect to the electron beam, moreover, the top row of atoms appeared lighter than the bottom two rows, demonstrated by superimposed spheres which suggest the Janus nanoribbon was in the S-Mo-Se orientation. 2D contrast analysis over the middle row of molybdenum atoms found the regular interatomic distance to be 0.29 nm (Figure 4.26b). Using a combination of structural modelling and TEM simulation (Figure 4.26a), the nanoribbon was confirmed to be in a tilted edge-on projection and was tilted by 5° in both the x and y-direction (Figure 4.27) and further confirmed by contrast analysis of the

simulation (Figure 4.26c). The directions of the tilts were classified in the same way as reported by Wang *et al*. for MoS_2 nanoribbons within carbon nanotubes (Figure 4.27).[29]

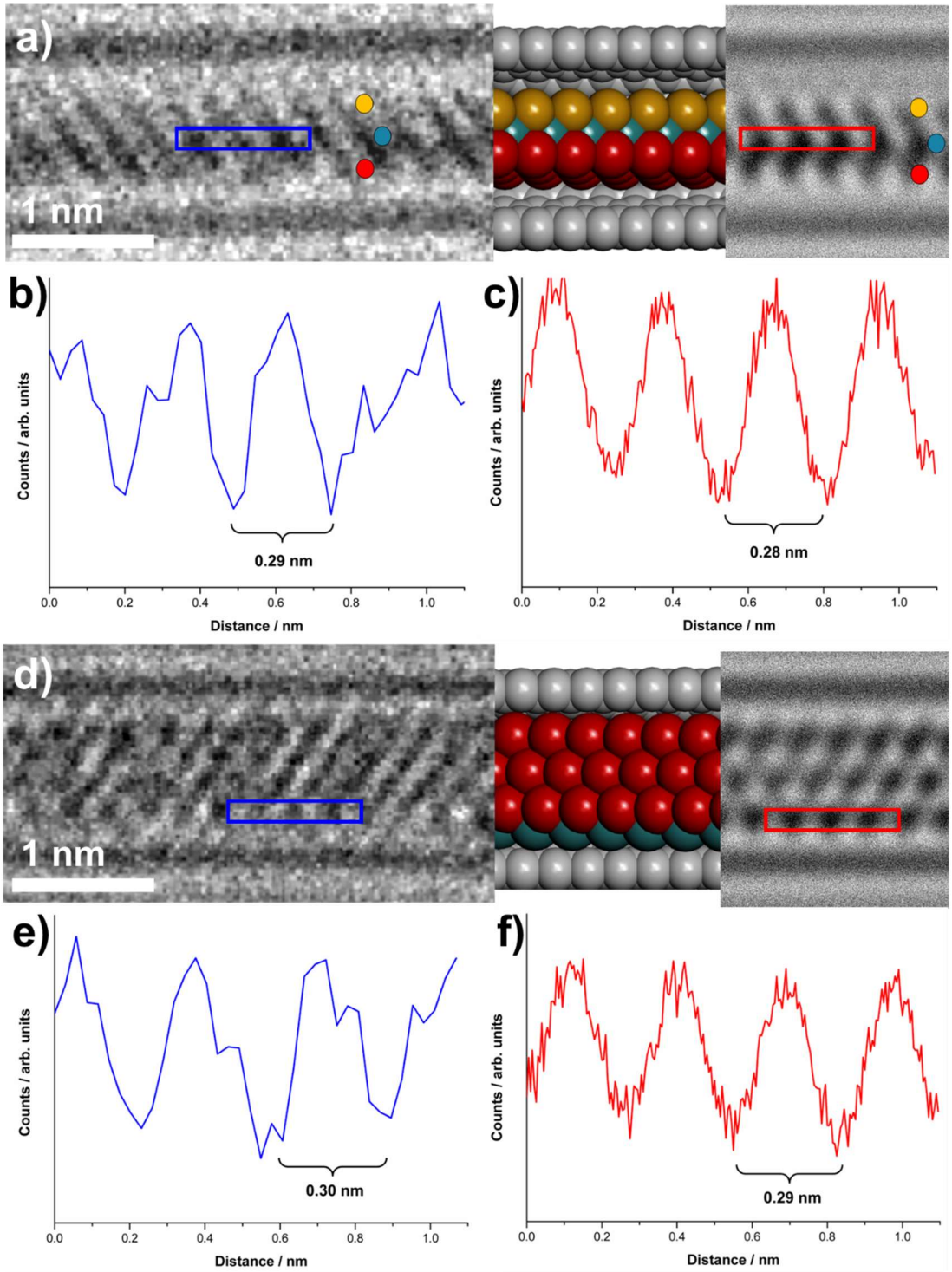


Figure 4.26. *(a) 60 kV AC-HRTEM image of a tilted edge-on Janus MoSSe nanoribbon within a SWNT (left), structural model of a tilted edge-on Janus MoSSe nanoribbon (middle),*

corresponding TEM simulation (right). Superimposed on the images are the relative positions of corresponding atoms in the structure, the yellow, blue, and red spheres correspond to sulfur, molybdenum, and selenium atoms respectively; (b) 2D contrast analysis of the experimental AC-HRTEM image indicated by the blue rectangle in a) which shows the interatomic distance along the row as 0.29 nm; (c) 2D contrast analysis of the TEM simulation indicated by the red rectangle in (a) which shows the interatomic distance along the row as 0.28 nm; (d) 60 kV AC-HRTEM image of a tilted face-on Janus MoSSe nanoribbon within a SWNT (left), structural model of a tilted face-on Janus MoSSe nanoribbon (middle), corresponding TEM simulation (right); (e) 2D contrast analysis of the experimental AC-HRTEM image indicated by the blue rectangle in (d) which shows the interatomic distance along the row as 0.30 nm; (f) 2D contrast analysis of the TEM simulation indicated by the red rectangle in (d) which shows the interatomic distance along the row as 0.29 nm.

The second image analysed showed the nanoribbon in a near face-on orientation, appearing as diagonal lines that overall had a larger width than observed in the previous image which fills the 1.5 nm diameter SWNT, whilst still retaining the 0.3 nm on each side to accommodate the thickness of the graphitic π-orbitals (Figure 4.26d).[30] 2D contrast analysis found the interatomic distance to be 0.30 nm (Figure 4.26e); which correlated with analysis of a TEM simulation of a face-on structural model (Figure 4.26d) of Janus MoSSe tilted by 30° in the x-direction and 15° in the y-direction (Figure 4.26f). Both of these projections confirm that the structure is a Janus MoSSe nanoribbon and the size correlates well with a single layer.

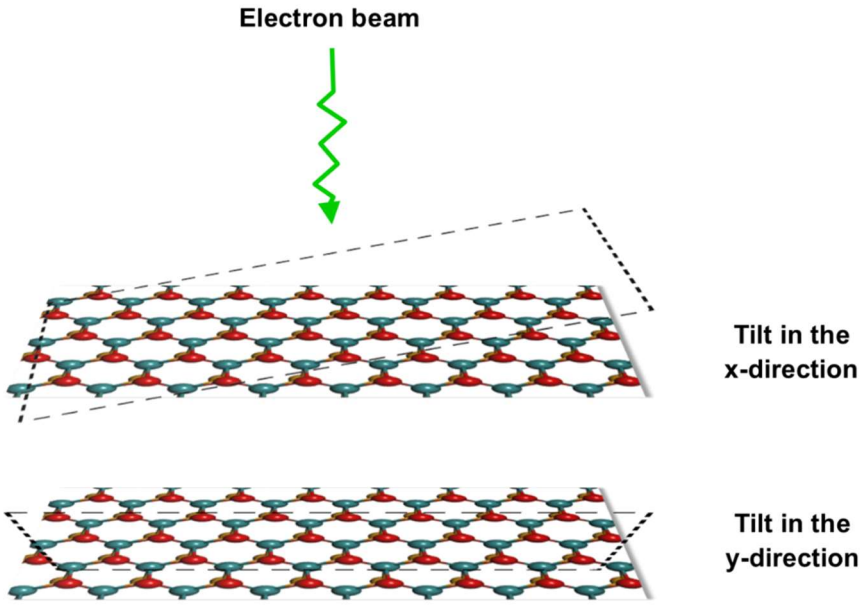
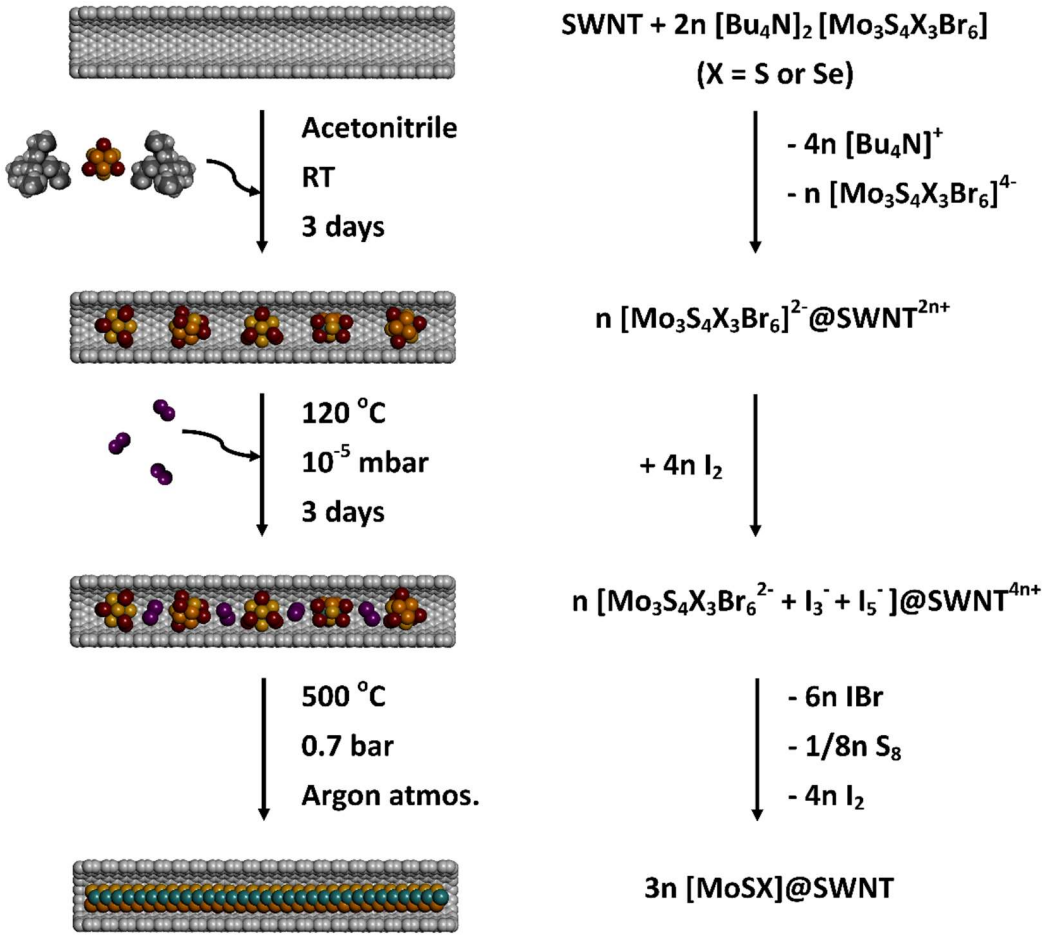


Figure 4.27. *Schematic diagram demonstrating the direction of x and y tilts of a species that is perpendicular to the electron beam.*

The formation of the Janus MoSSe structure is explained by the relative positions of the sulfur and selenium atoms with respect to the molybdenum plane in the parent cluster; the sulfur atoms of the bridging thio-seleno ligands are axial whilst the selenium atoms are equatorial and thus can be easily rearranged during the reaction to form the Janus structure. This is coupled by formation of the structure within the confinements of the ultrathin SWNT which are able to control and stabilise synthesised nanomaterials. To date, Janus MoSSe has only been formed twice previously, in the form of 2D monolayers using chemical vapour deposition techniques. The material is becoming a rapidly growing area of research due to the unusual properties that arise from the breaking of the mirror symmetry[28]; this includes being predicted to exhibit the Rashba and piezoelectric effects, and having a profound electrocatalytic ability towards the hydrogen evolution reaction.[31-34]

Overall, the use of metal chalcogenide clusters has shown promise towards the formation of quasi-1D dichalcogenide nanoribbons using iodine as a vapour transport agent (Scheme 4.1).



***Scheme* 4.1.** *Schematic diagram summarising the synthetic route towards the formation of the quasi-1D molybdenum dichalcogenides. The process starts with encapsulation the thiomolybdate-based cluster into SWNTs from a solution, followed by the sublimation of iodine into the SWNTs and thermal activation to form MoSX (where X = S or Se).*

4.3. Conclusions

The encapsulation of molybdenum chalcogen clusters into SWNTs was found to be aided by charge transfer from the SWNTs to the guest-molecule. A combination of imaging and spectroscopy techniques showed that the molecules retained their structure, composition and oxidation state upon insertion and thus the charge transfer must have occurred to exterior-bound clusters that were then washed away back into solution leaving a charge balanced host-guest system. The structure of the $[Mo_3S_7Br_6]^{2-}$ cluster was elucidated using

AC-HRTEM which, using complementary modelling and TEM image simulation analysis, and allowed individual orientations to be determined. However, the substitution of sulfur atoms for selenium atoms in the disulfide ligands caused asymmetry in the S-Se ligands resulting in fast rotational motion within the SWNT channel, leading to the orientations of individual clusters to not be resolved.

The reaction of n$[Mo_3S_7Br_6]^{2-}$@$SWNT^{2n+}$ with iodine resulted in the formation of continuous nanoribbons within the SWNT which were identified as MoS_2. However, despite aiding the production of MoS_2, a high amount of iodine was found to be intercalated within the SWNT despite a range of cleaning steps attempted. The thio-seleno variant cluster also produced nanoribbons on reaction with iodine but their composition was found to be the mixed chalcogenide MoSSe. In particular, the Janus MoSSe nanoribbon structure was revealed, by asymmetric TEM image contrast analysis and confirmed by EDX and XPS chemical analysis.

This is the first example of Janus MoSSe nanoribbons, with only two examples of 2D monolayers MoSSe being reported in the literature.[25, 26] These quasi-1D structures are predicted to be excellent electrocatalysts for processes such as the Hydrogen Evolution Reaction due to the high proportion of active edge sites.

4.4. Experimental

4.4.1. Materials

$[Bu_4N]_2[Mo_3S_7Br_6]$ and $[Bu_4N]_2[Mo_3S_4Se_3Br_6]$ were synthesised externally at the University of Valencia according to methods developed by Fedin *et al.*[5, 9] Single-walled carbon nanotubes were purchased from Carbon Solutions. The as-received SWNTs were refluxed in 3M nitric acid for two hours, washed with water (2L), and then heated to 600 ^oC for 17 mins.

Acetonitrile (Arcos Organics), iodine (Fisher Scientific), and argon gas (BOC) were all used as supplied.

4.4.2. Insertion of $[Bu_4N]_2[Mo_3S_7Br_6]$ / $[Bu_4N]_2[Mo_3S_4Se_3Br_6]$ into SWNTs

$[Bu_4N]_2[Mo_3S_7Br_6]$ (21 mg, 0.0066 mmol) or $[Bu_4N]_2[Mo_3S_4Se_3Br_6]$ (21 mg, 0.0061 mmol) were dissolved in acetonitrile (3.5 mL) forming yellow and red solutions respectively. Opened SWNTs (7 mg) were added to the mixture and left to stir for three days at room temperature. The mixture was then filtered using a Polytetrafluoroethylene (PTFE) membrane and washed with a further 5 mL of acetonitrile to remove the externally-bound species from the SWNT.

4.4.3. Reaction to form MoS_2@SWNT / MoSSe@SWNT

$n[Mo_3S_7Br_6]^{2-}$@$SWNT^{2n+}$ or $n[Mo_3S_4Se_3Br_6]^{2-}$@$SWNT^{2n+}$ (5 mg) and iodine (5 mg, 0.020 mmol) were sealed in a Pyrex ampoule at 10^{-5} mbar and heated to 120 °C for three days. The resultant material was then transferred to a second Pyrex ampoule and sealed under 0.7 bar of argon gas. The ampoule was then heated to 500 °C for one hour, then left to cool to room temperature, and then the product was collected.

4.4.4. Electron microscopy, energy-dispersive x-ray analysis, and wave-dispersive x-ray analysis

Materials for analysis were dispersed in isopropyl alcohol (Sigma Aldrich) and sonicated followed by being dropcast onto lacey carbon copper TEM grids (Agar Scientific). HR-TEM analysis was performed using a JEOL 2100F FEG-TEM electron microscope operated at either 100 or 200 kV. EDX analysis was conducted using an Oxford Instruments INCA X-ray microanalysis system. WDX analysis was performed using a JEOL 6490LV SEM with an electron microprobe to detect elements present. AC-HRTEM analysis was conducted at the University of Ulm using a C_c/C_s corrected sub-Ångström low-voltage electron microscope (SALVE) operated at 60 kV or on a C_s corrected FEI Titan 80-300 TEM operated at 80 kV.

4.4.5. Raman spectroscopy

Micro Raman spectroscopy was performed using a Horiba Jobin Yvon LabRAM HR Raman microscope. Spectra were acquired using either a 532 or 660 nm laser (at ~0.2 mW power), a 100x objective and a 200 µm confocal pinhole. To simultaneously scan a range of Raman shifts, a 600 lines mm^{-1} rotatable diffraction grating along a path length of 800 mm was employed, conferring a spectral resolution better than 1.9 and 1.2 cm^{-1} for the 532 and 660 nm lasers, respectively. Spectra were detected using a Synapse CCD detector (1024 pixels) thermoelectrically cooled to −60 °C. Before spectra collection, the instrument was calibrated using the zero-order line and a standard Si (100) reference band at 520.7 cm^{-1}. For single point measurements, spectra were acquired over a minimum range 125-3400 cm^{-1} with an acquisition time of 15-120 seconds and 2 accumulations to automatically remove the spikes due to cosmic rays and improve the signal to noise ratio. Spectra were collected from at least three random locations and averaged to give a mean spectrum.

4.4.6. X-ray photoelectron spectroscopy

Samples were analysed using the Kratos AXIS ULTRA with a mono-chromated Al kα X-ray source (1486.6eV) operated at 10 mA emission current and 12 kV anode potential (120 W.) Spectra were acquired with the Kratos VISION II software. A charge neutralizer filament was used to prevent surface charging. Hybrid –slot mode was used measuring a sample area of approximately 300 x 700 µm. The analysis chamber pressure was better than 5 x 10^{-9} mbar. Three areas per sample were analysed. A wide scan was performed at low resolution (Binding energy range 1400 eV to -5 eV, with pass energy 80 eV, step 0.5 eV, sweep time 20 minutes). High resolution spectra at pass energy 20 eV, step of 0.1 eV, and sweep times of 10 minutes each were also acquired for photoelectron peaks from the detected elements and these were used to model the chemical composition. The spectra were charge corrected to the C 1s peak set to 284.5 eV.

4.4.7. Structural modelling and TEM simulation

Structural models of filled nanotubes were created using the Discovery Studio Viewer software as well as using coordinate files from existing structures published in the literature, and a custom built nanotube builder programme. TEM simulations were conducted using the QSTEM software which is a multislice programme that utilises the Dirac-Fock scattering potential of Rez *et al*.[35] A fixed number of 20 slices per nanotube were chosen and a sampling of 0.05 Å was selected. The defocus parameters and aberration coefficients d_f, C_s, A_1, and B_2 were matched to the conditions used in the particular TEM experiment. The effect of limited electron dose was emulated by applying noise to the produced simulated images using a custom made Monte-Carlo program exploiting the Poisson statistics of electrons.

4.5. References

1. A. Muller, S. Sarkar, R. G. Bhattacharyya, S. Pohl and M. Dartmann, *Angew. Chem. Int. Ed.*, 1978, **17**, 535-535.
2. V. Fedorov, Y. Mironov, N. Naumov, M. Sokolov and V. Fedin, *Russ. Chem. Rev.*, 2007, **76**, 529-552.
3. A. L. Gushchin, R. Llusar, C. Vicent, P. A. Abramov and C. J. Gómez-Garcia, *Eur. J. Inorg. Chem.*, 2013, **2013**, 2615-2622.
4. R. Llusar, S. Uriel, C. Vicent, J. M. Clemente-Juan, E. Coronado, C. J. Gómez-García, B. Braïda and E. Canadell, *J. Am. Chem. Soc.*, 2004, **126**, 12076-12083.
5. V. P. Fedin, M. N. Sokolov, Y. V. Mironov, B. A. Kolesov, S. V. Tkachev and V. Y. Fedorov, *Inorg. Chim. Acta*, 1990, **167**, 39-45.
6. A. V. Virovets, M. Laege, B. Krebs, O. A. Geras'ko, V. E. Fedorov, O. V. Shishkin and Y. T. Struchkov, *J. Struct. Chem.*, 1996, **37**, 666-673.

7. R. Llusar, S. Triguero, S. Uriel, C. Vicent, E. Coronado and C. J. Gomez-Garcia, *Inorg. Chem.*, 2005, **44**, 1563-1570.

8. A. Alberola, R. Llusar, S. Triguero, C. Vicent, M. N. Sokolov and C. Gomez-Garcia, *J. Mater. Chem.*, 2007, **17**, 3440-3450.

9. V. P. Fedin, Y. V. Mironov, M. N. Sokolov, B. A. Kolesov, V. Y. Federov, D. S. Yufit and Y. T. Struchkov, *Inorg. Chim. Acta*, 1990, **174**, 275-282.

10. J. M. Garriga, R. Llusar, S. Uriel, C. Vicent, A. J. Usher, N. T. Lucas, M. G. Humphrey and M. Samoc, *Dalton Trans.*, 2003, 4546-4551.

11. Y. Lei, M. Yang, J. Hou, F. Wang, E. Cui, C. Kong and S. Min, *Chem. Commun.*, 2018, **54**, 603-606.

12. T. F. Jaramillo, K. P. Jørgensen, J. Bonde, J. H. Nielsen, S. Horch and I. Chorkendorff, *Science*, 2007, **317**, 100-102.

13. D. Recatalá, R. Llusar, A. L. Gushchin, E. A. Kozlova, Y. A. Laricheva, P. A. Abramov, M. N. Sokolov, R. Gómez and T. Lana-Villarreal, *ChemSusChem*, 2015, **8**, 148-157.

14. Y. Shang, X. Xu, B. Gao and Z. Ren, *ACS Sustain. Chem. Eng.*, 2017, **5**, 8908-8917.

15. A. Botos, J. Biskupek, T. W. Chamberlain, G. A. Rance, C. T. Stoppiello, J. Sloan, Z. Liu, K. Suenaga, U. Kaiser and A. N. Khlobystov, *J. Am. Chem. Soc.*, 2016, **138**, 8175-8183.

16. C. T. Stoppiello, J. Biskupek, Z. Y. Li, G. A. Rance, A. Botos, R. M. Fogarty, R. A. Bourne, J. Yuan, K. R. J. Lovelock, P. Thompson, M. W. Fay, U. Kaiser, T. W. Chamberlain and A. N. Khlobystov, *Nanoscale*, 2017, **9**, 14385-14394.

17. T. W. Chamberlain, J. Biskupek, S. T. Skowron, A. V. Markevich, S. Kurasch, O. Reimer, K. E. Walker, G. A. Rance, X. Feng, K. Müllen, A. Turchanin, M. A. Lebedeva, A. G. Majouga, V. G. Nenajdenko, U. Kaiser, E. Besley and A. N. Khlobystov, *ACS Nano*, 2017, **11**, 2509-2520.

18. M. V. Kharlamova, *Appl. Phys. A*, 2016, **122**, 791.

19. J. W. Jordan, G. A. Lowe, R. L. McSweeney, C. T. Stoppiello, R. W. Lodge, S. T. Skowron, J. Biskupek, G. A. Rance, U. Kaiser, D. A. Walsh, G. N. Newton and A. N. Khlobystov, *Adv. Mater.*, 2019, **31**, 1904182.

20. R. Vaidya, M. Dave, S. S. Patel, S. G. Patel and A. R. Jani, *Pramana*, 2004, **63**, 611-616.

21. A. K. Geim and I. V. Grigorieva, *Nature*, 2013, **499**, 419-425.

22. Y. Yoshida, Y. Ishii, N. Kato, C. Li and S. Kawasaki, *J. Phys. Chem. C*, 2016, **120**, 20454-20461.

23. J. Park, J.-G. Song, T. Choi, S. Sim, H. Choi, S. W. Han, H.-B.-R. Lee, S.-H. Kim and H. Kim, *Curr. Appl. Phys.*, 2016, **16**, 691-695.

24. S. Luo, X. Qi, L. Ren, G. Hao, Y. Fan, Y. D. Liu, W. Han, C. Zang, J. Li and J. Zhong, *J. Appl. Phys*, 2014, **116**.

25. J. Zhang, S. Jia, I. Kholmanov, L. Dong, D. Er, W. Chen, H. Guo, Z. Jin, V. B. Shenoy, L. Shi and J. Lou, *ACS Nano*, 2017, **11**, 8192-8198.

26. A.-Y. Lu, H. Zhu, J. Xiao, C.-P. Chuu, Y. Han, M.-H. Chiu, C.-C. Cheng, C.-W. Yang, K.-H. Wei, Y. Yang, Y. Wang, D. Sokaras, D. Nordlund, P. Yang, D. A. Muller, M.-Y. Chou, X. Zhang and L.-J. Li, *Nat. Nanotechnol.*, 2017, **12**, 744-749.

27. J. Qiao, F. Song, J. Hu, D. Huo, J. Yuan, J. Shen, L. Niu and A.-j. Wang, *Int. J. Hydrogen Energy*, 2019, **44**, 16110-16119.

28. R. Li, Y. Cheng and W. Huang, *Small*, 2018, **14**, 1802091.

29. Z. Wang, H. Li, Z. Liu, Z. Shi, J. Lu, K. Suenaga, S.-K. Joung, T. Okazaki, Z. Gu, J. Zhou, Z. Gao, G. Li, S. Sanvito, E. Wang and S. Iijima, *J. Am. Chem. Soc.*, 2010, **132**, 13840-13847.

30. A. N. Khlobystov, D. A. Britz and G. A. D. Briggs, *Acc. Chem. Res.*, 2005, **38**, 901-909.

31. Y. C. Cheng, Z. Y. Zhu, M. Tahir and U. Schwingenschlögl, *EPL (Europhysics Letters)*, 2013, **102**, 57001.

32. Q.-F. Yao, J. Cai, W.-Y. Tong, S.-J. Gong, J.-Q. Wang, X. Wan, C.-G. Duan and J. H. Chu, *Phys. Rev. B*, 2017, **95**, 165401.

33. L. Dong, J. Lou and V. B. Shenoy, *ACS Nano*, 2017, **11**, 8242-8248.

34. W. Shi, G. Li and Z. Wang, *J. Phys. Chem. C*, 2019, **123**, 12261-12267.

35. D. Rez, P. Rez and I. Grant, *Acta Crystallogr. A*, 1994, **50**, 481-497.

Chapter 5: Tungsten disulfide nanoribbons within carbon and boron nitride nanotubes: synthesis, structural and dynamic analysis by ChemTEM

5.1. Introduction

Tungsten disulfide (WS_2) is a layered transition metal dichalcogenide (TMDC) that, in the 2H (trigonal prismatic) phase, is a semiconductor with a bandgap of ~1.9 eV.[1] The photoluminescence (PL) properties of the material were previously found to strengthen in terms of intensity upon decreasing number of layers, as a result of an indirect-to-direct band gap transition for the monolayer;[2] as well an enhancement found for the edge sites compared to the basal plane.[3] This has led to more research into the formation of low-dimensional forms of WS_2, such as nanoribbons (NR), which have a high number of edge sites.[4, 5] A novel method that was used to synthesise WS_2 NRs was the unzipping of WS_2 nanotubes which was achieved by intercalation with K/Na alloy and then quenched with methanol producing H_2 and caused the unzipping.[6] The structures were characterised by transmission electron microscopy (TEM) and were found to be multi-layered and have widths above 200 nm. The electrocatalytic ability of the WS2 NRs towards the hydrogen evolution reaction (HER) was evaluated and found to outperform the original WS_2 nanotubes.

WS_2 NRs have been previously prepared using the confinements of single-walled carbon nanotubes (SWNTs) as size-restricting nano test tubes. Wang *et al*. filled pre-opened SWNTs with Keggin polyoxometalates (POM), $H_3PW_{12}O_{40}$ "{W_{12}}", by refluxing SWNTs in a saturated aqueous solution of the POMs. The encapsulated POMs were then reduced using a H_2/H_2S

mixture at high temperature (800 °C) to form WS_2@SWNT.[7] The resulting structures were characterised by TEM and energy-dispersive X-ray analysis (EDX) and were found to primarily have zigzag edges and range as small as four W atom in width (4ZWS_2NR). Botos *et al.* used a three step method to form WS_2 nanoribbons which started by subliming tungsten hexacarbonyl and iodine into SWNTs; the system was then thermally-activated to form octahedral $[W_6I_{14}]^{2-}$ structures, and then further reacted with dihydrogen sulfide, H_2S, to form WS_2 nanoribbons.[8] A combination of microscopy and spectroscopy techniques were employed to study not only the structure and composition of the products synthesised, but also to examine any electronic communication between the host and guests. This revealed the SWNT hosts to be acting as nanoreactors providing a reservoir of electrons that can be donated in order to stabilise the nanomaterials within.

SWNTs have long been established as containers for molecular species[9-11], as well as quasi-one-dimensional (1D) templates which enforce encapsulants to adopt different structures and geometries.[12-15] A newly emerging class of nanocontainers are boron nitride nanotubes (BNNT, Figure 5.1) which are hollow tubular structures that are isostructural with carbon nanotubes[16] apart from a very slight difference in bond lengths (1.42 Å C-C vs 1.46 Å B-N).[17, 18] However, three key differences arise in their optical, thermal, and electronic properties; they are optically transparent, have a higher thermal stability[19], and are insulators with band gap energies of ~ 5.5 eV.[20] The large band gap is a result of localisation of the π-electrons around nitrogen atoms, due to the difference in electronegativity between boron and nitrogen, compared to the delocalised π-system in SWNTs.[21]

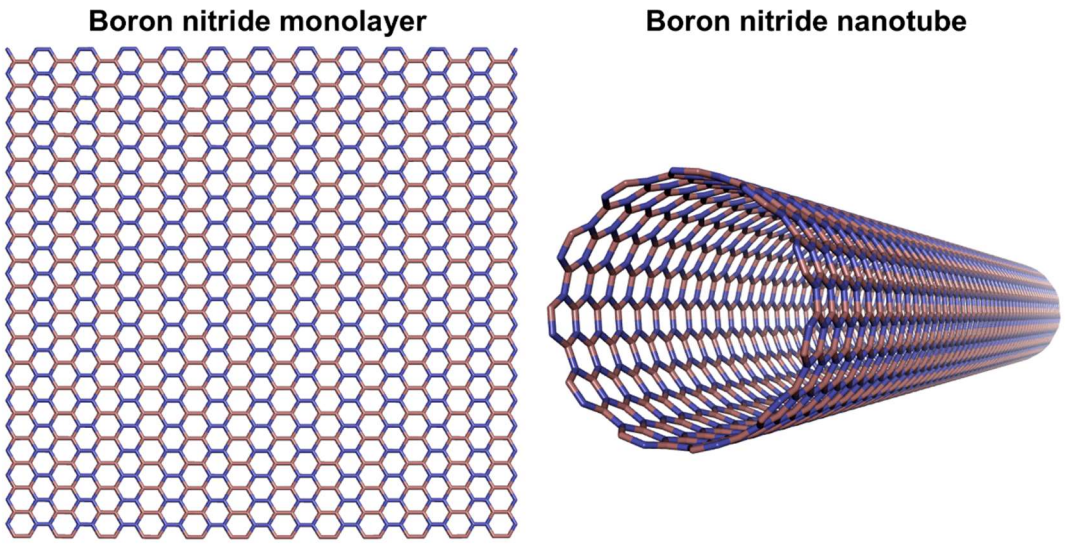


Figure 5.1. *Structural models of a monolayer of boron nitride and a boron nitride nanotube.*

BNNTs have been previously filled with different materials using both in-situ and ex-situ routes, in which the BNNTs are either filled during or post synthesis respectively. An early example of in-situ filling was with silicon carbide and the material was characterised using TEM.[22] Since then, many other materials have been filled during the synthetic process including metals such as molybdenum, iron, cobalt, and nickel.[23, 24] Molecules have also been encapsulated into BNNTs via ex-situ methods following either thermal treatment, or base treatment in which the nitrogen lone pair of ammonia interacts with the empty P_z orbital of boron which causes them to be susceptible to hydrolysis leading to removal of the BNNT end caps.[25] C_{60} fullerenes inserted into BNNTs were shown to exhibit different packing arrangements, which were not observed in the bulk material, enforced by the diameter of the host.[26] Furthermore, TEM and EDX were used to characterise the structures and compositions of a range of potassium halides within BNNTs by Han *et al.*[27] Inorganic transformations within the confinement of BNNTs have also been successfully attempted by pre-opening the BNNTs followed by the insertion of a molecular precursor and subsequent thermal activation. The first example was the formation of metal nanorods from metal salt precursors that were encapsulated from an ethanol solution by capillary-forces.[28] The second

example encapsulated fullerenes into the BNNT cavity using a sublimation technique, and subsequently underwent a thermal treatment to form a carbon nanotube (CNT@BNNT) producing a coaxial cable (Figure 5.2).[29] However, it is now needed to understand more complex reactions within boron nitride nanotubes such as the formation of TMDCs, such as WS_2, which are of interest due to their optoelectronic properties.[30, 31]

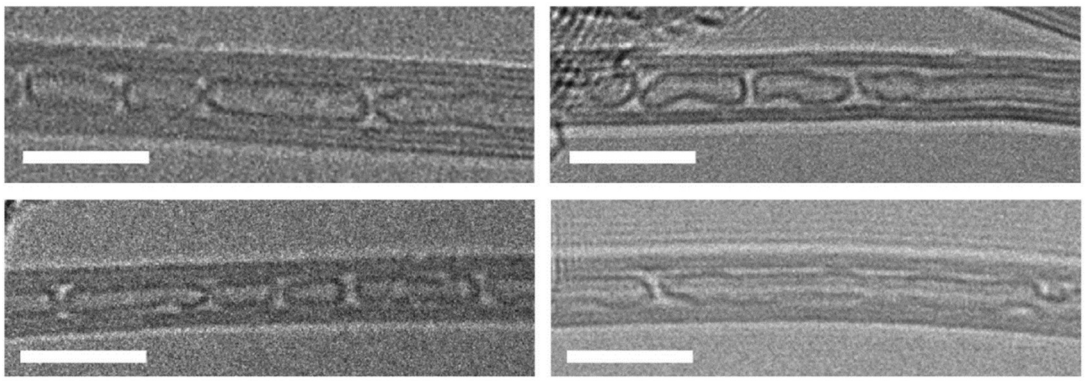


Figure 5.2. *100 kV TEM images of CNT@BNNT formed by the thermal activation of C_{60}@BNNT at 1200 °C. Scale bars are 5 nm.*[29]

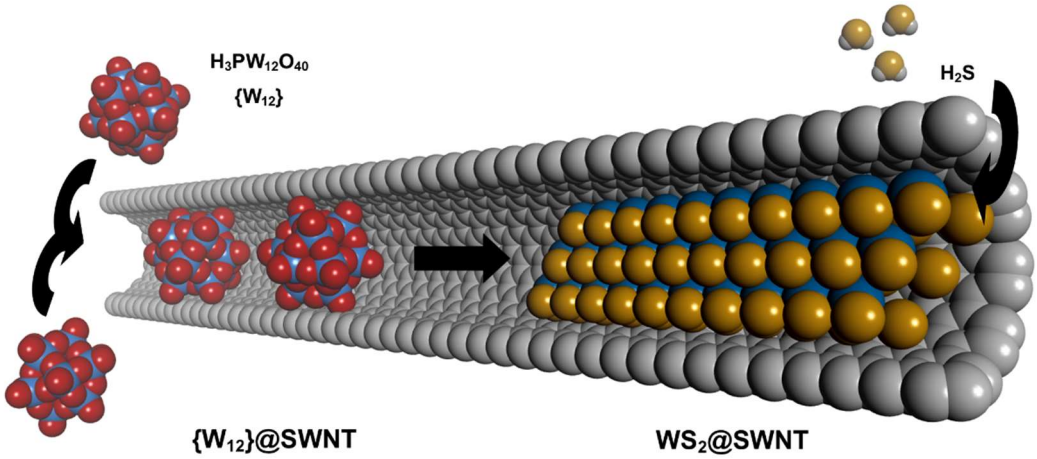
In this study, the aim is to develop a new route towards forming quasi one-dimensional tungsten disulfide nanoribbons initially using SWNTs as templates, and then subsequently BNNTs. The proposed synthetic route, for the formation of WS_2 nanoribbons, aims to further develop and combine existing current reaction methodologies; this includes the two-step route using POMs by Wang *et al*.[7], as well as the holistic characterisation and mechanistic understanding of Botos et al.[8] However, there will be some key changes; the first is the method of POM encapsulation which will be achieved using a solution-phase filling method developed by Jordan *et al*.[32] Previously, POMs have been encapsulated by reflux of an aqueous solution in the presence of SWNTs[7], but one of the disadvantages of this is the extra energy cost. A further problem is the entropic factor; the encapsulation process works against entropy and therefore increasing the temperature will further increase the entropy thus in order to keep the Gibbs free energy negative, the reaction requires lower

temperatures. Finally, the room temperature filling will also not affect the POM stability. A method developed by Fei *et al.* sonicated an aqueous solution of $H_3PW_{12}O_{40}$ with opened multi-walled carbon nanotubes, however, this will not be used for this system to avoid potential damage to the SWNTs.[33] The second is the use solely of H_2S and not H_2 as well, plus the reaction will be conducted at a lower temperature. It is proposed that the H_2S will be able to act as a reducing agent for the POMs which will allow them to transform into WS_2 nanoribbons using the unique extreme confinement of the interior of nanotubes. Furthermore, the two-step synthesis will be monitored using a holistic analytical approach which uses TEM and energy-dispersive X-ray analysis (EDX) to determine the structure and composition of products formed at each stage of the reaction, as well as probe any electronic communication between host and guest by examining shifts in vibrational modes of the nanotube hosts using Raman spectroscopy. This new methodology aims to provide a universal method for forming ultrathin WS_2 nanoribbons within both SWNTs and BNNTs; the latter of which will allow more detailed spectroscopy of the encapsulated nanowires to be examined due to the transparent nature of the BNNTs. As well as using the electron beam as a probe, it will also be used to simultaneously image and trigger chemical transformations within the nanotube interior channel, in a *ChemTEM* approach. This work will not only provide an alternative and universal route towards forming WS_2 nanoribbons within SWNTs and BNNTs, but will also explore their dynamics and stability under the electron beam.

5.2. Results and Discussion

5.2.1. WS_2 within single-walled carbon nanotubes

The first section of this chapter will examine the stepwise synthesis using single-walled carbon nanotubes as hosts (Scheme 5.1).



Scheme 5.1. *Schematic diagram showing the stepwise synthesis proposed for the formation of tungsten disulfide nanoribbons using polyoxometalate precursors. The methodology commences with the solution-phase encapsulation of tungsten Keggin polyoxometalates, $H_3PW_{12}O_{40}$; these are then reacted with dihydrogen sulfide gas under an inert atmosphere to form WS_2 nanoribbons which are size templated by the interior channel of the SWNT.*

The initial step of the synthesis was to encapsulate the {W_{12}} polyoxometalate precursors into the SWNTs. The Keggin tungsten POM (Figure 5.3), $H_3PW_{12}O_{40}$, was chosen as it should provide a complementary fit within SWNTs of between 1.2 – 1.8 nm, and has been shown to be an excellent precursor towards the formation of tungsten disulfide.[7] The structure consists of tungsten atoms surrounded by 6 oxygen atoms in an octahedral complex which are then bonded together by three bridging oxygen atoms, the structure is then completed by the presence of a central PO_4 group.[34]

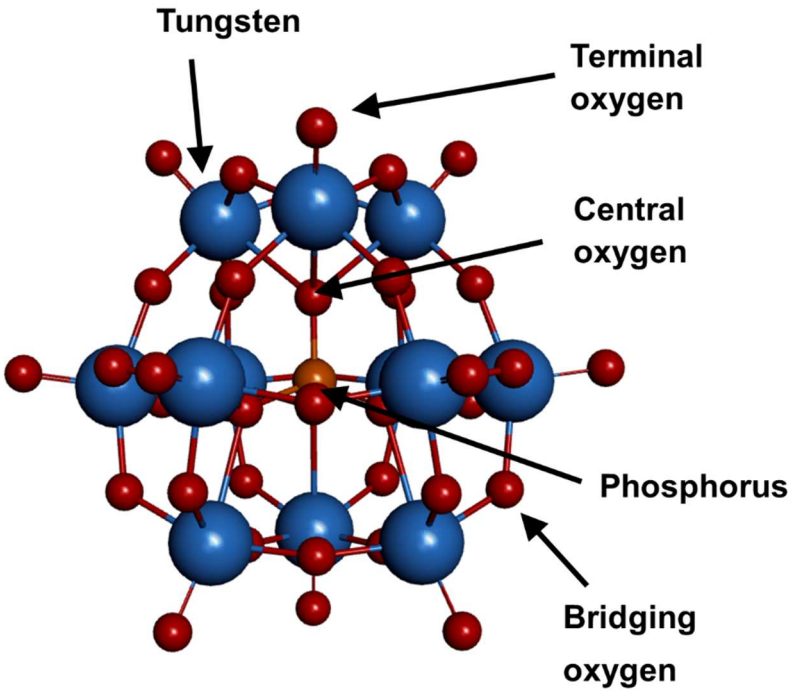


Figure 5.3. *Structural model of a Keggin $H_3W_{12}O_{40}$ polyoxometalate with the individual elements, and different oxygen environments labelled.*

5.2.1.1. Insertion of the {W_{12}} POM into SWNTs

The filling into SWNTs was achieved using a solution-phase method[32]; the POMs were first dissolved in water and the freshly opened SWNTs were added to the aqueous solution resulting in a colour change, of the solution, from colourless to blue. The material was then isolating by filtering the mixture and was subsequently washed with water to remove any excess material from the SWNT exterior. TEM imaging of the sample showed that the SWNTs were well filled with high contrast material appearing as discrete molecules (Figure 5.4a). The POMs also demonstrate a complementary fit within the 1.5 nm diameter SWNTs which was also verified by a structural model created (Figure 5.4b). Upon prolonged exposure to the 200 kV electron beam, the POMs proceed bonding together first forming dimers, then more extended structures, which occurs via a condensation mechanism triggered by the energy provided by the electron beam.[35] EDX, measured over a bundle of filled SWNTs,

identified the presence of; tungsten, oxygen and phosphorus from the POM cluster, as well as carbon from the host SWNTs (Figure 5.4c). Tungsten and oxygen were found to be in a 1: 4 atomic ratio which is close to the expected 1: 3.3 of the bulk material; the excess oxygen is most likely in the form of defects in the SWNT structure. The presence of copper was also detected but this is due to the nature of the TEM grid support. The composite material demonstrated a high degree of filling from thermogravimetric analysis (TGA, Figure 5.4d); the thermogram showed a single weight loss at 725 ^{o}C which is attributed to the oxidation of the SWNTs, this resulted in 33.5 % weight remaining attributed to the POMs. The temperature of SWNT oxidation was not shown to change compared to empty SWNTs.

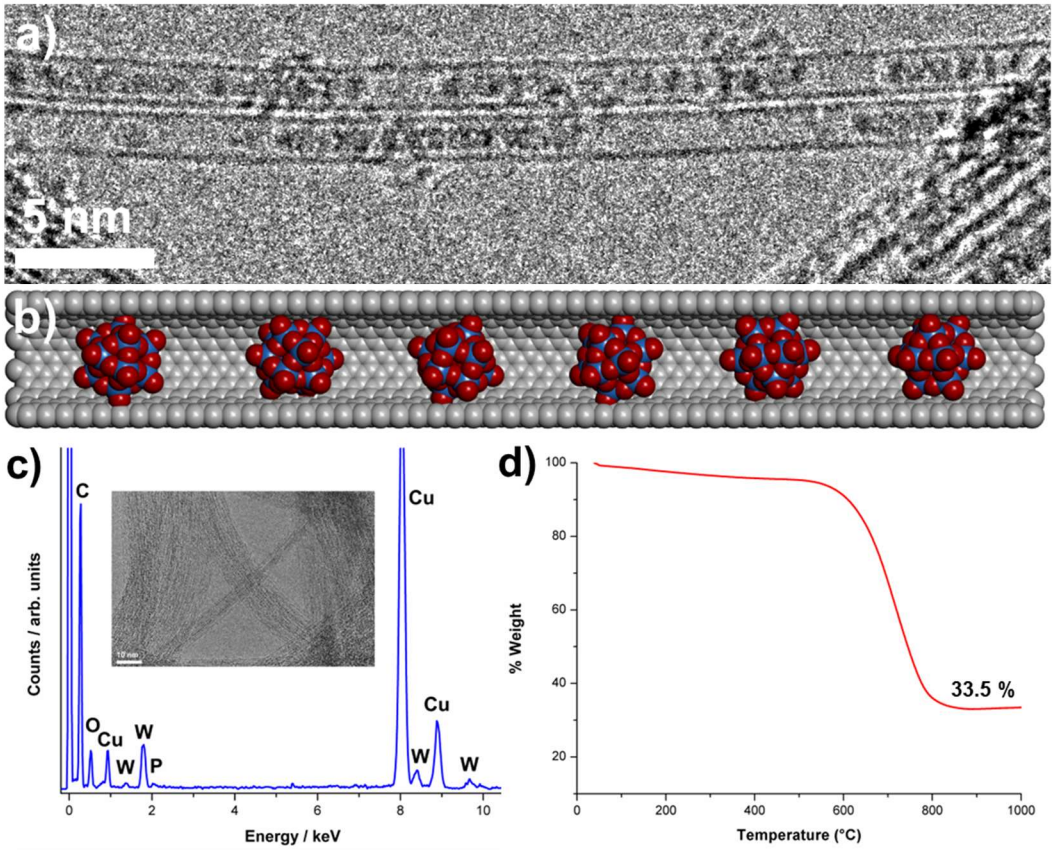


Figure 5.4. *(a) 200 kV TEM image of {W_{12}}@SWNT. The image shows the presence of discrete {W_{12}} clusters within two SWNTs in a bundle; (b) structural model of {W_{12}}@SWNT demonstrating the complementary fit of the POM structure within a 1.5 nm diameter SWNT; (c) EDX spectrum measured over a bundle of filled SWNTs (inset TEM image of the area of*

analysis). The spectrum shows the presence of W, P and O present from the POM, as well as C from the SWNTs, and Cu from the composition of the TEM grid; (d) Thermogram of {W_{12}}@SWNT in air showing a single loss at 725 ^{o}C which resulted in 33.5 % weight remaining.

Raman spectroscopy, using an excitation laser in resonance with metallic SWNTs, showed no direct evidence of POM Raman active modes, but did record a significant blue shift of the G band of 6.7 cm^{-1}, compared to empty SWNTs (Figure 5.5). Also exhibited was a change in the profile of the peak to resemble the G band of semiconducting SWNTs, exhibiting a more Lorentzian profile. These two factors indicate that the SWNTs are donating electron density to the POMs, which opens the band gap of the SWNTs causing a metallic to semiconducting transition.[36] The mechanism of encapsulation for POMs into single-walled carbon nanotubes was proposed by Jordan *et al* to occur via coulombic attraction[32]; the SWNT hosts donate electron density to some of the tungsten polyoxometalates causing them to become more negatively-charged and the SWNTs positively-charged; this then leads to electrostatically-driven encapsulation of the non-reduced POMs into SWNTs. The reduced POMs and leftover protons are then washed away from the exterior of the nanotubes. This mechanism also explains the change in colour of the aqueous solution upon addition of the SWNTs as a consequence of the formation of reduced POMs.

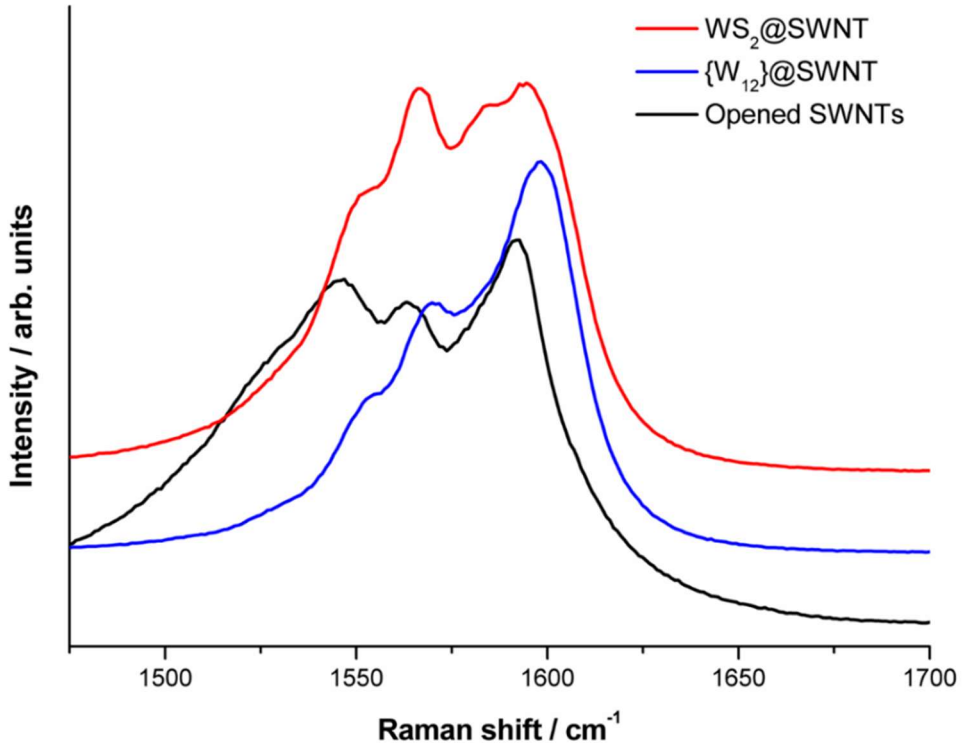


Figure 5.5. *Raman spectra overlay, using 660 nm laser excitation in resonance with metallic SWNTs, focussed on the G band region of opened SWNTs (black) as reference, {W_{12}}@SWNT (blue), and WS_2@SWNT (red).*

To confirm this mechanism, X-ray photoelectron spectroscopy (XPS) was conducted to examine if the POM structure had changed upon encapsulation by comparing against literature values. The W 4f region recorded a doublet at 36.2 and 38.3 eV which correspond to the 7/2 and 5/2 components respectively (Figure 5.6a); these values are upshifted by 0.4 eV compared to previous studies on the parent molecule[37], $H_3PW_{12}O_{40,}$ which is a reflection of the newly confined environment and not any change in oxidation state. Also noted in the high-resolution spectrum is the overlap with the component for W 5p 3/2 at 41.9 eV. The O 1s region was shown to consist of an overlap of many components which arise from the different oxygen environments present in the POM, as well as SWNT defects (Figure 5.6b)

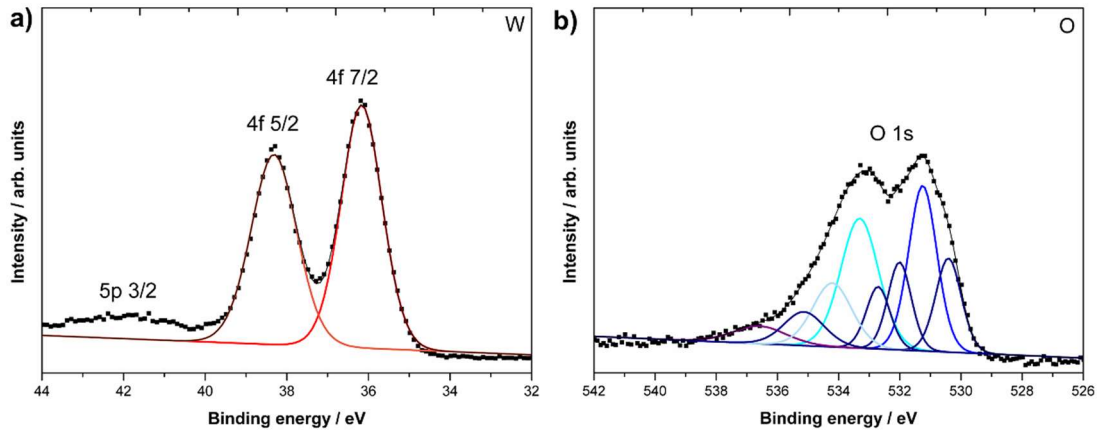


Figure 5.6. *XPS high resolution scans of {W_{12}}@SWNT focussed on the a) W 4f and b) O 1s regions.*

Overall, it was shown that the encapsulation of {W_{12}} into SWNTs was successful, occurring via a coulombic mechanism, previously observed, whilst retaining their structure and composition.

5.2.1.2. Reaction with H_2S to form WS_2 nanoribbons

The second and final step of the synthesis reacted {W_{12}}@SWNT with dihydrogen sulfide gas at 550 °C for two hours, to convert the POMs to tungsten disulfide. Initial TEM imaging demonstrated that an inorganic transformation had taken place as the SWNTs were filled with high contrast continuous nanoribbons instead of discrete molecules (Figure 5.7a and b inset). EDX, measured over a bundle of filled SWNTs, identified W and S from the guest species, as well as carbon and oxygen from the host SWNTs and any unreacted POM molecules (Figure 5.7b). The presence of phosphorus was also detected which may be trapped within the SWNT after the reaction of the POMs with H_2S. The reaction is thought to proceed via the reduction of tungsten in the POMs from +6 to +4 in WS_2, along with the production of water, and sulfur dioxide as primary by-products (Equation 5.1).

$$(3\,PW_{12}O_{40})^{3-}@SWNT^{3+} + 88\,H_2S \rightarrow (36\,WS_2)@SWNT + 88\,H_2O + 16\,SO_2 + 3P$$

Equation 5.1. *The transformation of encapsulated tungsten Keggin polyoxometalates with dihydrogen sulfide to produce quasi-1D tungsten disulfide nanoribbons.*

A thermogram was recorded of the material and found a single loss at 716 °C, which resulted in a residual weight of 32.1 % (Figure 5.7c). This shows the reaction occurred with high yield due to the very small final loading difference compared to {W_{12}}@SWNT. It also demonstrates the SWNTs were not affected in terms of thermal stability upon interior modification with WS_2 as the SWNT oxidation temperature was only slightly decreased when compared against empty SWNTs. Raman spectroscopy, in resonance with metallic SWNTs, of the material led to a red shift of the G-band compared to {W_{12}}@SWNT by 4 cm^{-1} but still a 2.7 cm^{-1} blue shift compared to empty SWNTs which suggests the WS_2 nanoribbons are slightly electron withdrawing in nature (Figure 5.5).

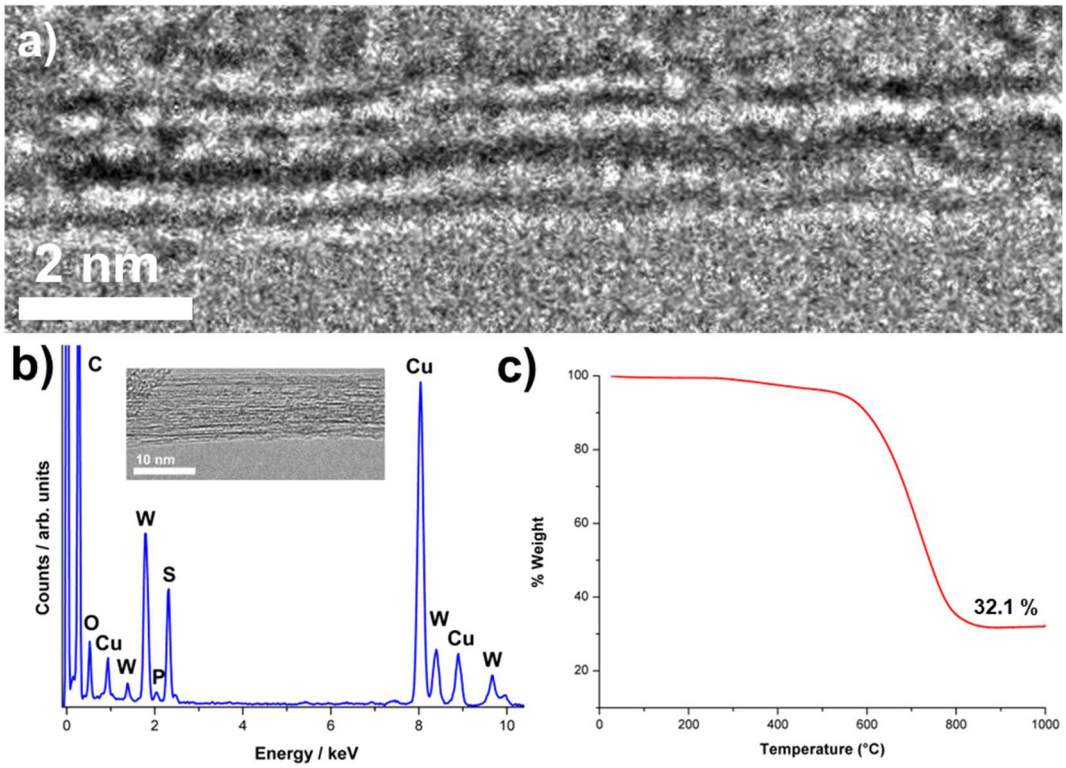


Figure 5.7. *(a) 200 kV TEM image of WS_2@SWNT. The material appears as a nanoribbon within the nanotube walls and is shown in edge on view; (b) EDX spectrum identifying W and*

S from the nanoribbon, C from the SWNTs, P leftover after the reaction, and Cu from the TEM grid; (c) Thermogram of WS_2@SWNT in air showing a single weight loss at 716 ^oC which resulted in 32.1 % weight remaining.

XPS analysis of the material was conducted, and the W 4f region consisted of two sets of doublets at 32.4 and 34.5 eV, as well as 35.6 and 37.8 eV (Figure 5.8a). These correspond well to the literature values of tungsten disulfide,[38] and the previous binding energies of the encapsulated $\{W_{12}\}$ respectively. The S 2p region was fitted to a single doublet at 162.4 and 163.8 eV which also correspond well to the known sulfur binding energies of WS_2 (Figure 5.8b). The downshift of the W 4f peaks and the presence of sulfur peaks both highlight that the transformation of POMs to WS_2 using this new method was successful, with only a small amount of POMs being unreacted.

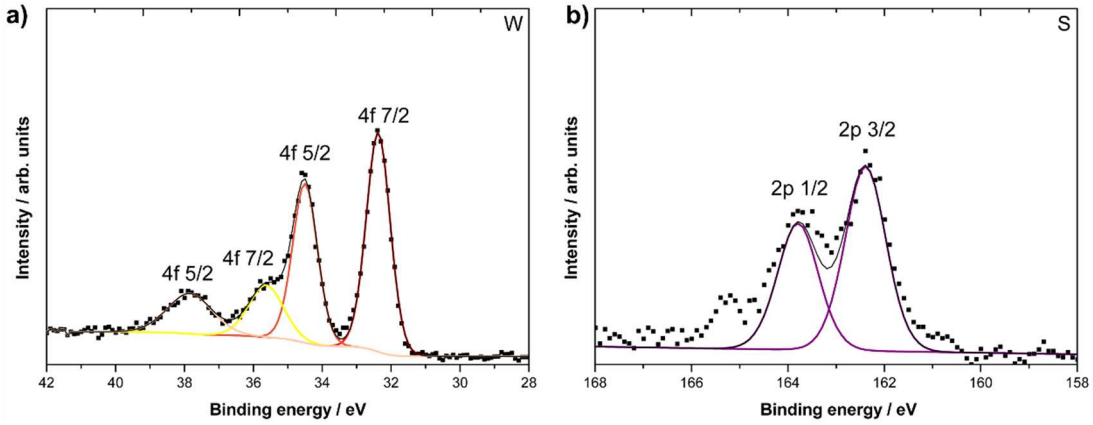


Figure 5.8. *XPS high resolution spectra focused on the (a) W 4f and (b) S 2p regions. The W 4f region shows two sets of doublets; the lower energy set corresponds to WS_2 and the higher energy set to unreacted tungsten POMs.*

Further elemental analysis was conducted using scanning transmission electron microscopy (STEM)-EDX mapping; bright field (BF, Figure 5.9a) and high-angle annular dark-field imaging (HAADF, Figure 5.9b) located an area that contained a SWNT filled with a high contrast

nanoribbon. STEM-EDX mapping (Figure 5.9c- f) was able to show that the host nanotube consisted of carbon, and the nanoribbon consisted of tungsten and sulfur. A localised EDX spectrum was also conducted over the same area which found tungsten and sulfur to exist in a 1:2 atomic ratio which confirms the composition of the nanoribbons as tungsten disulfide (Figure 5.9g).

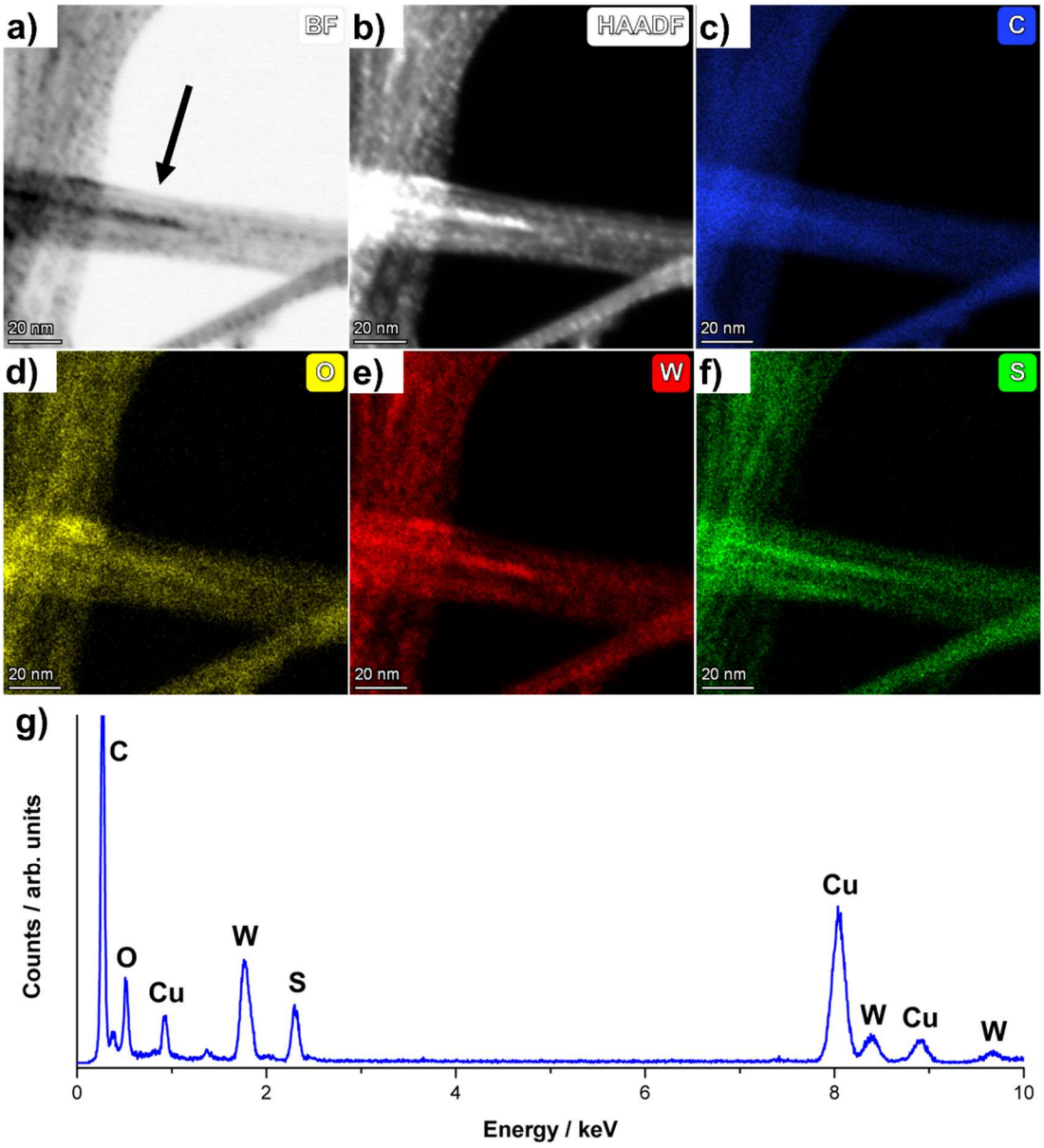


Figure 5.9. *WS_2@SWNT imaged using (a) bright-field and (b) high-angle annular dark-field modes which show the presence of a nanoribbon within a single-walled carbon nanotube. STEM-EDX mapping of the same area identifying the presence of (c) carbon, (d) oxygen, (e)*

tungsten, and (f) sulfur; (g) local EDX spectrum of the area in (a) which shows tungsten and sulfur present in the material in a 1:2 atomic ratio.

The structure was then further imaged by aberration-corrected high-resolution TEM (AC-HRTEM, Figure 5.10a) to examine if the structure matched with that of known WS_2 nanoribbons, which have hexagonal lattices. The AC-HRTEM image shows a face-on 3-atom thick tungsten disulfide nanoribbon with zigzag edges ($3ZWS_2NR$) and a hexagonal lattice, which is measured to have a width of 0.57 nm; this is the narrowest observed in previous studies reporting $4ZWS_2NR$ structures.[4, 7, 8] The interatomic distance between tungsten atoms in a row was found to be 0.31 nm which correlates well with the known structure of the bulk material and is demonstrated using a TEM simulation of a model of a $3ZWS_2NR$ in a (10, 10) SWNT (Figure 5.10b).

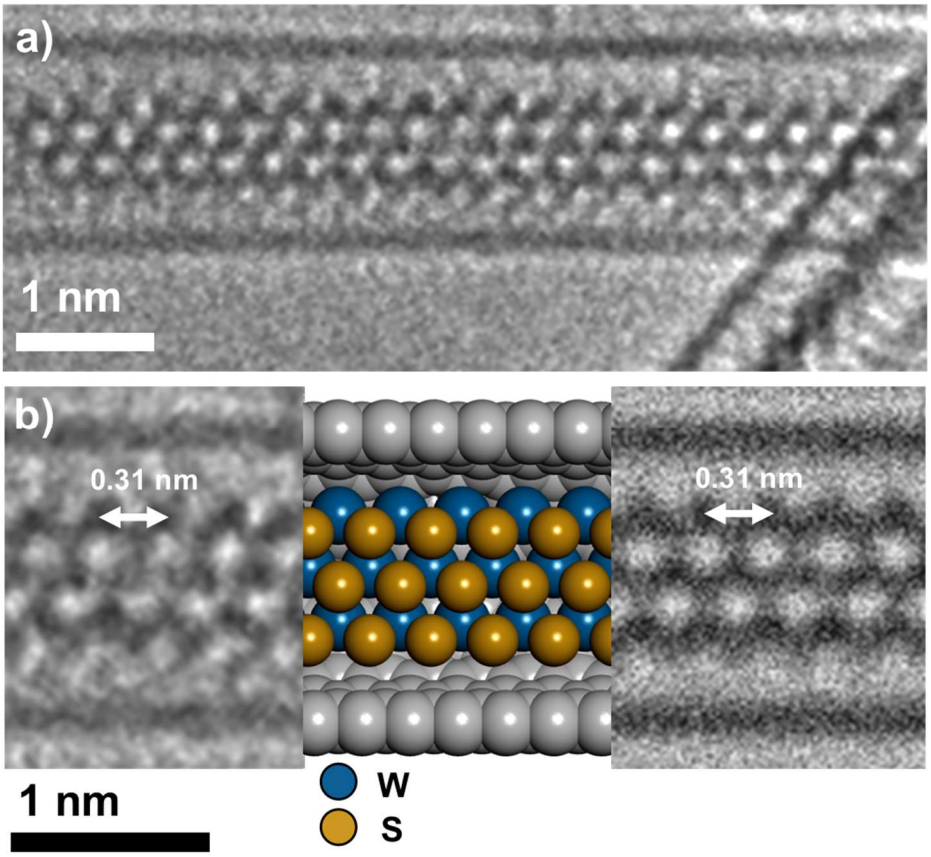


Figure 5.10. *(a) 60 kV AC-TEM image of WS_2@SWNT. The image shows a three atom thick nanoribbon with zigzag edges and thus is described as $3ZWS_2NR$; (b) Cropped and magnified*

image from (a) with the interatomic W-W distance measured from contrast analysis to be 0.31 nm (left); structural model of a 3ZWS$_2$NR inside a 10, 10 SWNT (middle); TEM simulation of the structural model (right) using imaging parameters in (a) which displays the same interatomic distance as the experimental image characteristic of WS$_2$ nanostructures.

The narrow width of the structure provides a large proportion of dangling bonds (e.g. 2/3 of W atoms are at the edges of nanoribbon) thus allowing dynamic transformations to be observed in real time whilst being imaged by the electron beam in a *ChemTEM* process[39]; various types of defects were observed during the 11 second time-series including; atomic defects, slip lines, and chain removal (Figure 5.11a- l). The first example, occurring during the first four seconds of imaging, is of multiple atomic defects forming resulting in reconstruction of the nanoribbon, which caused displacements of atomic rows of the quasi-1D crystal to form, which known as slip lines[4] (Figure 5.11a- e, indicated by red arrows). The second example is of two successive atomic defects, over two seconds of imaging (Figure 5.11f – h, indicated by yellow arrows). The first of the yellow arrows in the time-series show the presence of a pristine face-on section of the nanoribbon corresponding to two hexagons in width; the next arrow indicates one of the features in the second row of atoms becoming lighter in contrast which suggests that one sulfur atom has been removed leaving one remaining in the same position in projection, decreasing the overall contrast. It appears that the atom has not been lost from the nanotube and has indeed bonded to the top edge of the nanoribbon, shown one atom to the right of the yellow arrow in the second frame of the yellow arrow series (Figure 5.11g). The final frame then shows the second sulfur atom has been removed creating a vacancy defect in the structure (Figure 5.11h).

The final two examples of defect formation witnessed are the loss of atomic chains between sequential images, rather than the previous single atom defects formed (Figure 5.11h- k). In

both instances, indicated by the green and blue sets of arrows, a near pristine section of the nanoribbon undergoes the loss of a chain of the middle row of atoms. By measuring the distance of the voids formed, and using the known interatomic distances it can be approximated that, during the one second of imaging, there are 15 atoms ejected simultaneously in the section indicated by green arrows, and a chain of 12 atoms ejected in the section indicated by the blue arrows. The likely scenario for this, given that the process occurs over one second, is that chains of atoms are being ejected together. In terms of the reason for this phenomena it is unclear at this stage; it is unlikely to be a result of momentum transfer as within this timescale the atoms have time to relax after electronic collisions. The previous removal of fragments of BNNTs under electron beam was a result of charging of the species which led to coulombic explosions[40]; however, this process can only occur for insulating materials, and this composite material consists of a semiconductor within an electrically-conducting host. The final image of the series shows a section indicated by a pink box which highlights one of the voids in atomic detail and will be further studied by contrast analysis, modelling, and TEM image simulations to fully understand the structure formed in the nanoribbon under *ChemTEM* conditions (Figure 5.11l).

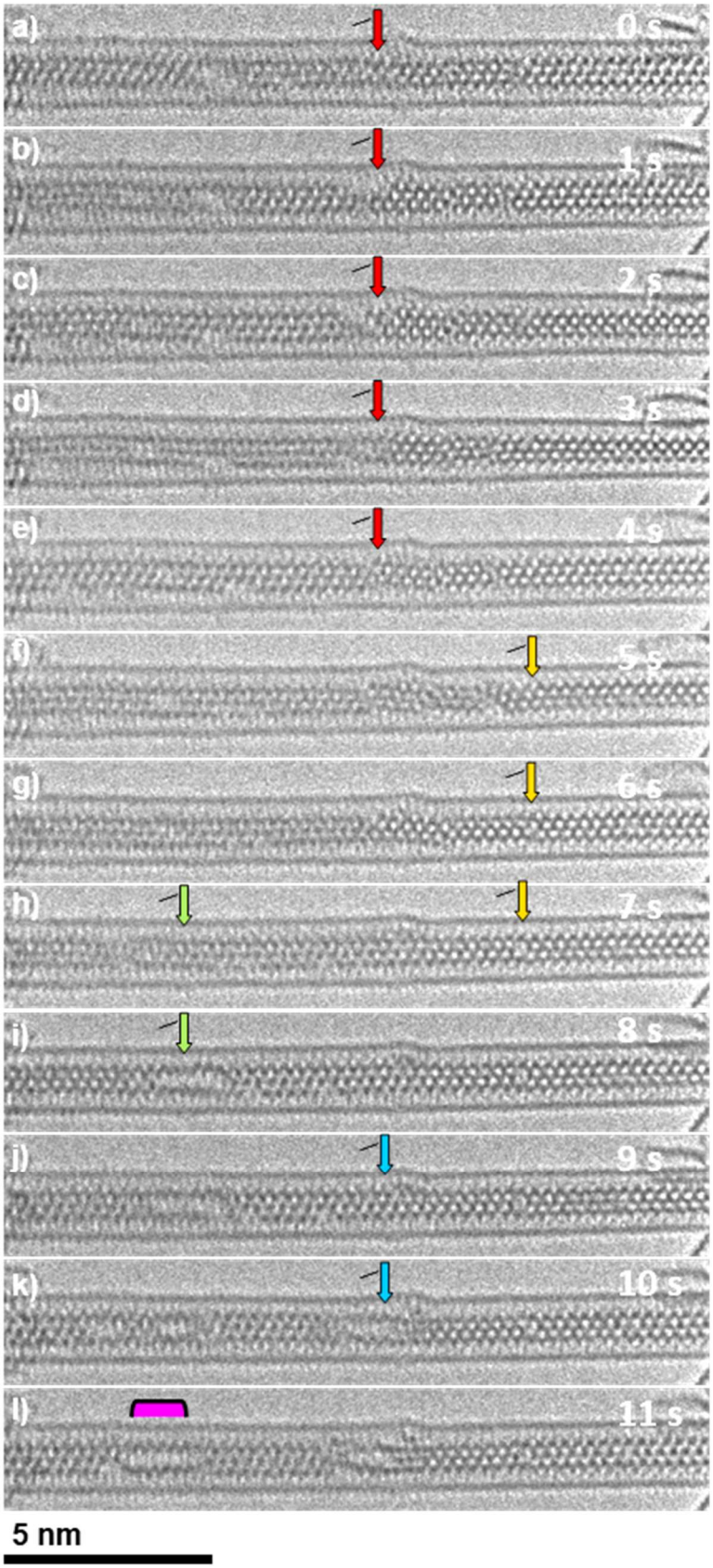


Figure 5.11. *(a - l) 60 kV AC-HRTEM series of WS_2@SWNT showing various e-beam induced defects in the nanoribbon. The red arrows display the process over defects reconstructing*

which results in the formation of a slip line (a-e). The yellow arrows indicate sequential single S atom defects occurring within a pristine section of the nanoribbon and the ejected atoms bonding to the top edge of the nanoribbon (f-i). The green and blue arrows show sections in which chains of atoms are removed in one step causing the loss of 12 to 15 atoms simultaneously (j, k). The pink section highlights a section which consists of the nanoribbon with the middle row of atoms ejected causing two strands of atoms to remain. Images were measured in one second time steps for a total of 11 seconds (l). The dose rate during imaging was 2.0 x 10^6 e^- nm^{-2} s^{-1}.

Detailed examination of the section of the nanoribbon containing the void indicated by the pink box in (Figure 5.11l) revealed the presence of two strands composed of two atomic rows of WS_2 each (Figure 5.12a and b). Two-dimensional (2D) contrast analysis of each of the two rows of the top strand revealed that there was a difference in contrast; the contrast intensity plots of the two rows were superimposed and revealed that the top row features were always lighter in contrast than the bottom row suggesting they consisted of S_2 units in projection, and tungsten atoms respectively (Figure 5.12c). Furthermore, the W…W interatomic distances measured for each row were both found to be 0.31 nm, the known interatomic distance in WS_2; this strongly suggests that the strands are ultrathin, zigzag edge chains of tungsten disulfide, 1ZWS_2NR. To confirm this hypothesis, a structural model of a 3ZWS_2NR within a (10, 10) SWNT was constructed and a section of the middle row of atoms was removed to leave two strands of two atomic rows remaining (Figure 5.12d); a TEM simulation, using parameters close to the experimental conditions, was then conducted on this model (Figure 5.12e). The simulation demonstrated the difference in contrast observed between the top and bottom atomic rows as well as the interatomic distances matching well the experimental images, confirming the structure of atomic chains to be a zigzag of WS_2 units with tungsten atoms on one side and pairs of sulfur atoms on the other (Figure 5.12f).

The dynamics of ultrathin WS_2 NRs supported by SWNTs and studied under the *ChemTEM* imaging conditions has proven the existence of WS_2 in a form of atomically thin wire, revealing atomistic mechanisms of transformation of nanoribbon to the atomic wires.

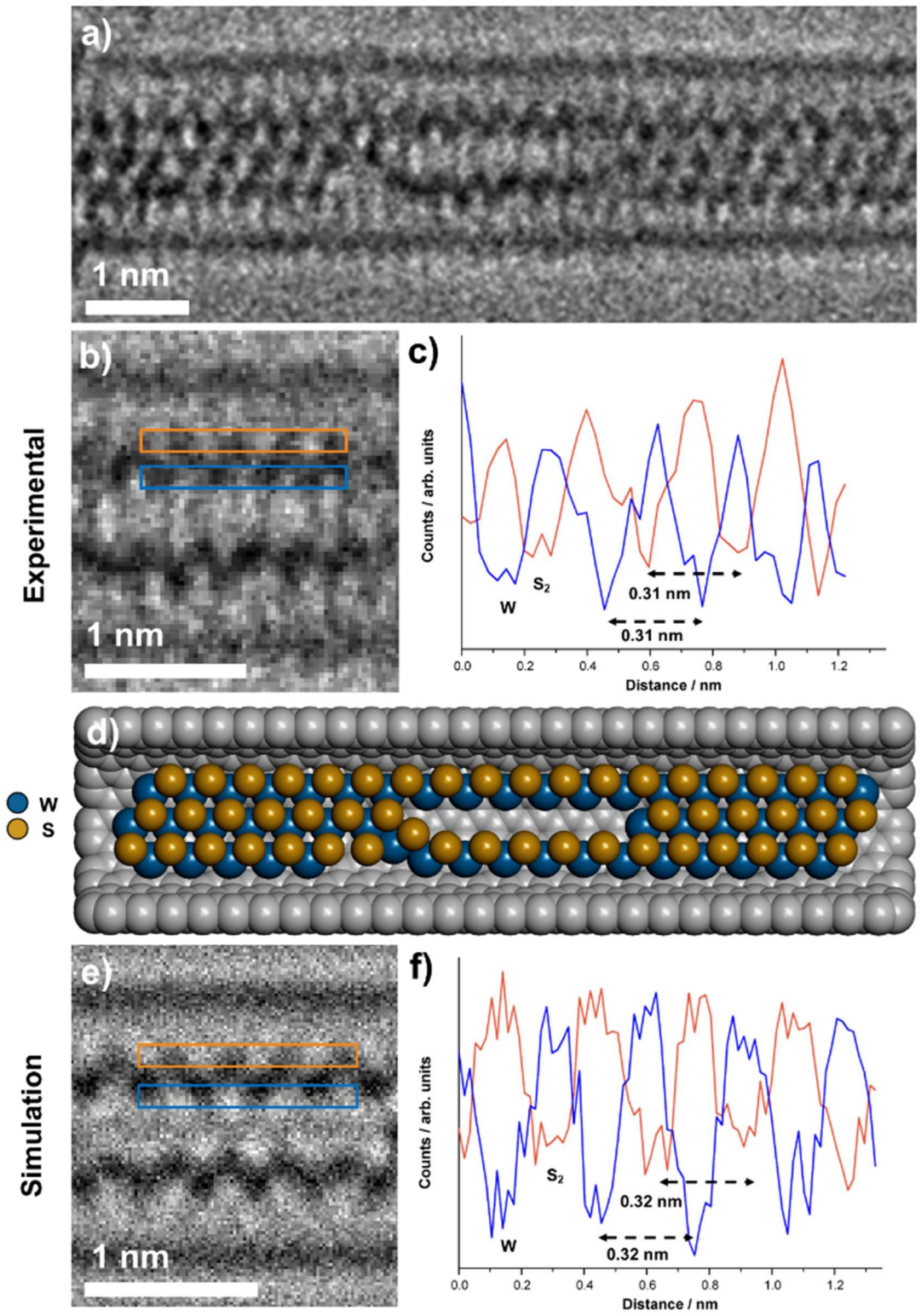


Figure 5.12. *(a) 60 kV AC-TEM image of WS_2@SWNT showing the presence of an atomic chain defect formed upon electron beam irradiation of a 3ZWS_2NR structure; (b) digitally-magnified image from (a) on which 2D contrast analysis was performed on the areas indicated by the*

two orange and blue rectangles; (c) 2D contrast analysis of the areas shown in (b) which shows the difference in contrast intensity between the top and bottom row of atoms as well as the interatomic distances recorded; (d) structural model of a modified 3ZWS$_2$NR within a (10,10) SWNT where the middle row of atoms have been removed; (e) TEM simulation of the structural model in (d); (f) 2D contrast analysis of the two areas indicated in (e) which confirm the experimental contrast intensity difference as well as the interatomic distances.

In both instances of the time-series in which a large void was created via chain ejection, and the examples of single atomic defects, it was the middle row of atoms that were affected. This is explained by the interactions of the nanoribbon with the nanotube interior sidewalls and the unique structure of the 3ZWS$_2$NR. The nanoribbon consists of a single layer and is three atoms in width, this means that only the outer two rows are in contact with the nanotube sidewalls and are thus stabilised compared to the middle row which has void space between it and the above and below sections of the nanotube wall, making it the least supported area, and thus weakest, of the rows (Figure 5.13). This is the first time that a 1Z dichalcogenide structure has been formed; the previous smallest nanoribbon was fabricated in a study by Liu *et al*. who produced two-atom thick MoS_2 nanoribbons by electron beam irradiation of a MoS_2 monolayer.[41] Previously WS_2 nanoribbons (of four W atoms in width) within SWNTs were found to undergo atomic defect formations upon irradiation with a 60 kV electron beam; the use of a lower voltage beam lowered the probability of a point defect forming by knock-on damage.[4] However, only single-atomic defects were observed during imaging and, in particular, W vacancies led to slip deformations as observed in this work. The removal of atoms in groups is known for boron nitride nanotubes,[40, 42] but this is a result of charging of the insulating species. A mechanism that was proposed by Kretschmer *et al*. found that excitations present in semiconducting species may result in the formation of atomic vacancies through energy transfer at electron energies below the knock-on threshold.[43] Therefore, the new phenomena of atomic groups being removed by the electron

beam at a relatively low voltage (60 kV) may be possible due to the combination of the unique structure of the 3ZWS$_2$NR, the entrapment within a SWNT offering stabilisation to the outer two rows of atoms, and the addition of excitations present may result in the loss of groups of atoms from the nanostructure.

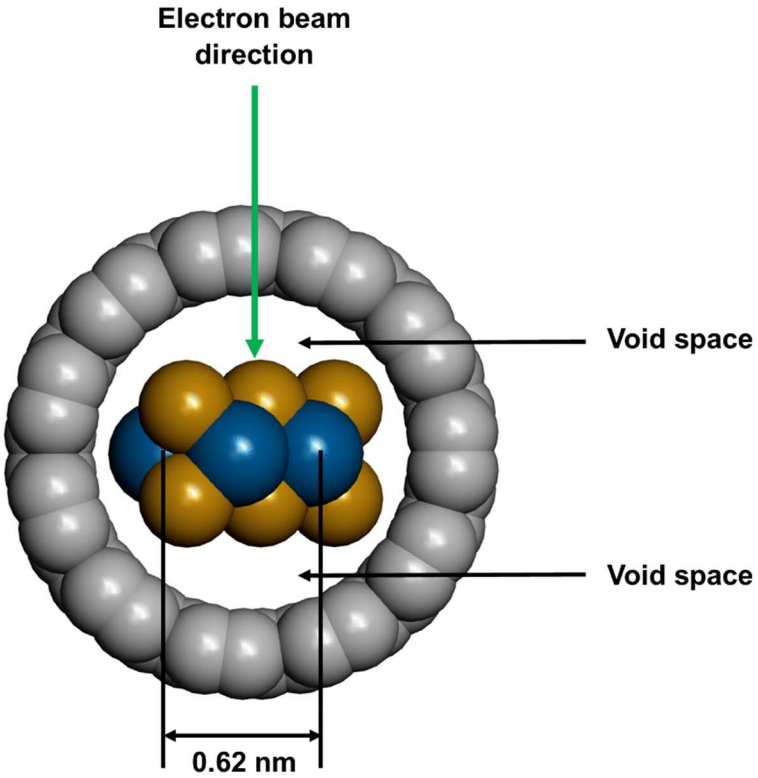
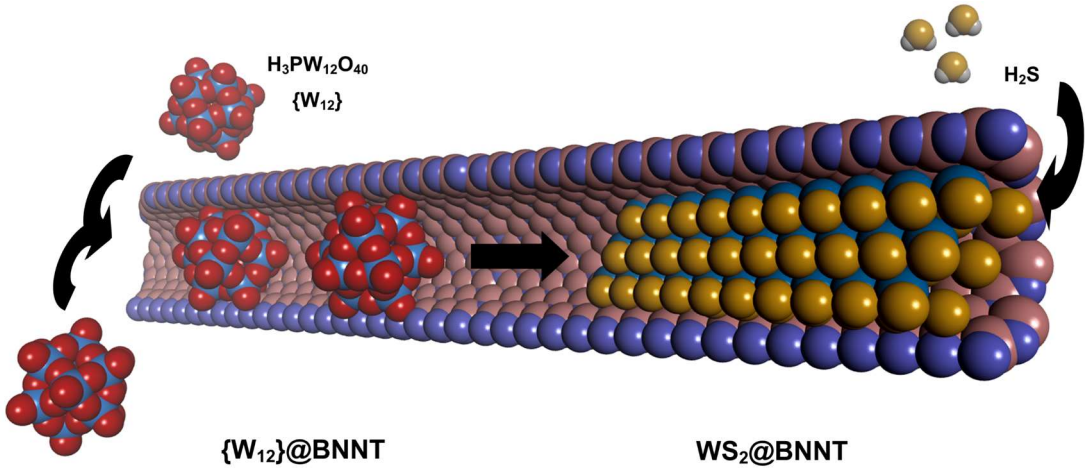


Figure 5.13. *Cross-sectional structural model of a 3ZWS$_2$NR inside a (10,10) SWNT. The model highlights the void space between the faces on the nanoribbon and the SWNT sidewall, as well as the direction of the electron beam.*

5.2.2. WS_2 within boron nitride nanotubes

In order to form tungsten disulfide nanowires in BNNTs, the same synthetic route that was proposed for SWNTs was used (Scheme 5.2). Previous work by Walker *et al.* synthesised carbon nanotubes within BNNTs; the BNNTs required a rigorous cleaning procedure involving ultrasonication in ammonium hydroxide as well as heating to 800 °C, and subsequent washing in hot water.[29] New advances in BNNT manufacturing has led to the production of a

batch denoted as *SP10-RX* which are more refined, do not require opening, and contain less impurities; the latter of which quenches photoluminescence of BNNT during light excitation, relating them more accurately to their bulk properties as insulators with large band gaps. The BNNTs contain >99% h-BN content, consist of between 1 to 5 walls per nanotube, have lengths up to 200 µm, and have a band gap of 5.7 eV.[44]



Scheme 5.2. *Schematic diagram showing the stepwise synthesis of tungsten disulfide nanoribbons within boron nitride nanotubes using polyoxometalate precursors.*

5.2.2.1. Insertion of the W_{12} POM into BNNTs

The BNNTs were first characterised by TEM, EDX, XPS, and Raman spectroscopy, in order to determine their structure and composition. TEM analysis showed that the BNNTs were empty with unmodified exteriors (Figure 5.14a), however, there were scarce examples of boron impurities present (Figure 5.14b inset). EDX analysis confirmed the presence of boron and nitrogen in a 1.6: 1 atomic ratio (Figure 5.14b). Further elemental analysis was conducted by measuring the peak positions of the elements by XPS; the boron 1s region contained two overlapping components, the highest intensity component at 190.3 eV and the lower intensity at 191.5 eV were assigned as the BNNT and B_2O_3 respectively (Figure 5.14c).[45, 46] The N 1s region contained one peak at 397.8 eV which was assigned to the BNNT (Figure

5.14d). The peak positions of B and N of the BNNTs were monitored during each step to examine any effects on the elemental states upon interior modification.

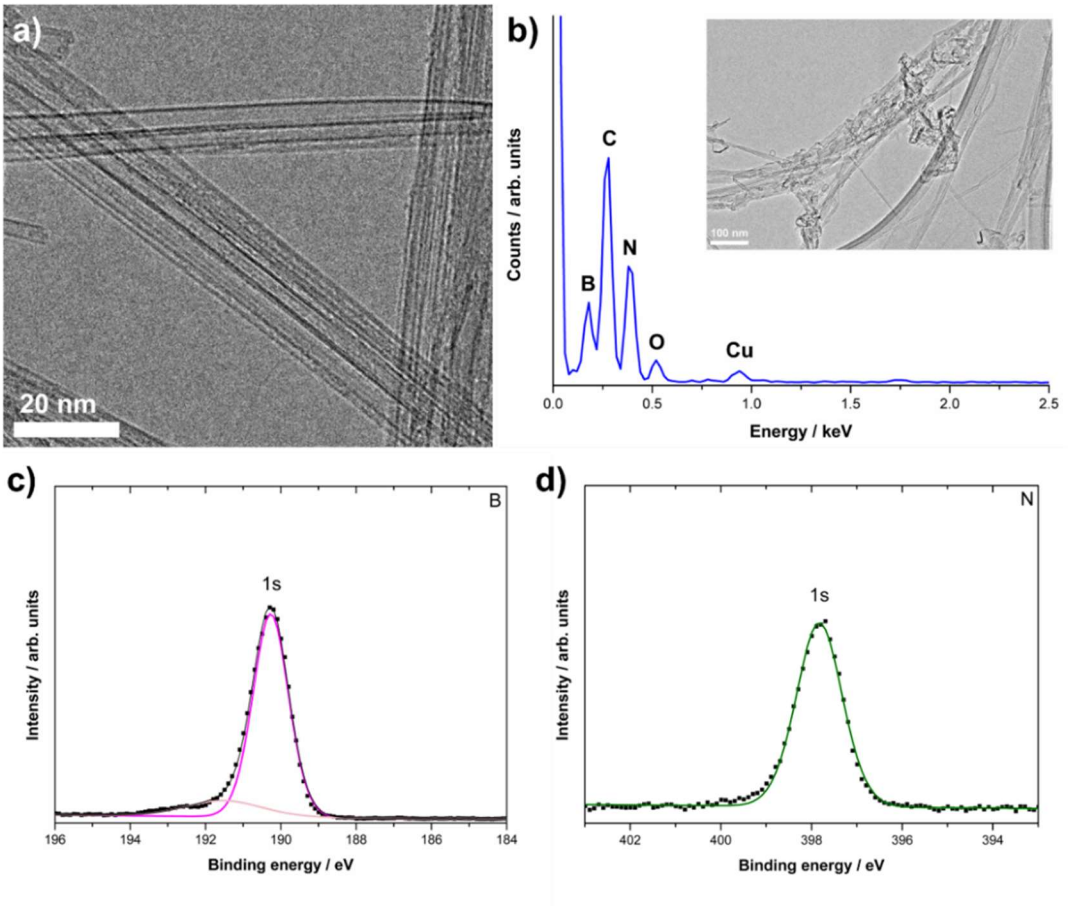


Figure 5.14. *(a) 200 kV TEM image showing bundles of empty and opened BNNTs; (b) EDX spectrum, measured over a region containing bundles of BNNTs as well as some boron impurities (inset) which confirmed the constituent elements of the host BNNT were present, along with carbon from the nearby lacey carbon film. XPS high resolution scans recorded over the (c) B 1s region and the (d) N 1s region.*

Raman spectroscopy, using a laser excitation of 660 nm, was conducted on the empty BNNTs which identified one primary peak at 1360 cm^{-1} which was characterised as the B-N E_{2g} stretching mode (Figure 5.15).[47] Two smaller peaks were also observed at 820 and 882 cm^{-1}; the first corresponding to the B-N out-of-plane buckling mode and the second to B_2O_3 contaminant, the latter of which correlating well with XPS observations. It was also clear

from the spectrum of BNNT that photoluminescence was not present as the baseline was flat.

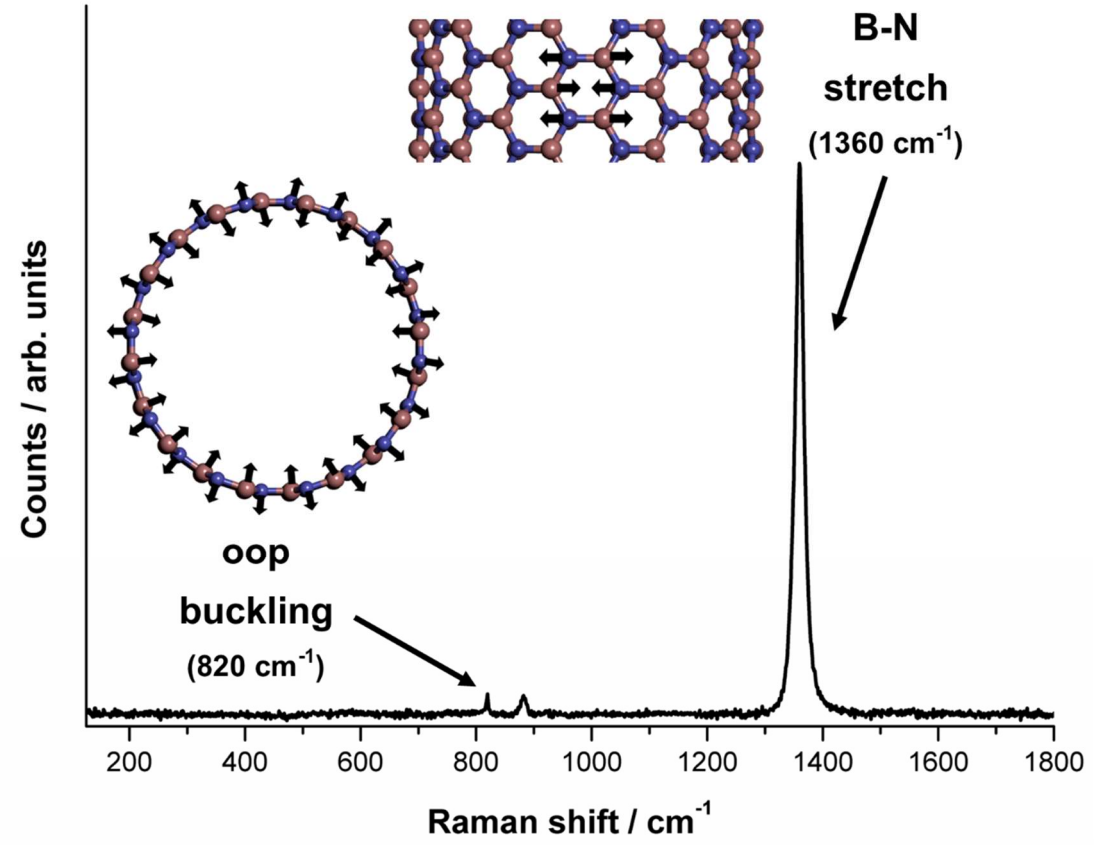


Figure 5.15. *Raman spectrum of BNNTs using a 660 nm laser source. The spectrum shows the presence of one primary peak, at 1360 cm^{-1}, which is due to the B-N stretching mode. Also observed is a smaller peak at 820 cm^{-1} corresponding to the out-of-plane buckling mode. Superimposed are structural models demonstrating these vibrational modes.*

The tungsten Keggin polyoxometalates, $H_3PW_{12}O_{40}$, were inserted into the BNNTs via a room temperature solution-phase filling method; this did not result in a colour change of the aqueous solution, as observed for the filling into SWNTs, and upon filtering, the BNNTs retained their white colour. HR-TEM imaging of a 350 nm long triple-walled BNNT showed excellent filling within the whole structure (Figure 5.16a - c) which was representative of the material. Magnification of the BNNT demonstrated the presence of isolated POM clusters as well some dimers and extended structures occurring via condensation reactions triggered by

the electron beam. EDX analysis of the long BNNT found a high atomic % of carbon present but this is a result of recording near to the lacey carbon film which the filled BNNT was suspended over. Also detected was the presence of boron and nitrogen from the host, as well as tungsten, oxygen, and phosphorus from the guest POMs (Figure 5.16d).

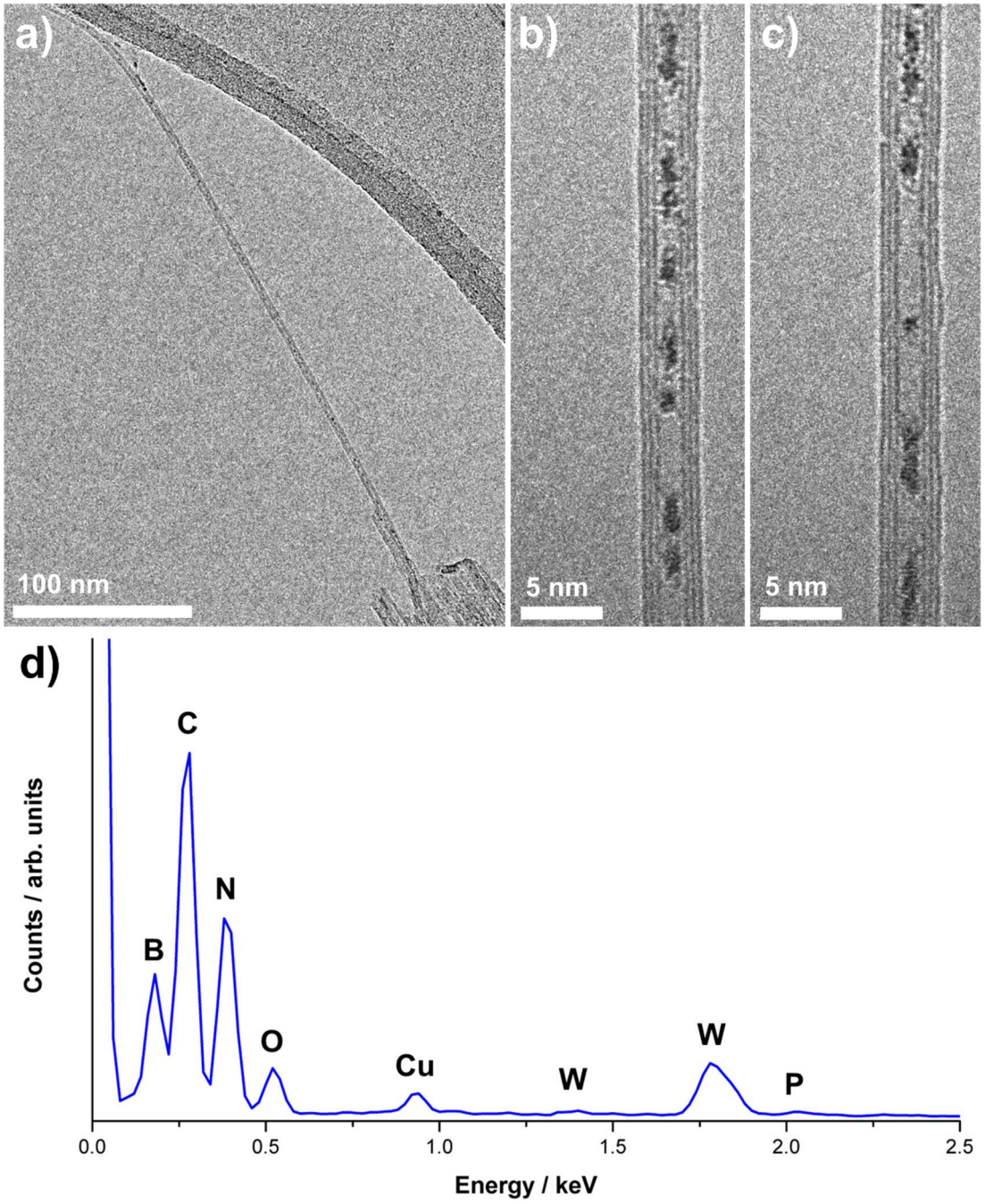


Figure 5.16. *200 kV TEM images of a 350 nm long triple-walled BNNT filled with POM clusters at (a) lower and (b – c) higher magnifications; (d) EDX spectrum of the area in (a) identifying*

the presence of B and N from the nanotube host, and W, P and O from the POM encapsulants. The presence of carbon is due to the nearby lacey carbon film which can be seen in the top right corner of (a), and Cu originates from the TEM grid composition.

The peak positions of the B 1s and N 1s photoelectrons, from XPS, were unchanged at 190.2 and 397.7 eV respectively suggesting the filling has no effect on the state of the host species, and the peak for B_2O_3 at 191.1 eV was still present (Figure 5.17a and b). The W 4f region contained three peaks originating from the expected 4f doublet at 35.8 (4f 7/2) and 38.0 eV (4f 5/2) and the overlap with the W 5p 3/2 peak at 41.6 eV (Figure 5.17c). The 4f doublet energies are identical to those measured of $H_3PW_{12}O_{40}$ previously[37], confirming that the POM structure or composition has not been changed upon encapsulation into BNNTs. The peak positions of the W 4f doublet are red shifted by 0.3 – 0.4 eV compared to $\{W_{12}\}$@SWNT and this is a result of the previous SWNT host being in electronic communication with the POMs. Multiple components were measured over the O 1s region which highlights the different O environments present in both the POM structure as well as the small amount contributed from B_2O_3 impurities (Figure 5.17d).

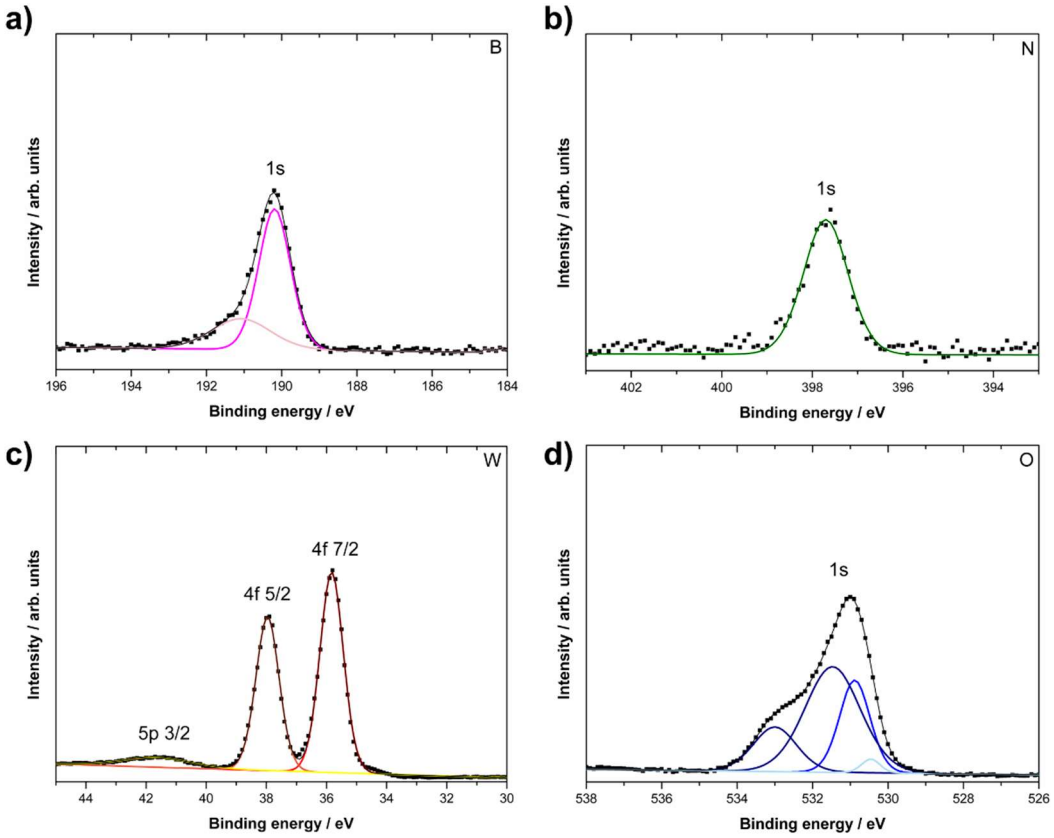


Figure 5.17. *High resolution XPS scans measured over the (a) B 1s; (b) N 1s; (c) overlapping W 4f and 5p; (d) O 1s regions.*

Raman analysis, using 660 nm excitation, of $\{W_{12}\}$@BNNT and the parent species, $H_3PW_{12}O_{40}$, were conducted to examine if the vibrational modes of the POM could be identified in the composite material (Figure 5.18). The spectrum of $H_3PW_{12}O_{40}$ identified a number of low frequency modes from 150 – 600 cm^{-1} as well as three primary characteristic stretches; ν_s (W=O) at 1013 cm^{-1}, ν_{as} (W=O) at 989 cm^{-1}, and ν_{as} (W-O_c-W) at 932 cm^{-1}.

The spectrum of $\{W_{12}\}$@BNNT presented as an approximate superposition of both the POM and BNNT spectra retaining the B-N stretch at 1360 cm^{-1} and the low frequency POM modes from 150-600 cm^{-1}. The three key POM stretches were also present in the 930-1020 cm^{-1} region but with some shifting; the symmetric W=O stretch had red shifted to 1009 cm^{-1}, the asymmetric W=O stretch had blue shifted to 993 cm^{-1}, and the asymmetric W-O_c-W stretch had significantly red shifted to 905 cm^{-1}. This highlights that when the polyoxometalates are

encapsulated within BNNTs, there is a preferential orientation which may arise from oxygen electron lone pairs interacting with empty boron p-orbitals (Figure 5.18b and c). A previous Raman study of $\{W_{12}\}$ within multi-walled carbon nanotubes reported a red shift of the terminal W=O mode which was explained by a strong interaction between the nanotube sidewall and the terminal W=O bonds.[33] The $\{W_{12}\}$@BNNT sample was also found to be stable to 100% laser power across multiple areas recorded, demonstrating thermal stability, and homogeneous filling.

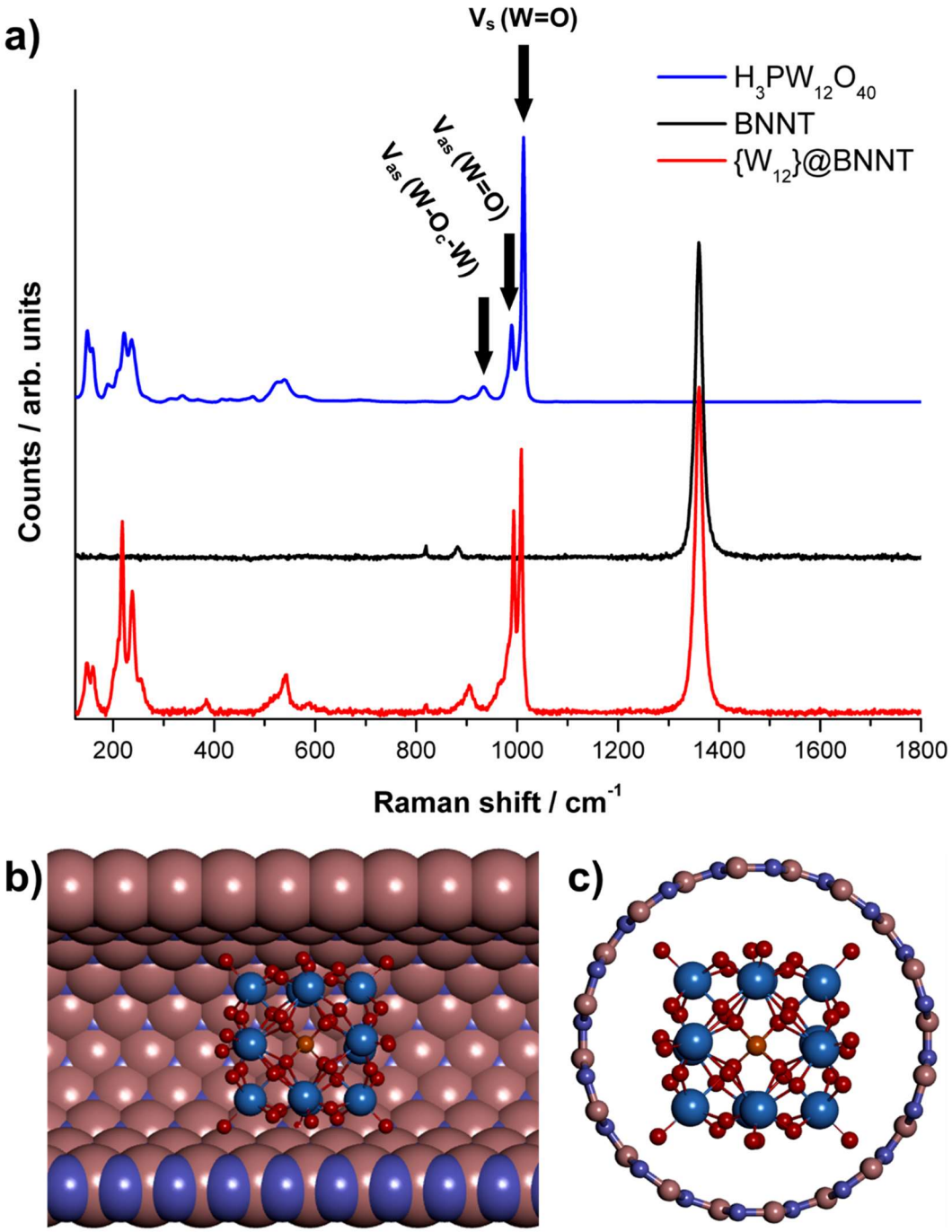


Figure 5.18. *(a) Raman spectra overlay of; $H_3PW_{12}O_{40}$ (blue), BNNT (black), and {W_{12}}@BNNT (red) measured using a 660 nm laser excitation. The spectrum of {W_{12}}@BNNT is an approximate superposition of the spectra recorded over the parent species and host BNNT, with some shifting of the three primary POM modes being recorded. Structural models of {W_{12}}@BNNT showing the (b) POM interaction with the nanotube sidewalls, and (c) cross-sectional view highlighting the fit of the POMs within BNNT.*

5.2.2.2. Reaction to form WS_2 in BNNTs

The {W_{12}}@BNNT sample was then reacted with dihydrogen sulfide under an inert atmosphere, and the resultant material changed colour from white to black. WS_2, as a bulk layered material, is grey/black in colour and it is suggested that due to the transparent nature of the BNNTs that the colour of the encapsulated WS_2 is being directly observed.

TEM imaging of a bundle of BNNTs showed two continuous edge-on nanowires within a 2.3 nm diameter BNNT (Figure 5.19a). 2D contrast analysis was performed perpendicular to the nanotube axis which measured the interlayer spacing to be 0.61 nm correlating well with the known (002) spacing of bulk WS_2 (Figure 5.19b and c).[48] Furthermore, EDX spectroscopy was used to determine the composition of the nanowires which found them to consist of tungsten and sulfur in a 1: 2 ratio (Figure 5.19d). Also observed was boron and nitrogen from the host nanotube as well as a carbon which was in a larger abundance than both boron and nitrogen despite the bundle not being near to lacey carbon film. The TEM image also displays the significant presence of exterior material appearing as light contrast wavy lines which may be the carbon observed in EDX.

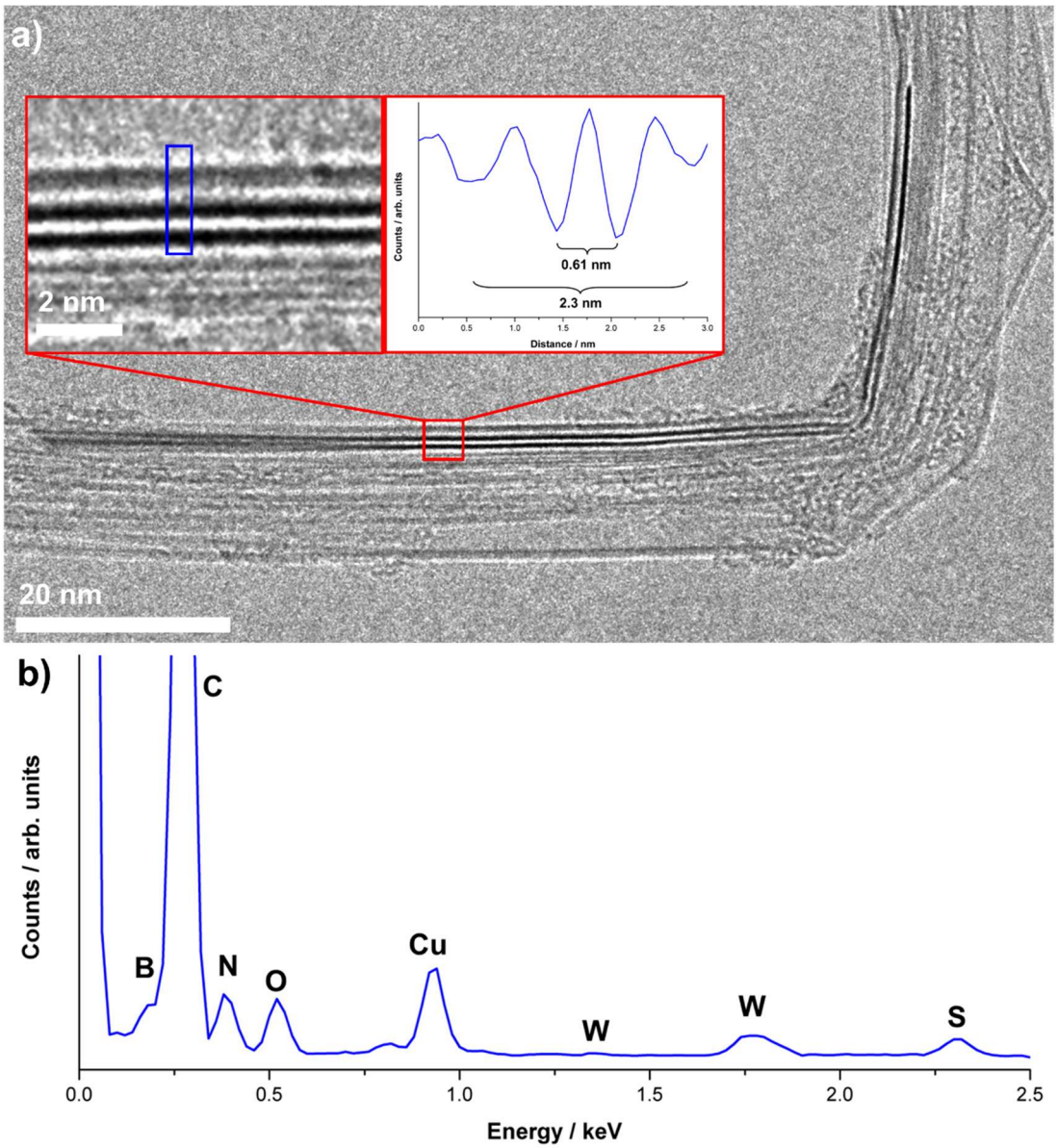


Figure 5.19. *a) 200 kV TEM of a BNNT filled with two WS_2 nanoribbons; b) digitally-magnified image showing the presence of the two nanoribbons in edge-on orientations (Inset is a line profile of the area conducted perpendicular across the area indicated in a) which depicts the interlayer spacing of the nanoribbons as 0.61 nm, as well as the BNNT diameter as 2.3 nm); b) EDX spectrum of WS_2@BNNT showing the presence of B and N from the host, and W and S from the nanoribbons in a 1: 2 ratio.*

Raman spectroscopy, measured using 660 nm excitation, identified the presence of two bands in the low-frequency region at 325 and 383 cm^{-1}, a broad feature around 1300 cm^{-1} attributed to carbon, and a large background attributed to photoluminescence (Figure 5.20).

The two low-frequency peaks are out of the expected region for the E_{2g} and A_{1g} modes of WS_2 and thus must be resonance enhancement of either a different phase or species. The high level of PL contributing towards the background is explained by the band gap of WS_2 (611 nm for the monolayer[49]) being close in energy to the 660 nm laser excitation. Also noted in the spectrum was an absence of the B-N stretch from the host BNNTs; the spectrum was measured using 1% laser power, compared to the 100% used for {W_{12}}@BNNT, as a result of a lower thermal stability of the material due to black material absorbing more photons, and thus because the B-N phonon mode is a weak scatterer it is not observed with respect to other modes, which have resonance enhancement. This highlights the importance of not solely relying on one technique for analysis but using a holistic analytical approach to understand the whole system from different points of view. Whilst Raman highlights the absence of the B-N stretch, TEM and EDX show that the BNNTs are present as the hosts of WS_2 nanoribbons, which are identified and characterised by all three techniques.

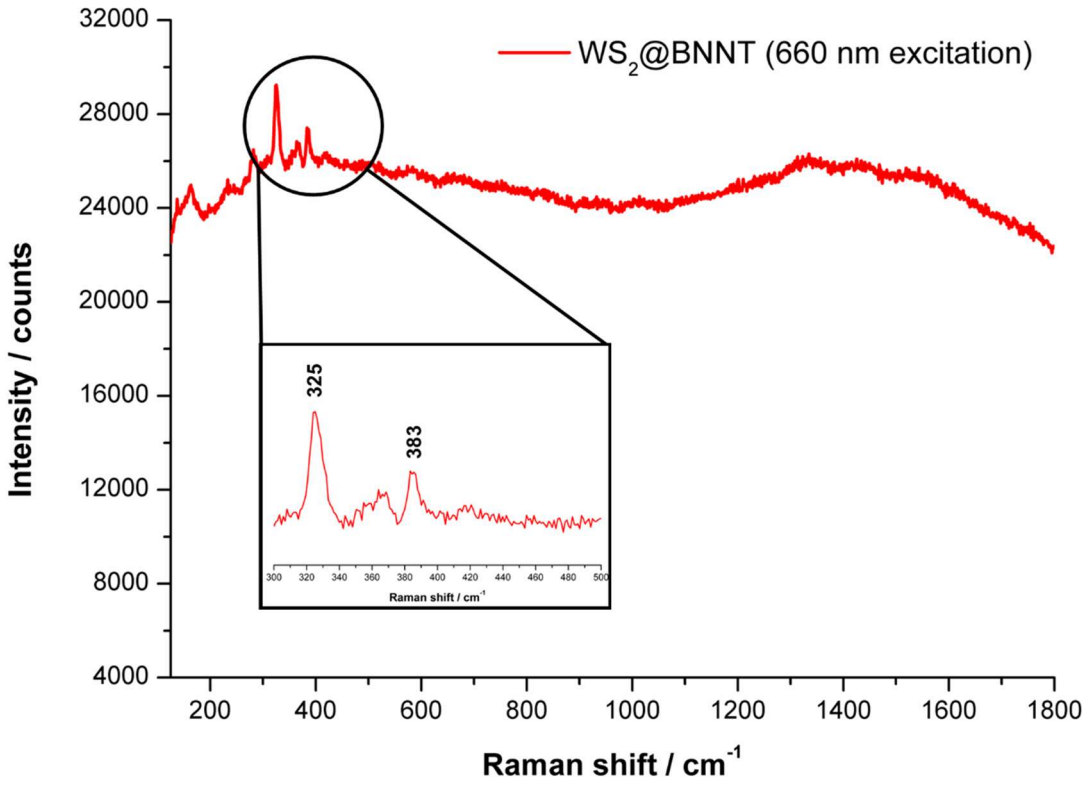


Figure 5.20. *Raman spectrum of WS_2@BNNT measured using a 660 nm laser excitation Superimposed on the image is a magnification of the 300 – 500 cm^{-1} region, which identifies the presence of two low frequency modes at 325 and 383 cm^{-1}.*

The final problem that required resolution in order to optimise the system was the high abundance of carbon in the material. It was hypothesised that it was the experimental setup that was responsible for this and not any contaminant from the precursor POMs, due to the lack of carbon bands in the Raman spectrum of $\{W_{12}\}$@BNNT. The reaction with H_2S uses two sets of Dreschel bottle gas bubblers before and after the furnace in the flow reaction which allow for any leaks in the flow system to be identified. However, the gas bubblers contain paraffin oil which is a source of saturated hydrocarbons, and it is proposed that the gas is transporting carbon from the bottles to the sample which is then reacted with the sample at high temperature. To minimise this effect; the experimental setup was modified by removing the Dreschel bottles at the position before the furnace (Figure 5.21). The as-synthesised

material still retained the black colour and thus this is an effect of having black/grey WS_2 nanoribbons within an optically-transparent BNNT host.

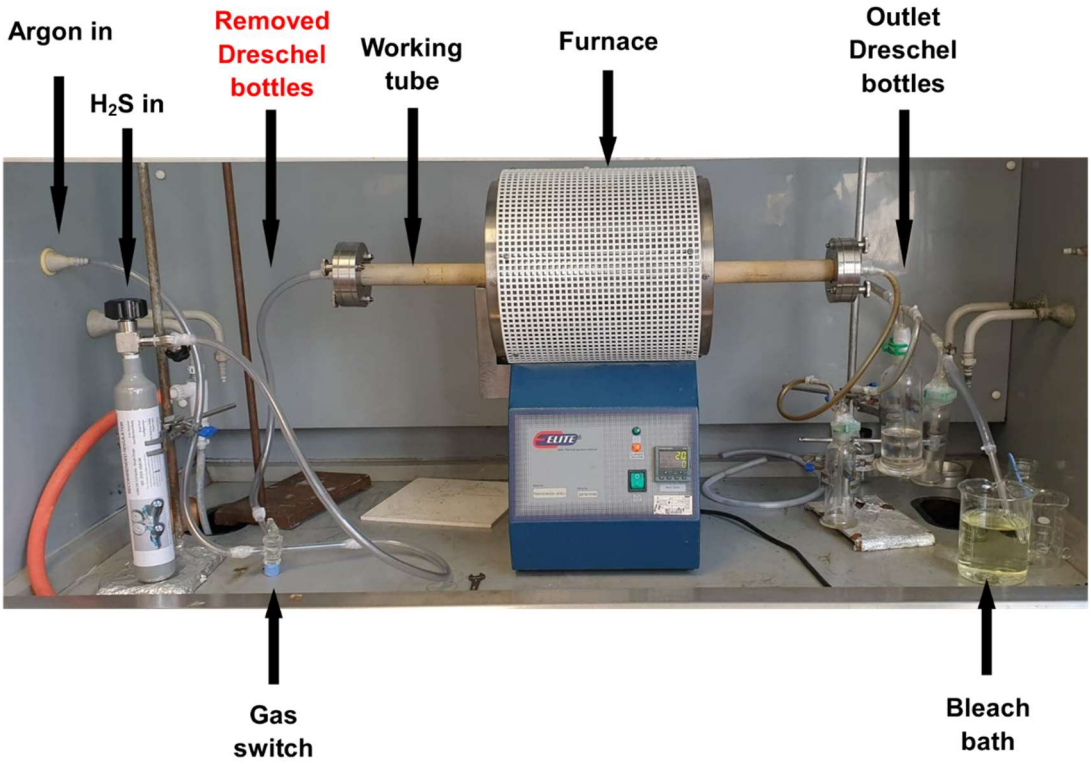


Figure 5.21. *Updated flow reaction set up which shows the two gas sources, the furnace complete with working tube containing the sample, the outlet Dreschel bottle set which leads to the bleach bas for H_2S neutralisation, and highlights the loss of the inlet Dreschel bottles and thus all carbon sources pre-furnace.*

TEM analysis correlated well with the previous unmodified setup identifying edge-on WS_2 nanoribbons within BNNTs (Figure 5.22a). However, the TEM image (Figure 5.22a) shows distinct gaps in the structure which suggests something was blocking the channel for nanoribbon growth, such as boron impurities. EDX analysis was recorded over a bundle of filled BNNTs in order to check the nanoribbon composition and determine the amount of carbon in the sample compared to boron and nitrogen (Figure 5.22b). As well as measuring a W: S atomic ratio at 1: 2.3; the B: N: C atomic ratio was found to be 2.4: 1: 0.3 which is significantly reduced compared to the unmodified setup. The peak positions, from XPS, of

the B 1s and N 1s photoelectrons were found to have only downshifted by 0.2 – 0.3 eV compared to those from {W_{12}}@BNNT previously (Figure 5.22c and d) which is not significant enough to conclude that the nanotube hosts have been affected. The W 4f doublet had significantly downshifted to 32.1 and 34.2 eV, for the 7/2 and 5/2 components respectively, compared to {W_{12}}@BNNT (Figure 5.22e); these values are in good agreement with XPS measured of WS_2 previously.[38] A doublet also appeared over the S 2p region with binding energies of 161.7 and 162.9 eV for the 3/2 and 1/2 components respectively. The presence of the new S peaks, as well as the downshift of the W 4f peaks, further highlights that the inorganic transformation from polyoxometalate to tungsten disulfide was successful.

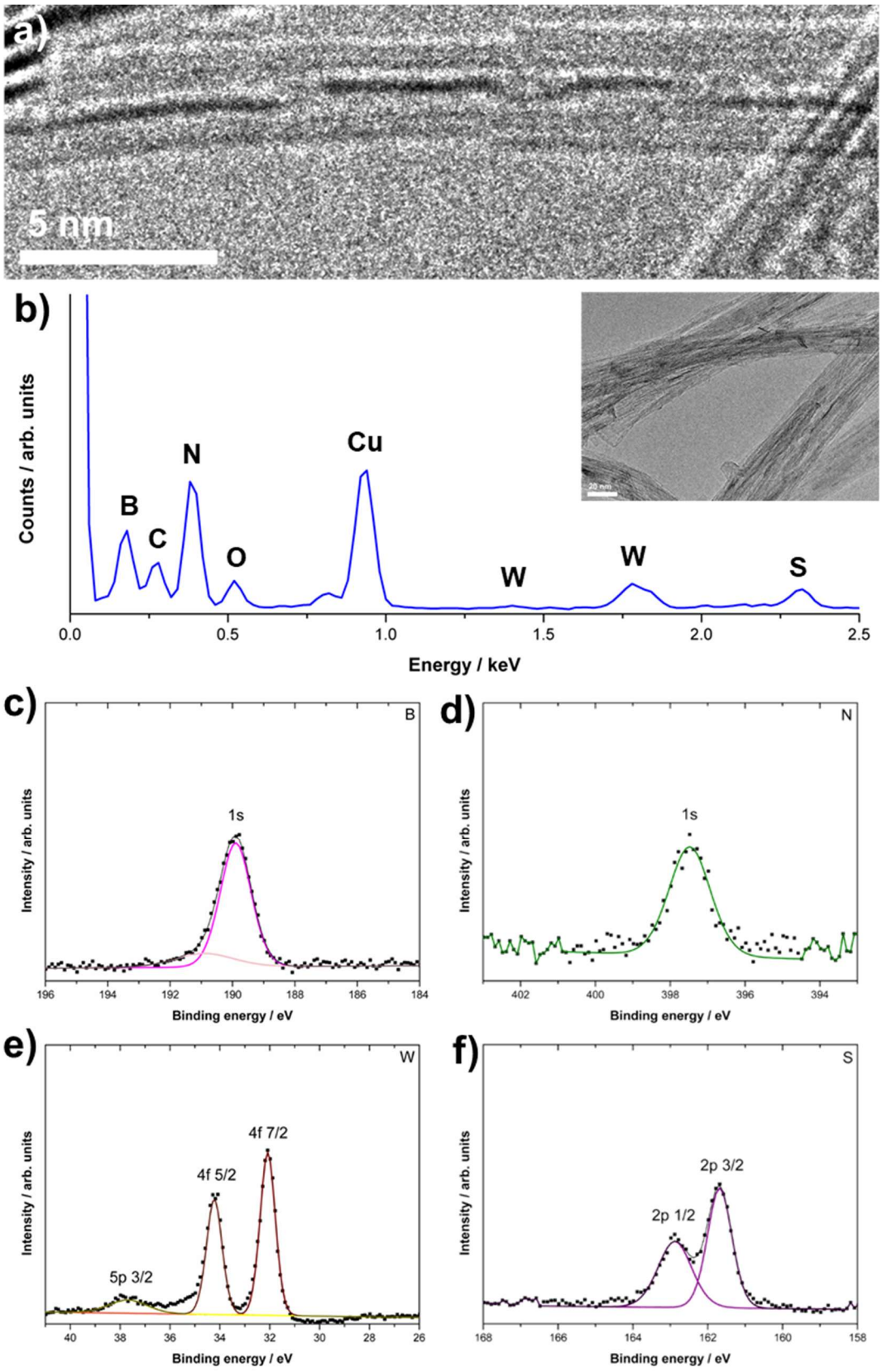


Figure 5.22. *(a) TEM images of WS_2@BNNT, after modification, showing the presence of an edge-on WS_2 nanoribbon; (b) EDX spectra, recorded over a bundle of BNNTs (inset),*

identifying boron and nitrogen from the host nanotube, as well as tungsten and sulfur in a 1: 2.3 atomic ratio. The presence of carbon was also detected but in a far lower abundance than previously observed. XPS high resolution spectra focussing on the (c) B 1s, (d) N 1d, (e) W 4f (and 5p), and (f) S 2p regions.

Raman spectroscopy was performed on the WS_2@BNNT material, synthesised using the modified experimental set up, using a 660 nm laser excitation (Figure 5.23). The spectrum was similar to the previous spectrum (before modification, Figure 5.20) showing the presence of a large PL background, and carbon peaks. This shows the power of resonance enhancement as despite the modification to the experimental set up and EDX showing significantly less carbon in the sample, the trace of carbon still present is being enhanced in the spectrum. A key difference of the new spectrum was the emergence of new low frequency modes at 353 and 414 cm^{-1} (as well as the previous set at 323 and 385 cm^{-1}) which are indicative of the E_{2g} and A_{1g} modes of WS_2.[50] This shows that the modified set up had improved the synthesis towards WS_2 nanoribbons.

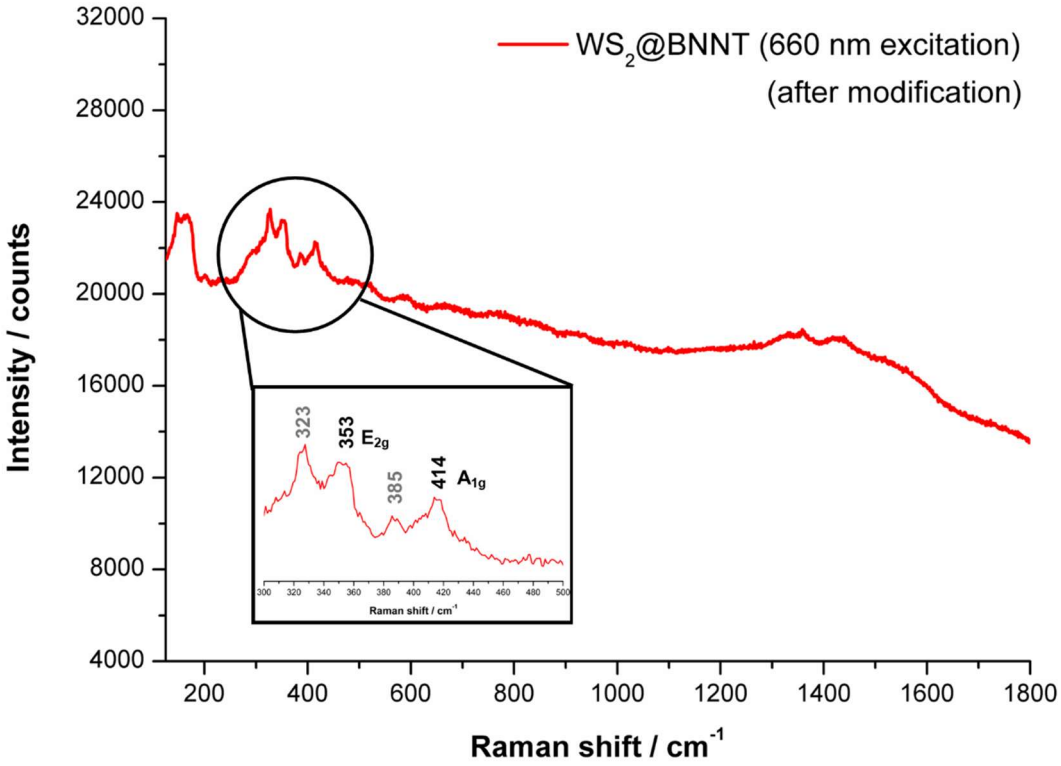


Figure 5.23. *Raman spectrum of WS_2@BNNT after modification, measured using a 660 nm laser excitation. Superimposed on the image is a magnification of the 300 – 500 cm^{-1} region, which identifies the presence of two set of low frequency modes at 323 and 385 cm^{-1}, and 353 and 414 cm^{-1}; the latter of which is indicative of the E_{2g} and A_{1g} modes of WS_2.*

The material was then imaged using AC-HRTEM in order to probe the structure at the atomistic level. The first area imaged shows a double-walled BNNT of internal diameter 1.8 nm that is on the end of a bundle of BNNTs (Figure 5.24a). Within the internal channel are two helical nanoribbons that are initially in a tilted face-on orientation, appearing as diagonal lines, and then twist to exhibit the edge-on layered structure which reveals the two layers present. A contrast analysis profile perpendicular to the nanotube axis across the layered area reveals the presence of the two nanotube sidewalls on either side, along with two high contrast features and four lower contrast features which are attributed to tungsten and S_2 units in projection respectively (Figure 5.24b). Moreover, the interlayer distance was found to be 0.61 nm which is the same as observed in bulk WS_2.

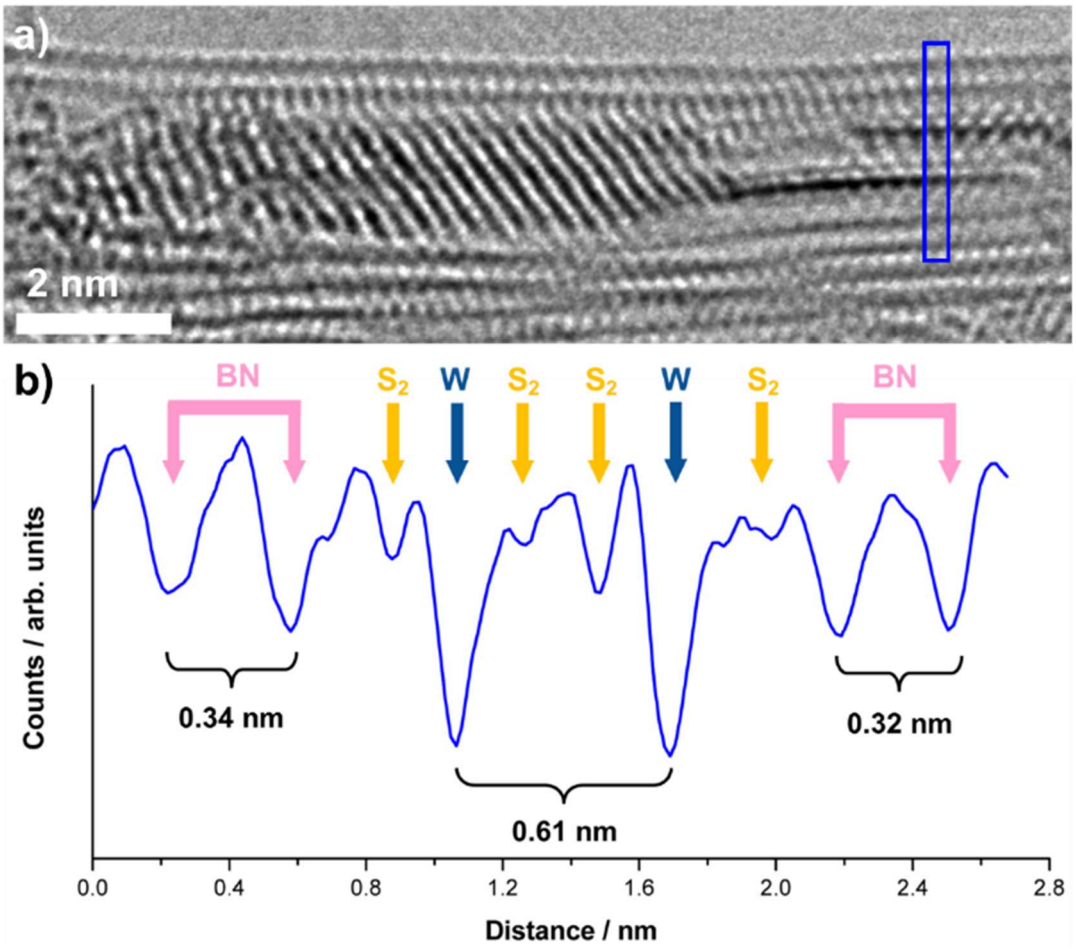


Figure 5.24. *(a) 80 kV AC-HRTEM image of WS_2@BNNT displaying two helical twisting nanoribbons, within a double-walled BNNT, which can be viewed in edge-on and face-on orientations; (b) 2D contrast analysis of the area indicated by a blue rectangle in (a), which shows the characteristic 0.61 nm inter-layer distance, difference in contrast between tungsten and S_2 units in projection, and the distances between the outer and inner nanotube walls.*

The second area analysed (Figure 5.25a) shows an 8-atom wide nanostructure with a hexagonal lattice within a double-walled BNNT of 2.6 nm internal diameter. The structure is confirmed to be tungsten disulfide due to the characteristic 0.32 nm W…W interatomic

distances observed and is proven further by a combination of modelling and TEM image simulation (Figure 5.25b). However, the structure is only approximately 7 nm in length and thus should be considered not as a nanoribbon but as a zero-dimensional quantum dot (QD). QDs are semiconducting nanoparticles which have optical properties that are highly tuneable based on their size,[51, 52] and have been previously shown to be of interest for applications in solar cells.[53] The growth of the quantum dot to become a nanoribbon appears to be halted by the presence of boron impurities within the BNNT, which can be observed on the left hand side of the image appearing as amorphous material. The product of the reaction conducted within SWNTs was not observed to produce quantum dots, only continuous nanoribbons, this is because the SWNTs were initially heat-treated to remove amorphous carbon potentially blocking interior sites.

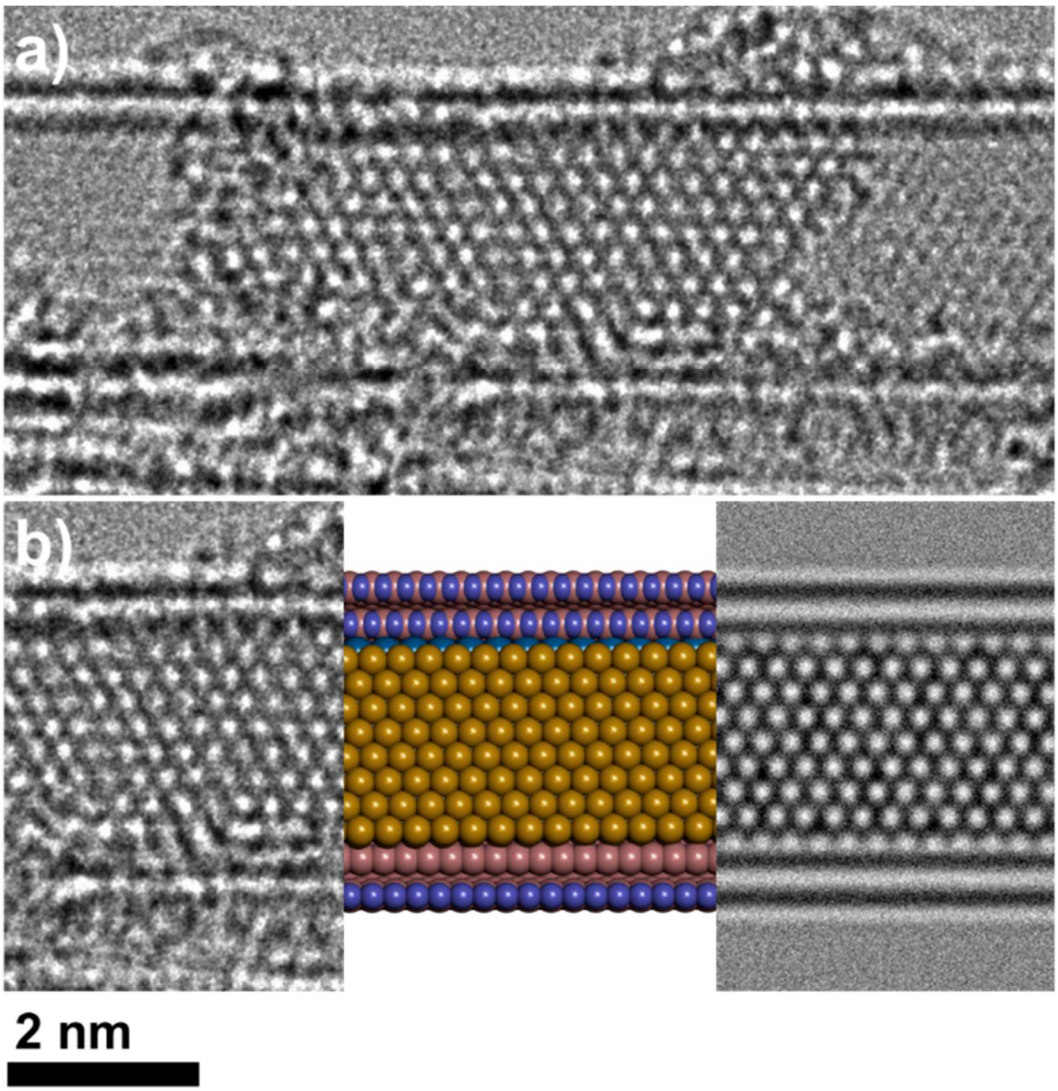


Figure 5.25. *(a) 80 kV AC-TEM analysis of WS_2@BNNT showing a 8ZWS_2QD within a double-walled BNNT of internal diameter of 2.6 nm; (b) 80 kV AC-TEM image (left), structural model of WS_2@double-walled BNNT (middle), and corresponding TEM simulation of the structural model (right).*

The last area that will be analysed featured a double-walled BNNT with an internal diameter of 1.8 nm and amorphous material within the interior channel (Figure 5.26a). The area was imaged over 350 seconds and revealed the profound effect of the electron beam on the system by both triggering and imaging chemical transformations via a *ChemTEM* process (Figure 5.26a – q).[39] The first process to occur, over a 51 second time period, was the rearrangement of amorphous material into more ordered nanoparticle structures; as a result

of this phenomenon, the volume of the material decreased within the BNNT channel (Figure 5.26a – c). Furthermore, after 108 seconds eight nanoparticles were formed which exhibited high crystallinity (Figure 5.26c – f). During the growth of the nanoparticles it can be simultaneously observed that they interact with the inner walls of the BNNT removing atoms producing chains of boron triggered by the 80 kV electron beam (Figure 5.26d – h). The process of removing boron atoms from the host BNNT occurs because the threshold for knock-on damage is 74 keV and 84 keV for boron and nitrogen respectively, which for pristine BNNT results in electron beam-induced boron vacancy formation, as determined by Zobelli *et al*.[54] Furthermore, Warner *et al*. have shown experimentally that the 80 kV e-beam initially ejected boron atoms from hexagonal-BN which was followed by nitrogen atoms that were present around the monovacancy defect.[55]

Between frames (i) and (j), over a period of 23 seconds, nanoparticles fourth and fifth from the left undergo coalescence to form a slightly larger nanoparticle (Figure 5.26i and j). The reasoning behind this phenomena is due to the nanoparticles attempting to reduce their surface energy by forming larger structures. This process is then repeated during the images taken at 231 and 272 seconds in which the first two nanoparticles on the left side also coalesce to form an extended structure resulting in six nanoparticles remaining (Figure 5.26k and l).

The final set of images taken from t = 286 s to t = 346 s show three main processes taking place; boron shell formation, particle migration, and coalescence (Figure 5.26m – q). Firstly, nanoparticles 2 to 4 are observed to transform elemental boron chains into shell-like structures (Figure 5.26p) which resemble carbon analogues formed by rhenium nanocatalysts within SWNTs imaged also by an 80 kV electron beam.[56] The boron structures formed are the nucleation of nanotube caps and are the start of the growth of boron nanotubes, however, they are not witnessed continuing to form any further nanostructures.

Instead, they continue to rearrange the boron into chains which separate the 1.5 nm diameter nanoparticles stopping them from coming into closer contact and coalescing (Figure 5.26q). The second process that is observed is the gradual migration of nanoparticle 5 towards nanoparticle 6 over a period of 44 seconds until they reach their closest approach (Figure 5.26m – p). This is then followed by coalescence to produce a structure of 5.0 nm diameter (Figure 5.26p – Q). The final image shows five crystalline nanoparticles of WS_2 with diameters ranging from 1.5 to 5.0 nm and thus allows them to be characterised as quantum dots within the BNNT channel (Figure 5.26q). The process of amorphous material undergoing coalescence within a SWNT to form crystalline species was the subject of an investigation by Cao *et al.*[57]

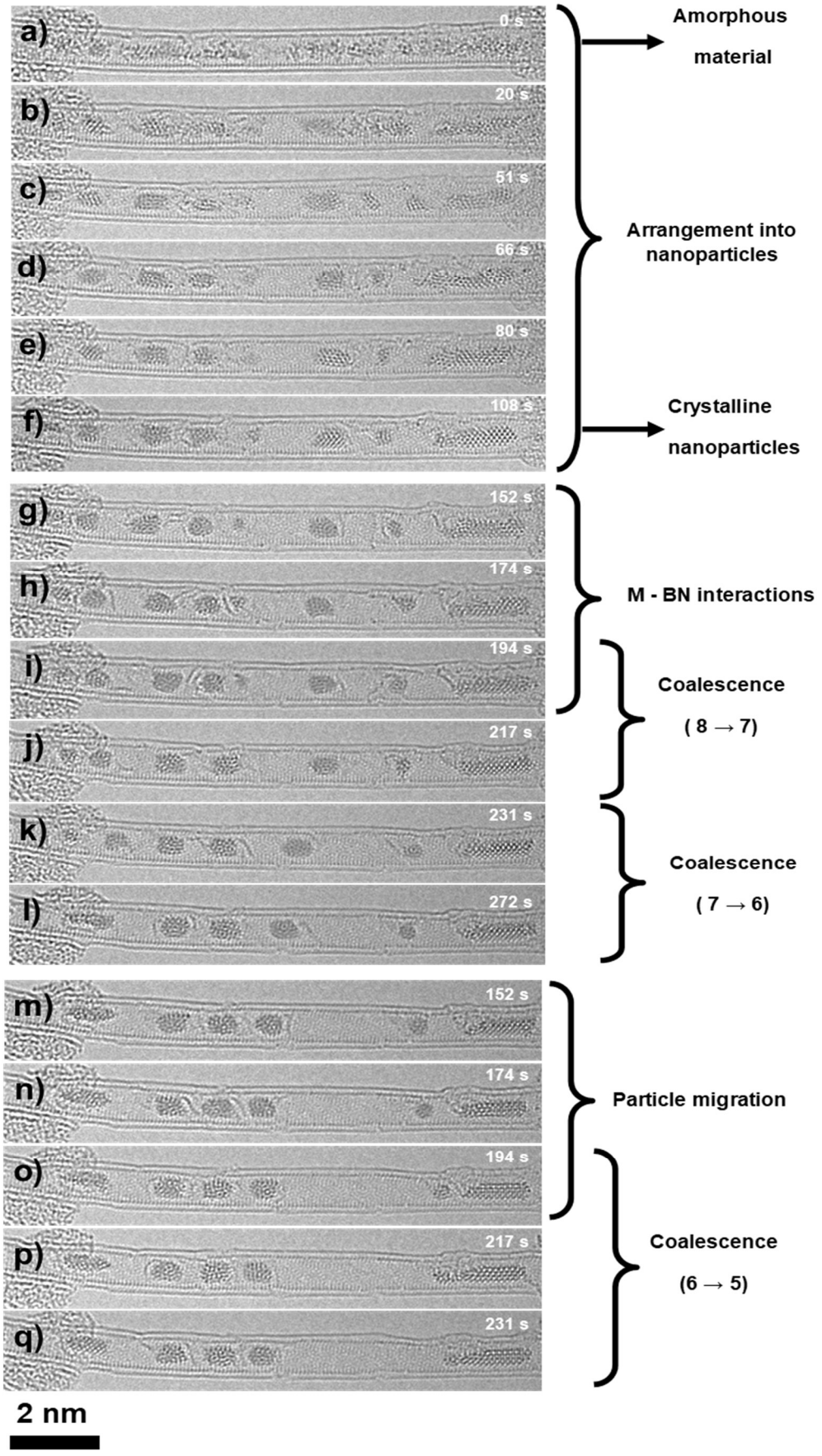


Figure 5.26. *80 kV AC-TEM time series images of WS_2@BNNT which shows a double-walled*

boron nitride nanotube filled initially (a) with amorphous tungsten sulfide material which then under the electron beam is transformed into (b - f) crystalline nanoparticles which undergo (g - l) coalescence and (m – q) migration processes within the internal BNNT channel.

The quantum dot on the far right hand side of the frame (Figure 5.26p) was studied in further detail to examine the structure (Figure 5.27a). The structure exhibited two different projections; hexagonal (green area), and diagonal (pink area) which are indicative of the face-on projection of WS_2 as well as a slight twist in the structure to form the diagonal view (Figure 5.27b). Furthermore, the structure is shown to be four W atoms in width and have a zigzag edge structure and thus is denoted as a 4ZWS_2NR. A 2D contrast analysis plot was conducted over a section of the diagonal projection across the second row of atoms which identified a W…W interatomic distance of 0.31 nm (Figure 5.27c). A structural model of the diagonal view of a 4ZWS_2NR within a (13,13) BNNT of 1.75 nm diameter which matched the measured diameter of the BNNT in the experimental AC-HRTEM image (Figure 5.27b). A TEM simulation confirmed not only the diagonal projection but also the 0.31 nm W…W interatomic distance and thus concluded that the structure was a 4ZWS_2NR (Figure 5.27d).

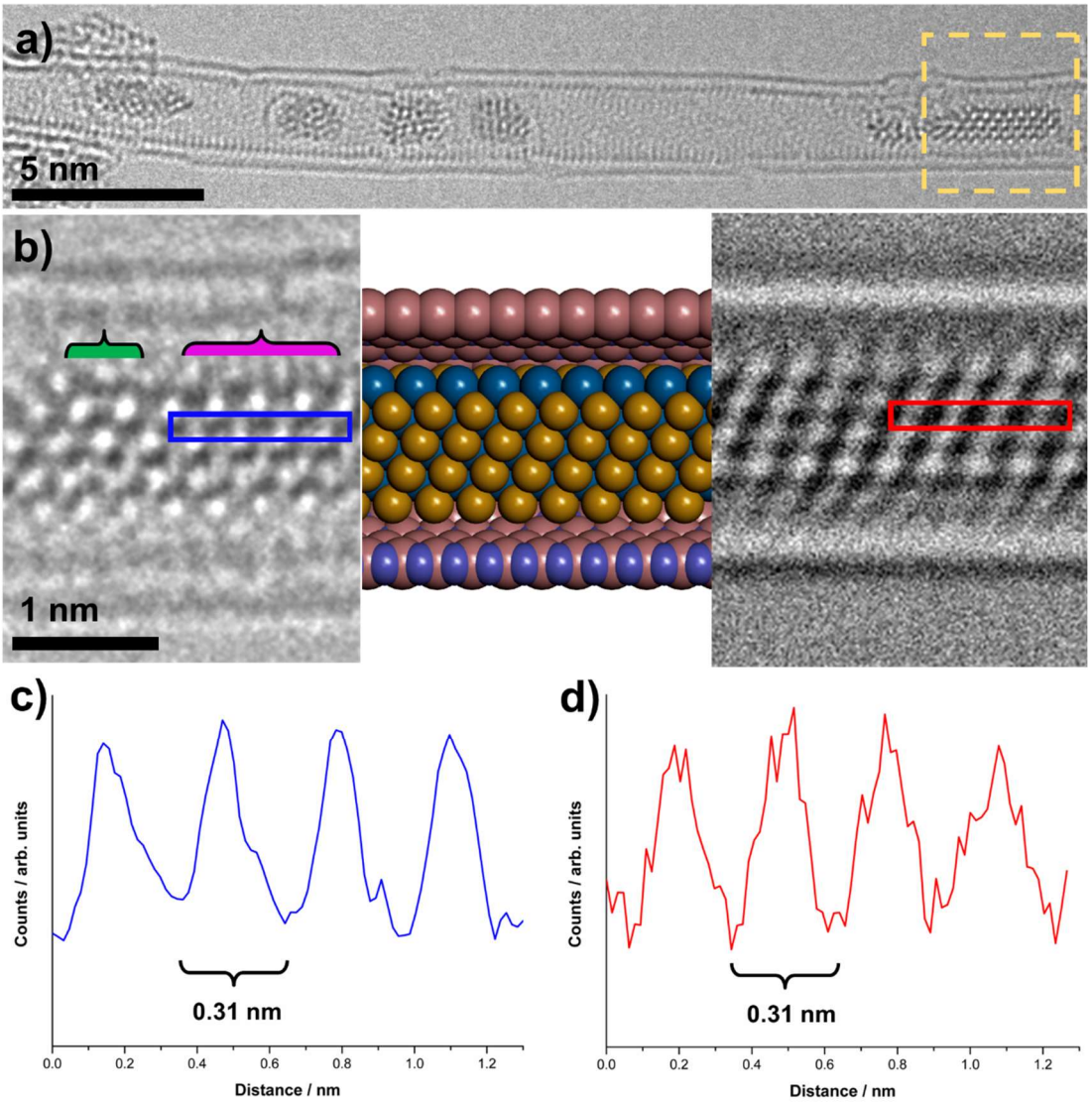


Figure 5.27. *(a) 80 kV AC-HRTEM image of WS_2 quantum dots within a double-walled boron nitride nanotube of 1.72 nm internal diameter; (b) digitally-magnified image from (a) showing the two distinct projections of the nanoribbon; hexagonal (green area), and diagonal (pink area, left), structural model of a 4ZWS$_2$NR within a (13,13) BNNT (middle), TEM simulation of the structural model (right); (c) 2D contrast analysis of the area indicated by the blue rectangle in the experimental AC-HRTEM image in (b) which shows the 0.31 nm W…W interatomic distances; (d) 2D contrast analysis of the area indicated by the red rectangle in the TEM simulation in (b) which shows the correlating interatomic distance.*

This AC-HRTEM image series shows remarkable transformations taking place within the BNNT channel which are all triggered and simultaneously imaged by the 80 kV electron beam. The nanotube initially contains amorphous material which then subsequently becomes crystalline nanoparticles. These are shown to undergo various coalescence processes to produce five crystalline quantum dots that are size-templated by the BNNT host, but are also length-templated by the amount of elemental boron blocking the channel. Crystallisation of a NaCl crystal, triggered and captured by the electron beam in TEM, was previously observed within the confinements of carbon nanotubes by Nakamuro *et al*. in which the nucleation, phase transition, and growth steps were all witnessed.[1] However, this is the first time the process has been observed for metal dichalcogenides, and within boron nitride nanotubes.

5.3. Conclusion

In summary, a new methodology for synthesising tungsten disulfide nanoribbons within both carbon nanotubes and boron nitride nanotubes has been established. The two step synthesis utilises less harsh reaction conditions to those used previously including a lower reaction temperature and the absence of hydrogen gas as a reducing agent. Within SWNTs, ultrathin WS_2 nanoribbons were proven to have been formed through a range of electron microscopy and spectroscopy techniques. The electron beam of TEM was found to be a powerful tool for not only imaging the structures, but also triggering the formation of different types of defects. Continued irradiation by the e-beam led to the removal of chains of W and S atoms as single units from the middle row of atoms in a 3ZWS_2NR, which led to the top-down fabrication of WS_2 nanowires that were one tungsten atom in width, in a *ChemTEM* process.

The methodology was shown to be transferrable to the boron nitride nanotube as a host material; encapsulation of the polyoxometalate precursors led to the shifting of POM Raman

modes which was a result of POM-BNNT interactions. Optimisation of the experimental set up led to the formation of WS_2 nanoribbons which were characterised using TEM, EDX and XPS primarily. The growth of the nanoribbons was found to sometimes be hindered by the presence of boron impurities within the BNNT interior channel resulting in the formation of structures with lengths below 7 nm that can be referred to as quantum dots. Finally, it was shown that TEM imaging of BNNTs that initially contained amorphous material caused the atoms to arrange themselves into crystalline nanoparticles which underwent coalescence in order to reduce their surface energy, resulting in the eventual formation of five quantum dots of WS_2. This new methodology which has been shown to be successful using both types of nanotubes and has highlighted fundamental differences in the structure of WS_2 when formed within carbon and boron nitride nanotubes. Moreover the physical properties of each host nanotube open up a range of different applications. WS_2 within electrically-conducting SWNTs may have particular applications where electron transport to and from the guest species is important such as in electrocatalysis.[2] On the other hand, optically-transparent BNNT hosts lead to applications in which photon access to the guest WS_2 species is the key factor, such as in optoelectronics,[3] solar cell manufacturing,[4] and photocatalysis.[5]

5.4. Experimental

5.4.1. Materials

SWNTs (P2-SWNTs, arc discharge, Carbon Solutions, USA) were refluxed in 3M HNO_3 for two hours and then annealed at 600 ^oC for 17 min to remove their end caps and any amorphous carbon present, resulting in a 50% weight loss observed. Phosphotungstic acid, $H_3PW_{12}O_{40}$, was synthesised externally in accordance to a procedure developed by Makoto *et al.*[6] BNNTs (SP10-RX, BNNT, USA) and hydrogen sulfide (Fisher Scientific) were used as supplied.

5.4.2. Insertion of $\{W_{12}\}$ into SWNTs/BNNTs

Opened SWNTs (5 mg) or as-received BNNTs (5 mg) were added to an aqueous solution of $H_3PW_{12}O_{40}$ (50 mg, 0.0174 mmol in 4.5 mL) and stirred at room temperature for three days. The resultant mixture was filtered using a Polytetrafluoroethylene membrane and washed on the filter with further water (10 - 15 mL). The product, $\{W_{12}\}$@NT, was left to dry and then collected.

5.4.3. Reaction to form WS_2@SWNT / WS_2@BNNTs

$\{W_{12}\}$@NT (3 mg) was loaded onto a quartz boat and placed within a tube furnace and exposed to a flow of argon for one hour, followed by a flow of hydrogen sulfide, both at a rate of 15 mL/min). The furnace was then heated to 550 °C for two hours under the flow of H_2S (15 mL/min) and then left to cool to room temperature under a flow of argon (15 mL/min). Excess H_2S from the flow reaction was released into the fumehood through a bleach bath (200 mL) to neutralise the gas.

5.4.4. Electron microscopy, energy-dispersive x-ray analysis, and STEM-EDX mapping

Resultant materials were dispersed in isopropyl alcohol using an ultrasonic bath and drop cast onto lacey carbon copper TEM grids (Agar Scientific). HR-TEM imaging was conducted on a JEOL 2100F FEG-TEM electron microscope operated at 200 kV. EDX spectra were acquired using an Oxford Instruments INCA X-ray microanalysis system. AC-HRTEM of WS_2@SWNT was performed at the Ulm University using the C_c/C_s corrected sub-Ångström low-voltage electron microscope (SALVE) operated at 60 kV. High angle annular dark filed imaging and STEM-EDX mapping was conducted on a Thermofisher Talos 200X operated at 120kV equipped with a SuperX window-less EDX detector. AC-HRTEM of WS_2@BNNT was performed at the Electron Physical Science Imaging Centre at Diamond Light Source on a JEM ARM300CF operated at 80 kV.

5.4.5. Raman spectroscopy

Micro Raman spectroscopy was performed using a Horiba Jobin Yvon LabRAM HR Raman microscope. Spectra were acquired using a 660 nm laser (at ~0.2 mW power), a 100x objective and a 200 µm confocal pinhole. To simultaneously scan a range of Raman shifts, a 600 lines mm^{-1} rotatable diffraction grating along a path length of 800 mm was employed, conferring a spectral resolution better than 1.2 cm^{-1} for the 660 nm laser. Spectra were detected using a Synapse CCD detector (1024 pixels) thermoelectrically cooled to −60 °C. Before spectra collection, the instrument was calibrated using the zero-order line and a standard Si (100) reference band at 520.7 cm^{-1}. For single point measurements, spectra were acquired over a minimum range 125-3400 cm^{-1} with an acquisition time of 15-120 seconds and 2 accumulations to automatically remove the spikes due to cosmic rays and improve the signal to noise ratio. Spectra were collected from at least three random locations and averaged to give a mean spectrum.

5.4.6. X-ray photoelectron spectroscopy

X-ray photoelectron spectroscopy: Samples were analysed using the Kratos AXIS ULTRA with a mono-chromated Al kα X-ray source (1486.6eV) operated at 10 mA emission current and 12 kV anode potential (120 W.) Spectra were acquired with the Kratos VISION II software. A charge neutralizer filament was used to prevent surface charging. Hybrid –slot mode was used measuring a sample area of approximately 300 x 700 µm. The analysis chamber pressure was better than 5 x 10^{-9} mbar. Three areas per sample were analysed. A wide scan was performed at low resolution (Binding energy range 1400 eV to -5 eV, with pass energy 80 eV, step 0.5 eV, sweep time 20 minutes). High resolution spectra at pass energy 20 eV, step of 0.1 eV, and sweep times of 10 minutes each were also acquired for photoelectron peaks from the detected elements and these were used to model the chemical composition. The spectra were charge corrected to the C 1s peak set to 284.5 eV.

5.4.7. Thermogravimetric analysis

Thermogravimetric analysis measurements were carried out using a TA Q500 thermogravimetric analysed. Materials were loaded onto platinum pans and heated in air from 25 to 1000 °C at a rate of 5 °C per minute, followed by an isothermal hold at 1000 °C for 10 mins.

5.4.8. Structural modelling and TEM simulations

Structural models were built using the Discovery Studio Viewer software. TEM image simulations were carried out using the multislice program QSTEM which uses the Dirac-Fock scattering potential of Rez *et al*.[7] A fixed number of 20 slices per nanotube were chosen and a sampling of 0.125 Å was selected. The defocus parameters and aberration coefficients d_f, C_s, A_1, and B_2 were matched to the conditions used in the particular TEM experiment. The effect of limited electron dose was emulated by applying noise to the produced simulated images using a custom made Monte-Carlo program exploiting the Poisson statistics of electrons.

5.5. References

1. W. Lei, J.-L. Xiao, H.-P. Liu, Q.-L. Jia and H.-J. Zhang, *Tungsten*, 2020, **2**, 217-239.
2. W. Zhao, Z. Ghorannevis, L. Chu, M. Toh, C. Kloc, P.-H. Tan and G. Eda, *ACS Nano*, 2013, **7**, 791-797.
3. H. R. Gutiérrez, N. Perea-López, A. L. Elías, A. Berkdemir, B. Wang, R. Lv, F. López-Urías, V. H. Crespi, H. Terrones and M. Terrones, *Nano Lett.*, 2013, **13**, 3447-3454.
4. Z. Liu, K. Suenaga, Z. Wang, Z. Shi, E. Okunishi and S. Iijima, *Nat. Commun.*, 2011, **2**, 213.
5. S.-L. Xiao, W.-Z. Yu and S.-P. Gao, *Surf. Sci.*, 2016, **653**, 107-112.

6. J. Lin, Z. Peng, G. Wang, D. Zakhidov, E. Larios, M. J. Yacaman and J. M. Tour, *Adv. Energy Mater.*, 2014, **4**, 1301875.

7. Z. Wang, K. Zhao, H. Li, Z. Liu, Z. Shi, J. Lu, K. Suenaga, S.-K. Joung, T. Okazaki, Z. Jin, Z. Gu, Z. Gao and S. Iijima, *J. Mater. Chem.*, 2011, **21**, 171-180.

8. A. Botos, J. Biskupek, T. W. Chamberlain, G. A. Rance, C. T. Stoppiello, J. Sloan, Z. Liu, K. Suenaga, U. Kaiser and A. N. Khlobystov, *J. Am. Chem. Soc.*, 2016, **138**, 8175-8183.

9. B. W. Smith, M. Monthioux and D. E. Luzzi, *Nature*, 1998, **396**, 323-324.

10. J. Wang, M. K. Kuimova, M. Poliakoff, G. A. D. Briggs and A. N. Khlobystov, *Angew. Chem. Int. Ed.*, 2006, **45**, 5188-5191.

11. J. Sloan, J. Hammer, M. Zwiefka-Sibley and M. L. H. Green, *Chem. Commun.*, 1998, 347-348.

12. J. Sloan, M. C. Novotny, S. R. Bailey, G. Brown, C. Xu, V. C. Williams, S. Friedrichs, E. Flahaut, R. L. Callender, A. P. E. York, K. S. Coleman, M. L. H. Green, R. E. Dunin-Borkowski and J. L. Hutchison, *Chem. Phys. Lett.*, 2000, **329**, 61-65.

13. J. L. Hutchison, J. Sloan, R. Dunin-Borkowski, A. I. Kirkland and M. L. H. Green, 2001.

14. L. Guan, K. Suenaga, Z. Shi, Z. Gu and S. Iijima, *Nano Lett.*, 2007, **7**, 1532-1535.

15. C. A. Slade, A. M. Sanchez and J. Sloan, *Nano Lett.*, 2019, **19**, 2979-2984.

16. N. G. Chopra, R. J. Luyken, K. Cherrey, V. H. Crespi, M. L. Cohen, S. G. Louie and A. Zettl, *Science*, 1995, **269**, 966-967.

17. S. W. Yang, H. Zhang, J. M. Soon, C. W. Lim, P. Wu and K. P. Loh, *Diamond Relat. Mater.*, 2003, **12**, 1194-1200.

18. S. S. Han, J. K. Kang, H. M. Lee, A. C. T. v. Duin and W. A. G. III, *J. Chem. Phys.*, 2005, **123**, 114704.

19. Y. Chen, J. Zou, S. J. Campbell and G. L. Caer, *Appl. Phys. Lett.*, 2004, **84**, 2430-2432.

20. X. Blase, A. Rubio, S. G. Louie and M. L. Cohen, *Europhysics Letters (EPL)*, 1994, **28**, 335-340.

21. Y. Muramatsu, T. Kaneyoshi, E. M. Gullikson and R. C. C. Perera, *Spectrochim. Acta A*, 2003, **59**, 1951-1957.

22. W. Han, P. Redlich, F. Ernst and M. Rühle, *Appl. Phys. Lett.*, 1999, **75**, 1875-1877.

23. D. Golberg, Y. Bando, K. Kurashima and T. Sato, *J. Nanosci. Nanotechnol.*, 2001, **1**, 49-54.

24. D. Golberg, F. F. Xu and Y. Bando, *Appl. Phys. A*, 2003, **76**, 479-485.

25. Y. Liao, Z. Chen, J. W. Connell, C. C. Fay, C. Park, J.-W. Kim and Y. Lin, *Adv. Funct. Mater.*, 2014, **24**, 4497-4506.

26. W. Mickelson, S. Aloni, W.-Q. Han, J. Cumings and A. Zettl, *Science*, 2003, **300**, 467.

27. W.-Q. Han, C. W. Chang and A. Zettl, *Nano Lett.*, 2004, **4**, 1355-1357.

28. T. Pham, A. Fathalizadeh, B. Shevitski, S. Turner, S. Aloni and A. Zettl, *Nano Lett.*, 2016, **16**, 320-325.

29. K. E. Walker, G. A. Rance, A. Pekker, H. M. Tohati, M. W. Fay, R. W. Lodge, C. T. Stoppiello, K. Kamaras and A. N. Khlobystov, *Small Methods*, 2017, **1**.

30. Q. H. Wang, K. Kalantar-Zadeh, A. Kis, J. N. Coleman and M. S. Strano, *Nat. Nanotechnol.*, 2012, **7**, 699-712.

31. S. Manzeli, D. Ovchinnikov, D. Pasquier, O. V. Yazyev and A. Kis, *Nat. Rev. Mater.*, 2017, **2**, 17033.

32. J. W. Jordan, G. A. Lowe, R. L. McSweeney, C. T. Stoppiello, R. W. Lodge, S. T. Skowron, J. Biskupek, G. A. Rance, U. Kaiser, D. A. Walsh, G. N. Newton and A. N. Khlobystov, *Adv. Mater.*, 2019, **31**, 1904182.

33. B. Fei, H. Lu, W. Chen and J. H. Xin, *Carbon*, 2006, **44**, 2261-2264.

34. J. F. Keggin, *Nature*, 1933, **131**, 908-909.

35. J. W. Jordan, K. L. Y. Fung, S. T. Skowron, C. S. Allen, J. Biskupek, G. N. Newton, U. Kaiser and A. N. Khlobystov, *Chem. Sci.*, 2021, 7377-7387.

36. M. V. Kharlamova, *Appl. Phys. A*, 2016, **122**, 791.

37. P. A. Jalil, M. Faiz, N. Tabet, N. M. Hamdan and Z. Hussain, *J. Catal.*, 2003, **217**, 292-297.

38. R. Jha and P. Guha, *J Mater Sci*, 2017, **52**, 1-13.

39. T. W. Chamberlain, J. Biskupek, S. T. Skowron, A. V. Markevich, S. Kurasch, O. Reimer, K. E. Walker, G. A. Rance, X. Feng, K. Müllen, A. Turchanin, M. A. Lebedeva, A. G. Majouga, V. G. Nenajdenko, U. Kaiser, E. Besley and A. N. Khlobystov, *ACS Nano*, 2017, **11**, 2509-2520.

40. X. Wei, D.-M. Tang, Q. Chen, Y. Bando and D. Golberg, *ACS Nano*, 2013, **7**, 3491-3497.

41. X. Liu, T. Xu, X. Wu, Z. Zhang, J. Yu, H. Qiu, J.-H. Hong, C.-H. Jin, J.-X. Li, X.-R. Wang, L.-T. Sun and W. Guo, *Nat. Commun.*, 2013, **4**, 1776.

42. X. Zhao, J. Kotakoski, J. C. Meyer, E. Sutter, P. Sutter, A. V. Krasheninnikov, U. Kaiser and W. Zhou, *MRS Bull.*, 2017, **42**, 667-676.

43. S. Kretschmer, T. Lehnert, U. Kaiser and A. V. Krasheninnikov, *Nano Lett.*, 2020, **20**, 2865-2870.

44. Boron nitride nanotube specifications, https://www.bnnt.com/nanotubes, (accessed July, 2021).

45. M. B. Jakubinek, K. S. Kim, C. Homenick, O. Kodra, S. Walker and B. Simard, *Can. J. Chem.*, 2019, **97**, 457-464.

46. W. A. Brainard and D. R. Wheeler, *J. Vac. Sci. Technol.*, 1978, **15**, 1800-1805.

47. C. H. Lee, J. Wang, V. K. Kayatsha, J. Y. Huang and Y. K. Yap, *Nanotechnology*, 2008, **19**, 455605.

48. W. J. Schutte, J. L. De Boer and F. Jellinek, *J. Solid State Chem.*, 1987, **70**, 207-209.

49. J. Gusakova, X. Wang, L. L. Shiau, A. Krivosheeva, V. Shaposhnikov, V. Borisenko, V. Gusakov and B. K. Tay, *Phys. Status Solidi A*, 2017, **214**, 1700218.

50. K. Kang, K. Godin and E.-H. Yang, *Sci Rep-Uk*, 2015, **5**, 13205.

51. H. Long, L. Tao, C. P. Chiu, C. Y. Tang, K. H. Fung, Y. Chai and Y. H. Tsang, *Nanotechnology*, 2016, **27**, 414005.

52. M. O. Valappil, A. Anil, M. Shaijumon, V. K. Pillai and S. Alwarappan, *Chem. Eur. J.*, 2017, **23**, 9144-9148.

53. N. Powar, G. Gopakumar, K. V. Ramanathan, S. Nair and M. Shanmugam, *Opt. Quantum Electron.*, 2020, **52**, 65.

54. A. Zobelli, A. Gloter, C. P. Ewels, G. Seifert and C. Colliex, *Phys. Rev. B*, 2007, **75**, 245402.

55. J. H. Warner, M. H. Rümmeli, A. Bachmatiuk and B. Büchner, *ACS Nano*, 2010, **4**, 1299-1304.

56. K. C. Cao, T. W. Chamberlain, J. Biskupek, T. Zoberbier, U. Kaiser and A. N. Khlobystov, *Nano Lett.*, 2018, **18**, 6334-6339.

57. K. Cao, J. Biskupek, C. T. Stoppiello, R. L. McSweeney, T. W. Chamberlain, Z. Liu, K. Suenaga, S. T. Skowron, E. Besley, A. N. Khlobystov and U. Kaiser, *Nat. Chem.*, 2020, 921-928.

Chapter 6: Measuring the hydrogen evolution ability of metal chalcogenide nanomaterials within carbon nanotubes.

6.1. Introduction

Energy consumption from 2010 to 2050 is expected to increase from 16 TW to 30 TW, on average[1], which will lead to increased energy demand for existing fossil fuels that are in finite supply and are already being used for 87% of primary power.[2, 3] Moreover, fossil fuels lead to the emission of CO, CO_2, NO_x, and SO_x, amongst other greenhouse gases, into the atmosphere which contribute heavily towards global warming.[4] This requires fossil fuel systems to be swapped for cleaner, more abundant alternatives. Hydrogen has been predicted to be the fuel of the future due to the high abundance of hydrogen as an element, along with the combustion producing cleaner products.[5, 6] However, the current most used method to forming hydrogen fuel is by steam reformation of methane which produces carbon dioxide; a greenhouse gas.[7]

6.1.1. Hydrogen Evolution Reaction (HER)

The hydrogen evolution reaction (HER, Equation 6.1) is the cathodic process of the electrochemical water splitting reaction and is thought to be a more viable alternative method for hydrogen production.[8, 9]

The Hydrogen Evolution Reaction: $2H^+ + 2e^- \rightarrow H_2$ ***Equation 6.1.***

There are two mechanistic pathways that the HER can take which both start with the Volmer reaction (Equation 6.2); this is the reduction of a proton and subsequent dissociative

adsorption of atomic hydrogen onto the catalysis surface. The first of the two pathways that the reaction can take is called the Heyrovsky reaction; this is the combination of adsorbed hydrogen with a proton and an electron to produce molecular hydrogen (Equation 6.3). Alternatively, the combination of two adsorbed hydrogen atoms can occur leading to the production of molecular hydrogen, which is coined as the Tafel reaction (Equation 6.4).[10, 11] To determine which mechanism is the rate controlling step of the HER for a particular catalyst, a plot of *ln J* vs η (where J is the current density and η is the overpotential) can be constructed. The slope value of the linear region of the plot then dictates which step is rate-controlling; slope values of 120, 40, or 30 mV dec^{-1} dictate that the Hydrogen Evolution Reaction is controlled by the Volmer, Heyrovsky, or Tafel steps respectively.[12]

Volmer: $H^+ + e^- \rightarrow H_{ads}$ ***Equation 6.2.***

Heyrovsky*:* $H_{ads} + H^+ + e^- \rightarrow H_2$ ***Equation 6.3.***

The Tafel reaction*:* $H_{ads} + H_{ads} \rightarrow H_2$ ***Equation 6.4.***

The performance of an electrocatalyst towards the HER has been primarily evaluated, in literature, by the overpotential required to reach a current density of -10 mA cm^{-2}; this relates to the approximate current density required for 10% efficient solar to fuel conversion under one sun illumination.[13] Often, previous studies will quote an onset potential for the reaction, however this has led to ambiguity towards the point at which this occurs.

6.1.2. Platinum as an electrocatalyst

Platinum has been previously shown to be the most effective electrocatalyst in acidic media as it was found to have a high exchange current density with a near-zero overpotential, due to the near-zero hydrogen adsorption energy of the metal (Figure 6.1).[14, 15] The exchange current density is a parameter that describes the rates of electron transfer, and the high

value of Pt is a description of the favourable catalytic surface.[16] However, the limitations are that it is both expensive and in low abundance, and thus alternative electrocatalysts need to be developed.[17]

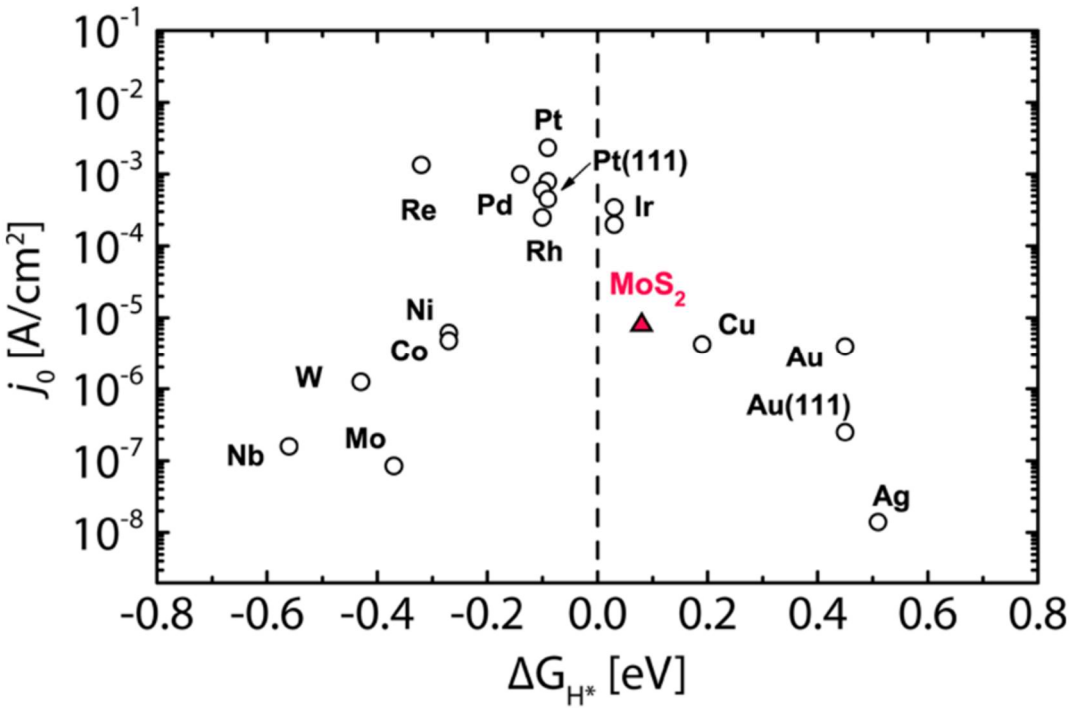


Figure 6.1. *Volcano plot of exchange current density against free energy of hydrogen adsorption for a range of metals and materials.[14] Platinum is shown at the top of the volcano plot as it has the highest current density at a near zero potential.*

6.1.3. MoS_2 performance

Molybdenum disulfide, MoS_2, has been the subject of many investigations as an alternative to Pt towards the HER due to the comparable near zero free energy of hydrogen adsorption ΔG^o_H (Figure 6.1).[14, 15, 18-21] Nevertheless, MoS_2 suffers from low conductivity, and an inert basal plane, which results in only the edge sites being active.[14, 22] Therefore, more studies are focussing on the fabrication of MoS_2-based nanomaterials, with a high number of active edge sites and testing them towards the HER (Table 6.1).

Table 6.1. *Summary of MoS_2 nanomaterials tested towards electrocatalysis of the Hydrogen Evolution Reaction, as well as Pt as a reference. Recorded are the list of nanomaterials along with their corresponding experimental details, and overpotential at -10 mA cm^{-2} (where applicable).*

Material	Acidic solution	Counter electrode	Overpotential at -10 mA cm^{-2}	Reference
Polycrystalline Pt	0.5 M H_2SO_4	RHE	-21 mV	[11]
MoS_2@N-CNT	0.5 M H_2SO_4	RHE	-110 mV	[23]
MoS_2/rGO	0.5 M H_2SO_4	RHE	-154 mV	[24]
3050 nm MoS_2 columnar film	0.5 M H_2SO_4	RHE	-204 mV	[25]
1T-MoS_2 nanosheets	0.5 M H_2SO_4	RHE	-207 mV	[15]
MoS_2 nanoflower	0.5 M H_2SO_4	RHE	-357 mV	[26]

6.1.4. Carbon nanotubes

Carbon nanotubes (CNTs) are cylindrical structures which are electrically-conducting; this property has often been exploited for previous studies by using their exterior surfaces as

supports for MoS_2-based species towards use as HER electrocatalysts with the nanotube acting as a nano-electrode.[27-29]

However, carbon nanotubes also allow materials to be encapsulated or synthesised within their interior channel, which protects the guest species from oxidation.[30] Thus, more investigations are probing the electrocatalytic ability of nanostructures within the interior of carbon nanotubes, combining the conducting and protection properties of the host with the catalytic ability of the guest material.[31] Deng *et al.* formed a range of 3d transition metal nanoparticles within CNTs and nitrogen-doped CNTs via an in-situ chemical vapour deposition technique; this led to excellent HER performances exhibiting low overpotentials.[32] Moreover, the materials were also found to be extremely durable up to 10000 cycles with only small growth of the overpotential during fixed current density studies. In addition, it has been shown that molybdenum carbide nanoparticles formed within single-walled carbon nanotubes (SWNT) performed better towards HER than those formed on the exterior as a result of a smaller particle size, enforced by the SWNT interior channel, producing more active surface sites.[33]

6.1.5. Aim and objectives

In this chapter, a range of encapsulated metal chalcogenides within SWNTs will be evaluated towards the HER as an initial proof of concept study; these nanomaterials will include quasi-one-dimensional (1D) nanoribbons and discrete nanocluster molecules. The performance towards HER of the host SWNTs will first be evaluated by comparing closed SWNTs with SWNTs that have been either heat treated, or acid-washed and heat treated to determine the effects of the accessibility of the interior concave surface, as well as how any contaminants such as amorphous carbon or nickel nanoparticles may affect HER electrocatalysis. Once the SWNT hosts are optimised, then a range of encapsulated metal

chalcogenide materials will be evaluated towards the HER; these will include encapsulated nanoclusters, and synthesised quasi-1D nanoribbons. Overall, the work in this chapter will provide a library of knowledge towards the HER electrocatalytic ability of metal chalcogenide nanomaterials within the confinements of SWNTs.

6.2. Results and Discussion

6.2.1. Evaluation of the SWNT hosts

In order to fully understand the effect the internal species have on the HER ability, it was necessary to first evaluate the ability of the host SWNTs as a reference. As-synthesised SWNTs possess end caps which are usually removed through a heat-treatment step to produce opened SWNTs; moreover, they contain nickel remaining from the SWNT synthesis which can be removed by acid-washing the SWNTs. Therefore the SWNTs, during each stage of their preparation, were tested towards the HER to find the optimum system before filling with metal chalcogenide species. The three sets of SWNTs catalytically tested were closed SWNTs, opened SWNTs by annealing in air, and acid-washed and annealed (AT) SWNTs; this would allow the heating and washing effects to be examined. TEM analysis of closed SWNTs (Figure 6.2a) identified nanotubes present with their end caps, along with a high contrast core-shell nanoparticle which was identified as a nickel core from EDX (Figure 6.2d) with a carbon shell; the atomic % of nickel was recorded as 1.0 %. The opened SWNTs, by annealing in air, revealed the end caps of the SWNTs were removed but still contained nanoparticles of nickel on the exterior of the SWNTs (Figure 6.2b and e), however, the amount of nickel had reduced by 70 % (from 1.0 to 0.29 atomic %). Finally, after acid-washing the SWNTs and then heat treating them, the result was opened SWNTs with minimal presence of nickel (0.05 % Figure 6.2c and f).

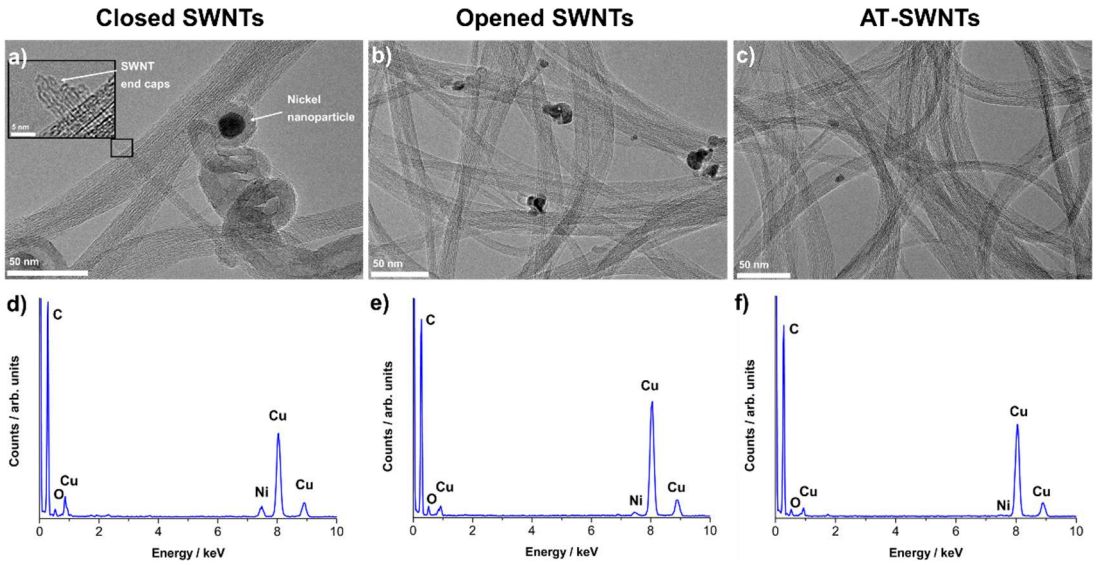


Figure 6.2. *200 kV TEM images of (a) closed SWNTs (inset is a magnified image of the SWNT end caps) which shows the presence of SWNTs bundles, and a nickel nanoparticle with carbon shells; (b) opened SWNTs displaying bundles of SWNTs with smaller exterior nickel nanoparticles, and (c) AT-SWNTs showing bundles of SWNTs with smaller nickel nanoparticles in isolated cases. (d - f) Corresponding EDX spectra for each of the SWNT types which show the presence of nickel.*

The SWNTs were then taken forward for electrocatalytic measurements towards the Hydrogen Evolution Reaction. The procedure used a three electrode set up consisting of; a modified glassy carbon working electrode with each material deposited on, a Ag/AgCl reference electrode, and a platinum counter electrode all submersed within 0.5 M H_2SO_4 electrolyte; these are tried and tested conditions used commonly in the literature.[28] Measurements were conducted using linear sweep voltammetry (LSV), and the overpotential values were then converted to be in reference to the reversible hydrogen electrode (RHE). [28]

$$E_{RHE} = E_{Ag/AgCl} + (0.059 \times \mathrm{pH}) + 0.1988$$

Equation 6.5.

The overpotential values at -10 mA cm^{-1} recorded for each of the SWNT sets were: <(-580) mV (closed SWNTs), -532 mV (opened SWNTs), and -510 mV (AT-SWNTs, Figure 6.3). All three sets of SWNTs exhibited a low performance towards the HER with the poorest catalytic material overall being the closed SWNTs. This can be explained by the presence of the end caps which seal off the interior concave surface; heat-treating SWNTs removes the end caps and thus allows access to both the exterior convex and interior concave surfaces; the latter of which will be important for proton access to the active sites of encapsulated materials. After both opening procedures (acid treatment and annealing), the AT-SWNTs will possess more dangling bonds and edge sites which should increase the electrochemically active surface area and thus improve the performance towards HER.

The improved performance of AT-SWNTs therefore presents three benefits for their continued usage during the evaluation of filled SWNTs; the electrocatalytic ability of the host has been optimised, their end caps being removed allows them to be filled with metal chalcogenide species, and their level of nickel has been minimised ensuring that the host and guest are the primary HER electrolytic contributing materials. This has shown that nickel appears to play no role in HER measurements of SWNTs, as demonstrated by the inverse relationship between atomic % of Ni and overpotential value being closer to zero.

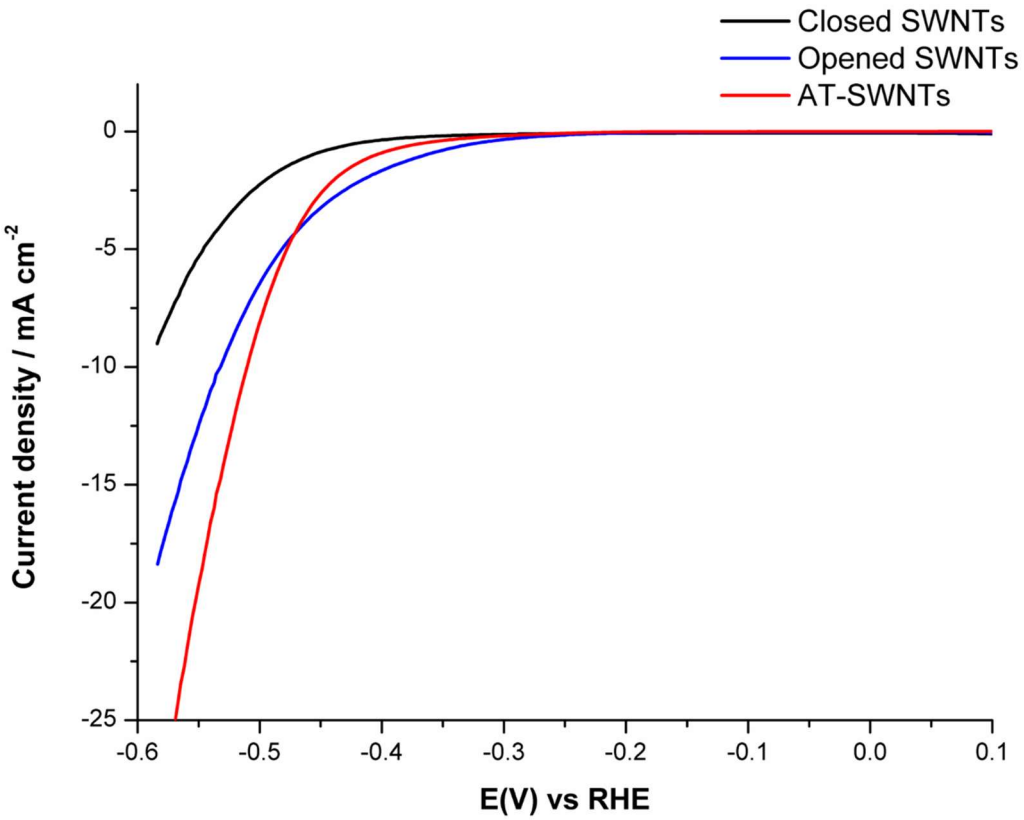


Figure 6.3. *HER polarisation curves for; closed SWNTs (black), opened SWNTs (blue), and acid and heat-treated (AT) SWNTs (red). The overpotential values, at a current density of -10 mA* cm^{-2}*, for each material were found to be <-580 (closed SWNTs), -532 (opened SWNTs), and -510 mV (AT-SWNTs).*

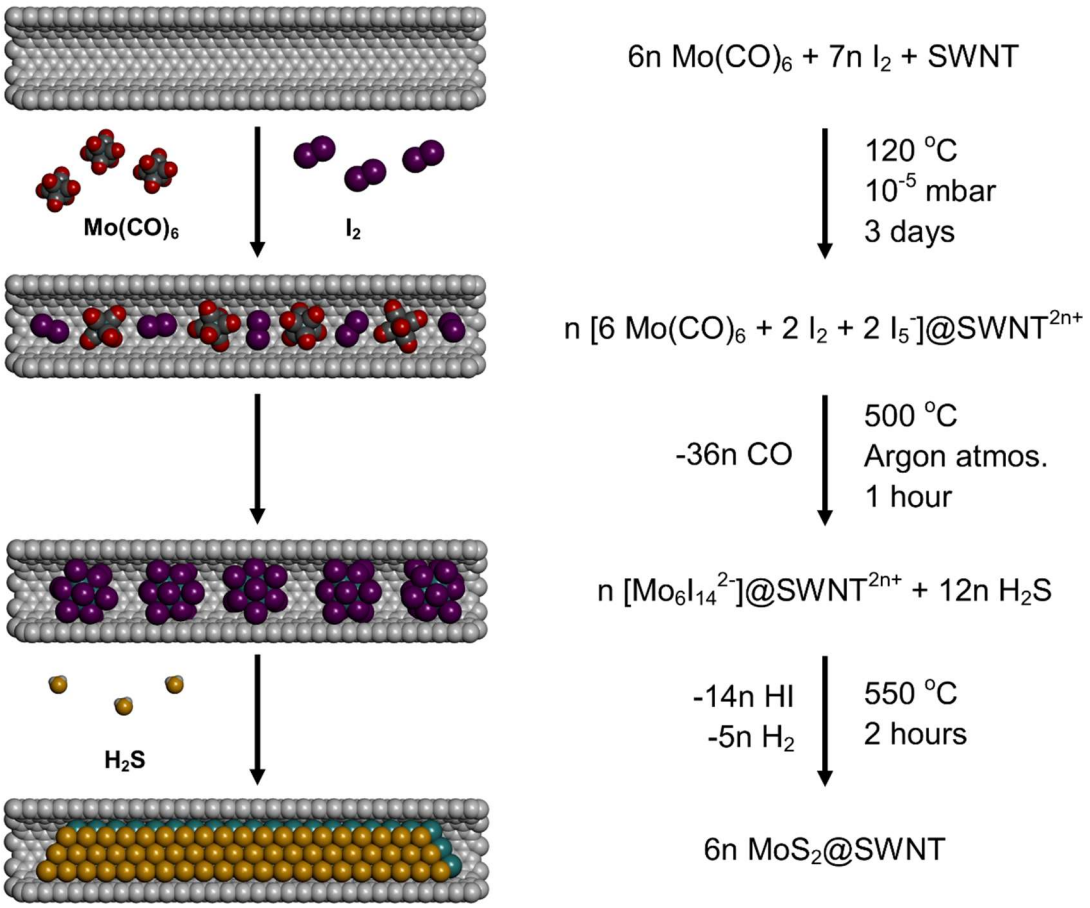
6.2.2. Comparison of 1D MoS_2 using different synthetic routes

After optimising the HER performance of the host SWNTs; three routes towards synthesising MoS_2 nanoribbons were then evaluated. The three routes that will be tested are; one existing method using molybdenum hexacarbonyl ($Mo(CO)_6$),[34] and two new methods, the first is an analogue of work presented in **Section 5.2.1.** utilising polyoxometallates, in this instance molybdenum Keggin-based structures ($H_3Mo_{12}O_{40}$), the second is via thiomolybdate hexabromide ($[Mo_3S_7Br_6]^{2-}$) which was developed in **Section 4.2.1**. The composite materials will be evaluated towards the HER by examining the overpotential required to reach a

current density of -10 mA cm^{-2}, allowing them to be compared to literature values. Stability tests are not included in this study due to the observation of platinum, from the counter electrode, contaminating the working electrode demonstrated by Bird *et al*.[9] This was shown to improve the electrocatalytic performance providing the illusion that some electrocatalysts perform better after cycling; it was established that to minimise this effect that a glassy carbon counter electrode was required and to be separated from the working electrode by a glass frit. The as-synthesised MoS_2@SWNT materials will be given the notation A ($Mo(CO)_6$ precursor), B ($H_3PMo_{12}O_{40}$ precursor), and C ($[Mo_3S_7Br_6]^{2-}$ precursor) to distinguish them more easily.

6.2.2.1. *Synthesis of MoS_2@SWNT-A (via $Mo(CO)_6$)*

The first route which aimed to synthesise molybdenum disulfide nanoribbons was via a stepwise method that utilises molybdenum carbonyl as the initial source optimised by Botos et al. (Scheme 6.1).[34] A primary advantage of this method is that the initial source of molybdenum has labile carbonyl ligands which can be easily substituted, moreover, transformation of the octahedral molybdenum iodide species to the disulfide nanoribbons was shown to occur in high yield. The main disadvantage with the methodology is the three steps required and the resulting number of intermediates and by-products that can be produced, which may negatively-impact the HER ability if entrapped within the SWNT inner channel.



Scheme 6.1. *Synthesis of MoS_2 nanoribbons in nanotubes from $Mo(CO)_6$. Molybdenum hexacarbonyl and iodine are simultaneously encapsulated into SWNTs and then are thermally-activated to form $[Mo_6I_{14}]^{2-}$ octahedral molecules, followed by a reaction with H_2S to produce MoS_2@SWNT-A.*

The first step of the synthesis commenced with the encapsulation of $Mo(CO)_6$ and I_2 simultaneously into the SWNTs (Scheme 6.1). Raman spectroscopy, in resonance with both semiconducting and metallic SWNTs demonstrated an initial large blue-shift of the G-band compared to empty SWNTs (+9.5 and +12.6 cm^{-1} respectively, Figure 6.4c and d) upon encapsulation of the precursors. The difference in magnitude of G-band shift is a result of the higher Fermi level of metallic SWNTs compared to semiconducting SWNTs. This was attributed to the SWNTs donating electron density to encapsulated iodine forming

polyiodide ions. The system was then thermally-activated to produce octahedral molybdenum iodide clusters, $n[Mo_6I_{14}]^{2-}@SWNT^{2n+}$. TEM imaging showed a high number of the clusters within the SWNT hosts (Figure 6.4a), and EDX confirmed the composition as expected (Figure 6.4b). Upon formation of the clusters, the Raman G-bands were still blue-shifted but to a lesser extent (+5.7 and +8.7 cm^{-1} in resonance with semiconducting and metallic SWNTs respectively, Figure 6.4c and d).

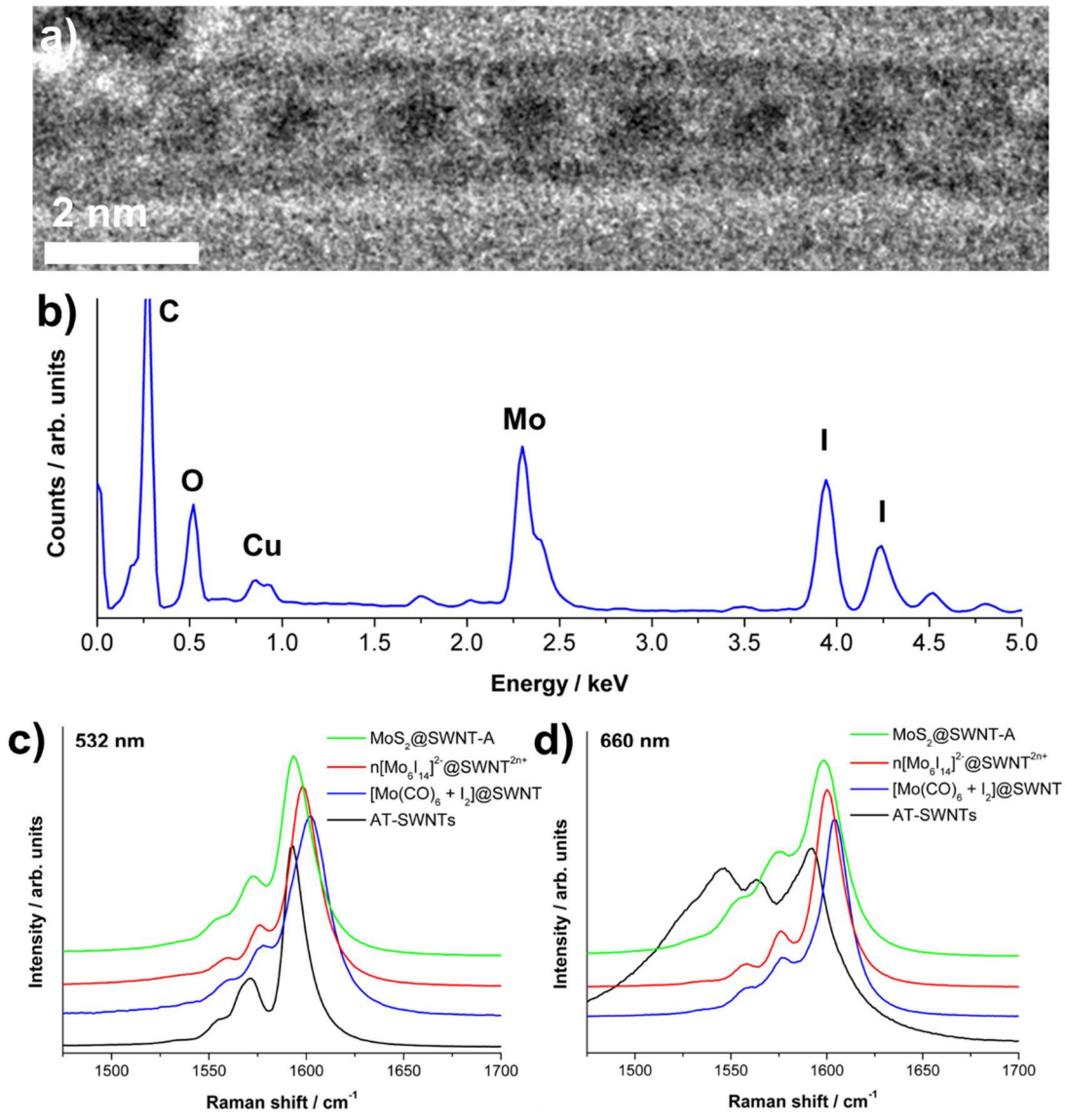


Figure 6.4. *(a) 80 kV TEM image of $n[Mo_6I_{14}]^{2-}@SWNT^{2n+}$ which shows a nanotube filled with discrete clusters; (b) EDX spectrum of $n[Mo_6I_{14}]^{2-}@SWNT^{2n+}$ showing the presence of Mo and I. The presence of copper and nickel peaks are due to the TEM grid support and SWNTs*

respectively; Raman spectra overlay of the materials in the stepwise synthesis using a laser excitation in resonance with (c) semiconducting SWNTs and (d) metallic SWNTs, focussed on the G-band region.

The final step of the synthesis was the reaction of $n[Mo_6I_{14}]^{2-}$@$SWNT^{2n+}$ with dihydrogen sulfide which produced continuous nanoribbons of MoS_2. TEM analysis of MoS_2@SWNT showed a single nanoribbon which was observed to have a helical twist point (indicated by the white arrow) in which there is a face-on to edge-on transition indicated by the higher contrast and narrower width (Figure 6.5a). EDX analysis found a 1: 3 Mo: S atomic ratio with only trace iodine remaining in the system, confirming the transformation was successful (Figure 6.5b). The excess of sulfur may be a result of sulfur termination of the MoS_2 nanoribbons, resulting in a high number of S edge sites. Raman spectroscopy recorded the G-band in resonance with semiconducting SWNTs back to near the original position for empty SWNTs, whilst for the spectrum in resonance with metallic SWNTs, the G-band was blue-shifted by +6.5 cm^{-1} suggesting the MoS_2 nanoribbons were behaving as electron acceptors (Figure 6.4c and d). Thermogravimetric analysis (TGA) was conducted on the material which resulted in a residual weight of 17.6 % after heating in air up to 1000 ^{o}C (Figure 6.5c).

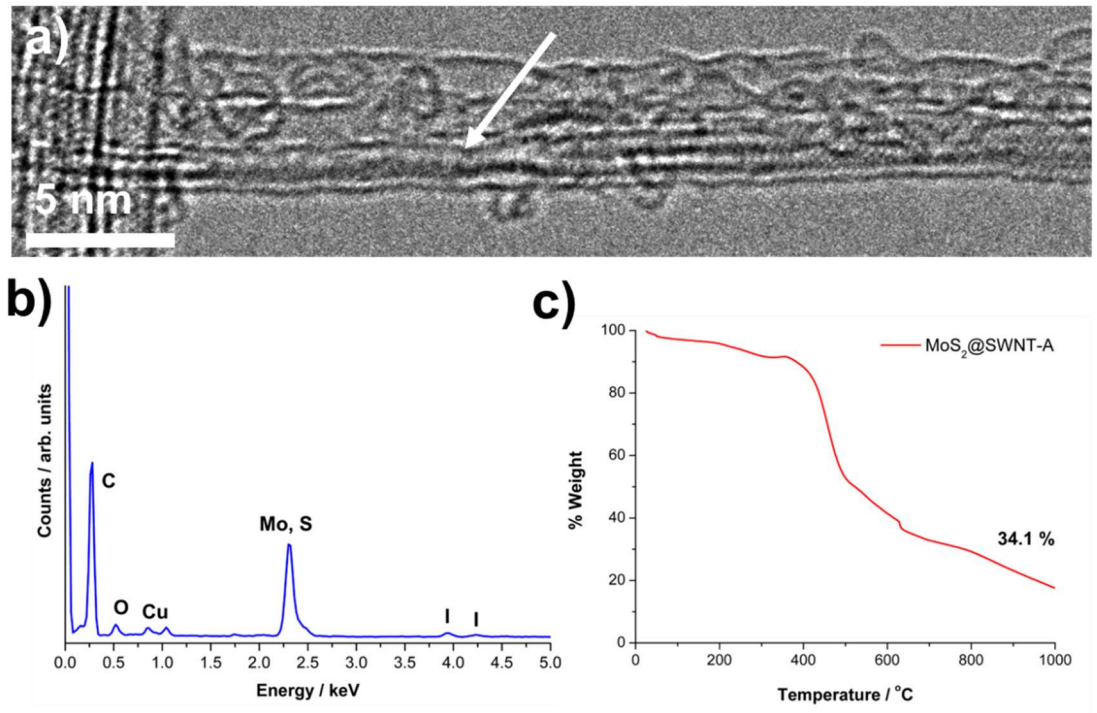
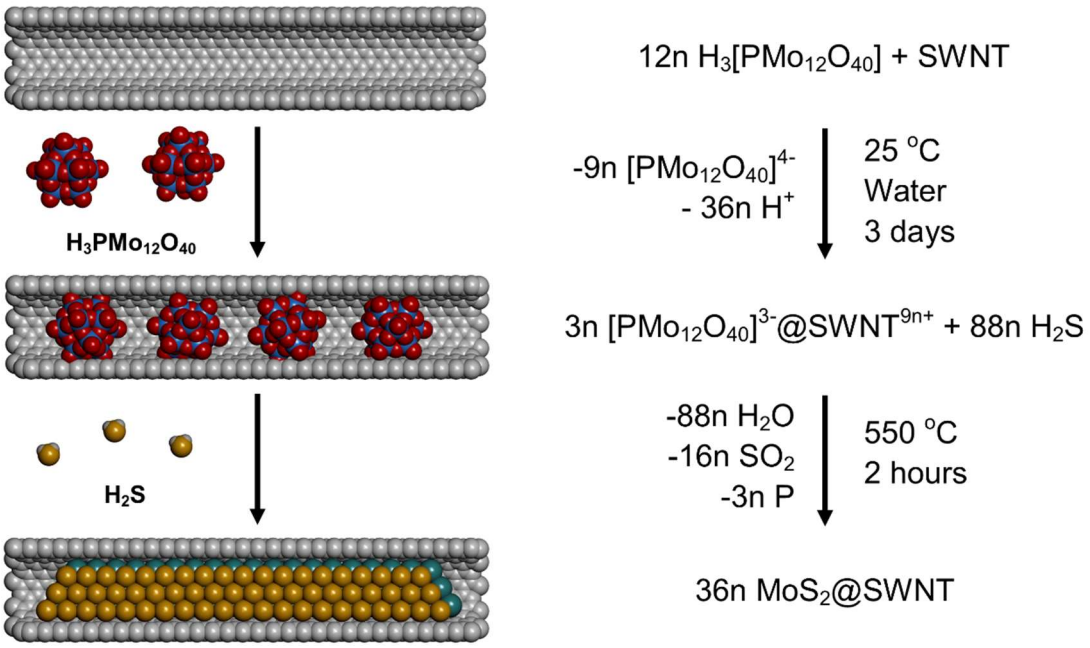


Figure 6.5. *(a) 200 kV TEM image of MoS_2@SWNT showing the presence of a twisting nanoribbon within the SWNT channel; (b) EDX spectrum, measured over a bundle of filled SWNTs, which identifies Mo and S in a 1: 3 atomic ratio, and trace iodine remaining from the previous step; (c) thermogram of MoS_2@SWNT-A displaying a residual weight % of 17.6 after heating to 1000 °C in air.*

6.2.2.2. *Synthesis of MoS_2@SWNT-B (via $H_3PMo_{12}O_{40}$)*

The polyoxometallate route utilises a stepwise synthesis first developed in **section 5.2.1.** for the synthesis of tungsten disulfide nanoribbons, but instead uses Mo Keggin polyoxometallate (POM) analogues, $H_3PMo_{12}O_{40}$ ({Mo_{12}}c). The two step method first encapsulates $H_3PMo_{12}O_{40}$ POMs via a solution-phase filling method to produce {Mo_{12}}@SWNT, and then they are subsequently transformed using H_2S gas to produce molybdenum disulfide nanoribbons (Scheme 6.2).



Scheme 6.2. *Stepwise route towards MoS_2@SWNT using a polyoxometallate precursor. The first step of the synthesis encapsulates $H_3PMo_{12}O_{40}$ into SWNTs via a solution-phase filling method. The encapsulated POMs are then reduced with a source of sulfur to produce MoS_2@SWNT-B.*

The encapsulation of the POM precursor was shown to be successful via TEM imaging which displayed the presence of high contrast features within the SWNT channels that match the size of Keggin POMs (Figure 6.6a). Complementary EDX analysis, of a bundle of filled SWNTs, confirmed the features observed consisted of molybdenum, oxygen, and phosphorus (Figure 6.6b); the Mo: O atomic ratio was found to be 1: 4.3 which is higher than the expected 1: 3.3 for $H_3PMo_{12}O_{40}$ but this is explained by oxygen being also present on the SWNT sidewalls in the form of defects as a result of the opening procedure previously. Raman spectroscopy, of {Mo_{12}}@SWNT, recorded +4.5 and +11.4 cm^{-1} blue shifts of the G-band, compared to empty SWNTs, in resonance with semiconducting and metallic SWNTs respectively (Figure 6.6c and d); moreover, the G-band profile of metallic SWNTs was found to change shape to resemble a more semiconducting profile. Both of these observations were a clear indication that the SWNTs were transferring electron density to the {Mo_{12}} POMs.

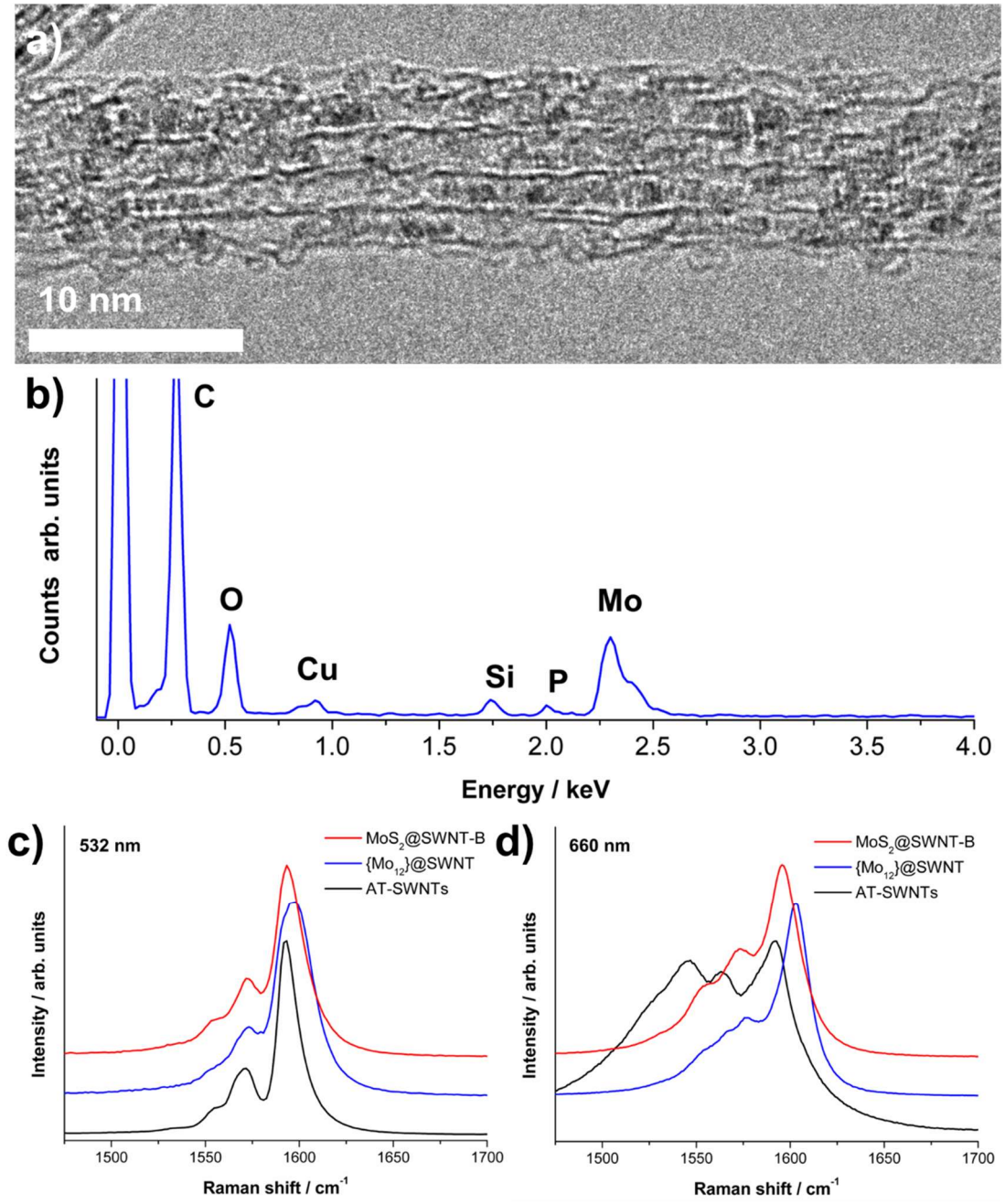


Figure 6.6. *(a) 200 kV TEM image of {Mo_{12}}@SWNT showing a bundle of SWNTs filled with high contrast features; (b) EDX spectrum recorded over a bundle of filled SWNTs (inset TEM image) which identifies the elements present from the host and guest, as well as copper from the TEM grid and Si from glass vial holders. Raman spectra overlay of each material formed during the stepwise synthesis, focussed on the G-band region, recorded using a laser excitation in resonance with (c) semiconducting SWNTs and (d) metallic SWNTs.*

{Mo_{12}}@SWNT was then reacted with H_2S gas at elevated temperatures to form MoS_2@SWNT-B; the result was the formation of continuous MoS_2 nanoribbons, from TEM imaging (Figure 6.7a). The image shows a bundle of SWNTs which contain continuous high contrast structures and are shown to be twisted, indicated by the superimposed arrow which highlights an area that changes from face-on to edge-on orientation, with respect to the electron beam, indicated by a change in contrast and smaller width. The atomic ratio of Mo: S was found to be slightly higher than the expected 1:2 ratio at 1:2.6 (Figure 6.7b), which may be explained by sulfur termination of MoS_2 nanoribbons, as also observed for MoS_2@SWNT-A synthesised using the carbonyl precursor method. The spectrum also showed a small atomic % of phosphorus (0.26 %) entrapped within the SWNTs after the reaction of the POMs with H_2S. The G-band of semiconducting SWNTs returned back to near the position of the empty SWNTs, conversely, the metallic contribution was found to be blue-shifted by +4.3 cm^{-1} (Figure 6.6c and d) and thus the MoS_2 nanoribbons were again behaving as electron acceptors as observed for MoS_2@SWNT-A ($Mo(CO)_6$ precursor). TG analysis recorded a residual weight of 12.5% after heating in air up to 1000 ^oC (Figure 6.7c); this is slightly lower than for MoS_2@SWNT-A synthesised from the $Mo(CO)_6$ precursor.

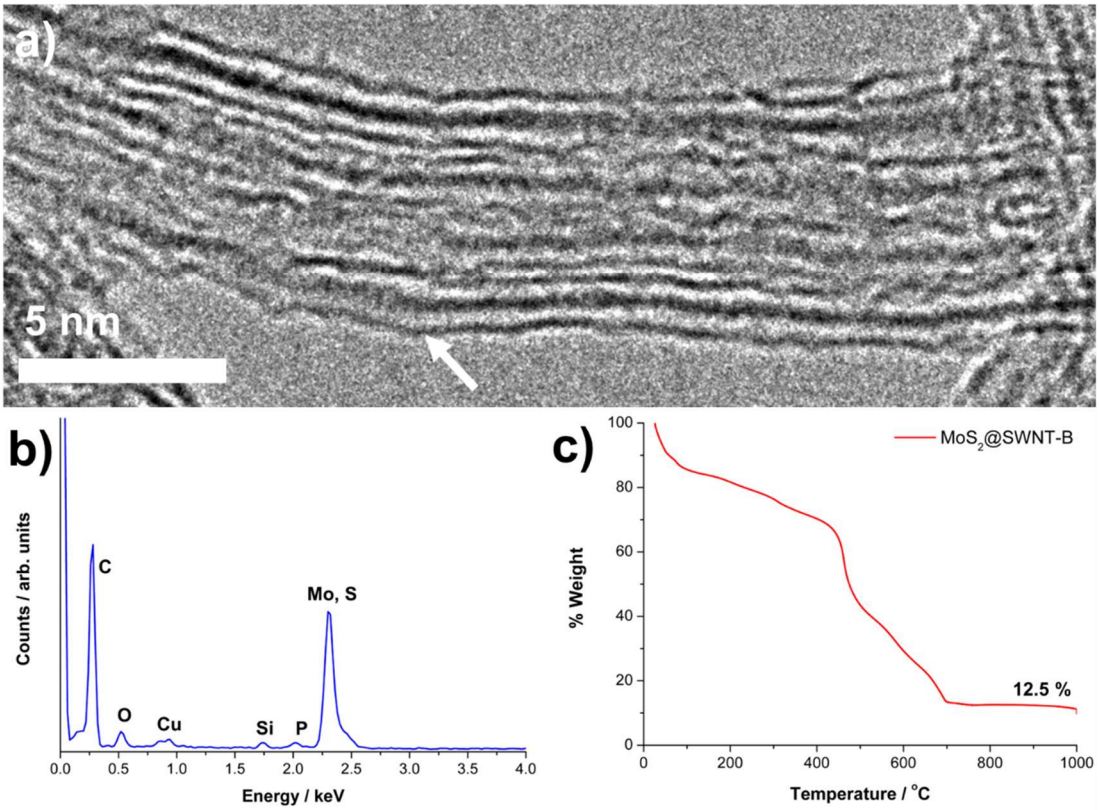


Figure 6.7. *(a) 200 kV TEM image of MoS_2@SWNT-B showing a bundle of SWNTs filled with MoS_2 nanoribbons (superimposed is a white arrow which indicates a twist point of the nanoribbon); (b) EDX spectrum, measured over a bundle of filled SWNTs, which shows Mo and S in a 1: 2.6 atomic ratio. Also observed is residual P from the POM structure; (c) Thermogram of MoS_2@SWNT-B displaying a residual weight % of 12.5 after heating in air up to 1000 °C.*

The MoS_2@SWNT-B material synthesised using $\{Mo_{12}\}$ was also examined by 60 kV aberration-corrected high-resolution (AC-HRTEM) imaging, along with modelling and TEM simulations to further characterise the structure of the formed nanoribbons as this was the first instance of using this methodology (Figure 6.8a and b). AC-HRTEM imaging showed a SWNT that was over 20 nm in length and was elliptically distorted as a result of the strong interactions between the SWNT host and the twisted nanoribbon guest. The MoS_2

nanoribbon starts in the face-on orientation which revealed the four-atom thick zigzag edged structure (4ZMoS$_2$NR), confirmed by modelling and simulation by the hexagonal structure and 0.31 nm Mo…Mo interatomic distances (Figure 6.8b); this resulted in a projected SWNT diameter of 1.6 nm. The nanoribbon undergoes a gradual twisting motion which results in the visualisation of the edge-on orientation and the contraction of the SWNT to produce a projected nanotube diameter of 1.1 nm which is decreased by 31 % compared to the face-on section. This elliptical distortion of the SWNT was also observed when MoS_2 nanoribbons were synthesised using POMs by Wang *et al*.[35] Also observed in the image are some extra atoms at the upper edge of the structure (white arrows, Figure 6.8b) which reveals that the structure is terminated with S-atoms and explains the higher atomic % of S in EDX (Figure 6.7b).

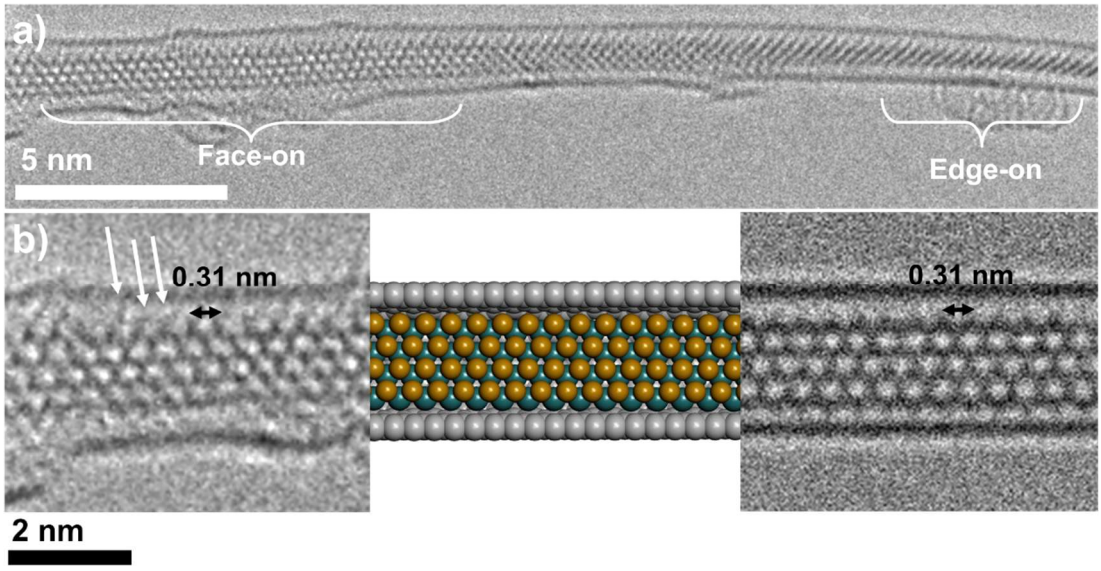
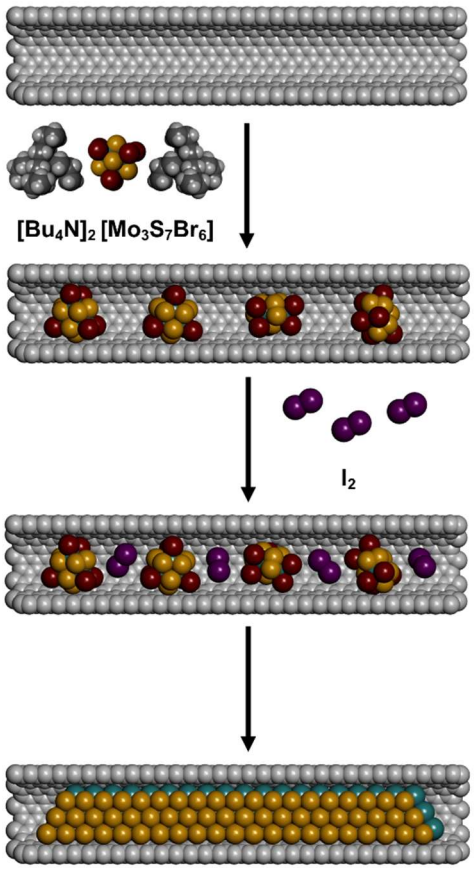


Figure 6.8. *(a) 60 kV AC-HRTEM image of MoS_2@SWNT-B showing a SWNT of 20 nm in length continuously filled with a twisted nanoribbon displaying the face-on and edge-on orientations; (b) Digitally-magnified face-on section of (a) which displays further detail of the hexagonal structure and the 0.31 nm interatomic distance (white arrows indicate extra sulfur atoms terminating the strucutre, left), structural model created using a SWNT of near-*

identical internal diameter and 4ZMoS$_2$NR (middle), 60 kV TEM simulation of the structural model (right).

6.2.2.3. *Synthesis of MoS$_2$@SWNT-C (via [Mo$_3$S$_7$Br$_6$]$^{2-}$)*

The third and final route towards forming MoS_2 nanoribbons within SWNTs was first developed in **section 4.2.1.** and utilises thiomolybdate hexabromide as the initial precursor (Scheme 6.3). The main advantage of this methodology is that the precursor is both the source of molybdenum and sulfur in a near 1: 2 stoichiometry. However, the use of iodine as a vapour transport agent for the formation of the quasi-1D MoS_2 nanoribbons does cause excess iodine/iodide intercalated within the SWNTs, which may affect the HER performance.



$2n\ [Bu_4N]_2\ [Mo_3S_7Br_6] + SWNT$

$-n\ [Mo_3S_7Br_6]^{4-}$ $-\ 4n\ [Bu_4N]^+$ ↓ 25 °C, Acetonitrile, 3 days

$n\ [Mo_3S_7Br_6]^{2-}@SWNT^{2n+}$

$+\ 4n\ I_2$ ↓ 120 °C, 10^{-5} mbar, 3 days

$n\ [Mo_3S_7Br_6^{2-} + I_3^- + I_5^-]@SWNT^{4n+}$

$-6n\ IBr$, $-n\ I_2$, $-1/8n\ S_8$ ↓ 500 °C, Argon atmos., 1 hour

$3n\ MoS_2@SWNT$

Scheme 6.3. *The stepwise synthetic route towards the formation of MoS$_2$@SWNT-C using thiomolybdate hexabromide as the source of both molybdenum and sulfur. [Mo$_3$S$_7$Br$_6$]$^{2-}$ is*

encapsulated into SWNTs using a solution-phase technique. Iodine is then introduced into the system via the vapour-phase, and the system is then subsequently thermally-activated under an inert atmosphere to produce MoS_2@SWNT-C.

In order to optimise the filling procedure, three different amounts of AT-SWNTs (3, 7, and 11 mg) were added to three aqueous solutions of $[Mo_3S_7Br_6]^{2-}$ of the same concentration, and their loadings were evaluated by thermogravimetric analysis (TGA, Figure 6.9). It was found that the two higher amounts of AT-SWNTs (7 and 11 mg) led to similar loadings of ~ 17- 18 %, whilst the lowest amount of AT-SWNTs (3 mg) demonstrated the highest loading of 28.4 % due to a maximised precursor to nanotube ratio. This material was then taken forward for the reaction with iodide to produce MoS_2 nanoribbons.

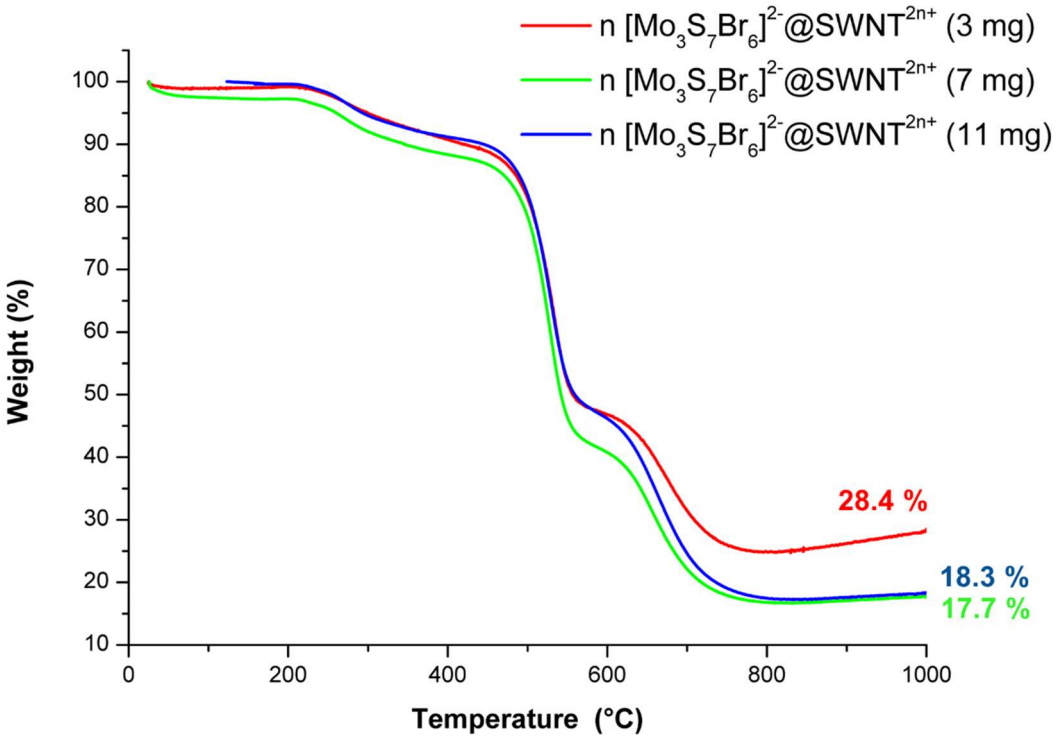


Figure 6.9. *Thermogram overlay for $n[Mo_3S_7Br_6]^{2-}$@$SWNT^{2n+}$ synthesised using different mass ratios of SWNT to $[Bu_4N]_2[Mo_3S_7Br_6]$ in each encapsulation which were; 3: 21 mg (red), 7: 21 mg (green), and 11: 21 mg (blue). The concentration of the $[Mo_3S_7Br_6]^{2-}$ aqueous solutions were kept the same in each experiment.*

n$[Mo_3S_7Br_6]^{2-}$@$SWNT^{2n+}$ synthesised using the lower mass ratio of SWNT to $[Bu_4N]_2[Mo_3S_7Br_6]$ (3: 21 mg) was imaged by TEM and was found to show the clusters in high yield within the SWNTs, appearing as dark elliptical features (Figure 6.10a). Complementary EDX analysis, recorded over a bundle of filled SWNTs, identified the elements of the host SWNT and guest species (Mo: S: Br in a 3.0: 7.0: 4.6 stoichiometry, Figure 6.10b). Upon encapsulation, the G-band of semiconducting SWNTs was found to only blue-shift by +1.1 cm^{-1} showing negligible charge transfer between host and guest (Figure 6.10c). A larger blue shift was measured for metallic SWNTs (+4.0 cm^{-1}) which demonstrates electron transfer from the host SWNT to the external $[Mo_3S_7Br_6]^{2-}$ (forming reduced $[Mo_3S_7Br_6]^{4-}$) which allows non-reduced molecules encapsulate via coulombic attraction, and reduced species to remain in solution (Figure 6.10d).

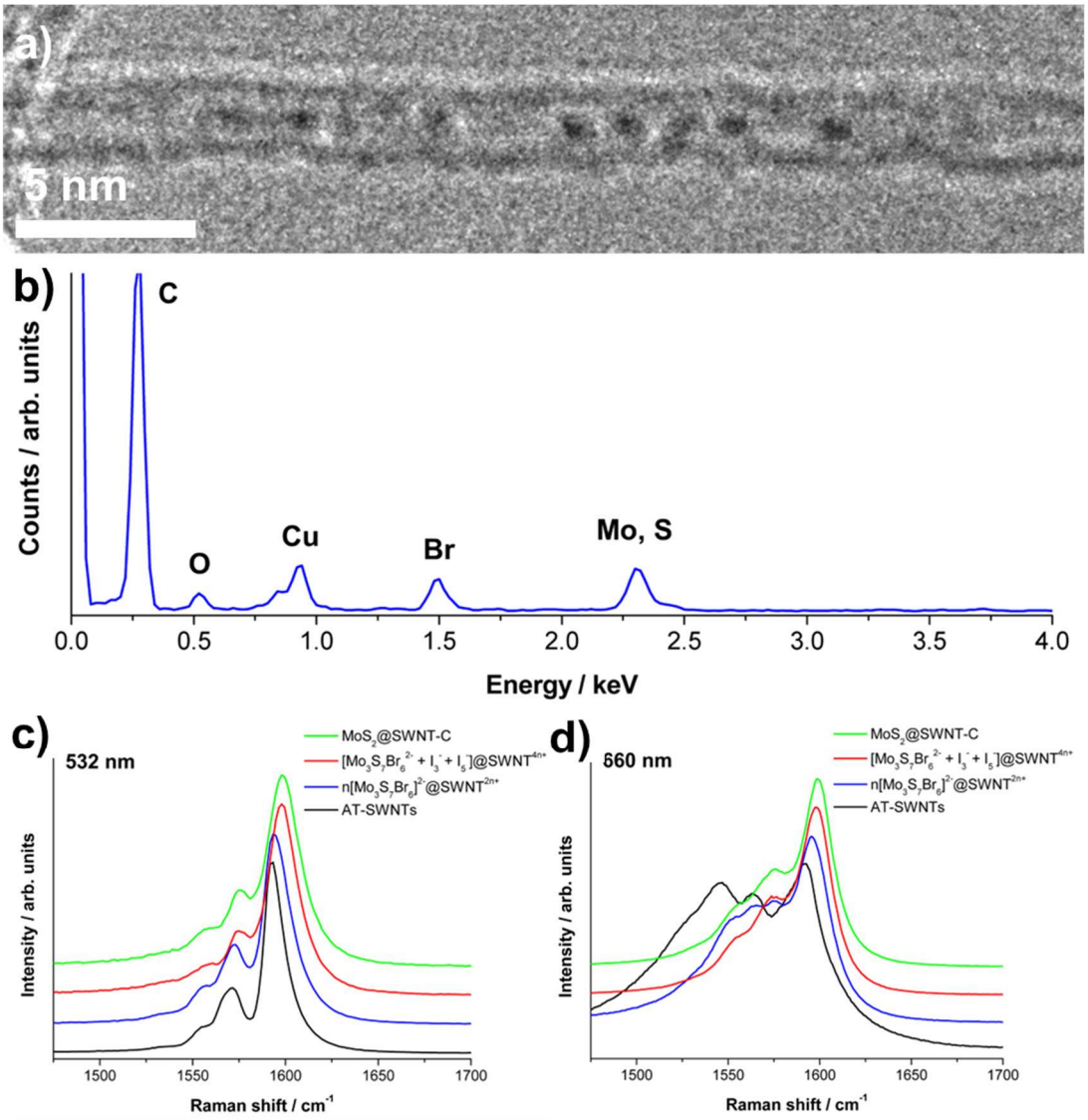


Figure 6.10. *(a) 200 kV TEM image of $n[Mo_3S_7Br_6]^{2-}$@$SWNT^{2n+}$; (b) EDX spectrum, measured over a bundle of filled SWNTs, identifying Mo, S, and Br in 3.0: 7.0: 4.6 atomic ratio. Raman spectra overlay of each material formed in the stepwise synthesis recorded in resonance with (c) semiconducting and (d) metallic SWNTs respectively.*

The insertion of iodine, $n[Mo_3S_7Br_6^{2-} + I_3^- + I_5^-]$@$SWNT^{4n+}$, caused a large blue shift of both G-bands and the emergence of polyiodide bands (I_3^- and I_5^-) in the low-frequency region of the 532 nm Raman spectrum (Figure 6.10c and d). Thermal activation, under an inert atmosphere at 500 °C, of the system was shown, by TEM and EDX, to produce MoS_2 nanoribbons demonstrated by the presence of continuous structures within the SWNT hosts (Figure 6.11a), the loss of Br in the EDX spectrum, and the presence of Mo and S in a 1: 2

stoichiometry (0.12 and 0.25 atomic %, Figure 6.11b). However, it was shown that a large amount of iodine remained encapsulated within the system (0.58 atomic %). This was also demonstrated by the negligible shift of the G-band for both semiconducting and metallic SWNTs compared to the G-band positions after the initial addition of iodine (Figure 6.10c and d). The intercalation of iodide species within MoS_2@SWNT introduces more surface sites but I_n^- may negatively impact the HER due to possible bonding with protons. TG analysis of the nanoribbon filled SWNTs, after heating in air at 1000 °C, produced a residual weight of 16.9 % (Figure 6.11c).

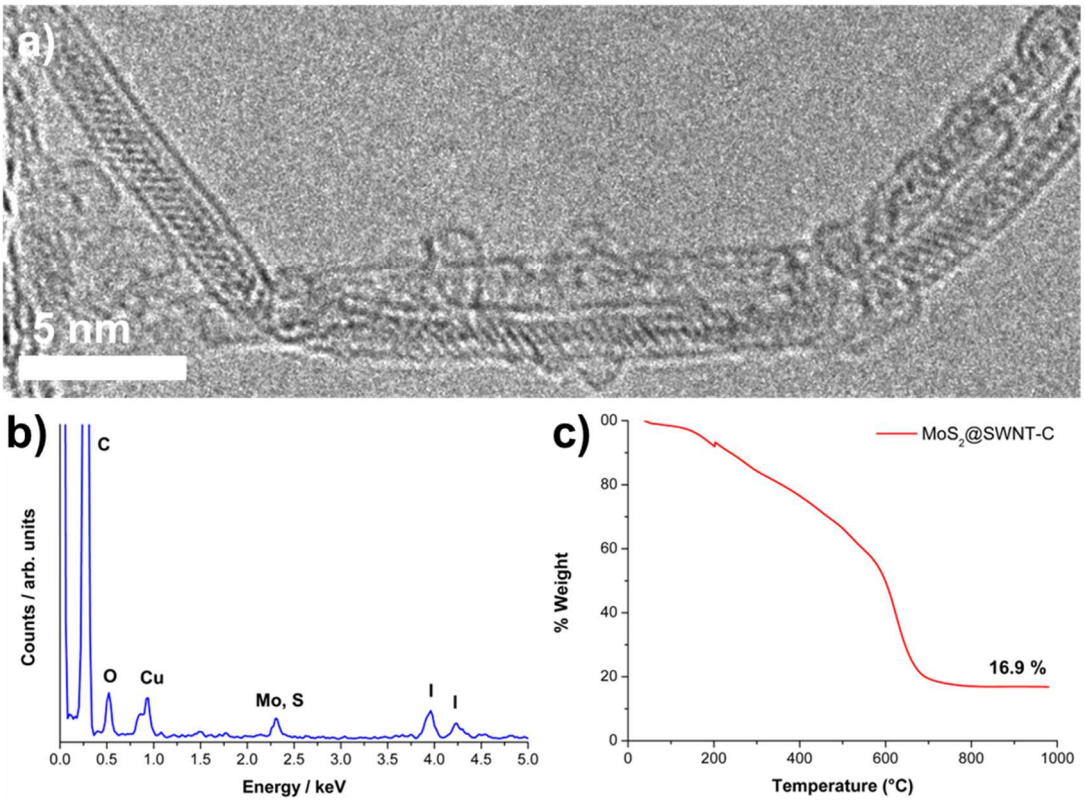


Figure 6.11. *(a) 200 kV TEM image of MoS_2@SWNT-C formed by thermal activation of the clusters with iodine, showing the presence of nanoribbons within the SWNTs; (b) EDX spectrum, recorded over the wider area of (e), identifying Mo and S in a 1: 2 stoichiometry (0.12 and 0.25 atomic % respectively), along with a presence of iodine (0.58 atomic %); (c) thermogram of MoS_2@SWNT-C displaying a residual weight % of 16.9 after heating in air up to 1000 °C.*

6.2.2.4. MoS_2@SWNT HER performance

Each of the MoS_2@SWNT samples (A, B, and C) were then evaluated towards the HER and compared to the empty AT-SWNTs to evaluate the effect of each interior modification (Figure 6.12). All three MoS_2@SWNT (A, B, and C) performed exceedingly better than the empty AT-SWNTs, exhibited by lower overpotentials, and demonstrate the improved electrocatalytic ability upon addition of an active guest species. The lowest performing material was MoS_2@SWNT-C ($[Mo_3S_7Br_6]^{2-}$ precursor) which required an overpotential of -373 mV to reach a current density of -10 mA cm^{-2}. MoS_2@SWNT-B ($H_3PMo_{12}O_{40}$ precursor) vastly improved the HER performance compared to MoS_2@SWNT-C ($[Mo_3S_7Br_6]^{2-}$ precursor), exhibiting an overpotential of -279 mV at -10 mA cm^{-2}. Finally, MoS_2@SWNT-A ($Mo(CO)_6$ precursor) was found to perform equally as well as MoS_2@SWNT-B, recording an overpotential of -278 mV at -10 mA cm^{-2}.

The low performance of MoS_2@SWNT-C is attributed to the high presence of iodine within the sample, displayed by EDX. Cleaning steps, including sublimation and washing with chloroform, were attempted but failed to eliminate the encapsulated iodine/ iodide species; this is a result of the strong coulombic attraction between the positively-charged SWNTs and the anionic polyiodide species. The near identical performance for MoS_2@SWNT-A and MoS_2@SWNT-B suggests that they are both the result of a high conversion of MoS_2 nanoribbons, with a little amount of by-products or other reactants (such as iodine) remaining entrapped that may negatively impact the HER performance. However, it was shown via TGA that MoS_2@SWNT-B produced a smaller residual weight than MoS_2@SWNT-A (12.5 and 18.0 % respectively) thus demonstrating that despite a lower filling, more of the nanotubes contained catalytic MoS_2 material. Moreover, the synthetic route used to produce MoS_2@SWNT-B requires fewer steps and the use of only molybdenum and sulfur-based reagents, which is beneficial compared to the three step procedure and use of iodine in the synthesis to produce MoS_2@SWNT-A. Compared to earlier examples of MoS_2-based species

catalysing the HER,[15, 23-25] the best two MoS_2@SWNT materials (A and B) still underperformed despite the high proportion of active edge sites coupled with the use of a SWNT to transport electrons. This can be rationalised by examining previous density functional theory (DFT) calculations on the differential free energies of hydrogen adsorption (ΔG^o_H) by Bonde *et al*. that were conducted on both the metal and sulfur edge sites for MoS_2, with optimum electrocatalysts possessing closer to zero free energies.[36] The Mo edge site was found to have ΔG^o_H values of 0.08, whilst the S edge site free energy for MoS_2 was determined to be 0.18 eV. It has been shown, for MoS_2@SWNT (A and B) that they contain a higher atomic % of sulfur and this was shown using AC-HRTEM to be terminating the MoS_2 nanoribbons creating more S edge sites than Mo. The data was then replotted as the overpotential against ln current density to produce tafel plots, and the slope values of the linear regions for each material were determined to be 47.3, 40.3, 37.1, and 36.4 mV dec^{-1} for AT-SWNTs, and MoS_2@SWNT-C, MoS_2@SWNT-B, and MoS_2@SWNT-A respectively (Figure 6.12 inset). These values suggest that each mechanism is rate-controlled by the Heyrovsky step.

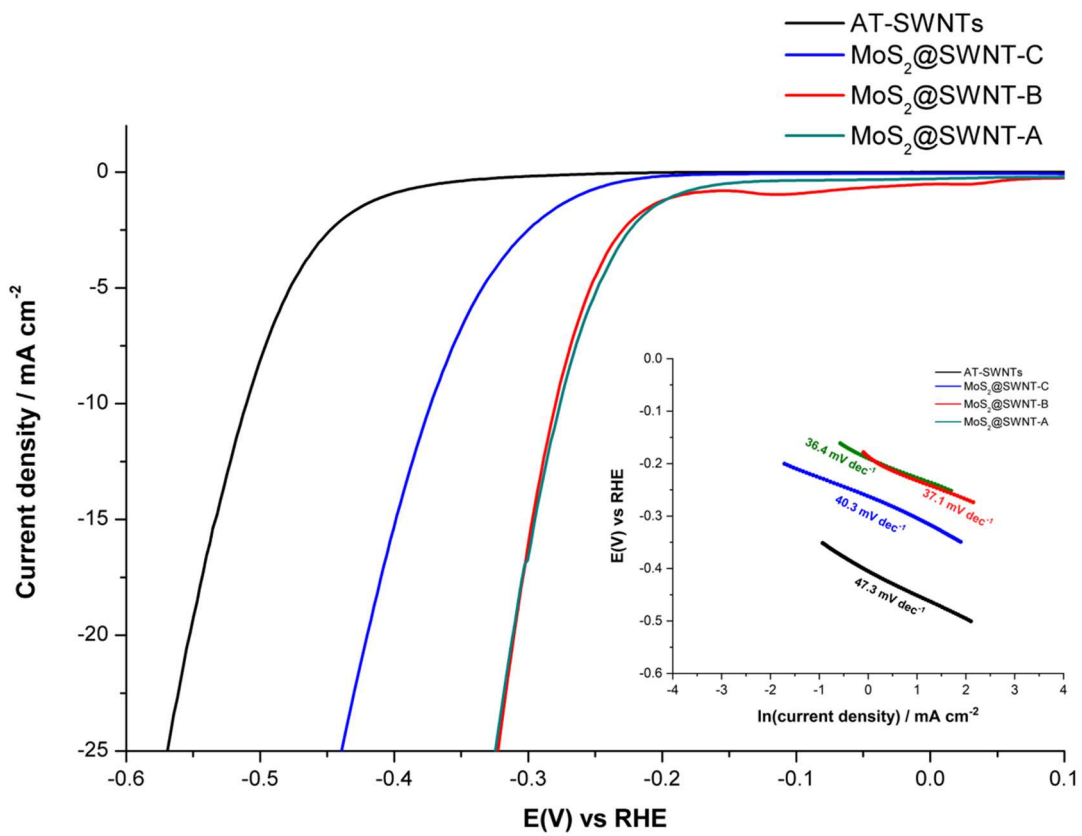


Figure 6.12. *Polarisation curve showing the HER performance of AT-SWNTs (black), and each of the host-guest materials; MoS_2@SWNT-C ($[Mo_3S_7Br_6]^{2-}$ precursor, blue), MoS_2@SWNT-A ($Mo(CO)_6$ precursor, green), and MoS_2@SWNT-B ($H_3PMo_{12}O_{40}$ precursor, red). The overpotential values for each material to achieve a current density of -10 mA cm^{-2} were; -373 mV (MoS_2@SWNT-C), -279 mV (MoS_2@SWNT-B), and -278 mV (MoS_2@SWNT-A). Inset is a Tafel plot for the four materials studied showing slope values of 47.3, 40.3, 37.1, and 36.4 mV dec^{-1} for AT-SWNTs, and MoS_2@SWNT-C, MoS_2@SWNT-B, and MoS_2@SWNT-A respectively.*

6.2.3. Changing the metal

The first variation in the measurement was to change the metal from molybdenum to tungsten in order to evaluate the effect of the heavier element. WS_2 has also been identified as a possible electrocatalyst towards the HER to replace the use of platinum[37]; however, WS_2

does have a higher differential free energy of hydrogen adsorption, which will affect its performance,[36] but the use of SWNTs as a template to form ultrathin WS_2 may help improve the performance by introducing a high proportion of catalytically-active edge sites. Due to the respectable performance achieved and the lower number of reaction steps by the MoS_2 formed using the Keggin POM, the WS_2@SWNT material was synthesised using the tungsten Keggin analogue, $H_3PW_{12}O_{40}$, in accordance with the experimental section outlined in **section 5.2.1**. This was shown to produce continuous tungsten disulfide nanoribbons of the expected structure and composition in high yield (32.1 % residual weight from TG analysis, Figure 6.13a - c).

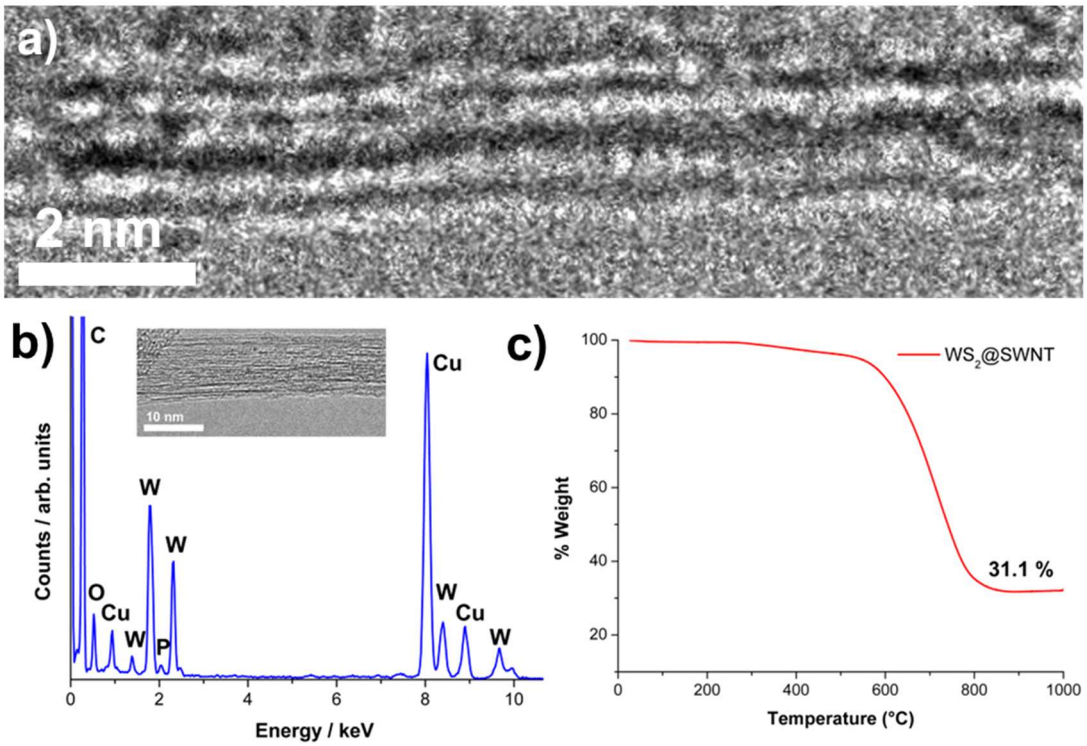


Figure 6.13. *(a) 200 kV TEM image of WS_2@SWNT, produced using $H_3PW_{12}O_{40}$ as the precursor; the image shows a typical high contrast continuous nanoribbon which is representative of the material; (b) EDX spectrum, recorded over a bundle of filled SWNTs, which identified the constituent elements of the nanoribbons (W and S) as well as residual phosphorus from the POM precursor; (C) thermogram of WS_2@SWNT displaying the residual weight % as 32.1 after heating in air up to 1000 °C. (Data taken from* ***section 5.2.1.2.****)*

The HER performance was measured and found to have achieved an overpotential of -318 mV at -10 mA cm^{-2} (Figure 6.14), which is 192 mV better than empty SWNTs, but was found to be 39 mv worse than MoS_2@SWNT-B formed using the same POM-based synthetic method (Figure 6.12). This can again be rationalised by differential free energies of hydrogen adsorption (ΔG^{o}_{H})[36] that found the W edge was higher in energy (0.22 eV) than the Mo edge (0.08 eV). This shows that despite WS_2 still being active towards the HER, it is not as effective as an electrocatalyst as MoS_2. Similarly to each MoS_2@SWNT measured previously, the mechanism was determined to be rate-controlled by the Heyrovsky step as demonstrated by a Tafel slope value of 36.3 mV dec^{-1}.

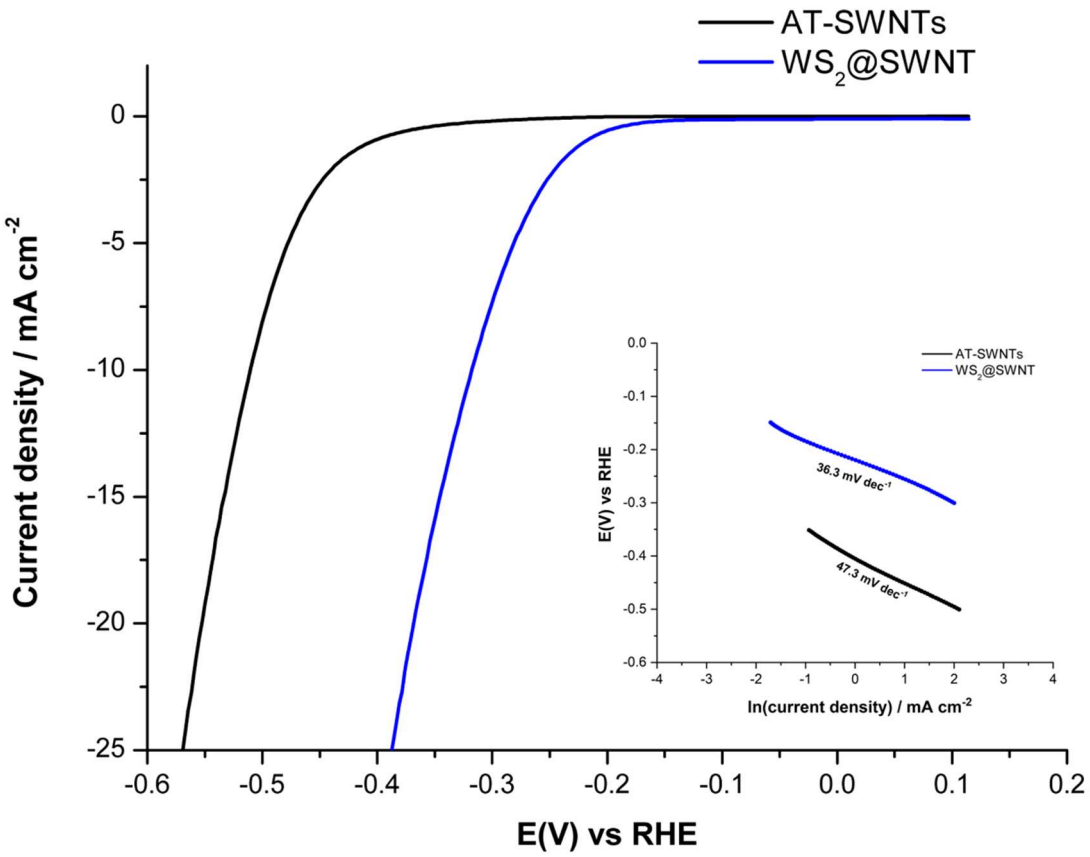


Figure 6.14. *Polarisation curve showing the hydrogen evolution performance of AT-SWNTs (black), and WS_2@SWNT (blue) which was synthesised using the $H_3PW_{12}O_{40}$ Keggin POM. The overpotential at -10 mA cm^{-2} was measured to be -318 mV. Inset is a Tafel plot for AT-SWNTs and WS_2@SWNT which display slope values of 47.3 and 36.3 mV dec^{-1} respectively.*

6.2.4. Comparison of the edge-site molecular mimic

So far in this study, the materials that have been studied have been synthesised through initial encapsulation of a precursor molecule into SWNTs followed by a reaction using a second (or third) reagent. MoS_2@SWNT-C was shown to be exhibit the lowest HER electrocatalytic ability which was attributed to the amount of iodine entrapped in the system negatively impacting the HER. However, MoS_2@SWNT-C was synthesised using $[Mo_3S_7Br_6]^{2-}$ as the precursor, which consists of molybdenum and sulfur in a close to 1:2 stoichiometry, and has a structure that is close in structure to being a molecular mimic of the edge-site of MoS_2 monolayers, with the addition of bromide ligands.[38-40] $[Mo_3S_7Br_6]^{2-}$ contains a higher proportion of surface atoms than the synthesised MoS_2 nanoribbons, and thus should be more electrocatalytically-active towards the HER. Moreover, the use of the encapsulated cluster, $n[Mo_3S_7Br_6]^{2-}$@$SWNT^{2n+}$, as the electrocatalyst rids of extra reagents such as iodine, which lower the HER performance, as well as use of the SWNTs as an excellent conduction path for electron transport to and from catalytic centres and providing stabilisation of molecules during redox processes.[41] Trinuclear molybdenum clusters of the framework $[Mo_3S_7]^{4+}$ have been shown previously to exhibit high performances towards the HER;[39, 40, 42-44] they have also been evaluated when physisorbed on the exterior surface of carbon nanotubes,[28] but this will mark the first occasion in which their electrocatalytic ability will be examined within the confinements of SWNTs.

$[Mo_3S_7Br_6]^{2-}$ was inserted into the SWNTs via a solution-phase filling method (**section 6.2.2.3.**) and the resultant material, $n[Mo_3S_7Br_6]^{2-}$@$SWNT^{2n+}$, was determined to retain the structure and composition of the cluster (Figure 6.10a and b). $n[Mo_3S_7Br_6]^{2-}$@$SWNT^{2n+}$ was found to outperform all MoS_2@SWNT composite materials, achieving an overpotential of -215 mV at a current density of -10 mA cm^{-2} (Figure 6.15). This is an important result as it demonstrates the profound effect of the performance of encapsulated clusters versus synthesised nanoribbons. Furthermore, the data was replotted as a Tafel plot and

n$[Mo_3S_7Br_6]^{2-}$@$SWNT^{2n+}$ displayed two linear regions with slope values of 88.1 and 22.4 mV dec^{-1} at low and high potential regions respectively. These values suggest that at high potential regions the Tafel step is rate-controlling but at low potential regions the mechanism transitions to a combination of the Volmer and Heyrovsky steps controlling the rate. This is in stark contrast to the single linear region of the Tafel slope of MoS_2@SWNT-C, synthesised using the same precursor cluster, which demonstrates the effect of extended structures versus discrete molecules on the mechanism of HER catalysis.

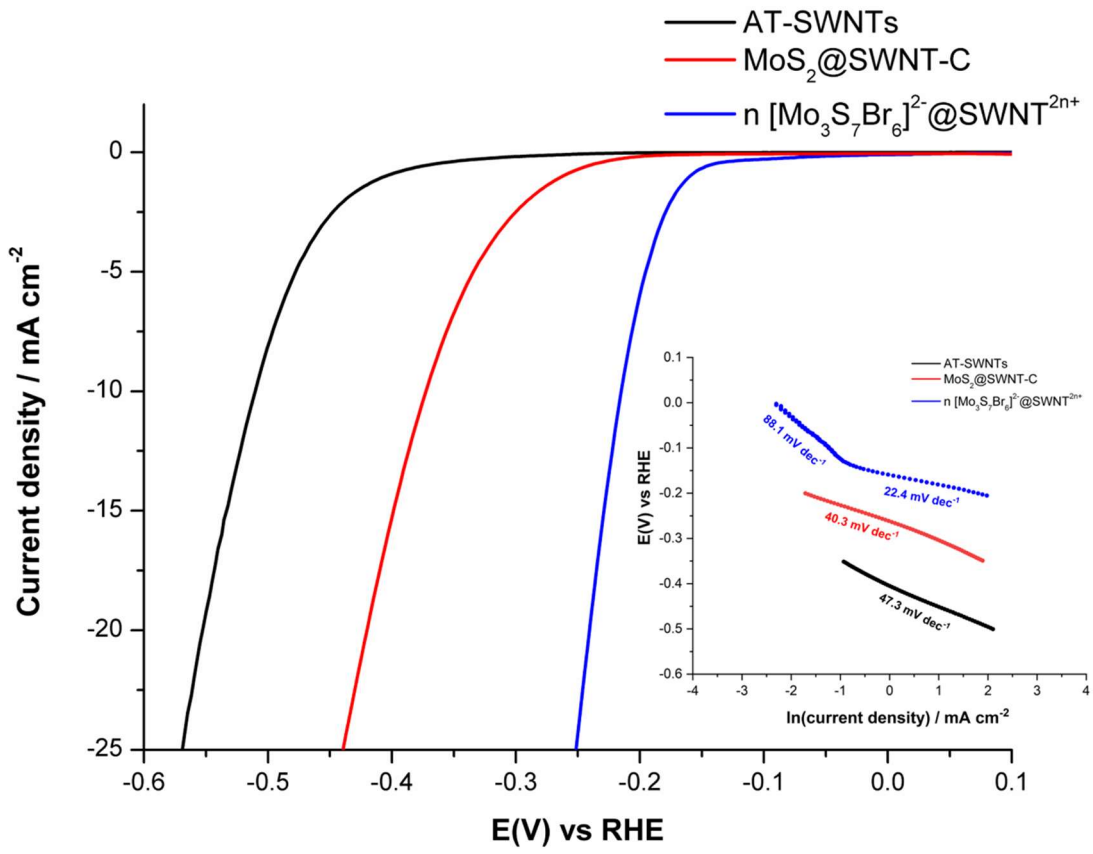


Figure 6.15. *Polarisation curves showing the HER performance of AT-SWNTs (black),* MoS_2*@SWNT-C (*$[Mo_3S_7Br_6]^{2-}$ *precursor, red) as references, and* n$[Mo_3S_7Br_6]^{2-}$@$SWNT^{2n+}$ *(blue). The overpotential values at -10 mA* cm^{-2} *were recorded as -510, -373, and -215 mV for each material respectively.* Inset is a Tafel plot for the three electrocatalytic materials which have slope vales of 47.3 and 40.3 mV dec^{-1} for AT-SWNTs and MoS_2@SWNT-C respectively.

Also shown are two slope values for n $[Mo_3S_7Br_6]^{2-}$@$SWNT^{2n+}$ of 88.1 and 22.4 mV dec^{-1} corresponding to the low and high potential regions respectively.

It is thus presented that there are two primary advantages of using encapsulated clusters as electrocatalysts; the first is that there is more control over the structure and composition than for materials synthesised via reaction of precursors, this includes a lack of by-products formed or reagents entrapped within the SWNT interior channel. The second is that the clusters contain a higher proportion of catalytically-active edge sites than MoS_2 nanoribbons, and they take up a lower volume of space within the SWNT channel allowing protons to access all of the active sites easily. The size templating ability of the SWNTs to form MoS_2 nanoribbons that have widths that fit tightly within causes void space to be present only above and below the nanoribbon (Figure 6.16a); whilst the clusters have void space fully surrounding them providing more space for protons to enter and interact with the catalytic surface (Figure 6.16b and c). Structural models are provided to illustrate this effect.

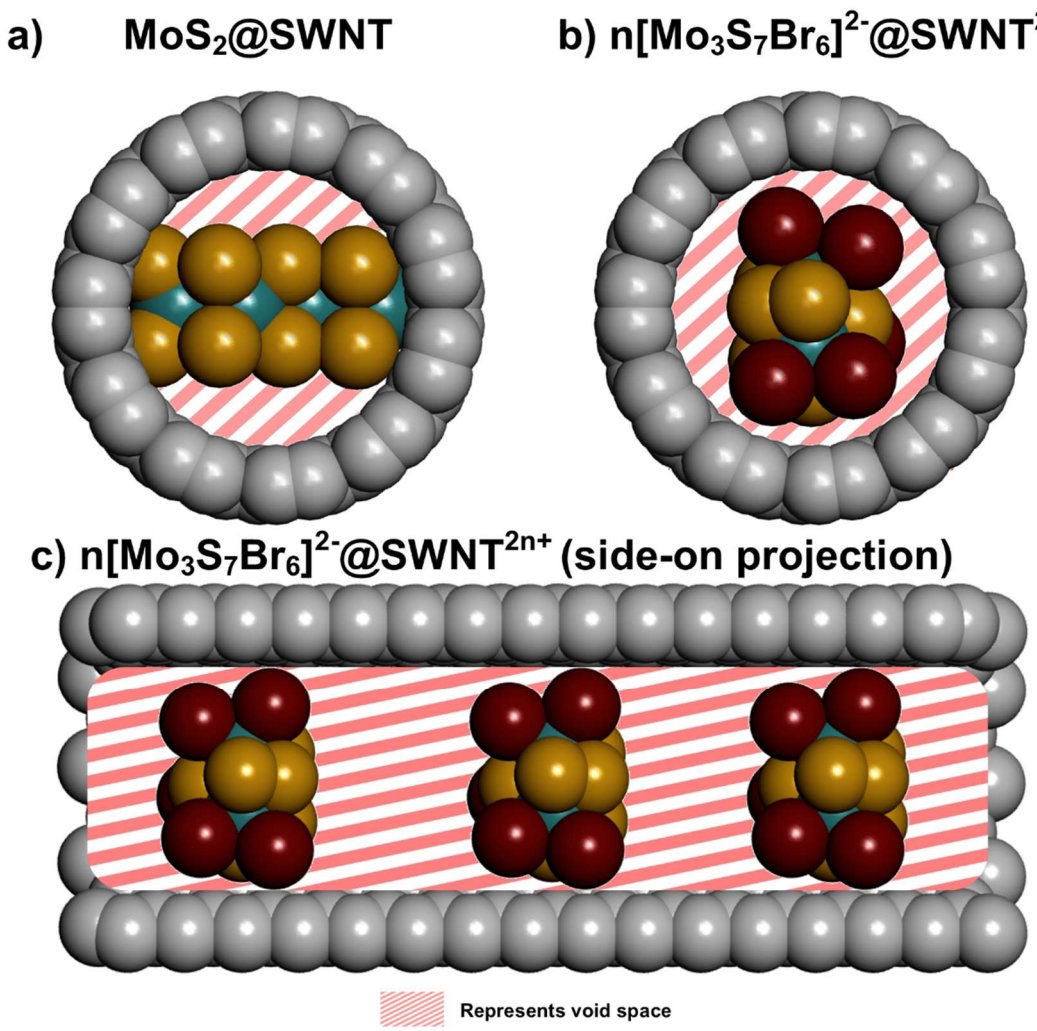


Figure 6.16. *Structural models of (a) MoS_2@SWNT constructed using a four atom wide MoS_2 nanoribbon within a (11,11) SWNT and (b) $n[Mo_3S_7Br_6]^{2-}$@$SWNT^{2n+}$ in edge-on projection, and (c) in side-on projection, both were constructed using a (11,11) SWNT with an internal diameter of 1.5 nm. The red and white striped regions represents the void space of each system.*

6.2.5. Janus MoSSe and corresponding molecular mimic

The final two materials that were studied as proof of concepts were synthesised Janus MoSSe nanoribbons, Janus MoSSe@SWNT, and the encapsulated parent molecule thio-selenomolybdate hexabromide, $n[Mo_3S_4Se_3Br_6]^{2-}$@$SWNT^{2n+}$, which were both synthesised in **section 4.2.2.** Janus MoSSe has extra strain in the structure as a result of the breaking of the

mirror symmetry compared to MoS_2; this activates the basal plane allowing more of the material to be active.[45-47] DFT calculations of the free energy of hydrogen adsorption were previously performed on Janus MoSSe monolayers on SiO_2/Si surfaces, which show that SeMoS with a single Se vacancy has a near zero ΔG^o_H value of -0.007 eV and SMoSe with a single S vacancy has a value of 0.060 eV.[47] These are far below the reported value for MoS_2 with a single S vacancy of 0.161 eV; moreover, the experimental electrocatalytic HER performances of SMoSe and SeMoS monolayers were found to far exceed those of MoS_2 correlating well with the theoretical findings. As well as testing the electrocatalytic ability of Janus MoSSe@SWNT; $n[Mo_3S_4Se_3Br_6]^{2-}$@$SWNT^{2n+}$ will also be evaluated which will further probe the performance of encapsulated clusters versus nanoribbons within SWNTs.

Janus MoSSe@SWNT was synthesised according to the synthetic procedure set out in **section 4.2.2.** which was shown to result in continuous nanoribbons that were asymmetric; moreover, a lower residual amount of iodine was found to be entrapped within the SWNT channel (comapred to MoS_2@SWNT-C) as a result of the larger atomic radii of selenium atoms present providing less space. The performance towards the HER was evaluated and an initial striking feature of the polarisation curve of Janus MoSSe@SWNT was the non-zero current density at the start of the measurement, which is due to the material exhibiting capacitance (Figure 6.17). The material recorded an overpotential of -227 mV at -10 mA cm^{-2} which outperformed all three MoS_2@SWNT materials, as well as WS_2@SWNT, and thus is the best performing synthesised quasi-1D nanoribbon species. Moreover, it is interesting in particular that this system performs better than MoS_2@SWNT-C using $[Mo_3S_7Br_6]^{2-}$ which both utilise the same synthetic route; this confirms that the presence of the asymmetric MoSSe structure has a profound effect on the HER due to the additional basal plane active sites. Moreover, there is less iodine and hence fewer Mo-I edge groups which reduce the electrocatalytic ability.

To further probe the hypothesis that encapsulated molecular mimics perform better than their nanoribbon equivalents; n[$Mo_3S_4Se_3Br_6$]$^{2-}$@SWNT^{2n+} was tested. The polarisation curve measured for n[$Mo_3S_4Se_3Br_6$]$^{2-}$@SWNT^{2n+} recorded an overpotential of -196 mV at -10 mA cm^{-2} (Figure 6.17); this was found to be the best performing material of any encapsulated cluster or synthesised nanoribbon tested. This proves that molecular edge site mimics are more catalytically-active than their nanoribbon counterparts when encapsulated within SWNTs due to the increased number of accessible active sites. Furthermore, it demonstrates the extraordinary electrocatalytic ability of mixed chalcogenide Janus structures towards the HER. The Tafel slope of MoSSe@SWNT was recorded to be 39.8 mV dec^{-1} suggesting the rate-controlling step is the Heyrovsky process, which agrees with values for all previous encapsulated nanoribbons (Figure 6.17 inset). Two linear regions were recorded for n[$Mo_3S_4Se_3Br_6$]$^{2-}$@SWNT^{2n+} which have slope values of 90.1 and 23.5 mV dec^{-1} in the high and low potential regions respectively. These values agree with those measured for n[$Mo_3S_7Br_6$]$^{2-}$@SWNT^{2n+} suggesting the same transition mechanism from the rate-controlling Tafel step at high potential regions to a combination of Volmer and Heyrovsky steps at low potential regions.

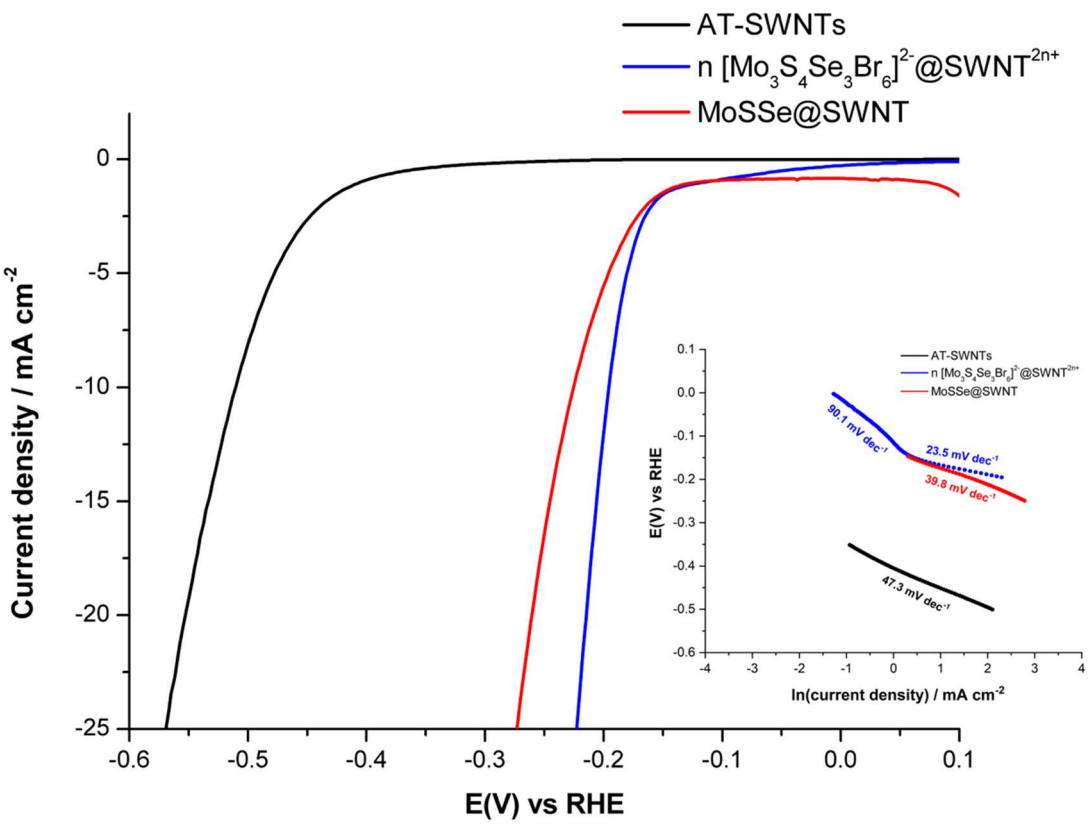


Figure 6.17. *Polarisation curves displaying the hydrogen evolution reaction catalytic performance of AT-SWNTs (black) as reference, MoSSe@SWNT (red), and n[$Mo_3S_4Se_3Br_6$]$^{2-}$@SWNT^{2n+} (blue) with overpotentials at -10 mA cm^{-2} of -510, -227, and -196 mV respectively. Inset is a Tafel plot for the three electrocatalytic materials which have slope vales of 47.3 and 39.8 mV dec^{-1} for AT-SWNTs and MoSSe respectively. Also displayed are the two slope values for n [$Mo_3S_4Se_3Br_6$]$^{2-}$@SWNT^{2n+} of 90.1 and 23.5mV dec^{-1} corresponding to the low and high potential regions respectively.*

6.3. Conclusion

In summary, a range of empty and filled single-walled carbon nanotube materials were evaluated electrocatalytically towards the HER as a proof of concept of the HER ability of confined metal chalcogenides. It has been demonstrated that both heat and acid treatment cleaning steps were required to optimise the SWNT hosts which removed the end caps,

allowing access to the interior surface, and removed excess nickel nanoparticles leftover from the synthesis of the nanotubes. Interior modification of the SWNTs with a metal chalcogenide-based guest species was always shown to improve the catalytic performance compared to empty SWNTs. Synthesised MoS_2 nanoribbons within SWNTs were evaluated and it was found that the synthetic route used can cause dramatic differences in the ability. MoS_2@SWNT-C ($[Mo_3S_7Br_6]^{2-}$ precursor) was determined to contain a high amount of iodine entrapped within the nanotubes which adds surface sites which negatively impact the HER. The two methodologies that used H_2S (A and B) produced MoS_2 nanoribbons which exhibited a higher than expected atomic % of sulfur which was attributed to sulfur termination of MoS_2 nanoribbons. Both of these materials were shown to require lower overpotentials to reach a current density of -10 mA cm^{-2} (compared to MoS@SWNT-C) and were found to be comparative to some other MoS_2 materials previously reported.[26] This was attributed to the higher proportion of S edge sites which have a higher hydrogen adsorption energy than Mo edges. Tungsten disulfide nanoribbons were shown to perform slightly worse than their MoS_2 analogues which was an effect of the free energy of hydrogen adsorption being higher for the W edge compared to the Mo edge of MoS_2. Synthesised Janus MoSSe nanoribbons were found to outperform MoS_2 nanoribbons which was attributed to the extra strain in the material, from the asymmetry of the chalcogenides, that causes the basal plane to become catalytically-active. Tafel slope analysis of all encapsulated nanoribbon species showed that it was the Heyrovsky step, the combination of adsorbed hydrogen with a proton and an electron to produce molecular hydrogen, which was the rate-controlling step in the HER.

Finally, encapsulated molecular mimics ($n[Mo_3S_7Br_6]^{2-}$@$SWNT^{2n+}$ and $n[Mo_3S_4Se_3Br_6]^{2-}$@$SWNT^{2n+}$) of the catalytic edge sites of metal dichalcogenides were found to outperform synthesised nanoribbons. This was explained by the higher number of accessible active sites as a result of more void space within the SWNT channel, hence easier proton diffusion in / H_2 diffusion out of SWNT, and a higher proportion of the guest species being active edge

sites. Moreover, the encapsulated clusters offer more control over the structure and composition of the electrocatalytic guest species, compared to synthesised nanoribbons which may form by-products or cause entrapment of reagents which negatively impact the HER ability. n$[Mo_3S_4Se_3Br_6]^{2-}$@$SWNT^{2n+}$ was the best performing electrocatalytic material overall due to the combination of a high number of active sites, as well as the presence of mixed S-Se bridging ligands. It was found by Tafel slope analysis that the encapsulated molecular mimics displayed two linear regions which demonstrated a transition in the rate-controlling step when moving between high and low potential regions.

Future studies should focus on the stability and durability of these electrocatalysts, as SWNTs have an ability to offer protection to guest species. As an initial screen of the electrocatalytic ability of these encapsulated metal chalcogenide nanostructures, they perform well when compared to literature measurements on larger nanostructures. This highlights that the architecture and design of nanoscale electrocatalysts is essential to improve performance. This includes the challenge of designing MoS_2@SWNT nanostructures that contain a higher number of Mo edge sites to further reduce the overpotential.

6.4. Experimental

6.4.1. Materials

$[Bu_4N]_2[Mo_3S_7Br_6]$ and $[Bu_4N]_2[Mo_3S_4Se_3Br_6]$ were synthesised externally at the University of Valencia using methods developed by Fedin *et al.*[48, 49] Phosphotungstic acid, $H_3PW_{12}O_{40}$, was synthesised externally in accordance to a procedure developed by Makoto *et al.*[50] SWNTs (P2-SWNTs, arc discharge, Carbon Solutions, USA) were either annealed at 600 ^oC for 17 mins to produce opened SWNTs, or refluxed in 3M HNO_3 for two hours and then annealed at 600 ^oC for 17 min to remove their end caps and any amorphous carbon present, producing AT-SWNTs.Molybdenum trioxide (Sigma Aldrich), bromine water (Alfa Aesar), phosphonic acid

(85 wt%, Fisher Scientific), Nafion (5%, Sigma Aldrich), sulfuric acid (68%, Sigma Aldrich), dimethylformamide (Arcos Organics), dihydrogen sulfide (Special Gases), nitric acid (68%, Fisher Scientific), acetonitrile (Arcos Organics), iodine (Fisher Scientific), Molybdenum hexacarbonyl (Arcos Organics), and bleach (Selden) were all used as received.

6.4.2. Formation of MoS_2@SWNT-A by using $Mo(CO)_6$

$Mo(CO)_6$ (15 mg, 0.057 mmol), iodine (30 mg, 0.12 mmol) and AT-SWNTs (5 mg) were all sealed in a Pyrex ampoule at 10^{-5} mbar and then heated at 120 °C for three days. The resultant material was then placed in a second ampoule, sealed under 0.7 bar of argon, and heated to 500 °C for one hour to thermally-activate the system. The thermally-treated material was then placed on a quartz boat in the centre of a tube furnace where it was subjected to a flow of argon gas (15 mL / min) for one hour followed by dihydrogen sulfide, H_2S (15 mL / min). The furnace was then heated to 550 °C for 2 hours under a flow of H_2S (15 ml / min) and then left to cool to room temperature under a flow of argon gas (15 mL / min). Excess H_2S from the flow reaction was released through a bleach bath (200 mL) to neutralise the gas. The MoS_2@SWNT-A product was then collected.

6.4.3. Preparation of $H_3PMo_{12}O_{40}$

$H_3PMo_{12}O_{40}$ was synthesised according to a procedure developed by Tsigdinos.[51] Molybdenum trioxide (30.8 g, 0.21 mol) was dissolved in aqueous phosphoric acid (85 %, 1.22 mL in 300 mL water) to form a yellow solution. The mixture was refluxed for four hours, causing the colour to darken, and then filtered by gravity. The mother liquor then turned green overnight which was reversed upon addition of a few drops of bromine water, and was then brought to boiling for eight hours until the volume reduced to 40 mL, resulting in a yellow precipitate formed. The mixture was filtered *in vacuo*, washed with ethanol (2 x 10 mL), and then left to air dry yielding phosphomolybdic acid hydrate (823 mg, 0.396 mmol, 2.22%). ^{31}P NMR; δ_P (162 MHz, D_2O) -3.88 ppm, m/z; 1825, 100%.

6.4.4. Formation of MoS_2@SWNT-B by using $H_3PMo_{12}O_{40}$

AT-SWNTs (5 mg) were added to an aqueous solution of $H_3PMo_{12}O_{40}$ (50 mg, 0.027 mmol in 3 mL of water) and left to stir at room temperature for three days. The resultant mixture was filtered using a Polytetrafluoroethylene membrane, washed on the filter with further water (10 - 15 mL), and then left to air dry. The product, {Mo_{12}}@SWNT, (3 mg) was loaded onto a quartz boat which was placed within a tube furnace and exposed to a flow of argon for one hour, followed by a flow of hydrogen sulfide, both at a rate of 15 mL/min). The furnace was then heated to 550 °C for two hours under the flow of H_2S (15 mL/min) and then left to cool to room temperature under a flow of argon (15 mL/min) to produce MoS_2@SWNT-B, which was collected.

6.4.5. Formation of $n[Mo_3S_7Br_6]^{2-}$@$SWNT^{2n+}$ and MoS_2@SWNT-C

$[Bu_4N]_2[Mo_3S_7Br_6]$ (21 mg, 0.0071 mmol) was dissolved in acetonitrile (3.5 mL) to form an orange/yellow solution, SWNTs (3, 7, or 11 mg) were added to the solution and was stirred for three days. The mixture was then filtered using a PTFE membrane, washed with acetonitrile (10 mL) until the filtered solution turned clear, and left to air dry resulting in $n[Mo_3S_7Br_6]^{2-}$@$SWNT^{2n+}$ which was collected. $n[Mo_3S_7Br_6^{2-}]$@$SWNT^{2n+}$ (3 mg) and iodine (3 mg, 0.012 mmol) were sealed in a Pyrex ampoule under a vacuum of 10^{-5} mbar. The ampoule was heated in a furnace for three days at 120 °C, and then left to cool and removed from the ampoule. The resultant material was then sealed in a Pyrex ampoule under 0.7 bar of Argon gas and then heated for one hour at 500 °C. The product, MoS_2@SWNT-C was then cooled to room temperature and collected.

6.4.6. Formation of WS_2@SWNT by using $H_3PW_{12}O_{40}$

WS_2@SWNT was synthesised using the experimental procedure in **sections 5.4.2. and 5.4.3.**

6.4.7. Formation of $n[Mo_3S_4Se_3Br_6]^{2-}$@$SWNT^{2n+}$ and Janus MoSSe@SWNT

The formation of $n[Mo_3S_4Se_3Br_6]^{2-}$@$SWNT^{2n+}$ and Janus MoSSe@SWNT were carried out using the experimental procedure described in **section 4.4.2.**

6.4.8. Electron microscopy and energy-dispersive x-ray analysis

Materials were dispersed in isopropyl alcohol using an ultrasonic bath and drop cast onto lacey carbon copper TEM grids (Agar Scientific). TEM analysis was performed using a JEOL 2100F field-emission gun transmission electron microscope operated at 80 or 200 kV. EDX analysis was carried out using an Oxford Instruments INCA X-ray microanalysis system. AC-HRTEM was performed using a C_c/C_s corrected sub-Ångström low-voltage electron microscope (SALVE) operated at 60 kV.

6.4.9. Raman spectroscopy

Materials were dropcast onto silicon (111) wafers using isopropyl alcohol or methanol. Micro Raman spectroscopy was performed using a Horiba Jobin Yvon LabRAM HR Raman microscope. Spectra were acquired using either a 532 or 660 nm laser (at ~0.2 mW power), a 100x objective and a 200 µm confocal pinhole. To simultaneously scan a range of Raman shifts, a 600 lines mm^{-1} rotatable diffraction grating along a path length of 800 mm was employed, conferring a spectral resolution better than 1.9 and 1.2 cm^{-1} for the 532 and 660 nm lasers, respectively. Spectra were detected using a Synapse CCD detector (1024 pixels) thermoelectrically cooled to −60 °C. Before spectra collection, the instrument was calibrated using the zero-order line and a standard Si (100) reference band at 520.7 cm^{-1}. For single point measurements, spectra were acquired over a minimum range 125-3400 cm^{-1} with an acquisition time of 15-120 seconds and 2 accumulations to automatically remove the spikes

due to cosmic rays and improve the signal to noise ratio. Spectra were collected from at least three random locations and averaged to give a mean spectrum.

6.4.10. Thermogravimetric analysis

Thermogravimetric analysis measurements were carried out using a TA Q500 thermogravimetric analyser. Samples were loaded onto platinum pans and heated in air from 25 to 1000 °C at a rate of 5 °C per minute, followed by an isothermal hold at 1000 °C for 10 mins.

6.4.11. Hydrogen Evolution Reaction Measurements

Electrochemical measurements were performed on a Metrohm PGSTAT302N Autolab workspace. HER measurements were carried out using a three-electrode cell with an electrolyte of 0.5 M H_2SO_4 using Ag/AgCl electrode as the reference electrode, and a Pt electrode as the counter electrode. The working electrode utilised a glass carbon electrode (diameter 3 mm) that was loaded with inks from the materials. In general, samples of X@SWNT (3 mg) and Nafion (5%, 25 µL) were dispersed in dimethylformamide (0.3 mL) and sonicated for 15 mins to produce the inks. 5 µL of each ink was dropcast onto the GCE surface and left to dry overnight. The scan rate for HER linear sweep polarisation measurements was kept at 5 mV s^{-1} and all potentials were calibrated to the reversible hydrogen electrode using the equation, $E_{RHE} = E_{Ag/AgCl} + (0.059 \times \mathrm{pH}) + 0.1988$.

6.5. References

1. N. S. Lewis and D. G. Nocera, *Proc. Natl. Acad. Sci. U.S.A.*, 2006, **103**, 15729-15735.
2. U. S. D. o. Energy, *International Energy Outlook 2013*, U.S. Energy Information Administration, Washington DC, 2013.
3. P. C. K. Vesborg and T. F. Jaramillo, *RSC. Adv.*, 2012, **2**, 7933-7947.

4. D. A. Lashof and D. R. Ahuja, *Nature*, 1990, **344**, 529-531.

5. I. Staffell, D. Scamman, A. Velazquez Abad, P. Balcombe, P. E. Dodds, P. Ekins, N. Shah and K. R. Ward, *Energy Environ. Sci.*, 2019, **12**, 463-491.

6. J. Tollefson, *Nature*, 2010, **464**, 1262-1264.

7. L. García, in *Compendium of Hydrogen Energy*, eds. V. Subramani, A. Basile and T. N. Veziroğlu, Woodhead Publishing, Oxford, 2015, pp. 83-107.

8. Z. W. Seh, J. Kibsgaard, C. F. Dickens, I. Chorkendorff, J. K. Nørskov and T. F. Jaramillo, *Science*, 2017, **355**, eaad4998.

9. M. A. Bird, S. E. Goodwin and D. A. Walsh, *ACS Appl. Mater. Interfaces.*, 2020, **12**, 20500-20506.

10. W. Sheng, Hubert A. Gasteiger and Y. Shao-Horn, *J. Electrochem. Soc.*, 2010, **157**, B1529 - B1536.

11. J. D. Benck, T. R. Hellstern, J. Kibsgaard, P. Chakthranont and T. F. Jaramillo, *ACS Catal.*, 2014, **4**, 3957-3971.

12. A. Alobaid, C. Wang and R. A. Adomaitis, *J. Electrochem. Soc.*, 2018, **165**, J3395-J3404.

13. C. C. L. McCrory, S. Jung, I. M. Ferrer, S. M. Chatman, J. C. Peters and T. F. Jaramillo, *J. Am. Chem. Soc.*, 2015, **137**, 4347-4357.

14. T. F. Jaramillo, K. P. Jørgensen, J. Bonde, J. H. Nielsen, S. Horch and I. Chorkendorff, *Science*, 2007, **317**, 100-102.

15. D. Voiry, M. Salehi, R. Silva, T. Fujita, M. Chen, T. Asefa, V. B. Shenoy, G. Eda and M. Chhowalla, *Nano Lett.*, 2013, **13**, 6222-6227.

16. Z. Ahmad, in *Principles of Corrosion Engineering and Corrosion Control*, ed. Z. Ahmad, Butterworth-Heinemann, Oxford, 2006, pp. 57-119.

17. N. Cheng, S. Stambula, D. Wang, M. N. Banis, J. Liu, A. Riese, B. Xiao, R. Li, T.-K. Sham, L.-M. Liu, G. A. Botton and X. Sun, *Nat. Commun.*, 2016, **7**, 13638.

18. Y. H. Chang, C. T. Lin, T. Y. Chen, C. L. Hsu, Y. H. Lee, W. J. Zhang, K. H. Wei and L. J. Li, *Adv. Mater.*, 2013, **25**, 756-760.

19. J. Hu, B. L. Huang, C. X. Zhang, Z. L. Wang, Y. M. An, D. Zhou, H. Lin, M. K. H. Leung and S. H. Yang, *Energy Environ. Sci.*, 2017, **10**, 593-603.

20. W.-H. Hu, G. Han, F.-N. Dai, Y.-R. Liu, X. Shang, B. Dong, Y.-M. Chai, Y.-Q. Liu and C.-G. Liu, *Int. J. Hydrogen Energy*, 2015, **41**.

21. L. Liao, J. Zhu, X. J. Bian, L. N. Zhu, M. D. Scanlon, H. H. Girault and B. H. Liu, *Adv. Funct. Mater.*, 2013, **23**, 5326-5333.

22. Z. Wu, B. Fang, Z. Wang, C. Wang, Z. Liu, F. Liu, W. Wang, A. Alfantazi, D. Wang and D. P. Wilkinson, *ACS Catal.*, 2013, **3**, 2101-2107.

23. D. J. Li, U. N. Maiti, J. Lim, D. S. Choi, W. J. Lee, Y. Oh, G. Y. Lee and S. O. Kim, *Nano Lett.*, 2014, **14**, 1228-1233.

24. Y. Li, H. Wang, L. Xie, Y. Liang, G. Hong and H. Dai, *J. Am. Chem. Soc.*, 2011, **133**, 7296-7299.

25. S. Xu, J. Xu, Y.-Z. Liu, Y. Hua, Z. Duan, Y. Wang, A. Neville and X. Gao, *ACS Appl. Energy Mater.*, 2019, **2**, 8974-8984.

26. C. H. Ravikumar, G. V. Nair, S. Muralikrishna, D. H. Nagaraju and R. G. Balakrishna, *Mater. Lett.*, 2018, **220**, 133-135.

27. H. Huang, W. Huang, Z. Yang, J. Huang, J. Lin, W. Liu and Y. Liu, *J. Mater. Chem. A*, 2017, **5**, 1558-1566.

28. Y. Shang, X. Xu, B. Gao and Z. Ren, *ACS Sustain. Chem. Eng.*, 2017, **5**, 8908-8917.

29. Y. Li, X. Yin, X. Huang, X. Liu and W. Wu, *Int. J. Hydrogen Energy*, 2020, **45**, 16489-16499.

30. F. Zhang, X. Pan, Y. Hu, L. Yu, X. Chen, P. Jiang, H. Zhang, S. Deng, J. Zhang, T. B. Bolin, S. Zhang, Y. Huang and X. Bao, *PNAS*, 2013, **110**, 14861-14866.

31. X. Han, Q. Gao, Z. Yan, M. Ji, C. Long and H. Zhu, *Nanoscale*, 2021, **13**, 1515-1528.

32. J. Deng, P. Ren, D. Deng, L. Yu, F. Yang and X. Bao, *Energy Environ. Sci.*, 2014, **7**, 1919-1923.

33. T. Cui, J. Dong, X. Pan, T. Yu, Q. Fu and X. Bao, *J. Energy Chem.*, 2019, **28**, 123-127.

34. A. Botos, J. Biskupek, T. W. Chamberlain, G. A. Rance, C. T. Stoppiello, J. Sloan, Z. Liu, K. Suenaga, U. Kaiser and A. N. Khlobystov, *J. Am. Chem. Soc.*, 2016, **138**, 8175-8183.

35. Z. Wang, H. Li, Z. Liu, Z. Shi, J. Lu, K. Suenaga, S.-K. Joung, T. Okazaki, Z. Gu, J. Zhou, Z. Gao, G. Li, S. Sanvito, E. Wang and S. Iijima, *J. Am. Chem. Soc.*, 2010, **132**, 13840-13847.

36. J. Bonde, P. G. Moses, T. F. Jaramillo, J. K. Nørskov and I. Chorkendorff, *Faraday Discuss.*, 2009, **140**, 219-231.

37. L. Cheng, W. Huang, Q. Gong, C. Liu, Z. Liu, Y. Li and H. Dai, *Angew. Chem. Int. Ed.*, 2014, **53**, 7860-7863.

38. M. Dave, A. Rajagopal, M. Damm-Ruttensperger, B. Schwarz, F. Nagele, L. Daccache, D. Fantauzzi, T. Jacob and C. Streb, *Sustain. Energ. Fuels*, 2018, **2**, 1020-1026.

39. M.-L. Grutza, A. Rajagopal, C. Streb and P. Kurz, *Sustain. Energ. Fuels*, 2018, 1893-1904.

40. Y. Lei, M. Yang, J. Hou, F. Wang, E. Cui, C. Kong and S. Min, *Chem. Commun.*, 2018, **54**, 603-606.

41. J. W. Jordan, G. A. Lowe, R. L. McSweeney, C. T. Stoppiello, R. W. Lodge, S. T. Skowron, J. Biskupek, G. A. Rance, U. Kaiser, D. A. Walsh, G. N. Newton and A. N. Khlobystov, *Adv. Mater.*, 2019, **31**, 1904182.

42. J. Kibsgaard, T. F. Jaramillo and F. Besenbacher, *Nat. Chem.*, 2014, **6**, 248.

43. D. Recatalá, R. Llusar, A. L. Gushchin, E. A. Kozlova, Y. A. Laricheva, P. A. Abramov, M. N. Sokolov, R. Gómez and T. Lana-Villarreal, *ChemSusChem*, 2015, **8**, 148-157.

44. C.-H. Lee, S. Lee, Y.-K. Lee, Y. C. Jung, Y.-I. Ko, D. C. Lee and H.-I. Joh, *ACS Catal.*, 2018, **8**, 5221-5227.

45. X. Ma, X. Wu, H. Wang and Y. Wang, *J. Mater. Chem. A*, 2018, **6**, 2295-2301.

46. W. Shi, G. Li and Z. Wang, *J. Phys. Chem. C*, 2019, **123**, 12261-12267.

47. J. Zhang, S. Jia, I. Kholmanov, L. Dong, D. Er, W. Chen, H. Guo, Z. Jin, V. B. Shenoy, L. Shi and J. Lou, *ACS Nano*, 2017, **11**, 8192-8198.

48. V. P. Fedin, M. N. Sokolov, Y. V. Mironov, B. A. Kolesov, S. V. Tkachev and V. Y. Fedorov, *Inorg. Chim. Acta*, 1990, **167**, 39-45.

49. V. P. Fedin, Y. V. Mironov, M. N. Sokolov, B. A. Kolesov, V. Y. Federov, D. S. Yufit and Y. T. Struchkov, *Inorg. Chim. Acta*, 1990, **174**, 275-282.

50. M. Makoto, M. Noritaka, K. Koichi, K. Atsushi, K. Yasuo, S. Kanji, O. Toshio and Y. Yukio, *Bull. Chem. Soc. Jpn.*, 1982, **55**, 400-406.

51. G. A. Tsigdinos, *Product R&D*, 1974, **13**, 267-274.

Chapter 7: Concluding Remarks

The design and tailoring of novel nanomaterials of sub-nm widths is a particular challenge of traditional synthetic chemistry, with problems such as dimensionality control, and oxidation by the atmosphere being primary drawbacks. Single-walled carbon nanotubes (SWNTs) are known as the world's smallest test tubes due to their nanometre-sized interior channel which templates the growth of quasi-1D structures. Once materials are encapsulated or synthesised within, the SWNT hosts are able to stabilise the guest species through electron donation or acceptance, as well as protect the ultrathin species from environmental damage.

This thesis has utilised the interior surface of SWNTs to produce a range of different transition metal dichalcogenide nanomaterials that, simply, are not possible to produce in bulk synthesis. Each chapter developed a methodology for synthesising a target species within SWNTs by initially selecting a suitable precursor that was able to be inserted via gas-phase or solution-phase encapsulation, and then transformed it via reaction with subsequent reagents that were also encapsulated within the channel, triggered by a source of energy or the electron beam in transmission electron microscopy (TEM).

In Chapter 2, a stepwise methodology towards the formation of ultrathin rhenium disulfide nanoribbons was developed; these nanostructures had only been previously studied computationally. A holistic analytical approach was employed to determine the structures, compositions, and electronic mechanisms at play. A combination of aberration-corrected transmission electron microscopy (AC-HRTEM) and energy-dispersive X-ray analysis were able to identify the structure of entrapped rhenium iodide as $[Re_6I_{14}]^{2-}$ clusters which were not known previously for rhenium. These clusters were established to be isostructural to tungsten analogues but were far more reactive under the electron beam producing $[Re_6I_{12}]_n$ continuous structures. The transformation of the rhenium iodide clusters to rhenium

disulfide resulted in twisted nanoribbons that, using a combination of structural modelling and TEM simulations, allowed the full structure to be determined. The distorted structure was the same as the bulk material, which has layer independent properties, but forming the quasi-1D structure within an electrically-conducting SWNT leads to applications as molecular scale electronic devices.

The successful formation of metal chalcogenides within SWNTs then led to the motivation to understand how the same starting material would behave when also physisorbed onto the convex surface of the SWNTs and subjected to the same reaction conditions as the material within the concave. Osmium was selected as the parent element to be studied as the iodide and disulfide species had not been studied before using SWNTs. To achieve the deposition of the starting material, $Os_3(CO)_{12}$, onto both surfaces, the material was sublimed in the presence of opened SWNTs followed by an absence of a cleaning step which ensured material remained on the convex surface. Upon formation of osmium iodide, both surfaces produced osmium monoiodide (OsI) but with different morphologies; the concave surface produced nanowires that were 3-coordiante whilst the convex surface with an absence of spatial confinement produced nanoparticles that were 6-coordinate species. The lower coordinate nanowires were found to be stabilised by the concave surface which curved around the structure. The transformation to produce osmium disulfide resulted in the concave surface again producing nanowires with helical twists, and the convex surface producing core-shell nanoparticles that consisted of a cubic core with hexagonal lattice shells. In terms of stabilisation of each species; the concave surface of the SWNT stabilised the OsS_2 nanowires, conversely, the cubic core of the nanoparticles contained a high number of dangling bonds which could not be stabilised by the convex due to the curvature away from the structure. Thus, a hexagonal lattice shell was constructed to minimise the surface energy. This was the first time OsI and the hexagonal form of OsS_2 were reported.

The two previous studies focussed on the production of metal disulfide species using metal carbonyls as the precursor due to their labile ligands. However, in Chapter 4 triangular molybdenum chalcogen clusters were encapsulated within SWNTs and studied using a combination of electron microscopy and spectroscopy techniques. These clusters can be viewed as molecular mimics of the edge sites of molybdenum disulfide monolayers and are of particular interest for catalytic studies. Raman spectroscopy was used to monitor any shifts in the position of the G-band of SWNTs; the insertion of $[Mo_3S_7Br_6]^{2-}$ and $[Mo_3S_4Se_3Br_6]^{2-}$ led to them acting as electron acceptors which resulted in their encapsulation being stimulated by coulombic attraction. Complementary X-ray photoelectron spectroscopy and TEM analysis were used to determine that the structure and composition of the clusters were retained upon insertion. Their subsequent transformations using iodine as a vapour transport agent produced MoS_2 and Janus MoSSe nanoribbons, with varying levels of iodine intercalation observed. Janus MoSSe had only previously been formed as a monolayer via either MoS_2[1] or $MoSe_2$[2] undergoing partial substitution, but formation of sub-nm structures is complicated by the exact 1:1:1 stoichiometry and asymmetrical arrangement required. This was overcome by the precursor cluster already having the required chalcogens preset in their positions above and below the molybdenum plane in a near correct atomic ratio.

For the most part of the previous investigations, the electron beam was used an imaging tool to determine the structure of nanomaterials. However, the electron beam has also be shown to be a source of energy that can trigger chemical reactions within the confinements of SWNTs.[3] Tungsten disulfide (WS_2) nanoribbons were synthesised within SWNTs using a new methodology that utilised fewer steps, as well as less harsh, and more energetically favourable conditions than previous studies.[4, 5] Their structure was initially probed using AC-HRTEM, but it was also found that the electron beam triggered the formation of atomic defects initially and then subsequently the removal of atomic chains which resulted in the top-down production of WS_2 nanowires of only one W atom in width; the narrowest in

literature. The synthetic procedure which employed polyoxometallates as the source of tungsten was then transferred to boron nitride nanotubes (BNNT) as the hosts. As well as nanoribbons being formed, quantum dots of WS_2 were also produced when excess boron blocked the nanotube channel ceasing the growth process. An extraordinary phenomenon was observed during the imaging of BNNT that contained amorphous material; the electron beam initiated and simultaneously captured the rearrangement of atoms into crystalline WS_2 quantum dots that underwent processes such as migration, and coalescence to minimise their surface energies.

As well as the synthesising novel materials, the potential applications of molybdenum and tungsten chalcogenide nanomaterials within electrically-conducted SWNTs were evaluated towards the Hydrogen Evolution Reaction. In Chapter 6, the electrocatalytic performance of MoS_2@SWNT, synthesised using three different methods, was examined. It was found that the synthetic route can have a dramatic effect on the performance, with species such as iodine having a negative impact. Quasi-1D WS_2 nanoribbons were found to perform slightly worse than their molybdenum analogues, produced using the same synthetic route, which was attributed to tungsten having a worse free energy of hydrogen absorption value. Encapsulated molecular mimics achieved higher catalytic abilities than continuous nanoribbons due to them possessing more accessible active sites. Finally, Janus MoSSe nanoribbons and their molecular mimics were found to be extremely effective electrocatalysts which is a result of the extra strain in their structures due to the asymmetry of the chalcogenides.

In conclusion, the work in this thesis has advanced the existing knowledge of transition metal dichalcogenides at the nanoscale by forming novel compounds and existing materials that have different structures and properties compared to their bulk equivalents. The holistic analytical approach, consisting of electron microscopy and a range of complementary

spectroscopic techniques, has probed not only the structures and compositions during each stage of each stepwise synthesis developed, but also the electronic mechanism at play providing new insights into how SWNTs communicate with different guest species. Moreover, these materials produced under the extreme confinement of SWNTs have proven to be much more than just the product of fundamental investigations by being functional as excellent electrocatalysts towards hydrogen production, which is viewed as the fuel of the future.

7.1. References

1. A.-Y. Lu, H. Zhu, J. Xiao, C.-P. Chuu, Y. Han, M.-H. Chiu, C.-C. Cheng, C.-W. Yang, K.-H. Wei, Y. Yang, Y. Wang, D. Sokaras, D. Nordlund, P. Yang, D. A. Muller, M.-Y. Chou, X. Zhang and L.-J. Li, *Nat. Nanotechnol.*, 2017, **12**, 744-749.
2. J. Zhang, S. Jia, I. Kholmanov, L. Dong, D. Er, W. Chen, H. Guo, Z. Jin, V. B. Shenoy, L. Shi and J. Lou, *ACS Nano*, 2017, **11**, 8192-8198.
3. T. W. Chamberlain, J. Biskupek, S. T. Skowron, A. V. Markevich, S. Kurasch, O. Reimer, K. E. Walker, G. A. Rance, X. Feng, K. Müllen, A. Turchanin, M. A. Lebedeva, A. G. Majouga, V. G. Nenajdenko, U. Kaiser, E. Besley and A. N. Khlobystov, *ACS Nano*, 2017, **11**, 2509-2520.
4. A. Botos, J. Biskupek, T. W. Chamberlain, G. A. Rance, C. T. Stoppiello, J. Sloan, Z. Liu, K. Suenaga, U. Kaiser and A. N. Khlobystov, *J. Am. Chem. Soc.*, 2016, **138**, 8175-8183.
5. Z. Wang, K. Zhao, H. Li, Z. Liu, Z. Shi, J. Lu, K. Suenaga, S.-K. Joung, T. Okazaki, Z. Jin, Z. Gu, Z. Gao and S. Iijima, *J. Mater. Chem.*, 2011, **21**, 171-180.